Alma Mater Studiorum – Università di Bologna

DOTTORATO DI RICERCA IN

SCIENZE DELLA TERRA, DELLA VITA E DELL'AMBIENTE

Ciclo XXXII

Settore Concorsuale: 04/A3

Settore Scientifico Disciplinare: GEO/04

UNSATURATED FLOW IN A STRUCTURALLY COMPLEX KARST AQUIFER

Presentata da: Alessia Nannoni

Coordinatore Dottorato

Prof. Giulio Viola

Supervisore

Prof. Jo De Waele

Co-Supervisore

Prof. Marco Antonellini

Esame finale anno 2020

Summary

The hydrological and hydrochemical data belong to the Bossea cave laboratory of karst hydrogeology, Polytechnic of Turin, coordinator Prof. Bartolomeo Vigna.

Thesis Abstract

The objective of this doctoral project was to unravel the functioning of the unsaturated zone of a karst aquifer that developed in a complex structural setting. The studied system, *Bossea* cave (Southern Piedmont, Italy) is located in the Ligurian Alps, in the vicinity of the tectonic limit between two tectonic sub-domains, the *Internal* and *External Briançonnaise*. A multidisciplinary approach was adopted to investigate the unsaturated flow dynamics of the system. Classical geological surveys coupled with structural analysis and thin-section microscopy permitted to draw a new geological map of the area and to recognize the main circulation pathways in the system. It appears that *Bossea* karst system developed taking advantage of a peculiar structural setting in which transpression between two regional left-lateral strike slip faults led to a disharmonic deformation of the Permian basement and the Mesozoic carbonates. Flow circulation developed along the bedding planes of the folded carbonate sequence, but when the water reached the disharmonic surface mechanical erosion of the basement non-carbonate rocks started. The downstream part of the cave developed along the disharmonic surface where the main underground river eroded huge volumes of the basement rocks, creating large rooms. The underground river and several secondary tributaries were equipped with multiparametric probes to monitor water level, temperature and electrical conductivity. The hydrological monitoring permitted to recognize a complex and heterogeneous architecture in the unsaturated zone. The secondary perennial tributaries that discharge water along the disharmonic surface are fed by small reservoirs developed in the fractured carbonate rocks above the detachment and partly in the basement rocks of the damage zone related to the detachment. These systems are influenced by the percolation dynamics in the unsaturated zone in case of overflow. The inflows that discharge from the cave roof show their characteristic hydrological behavior that is in turn controlled by the fracture organization and permeability in the unsaturated zone. The drip sites show a piston flow behavior, but each inflow has peculiar flow characteristics that are related to the drainage of small perched reservoirs in the fractured rocks of the unsaturated zone. The behavior of each inflow depends upon the permeability of the drained fracture networks. The recession analysis coupled with cubic law inversion and fractal analysis confirmed that the fracture network architecture controls the discharge of the vadose inflows. The heterogeneity of the system was also confirmed by hydrochemical investigations that permitted also to recognize the influence of the different lithologies on the discharge of the studied inflows. This cave represented a unique opportunity to study in detail

the dynamics of an unsaturated zone that is strongly influenced by inputs from different lithologies, in addition to the carbonates. Moreover, the availability of a huge amount of data collected for more than 15 years permitted to study this peculiar system in a wide range of conditions, from drought to extreme flooding events.

Chapter 1. Introduction

1.1. Hydrogeology of karst systems and introduction to the unsaturated zone

A karst system commonly develops in a highly fractured carbonate volume in which the permeability of the substrate has increased over time to the extent that the majority of water movement occurs below the surface (Bradley et al., 2010). Concentrated and diffuse seepage of autogenic and allogenic water due to precipitation and infiltration from surface runoff, progressively enlarge voids by dissolution. This process can lead to the formation of karst systems if protracted for extended periods of time. Three different kinds of porosity can be commonly distinguished in karstified rocks (Ford and Williams, 2007): 1) primary porosity of the host rock, generally extremely limited; 2) secondary porosity associated with open fissures (*sensu* Klimchouk and Ford, 2000) and; 3) tertiary porosity with solution-enhanced conduits. A classification of karst based on the proportion of these three types of porosity was made by Atkinson (1985) who related them to the predominant flow regime. The most characterizing feature of karst aquifers respect to porous aquifers is preferential flow of groundwater through open conduits rather than fractures (parallel flow) and matrix permeability (White, 2002).

Water circulation in karst aquifers is characterized by infiltration (diffuse vs concentrated), percolation (vadose vs phreatic) and flow (diffuse vs concentrated) dynamics (Hobbs and Smart, 1986; Smart and Friedrich, 1987; Perrin et al., 2003a; Ford and Williams, 2007). As Hobbs and Smart (1986) pointed out, these attributes are independent from each other and have different time scales so they can be distinguished. The distinction between diffuse and concentrated infiltration was first introduced by Burdon and Papakis (1963) who pointed out that the recharge style does not necessarily reflect the flow dynamic in the saturated zone. White (1969) coined the terms “diffuse flow” for diffuse circulation style and “conduit flow” for localized circulation. His classification of carbonate aquifers, therefore, is based upon the range of flow types that occur. Storage can occur in different portions of the system: soil (if there is any), epikarst, unsaturated zone and phreatic (saturated) zones.

Every karst system has its unique combination of lithology, structure, geomorphological history and climate (Williams, 2008). Clarifying the relationships among regional tectonics, local geological structures, and speleogenesis is important to predict the development of unconventional karst systems such as those where speleogenesis is strongly controlled by the geological setting rather than the chemical dissolution of the carbonate rocks. Examples of

unconventional karst systems are represented by those that develop at the contact between insoluble rocks and carbonates and/or in the presence of major tectonic discontinuities. In this situation, cave development is aided by the presence of tectonically deformed rock in the core and damage zones of faults, which is easily eroded by fast-running water (Antonellini et al., 2019). The prediction of karst development at a regional scale, in fact, is particularly challenging where solution speleogenesis is secondary and other processes (erosion and collapse) control cave formation. Nevertheless, knowledge of the spatial position, development, and depth of unconventional karst systems is important for water resources exploration, water pollution protection, and for the zoning of areas potentially exposed to flooding, subsidence or ground collapse (Gutiérrez et al., 2014). In recent years, structural geologists have focused their attention on the architecture of fault zones in different rock types, because of the strong control that faults exert on fluid flow (Caine et al., 1996; Kim et al., 2000; Rawling et al., 2001; Schultz and Fossen, 2008; Bense et al., 2013). The strongly deformed rock associated with fault zones, on the other hand, has also mechanical characteristics that promote erosion and chemical attack (Caine et al., 1996). Given that the rock is mechanically weakened in the core and damage zones of faults (Choi et al., 2016), it can be eroded by subterranean water circulation and contribute to the formation of underground cavities. Recently, Shanov and Kostov (2015) reviewed the relationships between tectonics and karst. The fundamental notion they highlight is the role of the tectonic and in-situ stress field in controlling brittle fracturing, which, in turn, controls the development of karst. The role of fractures and faults on controlling speleogenesis in different karst systems has been widely recognized (Klimchouk and Ford, 2000; Goldscheider, 2005; Stafford et al., 2005; Šušteršič, 2006; Pepe and Parise, 2014; Klimchouk et al., 2016; Čar, 2018). On the contrary, the control of the regional tectonic framework, of strongly deformed rocks or the assemblage of different structural elements (folds, large offset faults, transfer structures, detachment surfaces, disharmonic deformation structures, etc.) on karst formation is scarcely documented in the literature. A few studies described how regional tectonic uplift and neotectonics provided the energy necessary to karst development. In other words, different uplift rates contributed to the formation of different karst types (Ekmekçi, 2003, 2005). Miller (1996) relates the extent and position of karst systems in Belize to a control by major bounding faults. Goeppert et al. (2011) documented that small-scale poljes develop along the depression associated with the axis of a syncline fold in the Northern Alps of Austria. Weinberger and Rosenthal (1998) and later Frumkin and Fischhendler (2005) studied the

development of the karstic aquifers of the Judean Group in the region comprised between Tel Aviv to the west, and Judea-Samaria mountains to the east (Israel). They found out that groundwater lateral flow occurred from the axis of an anticline (where most of the autogenic recharge occurs) towards structurally and topographically lower regions where several small caves are found along the axes of other anticlines and synclines. Čar (1974) defined "covered karst" a system of vertical shafts developed below thrust fronts in the *Idrija* region, Slovenia; there the karst developed at the boundary between the overthrusted dolostone cap and the underlying limestone of the footwall. Pepe and Parise (2014) showed that the morphological pattern of the Apulian karst in Italy mainly follows the regional tectonic structures. Apulian river-karst valleys, in fact, are limited to the fault scarps bounding the *Serre Salentine*. Similarly, tectonics and major structures strongly controlled the development of karst corridors in the Southern Carpathians of Romania (Tîrlă and Vijulie, 2013). Recent works in Brazil showed how structural elements control karst development in both epigene (Silva et al., 2017) and hypogene conditions (Ennes-Silva et al., 2016; Klimchouk et al., 2016; Cazarin et al., 2019). Also, in epigenic evaporite karst systems the morphology of the voids is largely controlled by structural elements (Pisani et al., 2019).

The unsaturated zone of a karst aquifer is the portion of the system comprised between the land surface and the phreatic zone. From top to bottom, it is made up of a skin of soil (where it is present), the epikarst and the transmission zone (Bakalowicz, 1995; Fig. 1.1). Its thickness depends on the balance between the surface topography lowering rate by denudation and the rate of the water table falling by progressive opening of the voids due to karstification. The resultant thickness is a function of the relative rates of movement of its upper and lower limits. The development is also influenced by lithological heterogeneities, the presence of tectonic structures, and peculiar geomorphological features (Ford and Williams, 2007). The vadose zone plays a fundamental role in regulating the aquifer recharge by exerting control on both storage and downward water transfer. The relative importance of vadose storage and modes of transfers depends on the intensity of recharge and the saturation state of the system for a given geological context and system geometry (Arbel et al., 2008; Poulain et al., 2018). The epikarst is the topmost part of the vadose zone; it consists of a weathered zone of carbonate rocks that gradually gives way to the transmission zone that represents the main body of the unsaturated zone (mostly unweathered rocks). The definition of epikarst, its hydrological role in delaying the rainfall input to the saturated zone, and its significance in the geomorphological evolution

of the surface were defined during the 70s-80s (Bakalowicz, 2004 and Williams, 2008 and references therein). Several authors have highlighted epikarst efficiency in water percolation, especially in its bottom part where it focuses the water along vertical to sub-vertical pathways (Williams, 1983; Klimchouk et al., 1996; Klimchouk, 2000; Perrin et al., 2003a; Tooth and Fairchild, 2003; Hu et al., 2015).

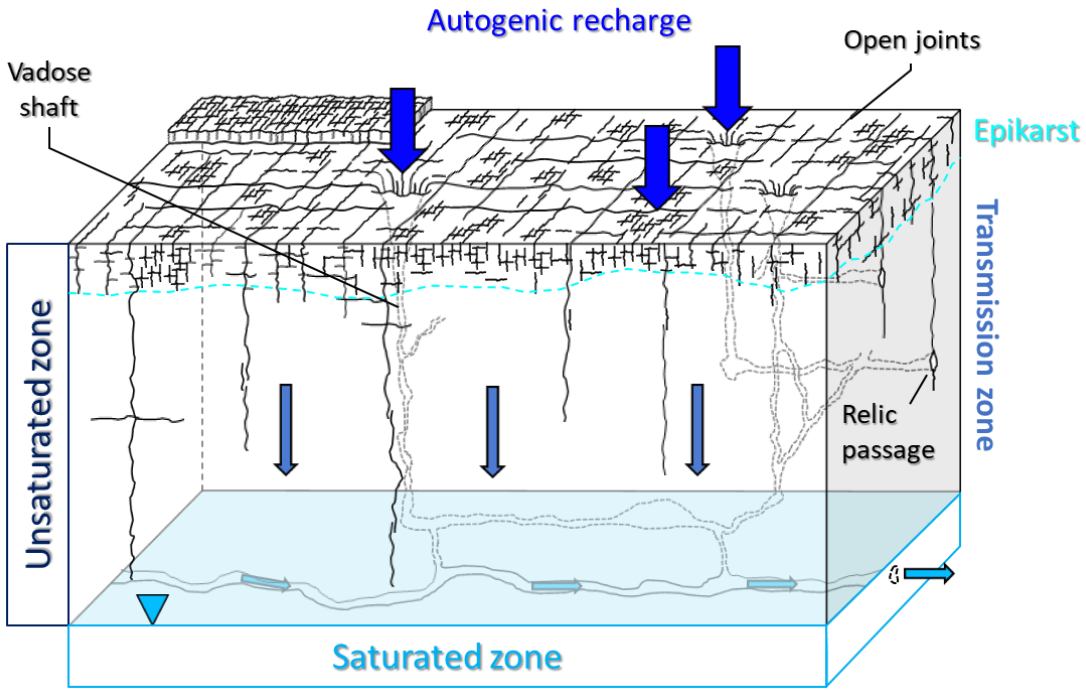

Fig. 1.1. Simplified sketch of a karst system (redrawn after Fairchild and Baker, 2012).

The storage in the epikarst is particularly important in case of thin to skeletal soil, especially during the dry seasons; in these contexts the uptake of water is strictly dependent upon the characteristics of the rock, largely its vertical hydraulic conductivity (Williams, 2008). The epikarst storage role is responsible for delay, mixing and dilution of recharge and the source of sustained feeding of vadose percolation during droughts (Genty and Deflandre, 1998; Baker and Brunsdon, 2003). Epikarst storage capacity, however, depends on its maturity and on the contrast in hydraulic conductivity between the epikarstic zone and the underlying vadose zone, hence its capacity changes throughout the karst evolution (Klimchouk, 2000).

Percolating water can potentially follow a variety of flow pathways through the karst system, depending upon the configuration of the drainage system but also on the factors that concur to surface water balance such as evapotranspiration and precipitation (Bradley et al., 2010).

Regarding the study of subsurface hydrology, the understanding of flow and transport in unsaturated fractured rocks is a challenging task because of the complexity of fracture-matrix interaction mechanisms and their nonlinear response to flow (Liu et al., 1998). Water flow in fractured rocks is further complicated in an unsaturated system due to the heterogeneity of fractures distribution at different scales. These planar features potentially have variable frequency, orientations, spatial extent, interconnections and apertures. Multiple conceptual models were developed for describing fracture flow and they all rely on the physical properties and geometry of individual fractures (Liu et al., 1998; Evans et al., 2001). The geometry of the fracture network strongly affects flow in multiple ways. The driving force for vadose fracture flow is gravity so that a vertical hydraulic gradient is established. When flow is restricted to fracture planes this assumption is correct if the fractures are vertical, otherwise the hydraulic gradient is reduced proportionally to the fracture dip. Gravity then acts in the direction of the dip of conductive fractures. Moreover, another possible consequence of fracture network geometry is flow focusing due to the presence of flow barriers and/or fracture intersections. Fractures force fluids to flow on discrete pathways which may be highly discontinuous. Continuity is the requirement for a fracture pathway to link surface recharge and subsurface storage. Variable connectivity of fracture networks is therefore a potential booster for focusing and hindering flow (Doe, 2001).

The study of the unsaturated flow has implications in many technical issues such as nuclear waste disposal, water quality assessments, long-term water management, and transport of contaminants (Dahan et al., 2001; Evans et al., 2001; Phillips, 2001; Pronk et al., 2008; Amiaz et al., 2011). Another important implication is the influence that vadose hydrology exerts on the growth of speleothems and the consequent implications on their use as paleoclimatic archives; understanding how the geochemical signal contained within them relates to past climate requires an understanding of the unsaturated zone hydrology (Baldini et al., 2006, 2012; Fairchild et al., 2006; Fairchild and Baker, 2012; Hartland et al., 2012; Tremaine and Froelich, 2013; Hartmann and Baker, 2017).

Determining the structure and the properties of the unsaturated zone, and of a karst aquifer in general, is difficult because only small portions of these systems are directly accessible (caves, boreholes) and direct acquisition of data is restricted to input (precipitation and runoff) and output (springs at catchment scale, drip sites for the unsaturated zone). An approach commonly used in the past was to model aquifer functions in terms of response to rainfall (input/output)

to treat a system as a black box, but it tells little of the structure and behavior of the karst aquifer. As Ford and Williams (2007) suggested, a more realistic approach is to treat the karst aquifer as a grey box, so that all the gathered information on subterranean conditions are used to infer the structure and to understand the behavior of the system.

The primary evidence of vadose flow is represented by drip sites that discharge water from the unsaturated portion of the aquifer. The heterogeneity of flow and storage in the unsaturated zone results in different drip flow characteristics (Fig. 1.2), as pointed out first by Gunn (1983), Smart and Friedrich (1987), Bottrell and Atkinson (1992), and then confirmed by Baker et al. (1997), Kogovšek (1997), Baldini et al. (2012), and Baker and Brunsdon (2003), who recognized the non-linearity of percolation response and the possibility of variable flow regime for an individual drip depending on the saturation conditions. The co-existence of four main flow mechanism were recognized and they have been conventionally adopted henceforth.

- "Subcutaneous flow" is defined as water flowing laterally through the epikarst.
- "Shaft flow" is defined as water flowing as films on the walls of vertical shafts.
- "Vadose flow" represents the vertical movement of water through enlarged fissures.
- "Seepage flow" is characterized by the vertical movement of percolating water through small, tight fissures and intergranular pores.

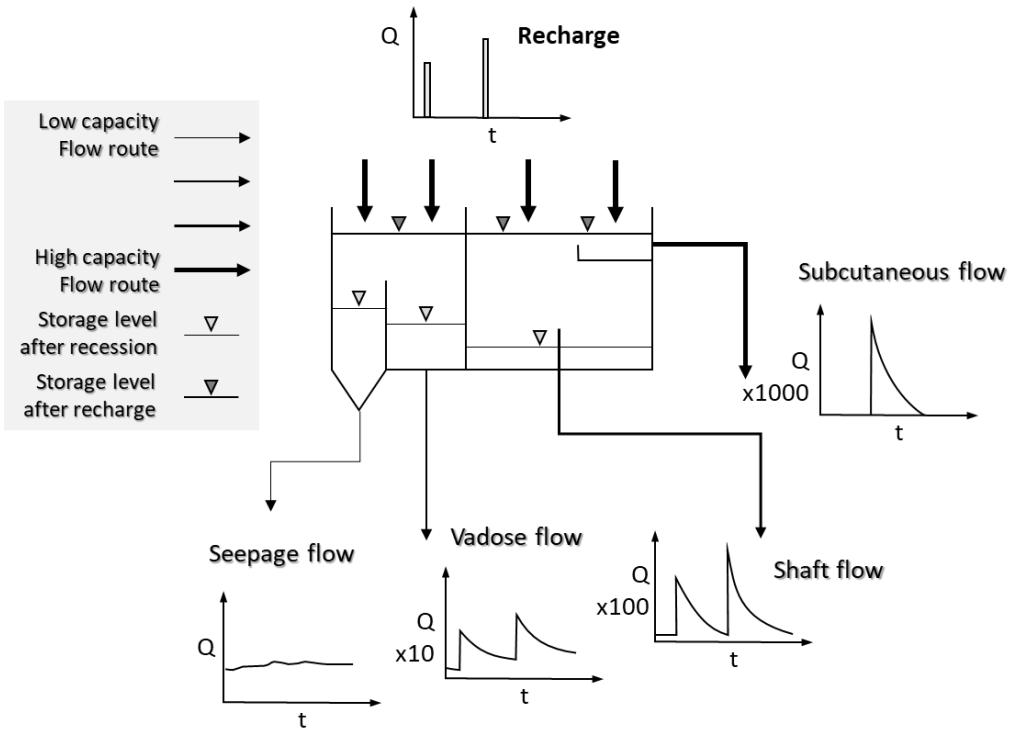

Fig. 1.2. Functional model of the unsaturated zone based on an analogy with pipes and partitioned storage tanks (Smart and Friedrich, 1987).

As a consequence, different drip types are distinguished by their dynamical behavior: (1) post-storm drips that only activate after considerable rainfall events, (2) seasonal drips that are active only during the wet season of the hydrological year, (3) perennial drips that are active throughout the whole year, and (4) overflow drips that activate only after infiltrated volumes exceeding a certain threshold (Hartmann and Baker, 2017).

The intrinsic complexity of karst systems, as highlighted in the previous paragraphs, demands to use multidisciplinary approaches to characterize their structure and the hydrological behavior. Several authors studied the seasonal behavior of either karst springs or vadose inflows. One of the most common approaches is karst spring monitoring of water discharge, temperature and conductivity that are easy to measure with relatively inexpensive data loggers, allowing for the collection of high-frequency data over long time periods (Berglund et al., 2019). The classical approach is to study the spring hydrograph response to recharge to measure the karstification of the aquifer and to infer the structure and transfer functions for the drainage in the system (Mangin, 1975; Bakalowicz, 1977; Bakalowicz and Mangin, 1980; Fiorillo, 2011, 2014). A common method to get insight on the water flow path and advection velocity is dye tracing. Artificial tracers are useful to define connections and to delineate spring catchment areas, to estimate geometric and hydraulic properties, and to identify the origin and fate of contaminants (Bottrell and Atkinson, 1992; Goldscheider et al., 2008; Hartmann et al., 2014; Poulain et al., 2015). Natural tracers such as water stable isotopes provide further information about karst systems although they do not allow on the identification of input locations. In particular, the variation of the $\delta^{18}O_{drip}$ signal has been broadly used for estimating flow transit times and for investigating the relationship between seasonality of the precipitation isotopic signature and the isotopic composition found in drip water. It has been found that the former mostly depends on the specific drainage system rather than the climate because of the several factors that alter the input rainfall signal (Even et al., 1986; Bar-Matthews et al., 1996; Perrin et al., 2003a; Lachniet, 2009; Hu et al., 2015; Duan et al., 2016). Another approach is to study the spatial variability of response of karst systems to infiltration by means of signal processing of rainfall and spring discharge time series data (Herman et al., 2009; Chen and Goldscheider, 2014; Delbart et al., 2014, 2016; Jukić and Denić-Jukić, 2015; Poulain et al., 2018). Other researchers focused on the hydrochemistry of either the unsaturated zone (Perrin et al., 2003b) or karst springs (Caetano Bicalho, 2010; Caetano Bicalho et al., 2012; Ravbar et al., 2012) to infer information on aquifer interconnectivity and sources at different catchment scales.

Hydrology exerts a dominant control on water chemistry and residence time, both of which determine the degree and characteristics of the water and its interaction with the host rock.

The intrinsic heterogeneity of karst flow is further complicated in case of structurally complex systems where the architecture of the aquifer is strongly controlled by tectonics and/or the drainage network that developed in different lithologies. In such systems, the use of multiple hydrochemical indicators is recommended to understand the contribution to flow from different compartments of the aquifer (Mudarra and Andreo, 2011; Raiber et al., 2012, 2015; Berglund et al., 2019). For this purpose, it is useful to consider major ion, trace element, and Rare Earth Element (REE) analyses together with chemograph interpretation. REE are a group of 14 elements including the Lanthanides that have similar chemical properties (Henderson, 1984). They are particularly useful in catchments with contrasting lithologies, because their concentrations and distributions in natural waters derive from the host rock composition. They can be used as tracers for inter-aquifer linkage (Johannesson et al., 1997b; Banks et al., 1999; Dia et al., 2000; Möller et al., 2006; Biddau et al., 2009; Noack et al., 2014; Gill et al., 2018) and to investigate the seasonal variability of recharge and mixing processes (Johannesson et al., 1997a; Tweed et al., 2006; Shiller, 2010; Duvert et al., 2015).

The aforementioned studies improved conceptual models of karst aquifers but, as pointed out by Berglund et al. (2019), critical knowledge gaps persist regarding flow paths and recharge processes. These gaps of knowledge are even more pronounced when dealing with exceptional conditions such as extreme flood events. Previous studies dealt with either karst springs or drip sites responses to precipitation events of various magnitudes but an integrated approach that involves the investigation of both springs and vadose inflows is not common. Studies on karst system response to flood events involved the monitoring of discharge and physico-chemical properties (water temperature and electrical conductivity) of karst springs and wells (Hess and White, 1988; Desmarais and Rojstaczer, 2002; Vesper and White, 2004; Doctor et al., 2006), commonly coupled with hydrochemistry and stable isotope analyses. The same approach was used also for drip site monitoring during floods (Baldini et al., 2006, 2012; Liu et al., 2014). Moreover, the monitoring of extreme events is difficult for the nature itself of this kind of phenomena: their recurrence interval spans from a couple of years to decades, depending on the climate conditions, especially in temperate regions, whereas they are more common in the monsoon region and consequently are better studied (Liu et al., 2004, 2007; Wu et al., 2018).

The main goal of this PhD thesis is to infer the flow dynamics in the unsaturated zone of a structurally complex karst system, the *Bossea* cave system (Southern Piedmont, Italy). The idea is that the study of vadose zone hydrology should be focused on individual systems because of the peculiar characteristics that each karst system displays due to the several factors that concur to its development and functioning. This individual site approach has been recently pointed out by authors that carried out high spatial and temporal resolution investigation of drip sites in different cave systems. They concluded that the extreme variability that they observed in the hydrodynamic response of each drip reflects a strong complexity of the unsaturated zone, constraining the study of recharge-vadose discharge to the individual systems (Jex et al., 2012; Markowska et al., 2015). It is also fundamental to use a multidisciplinary approach in order to obtain a more reliable characterization of the karst aquifer hydrogeology, even limiting the investigation to the unsaturated portion. This is even more true for unconventional karst systems such as *Bossea* where speleogenesis and hydrodynamic behavior were strongly affected by multiple phases of the Alpine orogenesis. Moreover, the *Bossea* cave is a good test site for unsaturated zone hydrology investigations, because it hosts an underground scientific laboratory that monitors karst hydrology, cave air quality, and cave fauna since the 70s (Vigna et al., 2017b).

1.2. Thesis structure

The thesis chapters are organized as follows: the first part of the thesis concerns the speleogenesis of the system and how it was influenced by the local geology (Chapter 2). This part was necessary to understand how water flow is organized in *Bossea*, moreover, a detailed geological knowledge of the study area was lacking. Chapter 3 gives an overview of the hydrological characteristics of the drip sites (vadose inflows and tributaries) monitored inside the cave that are compared with each other and with the hydrodynamic behavior of the main underground river that is fed by these secondary tributaries. Chapter 4 describes the methods used to unravel the architecture of the drainage system of the most important drip sites and springs as well as their relationship with the structural setting. Chapter 5 deals with the hydrochemistry of the monitored inflows described in the previous chapters and discussing their relationship with the hydrodynamic conditions. Finally, Chapter 6 describes the behavior of the system (both unsaturated inflows and the underground river) during extreme conditions such as those occurred during a flood event happened in November 2016 and in 2011. A scientific paper

based on Chapter 2 was published in Geomorphology (Antonellini et al., 2019), whereas another manuscript based on Chapter 6 is going to be submitted to the Journal of Hydrology.

Chapter 2. Geological setting and speleogenesis of Bossea cave

2.1. Geological and geomorphological overview

2.1.1 Regional geological setting: the Ligurian Alps

The study area is located in the western Ligurian Alps (Fig. 2.1), near the junction with the Maritime Alps, in a NW-SE striking area comprised between *Col de Larche* to the W and the upper *Tanaro* valley to the E (d'Atri et al., 2016). This area represents the southernmost termination of the Western Alps, where the outcropping tectonic units belong to four different paleogeographic domains (Decarlis et al., 2013). These adjacent domains represent the transition from the oceanic realm to the passive continental margin of Europe that were progressively stacked during the Alpine orogenesis (Cortesogno and Vanossi, 1984; Vanossi, 1984). From top to bottom there are the Piedmont-Ligurian units (oceanic crust and its cover), the Prepiedmont nappes (margin of the European continent), the Briançonnais (transition between proximal and distal continental margin) and the Dauphinois (distal continental margin). The present-day architecture of the Ligurian Alps is the result of the successive deformation phases occurred during the Alpine orogenesis. According to the literature, four to five main deformation events were recognized in this sector of the chain (Seno et al., 2005a; Piana et al., 2009; Bonini et al., 2010; Mosca et al., 2010; Maino et al., 2013; Barale et al., 2016; d'Atri et al., 2016; Maino et al., 2013; Mosca et al., 2010; Piana et al., 2009; Seno et al., 2005a):

I. A first composite ductile deformation phase (D1) locally referred to Late-Eocene – Early Oligocene and caused by the subductive-accretionary processes; the tectonic units underwent different degrees of metamorphism, depending on their position within the orogenic wedge. The first exhumation processes that are responsible for the thrusting towards SSW of the Briançonnais units and for the development of steep sinistral transpressive shear zones occurred during this phase.

II. A second ductile phase (D2, Chattian – Aquitanian) that corresponds to coaxial back-folding associated to transpression in lower greenschist conditions. The new generation of folds are generally tight and NE-vergent with vertical to steeply SW-dipping axial planes and fold axes gently dipping towards NW or SE. A well-spaced crenulation is associated to the folding. During this stage, the NW-SE striking shear zones were re-activated mostly in a dextral transpression regime and steep reverse major faults cut the

D1 structures. These structures are ascribed to the switch from sinistral transpression to compression in the whole Western Ligurian Alps.

III. A third phase (D3) that generated weakly SSW-vergent open folds and SW-vergent thrusts with an associated subvertical N-dipping fracture cleavage. Flower structures developed in the most internal part of the chain. This deformation phase is ascribed to the N-S shortening during middle Miocene.

IV. Two secondary brittle phases (D4, D5) that caused minor displacement along E-W and NNE-SSW striking faults. Their stress/strain regime and timing are poorly resolved because they resulted from the concomitance of several tectonic events, such as the spreading of the Liguro-Provençal basin, the rotation of the Ligurian Alps-Piedmont Tertiary Basin system and the drifting of the Corsica-Sardinian block. The late-orogenic evolution (D4-D5) of the Ligurian Alps is coeval with the deposition of the Piedmont Tertiary Basin (PTB) sedimentary succession.

After these main stages, other relevant brittle deformation phases occurred from late Miocene to early Pleistocene, as recently recognized in the Piedmont Tertiary Basin (Ghielmi et al., 2019). Compression and transpression alternated during these late phases, reactivating NW-SE and NE-SW striking faults. The current geometric arrangement is mainly due to the D2 and D3 phases (responsible for the alignment along the WNW-ESE direction of these units) and secondarily to the late brittle phases.

The rocks outcropping in the study area belong to the Briançonnais domain. This domain is well exposed from the central to the Ligurian Alps, where it is named Ligurian Briançonnais. More specifically, the *Bossea* karst system is located in the Internal Ligurian Briançonnais (ILB), about 10 km north of the boundary with the External Ligurian Briançonnais (ELB). The main difference between the two sub-domains is that the ILB was involved in the subduction during the Alpine orogenesis, while the ELB was not. The result is a difference in the metamorphic grade exhibited by the two sub-domains, the ELB showing from no-metamorphism to the anchizonal one (preserving most of its sedimentary structures), while ILB displays greenschist to blueschist facies (Messiga, 1987). The ILB shows a progressively lower metamorphic grade going from NW (blueschist) to SE (greenschist). The boundary between the ILB and ELB is marked by a km-wide shear zone referred alternatively to *Verzera* shear zone (Seno et al., 2005b; Piana et al., 2009), *Pian Bernardo* fault (Bonini et al., 2010) or Internal Briançonnais Front (d'Atri et al., 2016); this structure is NW-SE oriented and shows individual

ductile to brittle shear zones throughout its development. The ELB outcropping to the SE of the study area is represented by a complex system of sinistral transpressive faults arranged in an anastomosed setting that resembles an asymmetric flower structure (*Limone-Vionzene* Zone; Piana et al., 2009; d'Atri et al., 2016).

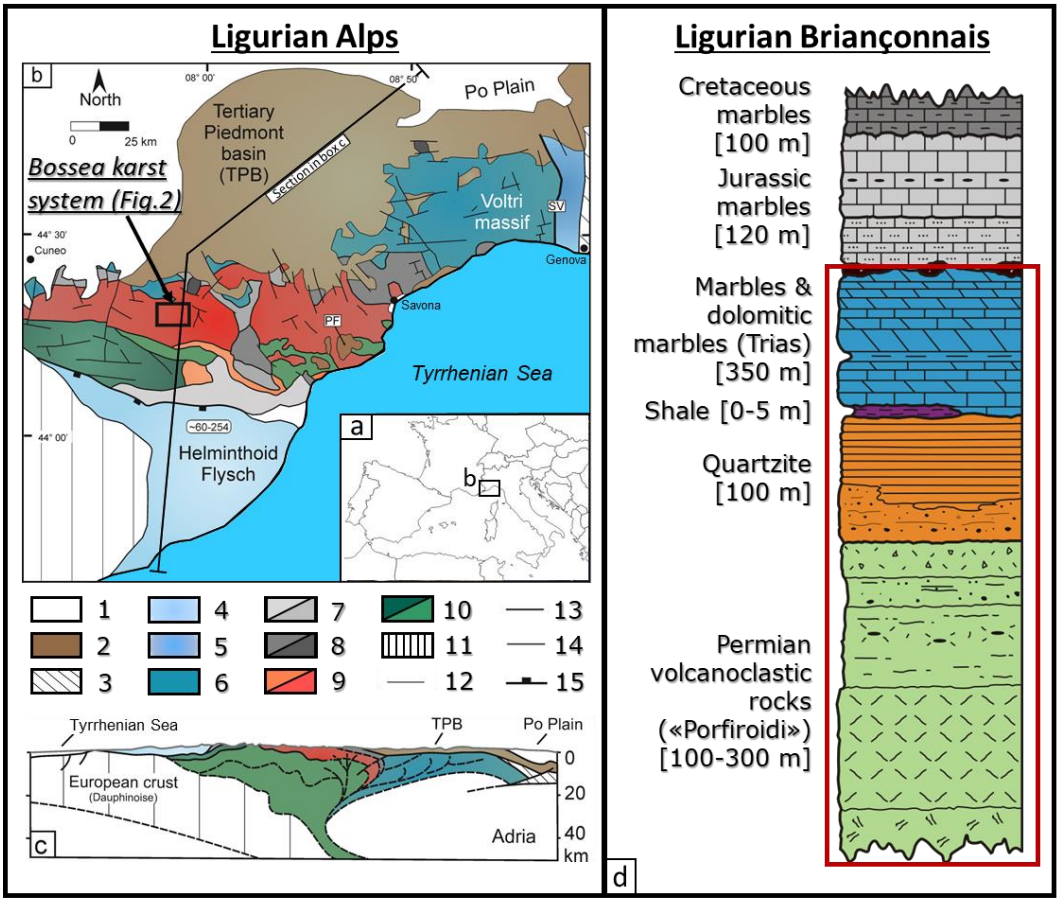

Fig. 2.1. Map of the Ligurian Alps and location of the *Bossea* karst system (modified after Maino et al., 2012). (a) Index map. (b) Simplified regional geological map. Legend: 1. Plio-Quaternary deposits, 2. Oligo-Miocene deposits, 3. Apennine units; Piedmont-Ligurian units: 4. Helminthoid Flysch, 5. *Sestri-Voltaggio* zone, 6. Ophiolitic units; Pre-piedmont units: 7. Meso-Cenozoic cover, 8. Pre-Variscan basement; *Briançonnais* units: 9. Internal units, 10. External units; 11. *Dauphinois* units. Structural elements: 12. Unconformity, 13. Thrust, 14. Major late/post orogenic faults (D4/D5), 15. Detachment fault. Late alpine faults: PF. Pietra Finale, SV: Sestri-Voltaggio. (c) Crustal cross-section across the Western Alps. The trace of the cross-section is in (b). (d) Stratigraphic section for the Ligurian *Briançonnais*, the red rectangle evidences the portion outcropping in the *Bossea* area.

2.1.2. Stratigraphy

The Ligurian Briançonnais consists of Permian volcanic and volcanoclastic rocks covered by a partially detached Meso-Cenozoic sedimentary sequence. The Late Paleozoic volcano-sedimentary succession rests unconformably on the Variscan basement (not outcropping in the

study area). The Ligurian Briançonnais shows different degrees of deformation and metamorphism, both decreasing from the internal to the external sectors (Bertok et al., 2011). The ILB generally shows a less complete stratigraphic succession with respect to the ELB.

The deformed sedimentary sequence exposed in the study area pertains to the ILB (Fig. 2.1d). The succession starts with the highly-deformed Permian volcanoclastic rocks traditionally named *Porfiroidi di Melogno*. This volcano-sedimentary succession is highly variable in terms of thickness and facies (Vanossi, 1991; Decarlis et al., 2013) and locally is represented by the lithozone B that is composed of rhyolitic to rhyodacitic ignimbrite deposits with abundant quartz and K-feldspar phenocrysts. The succession then continues with the Briançonnais *Verrucano*, represented by the coarse-grained quartz-arenite and conglomerates of the *Ponte di Nava* Quartzites, followed by thin beds of *Case di Valmarenca* Pelites. The Meso-Cenozoic succession begins with the Triassic carbonate (dolostones and limestones) platform of *Costa Losera-San Pietro dei Monti* formations, mostly eroded in the ILB due to the uplift of the internal sectors of the Briançonnais. During the Upper Triassic, the Ligurian Briançonnais carbonate platform emerged, interrupting the sedimentation. The resulting sedimentation gap is marked by the *Siderolitico* paleo-karstic level (Decarlis and Lualdi, 2008). The sequence continues, outside of the study area, with the *Val Tanarello* limestones that witness the progressive drowning of the platform (Decarlis and Lualdi, 2008). The deposition of these limestones ended between Late Jurassic and Early Cretaceous and its upper limit corresponds to a regional unconformity (Decarlis et al., 2013). The sequence ends with the deposition of hemipelagic sediments in the Upper Cretaceous (d'Atri et al., 2016).

Metamorphic conditions in the *Bossea* area should be those typical of the greenschist facies, where chlorite–albite paragenesis developed in basement and Carboniferous–Permian rocks, pointing to temperatures of about 350 °C and pressures less than 0.4 GPa (Messiga, 1987). The whole sequence outcropping in the study area is metamorphosed, so that meta-volcanics, quartzite, shales and marbles are found instead of their corresponding protoliths.

2.1.3. Bossea Karst System

The *Bossea* karst system is located in the Ligurian Alps of Southern Piedmont (Northern Italy). It belongs to the most extended karst area of Piedmont, going from Colle di Tenda in the southwest to the Ligurian border in the southeast. More specifically, the study area is part of the *Marguareis-Mongioie-Tanaro* valley karst sector (Fig. 2.2). This karst area is characterized

by several carbonate blocks separated by subvertical tectonic lineaments broadly ENE-WSW striking (Fig. 2.2). These high-angle faults put the Mesozoic carbonate sequence laterally in contact with the originally underlying Permian (meta-volcanoclastic breccia) to lower Triassic continental (quartzite and shales) sequence. Compartments of meta-carbonate rocks (marbles) are separated from each other by the interposition of the Permian volcanoclastic sequence and quartzite slabs that act as aquicludes (*Impermeable complex*, Fig. 2.2), limiting the areal development of karstification and creating independent hydrogeological sectors, occasionally interconnected in complex structures (Civita and Vigna, 1985).

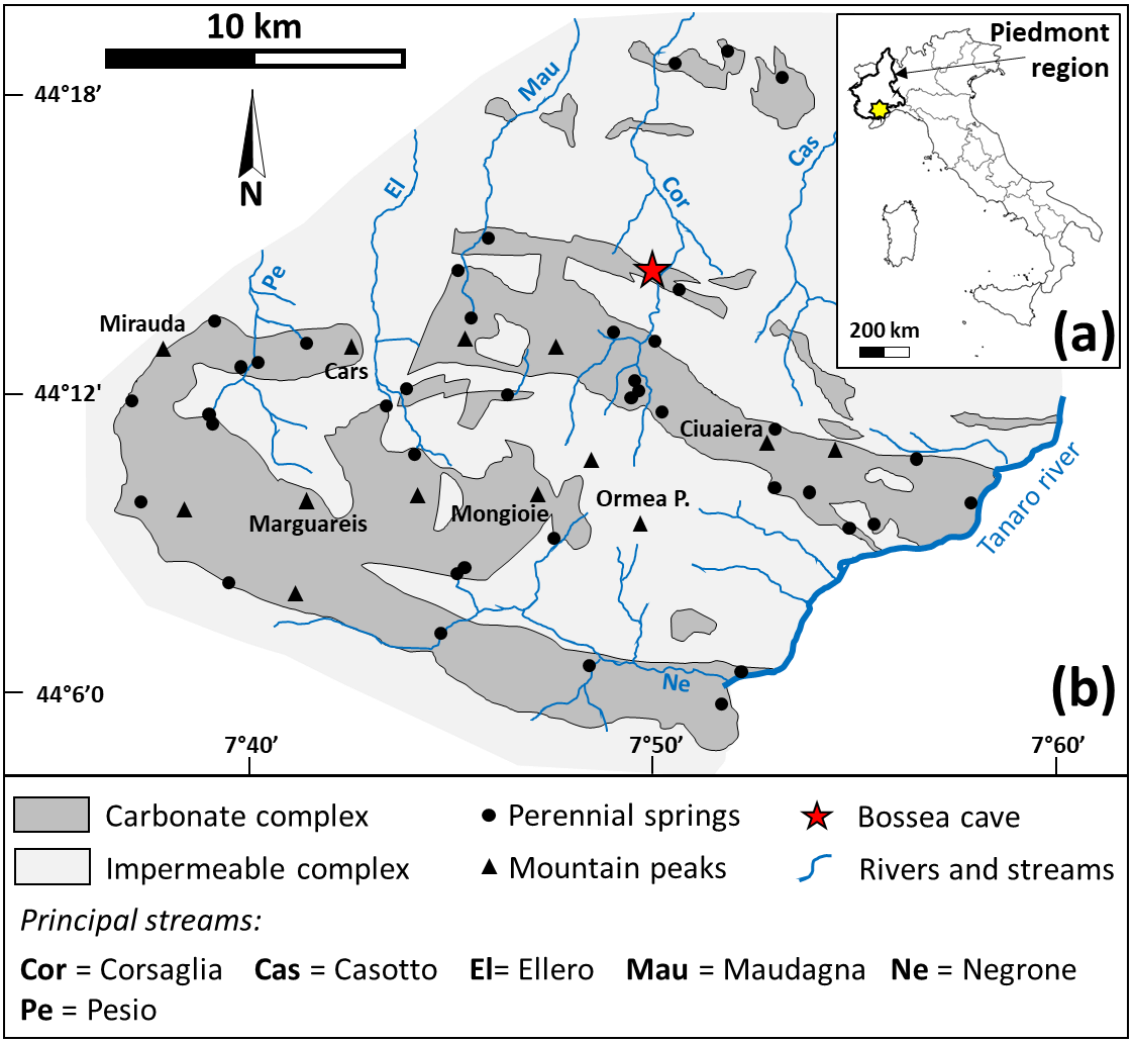

Fig. 2.2. (a) Map of Italy and position (yellow star) of the area reported in (b). (b) Overview of the karst systems in the carbonate outcrops of Southern Piedmont. Modified after Civita and Vigna (1985) and Civita et al. (1990).

The *Bossea* catchment is comprised between 800 and 1700 m asl and it drains water from the mid-section to the upper section of *Corsaglia* valley and from the uppermost section of

Maudagna valley (Civita and Vigna, 1985; Peano et al., 2005; Vigna and Doleatto, 2008). It is a colluvium covered mid-altitude karst: the surface morphology is characterized by steep SE facing slopes with bare rock outcrops and thin soil cover. Land cover, where it is present, is mainly composed of broadleaf forest with *Laryx* alternated with mountain meadows (Vigna et al., 2017a). Recharge is partly diffuse and partly from allogenic streams and brooklets that drain the less permeable meta-Permian rocks and the quartzite (Banzato et al., 2011). The catchment covers an area of about 5.5 km^2.

The recharge area comprises a series of losing valleys (*Roccia Bianca* and *Bertino* brooks) with modest flowrates that vary according to the meteorological conditions. The western limit of the karst system lies in correspondence of the *Prato Nevoso* doline, that acts as groundwater divide with the *Maudagna* catchment, the surface divide being *Colle del Prel* (Civita and Vigna, 1985). The karst system is bordered by two WNW-ESE striking strike-slip faults segments, the *Prel* line to the north and the *Fontane* line to the south, locally interrupted and displaced by an orthogonal (broadly N-S) secondary strike-slip fault that lies close to the *Prato Nevoso* ski station. The downstream terminal part of the karst system is represented by the *Bossea* show cave. The cave is nearly 3 km long and can be subdivided in two portions: an upper and a lower one (Fig. 2.3). In the upper portion, the main underground river (*Mora* creek) flows along a canyon carved in a Mesozoic meta-carbonate (marble) sequence. A complex system of relic phreatic tunnels develops above the canyon segment. The uppermost upstream part of the cave ends with two sumps (964 m asl) connected by a network of phreatic conduits. The submerged part of the system was explored by cave divers for a few hundreds of meters (reaching a water depth of -70 m below ground), but it probably extends up to some kilometers (Vigna and Doleatto, 2008; Peano et al., 2011; Vigna et al., 2017a). The lower portion starts at *Ernestina*'s waterfall (942 m asl) and develops along the contact between the Mesozoic marbles and the underlying Permian meta-volcanic sequence. Large rooms and massive gravitational collapses characterize this segment of the cave. Over 70% of the rock volume removed during the development of the rooms was occupied by meta-volcanic rocks, the marble sequence outcropping mostly on the cave roof. There are abundant speleothem deposits all over the cave, covering most of the Permian-Mesozoic sequence. Some of these large flowstones and stalagmites are inclined or deformed due to not fully understood mechanisms. The water resurfaces 130 m lower (812 m asl) in the *Corsaglia* River (one of the main tributaries of *Tanaro* River) from a set of springs. The cave entrance (836 m asl) is a semi-active tunnel that drains

water during very strong rainfall events, when the springs of *Bossea*, developed along narrow fractures, are not able to discharge the entire water flow (Peano et al., 2005).

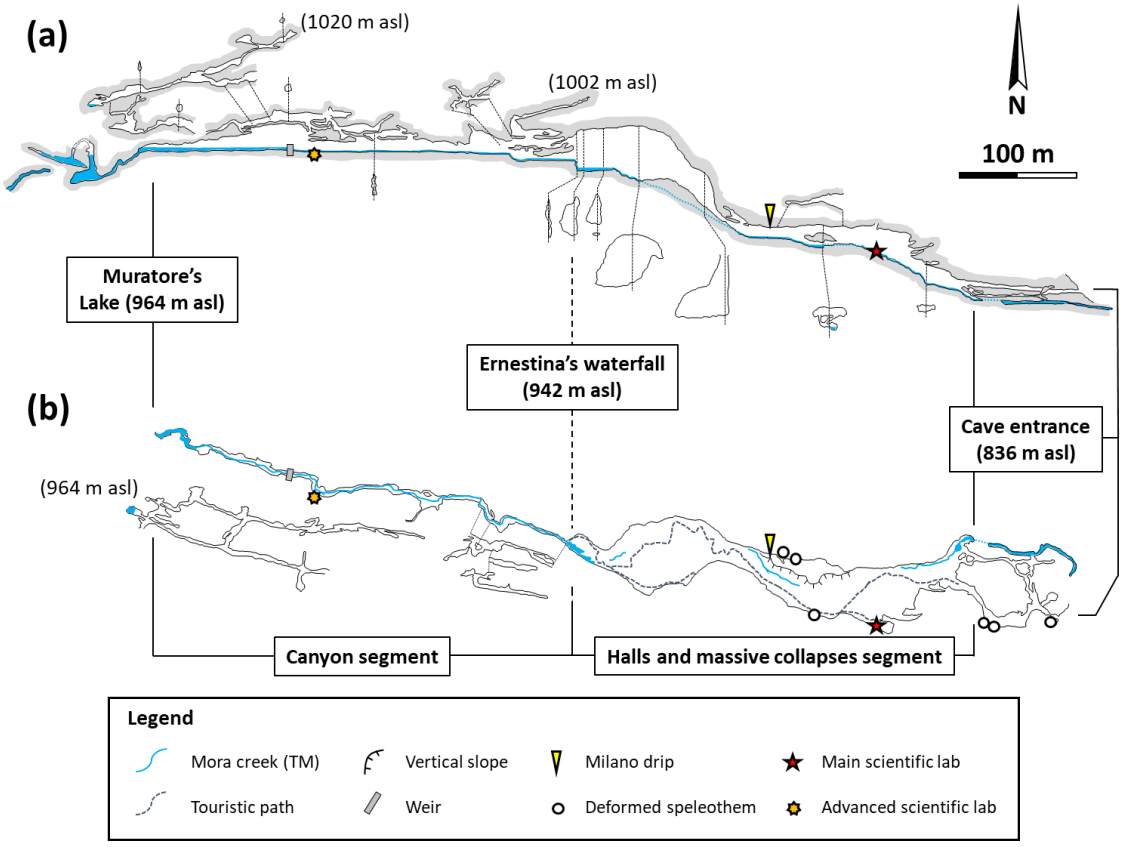

Fig. 2.3. Vertical long profile (a) and plan view (b) of the *Bossea* karst system (modified after Balbiano D'Aramengo, 1993). See Fig. 2.4a for the position of *Bossea* cave.

2.2. Methods

2.2.1. Structural Geology Survey

Classical surveying and structural geology mapping techniques were used both at the surface outcrops and in the underground environment (cave) to characterize the attitude of bedding, cleavage, fractures, their geometry, and their crosscutting relationships. Cleavage refers to a large subgroup of foliation found in very low-grade to barely metamorphic rocks (Powell, 1979; Fossen, 2016). The term fracture is here used as a general definition *sensu* Aydin (2000), which includes the following tectonic discontinuities: veins, stylolites, joints, and faults. Faults are considered fractures with shear displacement (II or III mode), joints are opening mode I fractures, and veins are opening mode I fractures filled with mineral (Pollard and Segall, 1987;

Schultz and Fossen, 2008). The surface data points coordinates were acquired with a high-resolution GPS system. All data were organized in an Excel™ database and then imported into a Geographic Information System (Qgis version 2.1.8 2017) with base maps of the *Regione Piemonte*. The orientation of bedding, cleavage, and fractures were measured with a Brunton™ geologic compass. The attitude data of the bedding, cleavage, fold axes, and fractures (joints, veins, and faults) were plotted by using the Stereonet v.9.3.3 software by Allmendinger et al. (2011). We also used high-resolution digital photographs (1500 dpi), enlarged to a scale ranging from 1:1 to 1:20, to document the details of the fracture network.

A total of 215 structural measurements were collected both inside the *Bossea* cave and in surface outcrops surrounding the cave. The rock sequence is perfectly exposed along *Corsaglia* riverbed where the rock sequence is perfectly exposed due to a recent flooding event (November 2016) that removed the river bottom sediments. Other outcrops are on the slope above the cave and on the slopes on the other side of the *Corsaglia* valley. The *kmz* file with the location of all surface outcrops can be found in the supplementary material.

Disharmonic deformation refers to a part of a layered sequence that detaches from the basement or from another section of the sequence itself and deforms differently from the rest of the sequence or basement (an example are the tight isoclinal folds in the marble above the meta-volcanics) (Twiss and Moores, 1992). Disharmonic folds occurring above a detachment surface are also called detachment folds. A detachment surface (or disharmonic tectonic surface) is the surface separating the two parts of the sequence that have deformed with different styles (tight isoclinal disharmonic detachment folds in the marbles – intense cleavage and buckling in the meta-volcanics).

Regarding the nomenclature of faults zones, the one presented by Caine et al. (1996) is used. In particular, the core of the fault is the narrow, high strain zone where most of the slip and shear is accommodated and cataclastic rocks and breccia occur; it may contain one or more slip surfaces. The damage zone of the fault is the rock volume surrounding the core where the fracture frequency is above the background values of the undeformed protolith (Caine et al., 1996; Choi et al., 2016).

2.2.2. Microstructural analysis

Fifteen oriented samples were collected for microstructural analysis. Seven samples come from the surface outcrops of Triassic marble and carbonate rocks. Nine samples were collected in the

cave: (a) three samples from the fault rock (core zone) at the tectonic contact between the folded marbles and the meta-volcanics; (b) three samples in the deformed meta-volcanic basement rocks (damage zone of the detachment); (c) Two samples from the tectonically deformed Triassic quartzite next to the major shear zone; (d) one sample in the Triassic dark shales. A set of 25 thin-sections impregnated with clear epoxy were prepared from the samples listed above and analyzed at the microscope under polarized and crossed nicols light to study the mineralogy, the micro-deformation processes, and to assess the primary and secondary porosity.

The thin sections were investigated with a polarizing microscope Wild M420 equipped with a digital camera at 12 megapixels resolution (Nikon D4400). Standard optical microscopy analysis was performed on the thin sections to recognize also the different kind of grains, the pore types, the types of cement, and the diagenetic history of the samples.

2.3. Results

2.3.1. Structural setting of the Bossea area

The results of the structural geology surveys and cross-sections are shown in Figures 2.4 and 2.5. Two major E-W to WNW-ESE oriented, vertical left-lateral strike-slip faults (*Linea del Prel* and *Linea di Fontane*, Fig. 2.4 and 2.6c) with offsets in the order of hundreds of meters (or more) confine the marble outcrops to a strip with a width of about 1 km. The strike-slip fault in the north (*Linea del Prel*) puts in tectonic contact the Triassic quartzite with the marbles of the Triassic carbonate sequence. The strike-slip fault in the south (*Linea di Fontane*) puts in tectonic contact the marbles with the meta-volcanics. The marbles of the carbonate sequence in the overlap region between the major faults are tightly folded (isoclinal folding) with fold axes oriented NW-SE in the western portion of the area and WNW-ESE in the eastern portion (Figs. 2.4 and 2.6d). Steeply-dipping bedding-parallel reverse faults with offsets from below a meter to a few tens of meters are oriented parallel to the fold axes (Fig. 2.4). Some of these reverse faults put in tectonic contact the quartzite with the marbles. In addition, a few bedding-parallel left-lateral strike-slip faults with well-developed horizontal striae were observed along the *Corsaglia* River; the offset along these faults is in the order of meters to a few tens of meters. A NE-SW-oriented lineament cuts across the *Bossea* Cave (Figs. 2.4 and 2.5b).

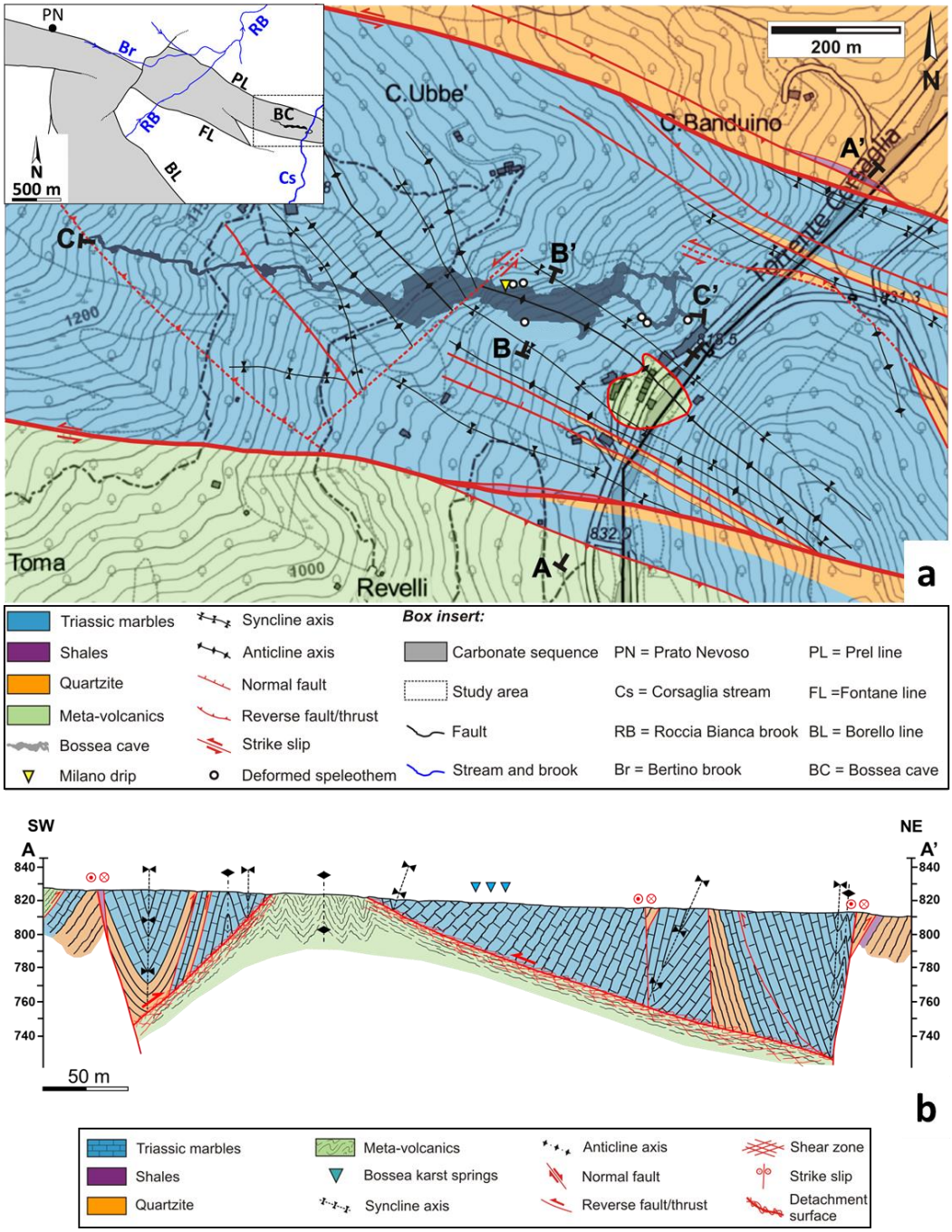

Fig. 2.4. (a) Geological map of the *Bossea* area from surface and cave surveys, the topographic map of the area (equidistance of 50 meters) is used as base map for the geological map. (b) AA' cross-section.

This lineament divides the upper part of the Bossea karst system from the lower one and also marks the change in orientation of the fold axes as mentioned above; it probably has a normal and left-lateral component of movement. It may also be a splay of the detachment surface below (see cross-section in Fig. 2.5b).

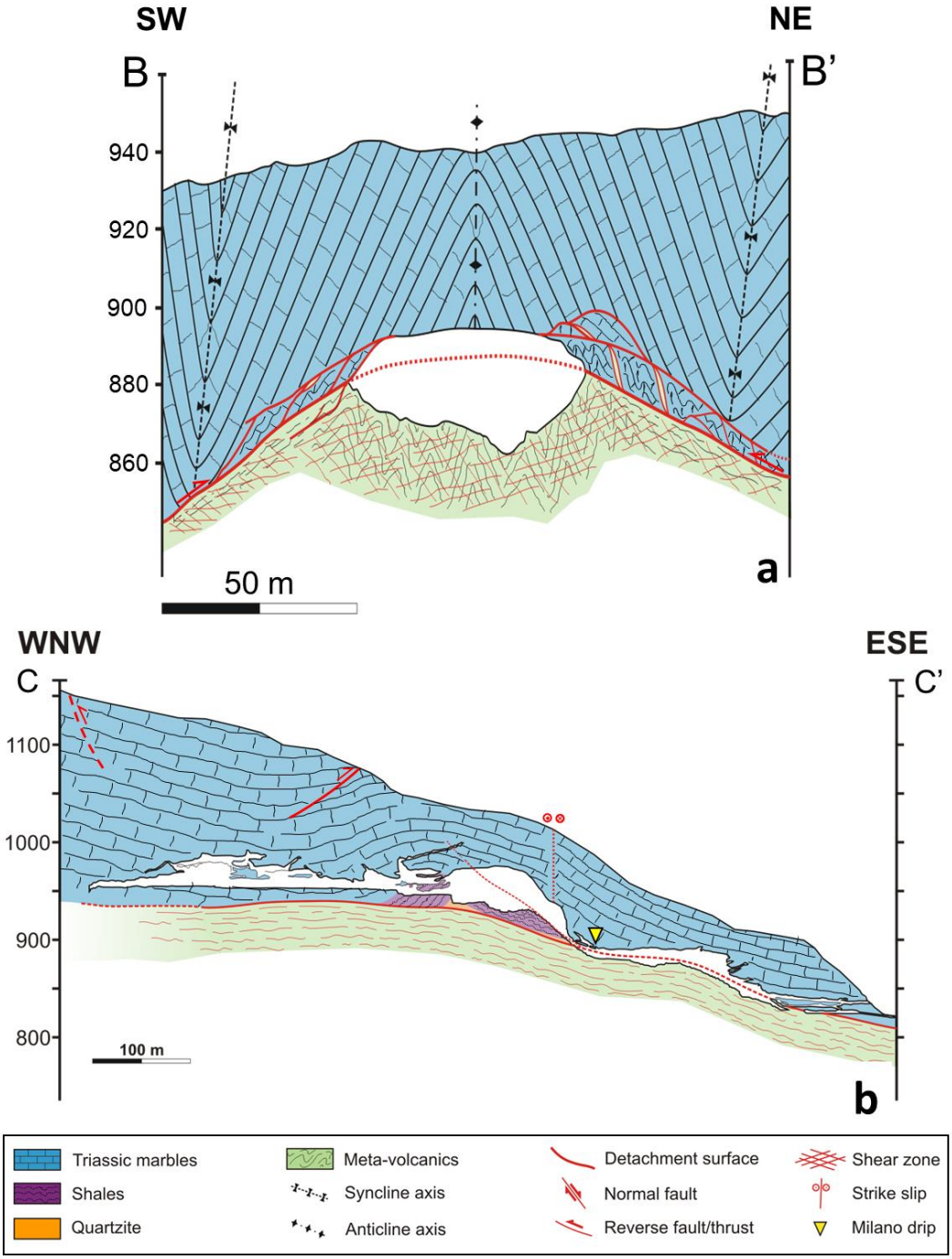

Fig. 2.5. Cross-sections of the cave. (a) BB' cross-section. (b) CC' cross-section. For location of cross-sections see Fig. 2.4a.

The highly deformed (pervasive cleavage) Permian meta-volcanics outcrop in a tectonic window along the Corsaglia River just south of the Bossea cave entrance. The tectonic window is about 100 m long and wide.

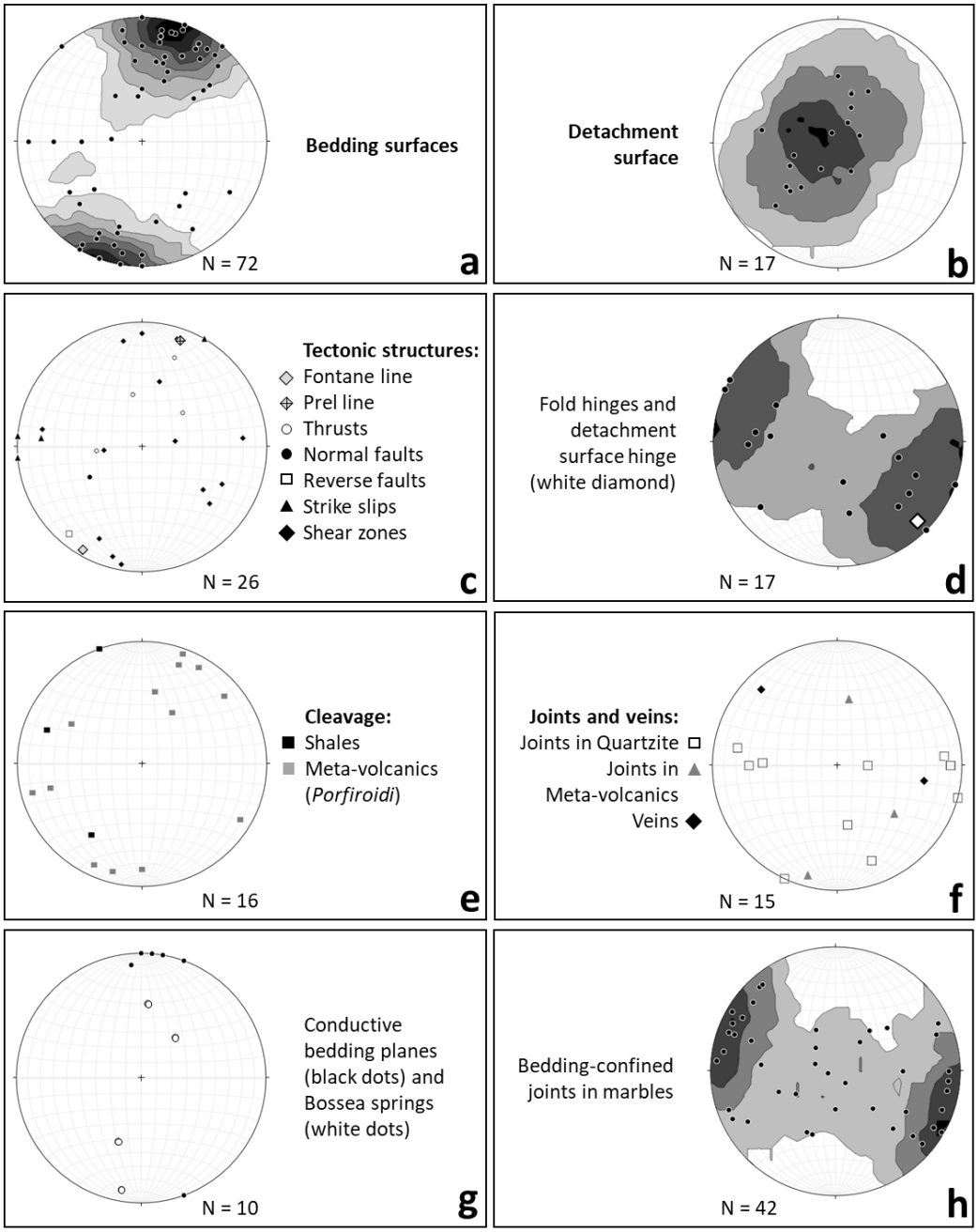

Fig. 2.6. Stereoplots of tectono-stratigraphic structures (bedding, faults, shear zones, folds, cleavage; from *a* to *e*) observed at the surface and in the cave. The structures plotted in (f) are potentially water-conductive whereas those in (g) and (h) are effectively water-conductive. The Bossea springs are aligned along bedding surfaces (plotted in the stereoplot *g* as springs).

The disharmonic contact between the marbles above and the meta-volcanics below (Fig. 2.4b) has an antiformal structure (Figs. 2.4b and 2.6b) with flanks that are parallel to the bounding strike-slip faults. The axis of the antiform follows the development direction of the Bossea karst system (roughly E-W, Fig. 2.4a) and it plunges about 15° to the ESE (Fig. 2.6d).

2.3.2. Detachment zone

The detachment zone (Figs. 2.4b, 2.7a, 2.7b, 2.8b) at the boundary between the disharmonic folds in the marbles above and the buckled meta-volcanics below is complex and made up of several elements.

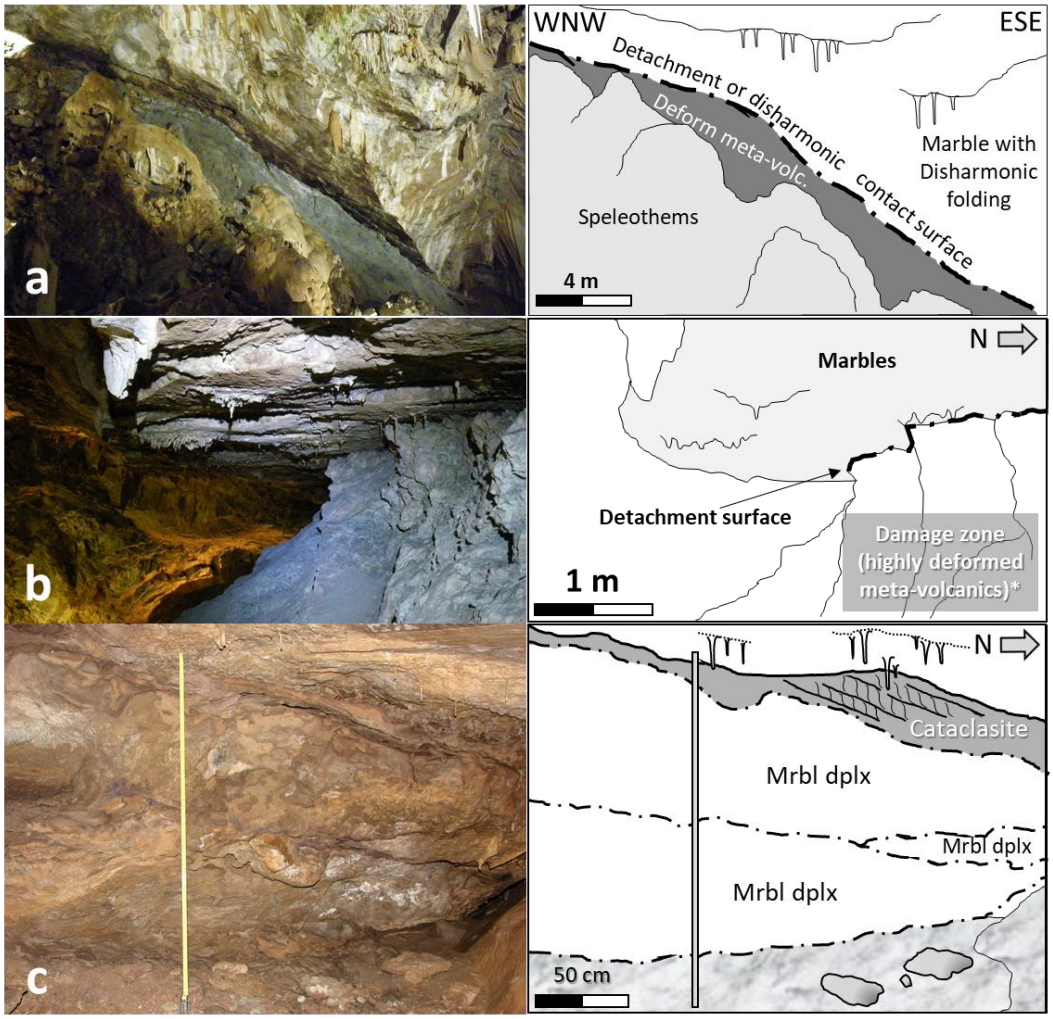

Fig. 2.7. Detachment surface and related damage zone. (a) Detachment surface at the contact between the marbles and the meta-volcanics. (b) Detachment surface and related shear zone with a thickness up to several meters; (*) the details of the structures in this portion are shown in Fig. 2.8b and 2.8c. (c) A few duplexes in the damage zone above the detachment.

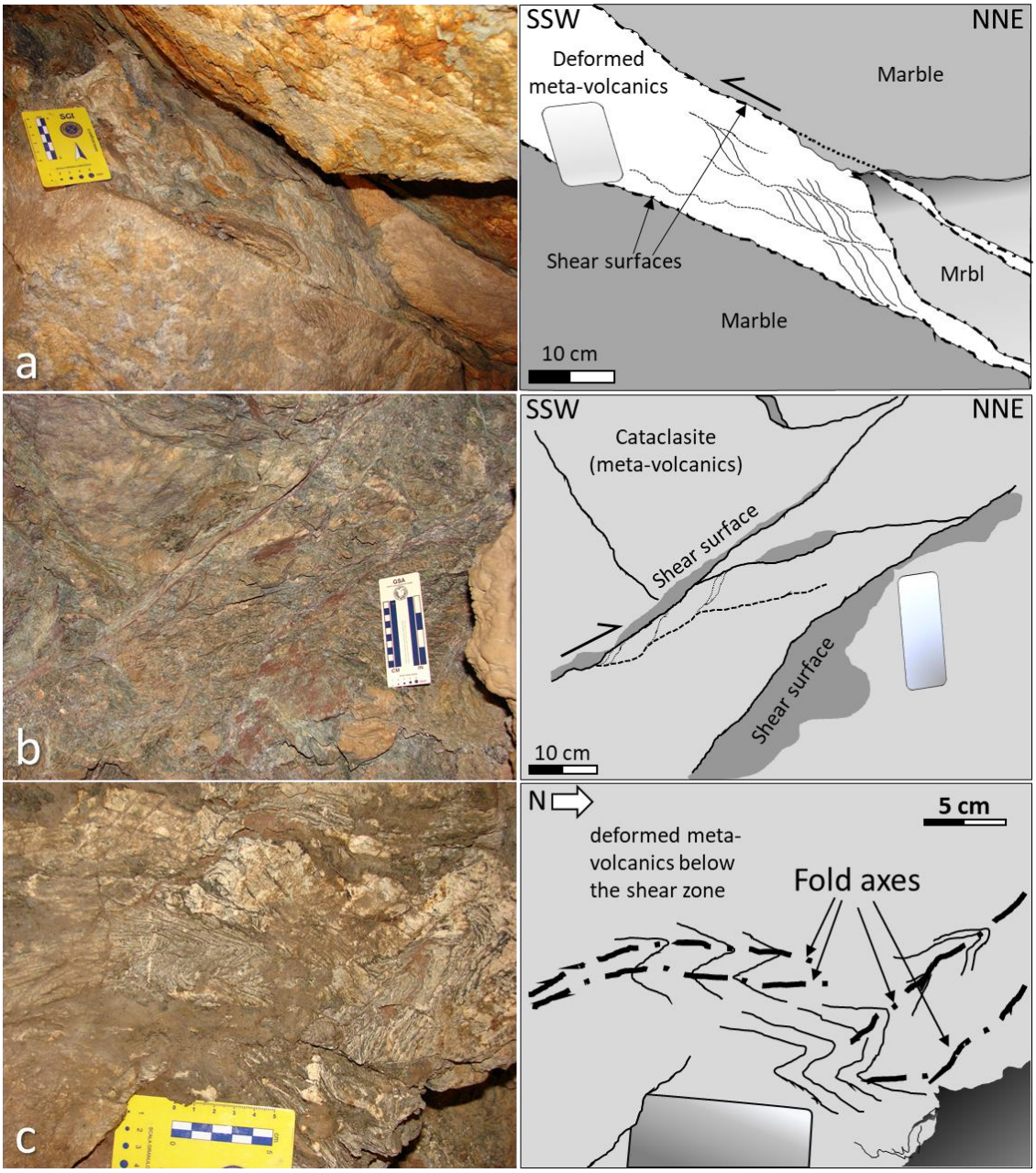

Fig. 2.8. Details of deformation in the damage zone of the detachment. (a) Deformed meta-volcanics sliver in between two marble duplexes in the damage zone above the detachment (top to SSW, northeastern side of the antiform). (b) Shear bands within the cataclastic meta-volcanics of the detachment core zone (top to NNE, southwestern side of the antiform). (c) Tight isoclinal and recumbent folds in the damage zone below the detachment surface.

Overall, as mentioned above, the shape of this surface is antiformal with a hinge line plunging to the ESE with a dip of 10-15° (Figs. 2.4a, 2.4b and 2.6d). At places, the contact zone is a sharp surface where the marble is in tectonic contact with strongly deformed meta-volcanics showing pervasive cleavage. In other places, the detachment zone is several meters thick (10 m) and has the characteristics of a shear zone with S-C structures (shear bands and *boudinage*)

and/or cataclastic material including mostly meta-volcanics, quartzite, and black shales (Figs. 2.7b, 2.8b). The damage zone below the detachment includes pervasively cleaved meta-volcanics (mm to cm spacing) up to a thickness of tens of meters (Figs. 2.7b, 2.8c). The damage zone above the detachment can be 20-30 m thick and it includes recumbent marble folds and stacks of duplexes with 0.05 to 0.5 m slivers of highly deformed and thinned meta-volcanics (Figs. 2.7c, 2.8a). The core of the detachment zone is disaggregated. The damage zone in the marbles includes large blocks (duplexes or drag folds) that have surfaces parallel to the roof of the cave and are usually separated from each other by intervening slivers of deformed meta-volcanics or slip surfaces (Figs. 2.7c, 2.8a).

2.3.3. Meso-structural elements

There are several meso-scale structural elements important for the development of the karst system. Stereoplots of some of these elements are reported in Fig. 2.6 and their characteristics are described in the following sections.

2.3.3.1. Bedding surfaces

Bedding surfaces were measured in marbles (the metamorphic level of the marbles still allows to recognize the original bedding), quartzites and shales both in outcrop and in the cave. Bedding orientations strike E-W to WNW-ESE and steeply dip to the N or S; the statistics are reported in the stereoplot of Fig. 6a. Many bedding surfaces in outcrop (Fig. 2.9a) show signs of dissolution and are associated with active paths for water flow, as shown by the karst springs in the *Corsaglia* River (Figs. 2.9b, 2.9c). Bedding surfaces localize reverse and strike-slip faults. In the intensely deformed zones next to the major bounding faults, bedding is stretched with an elongation of 15 to 40% forming *boudinage*, sigmoidal veins, and drag folds (Fig. 2.10a).

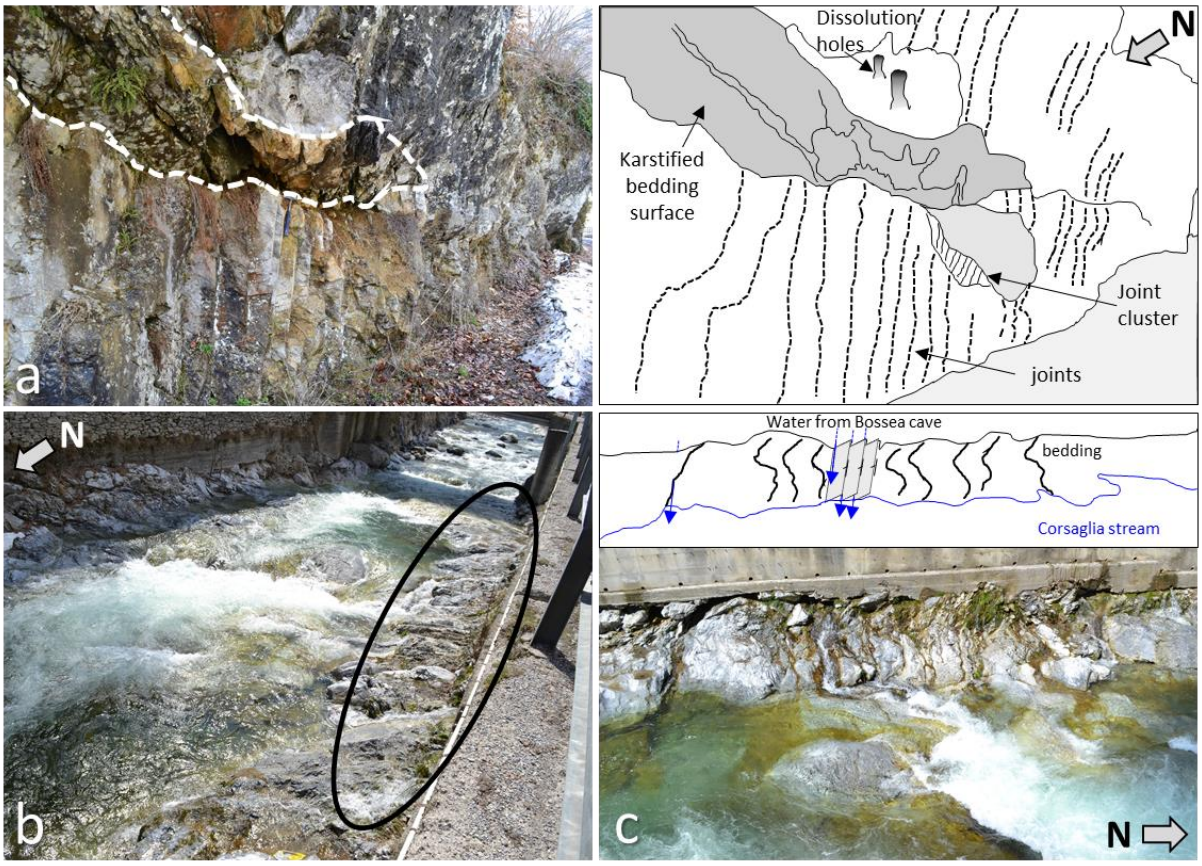

Fig. 2.9. Fluid conductive structures. (a) Karstified zone along a bedding surface (b) Resurgent springs exploit bedding contacts along the *Corsaglia* River. (c) Detail of the *Bossea* springs.

2.3.3.2. Joints

Joints (mode I fractures) are secondary structures in the *Bossea* karst system and are mostly confined to the marbles and the quartzite. They are striking NNE-SSW to NE-SW with variable dip direction and dip angle (most of them are steeply dipping; see stereoplots in Fig. 2.6f and 2.6h). Joints are open fractures and allow water to flow through. Joints are usually bedding-confined and bedding-perpendicular, their length ranges from a few cm to several meters (Fig. 2.9a, 2.11a). At the surface, they are often associated with alteration haloes or reactive fronts (Fig. 2.11b); underground, joints are observed at the rooftop of some cavities and they are associated with speleothems (soda straws and thin stalactites) (Fig. 2.11a). Joint openings (from a few µm to 1 mm) are often partially filled with calcite cement (Fig. 2.11b).

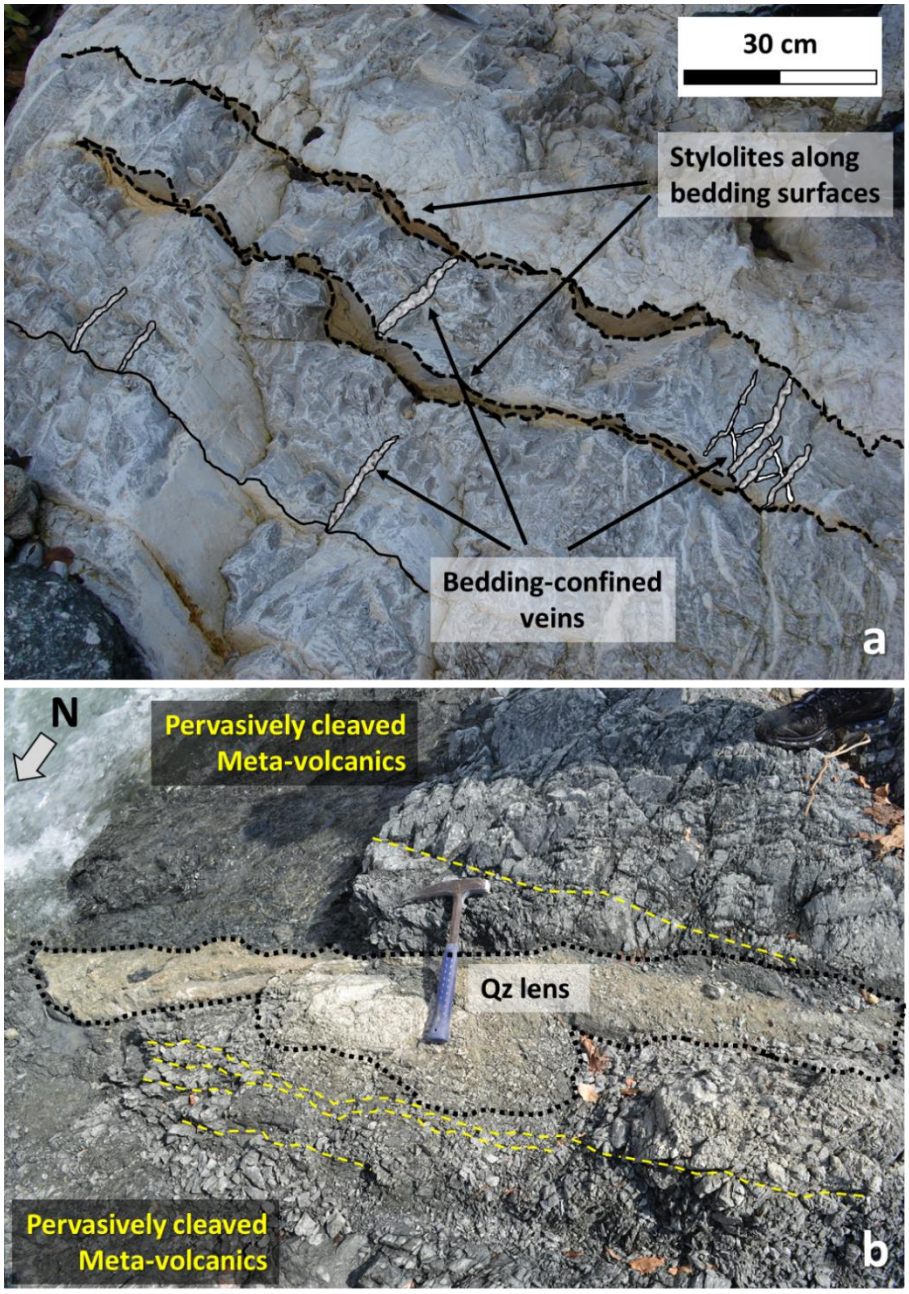

Fig. 2.10. Cleavage, veins, and stylolites. (a) Veins in marble near the northern left-lateral strike-slip fault. Note the high frequency of veins. Stylolites define the bedding surfaces and are altered and karstified. (b) Pervasive cleavage in the meta-volcanic rocks close to the southern major bounding fault (dashed yellow lines); a lens of detached quartzite is embedded in the meta-volcanics, probably due to the high deformation near the fault.

2.3.3.3. Veins

Veins (mode I fractures filled with cement) are pervasive in the highly-stretched marble and quartzite beds. In some of these steeply dipping beds, the volume occupied by the veins accounts for 15-40 % elongation observed next to the major bounding faults (Fig. 2.10a). Veins are bedding-confined and usually normal to bedding surfaces. Vein orientation is similar to that

of the joints (Fig. 2.6f) but their length is usually smaller and it ranges from a few centimeters to less than 1 m. In the massive marble outcropping in the central part of the *Corsaglia* River and next to the *Milano* drip in the cave (see Fig. 2.2, 2.4a and 2.5b for its position), the veins form a pervasive network made up of 2-10 mm wide and 20 to 100 mm long elements without a uniform orientation. Veins make up about 15-20% of the rock volume in this latter part of the carbonate sector.

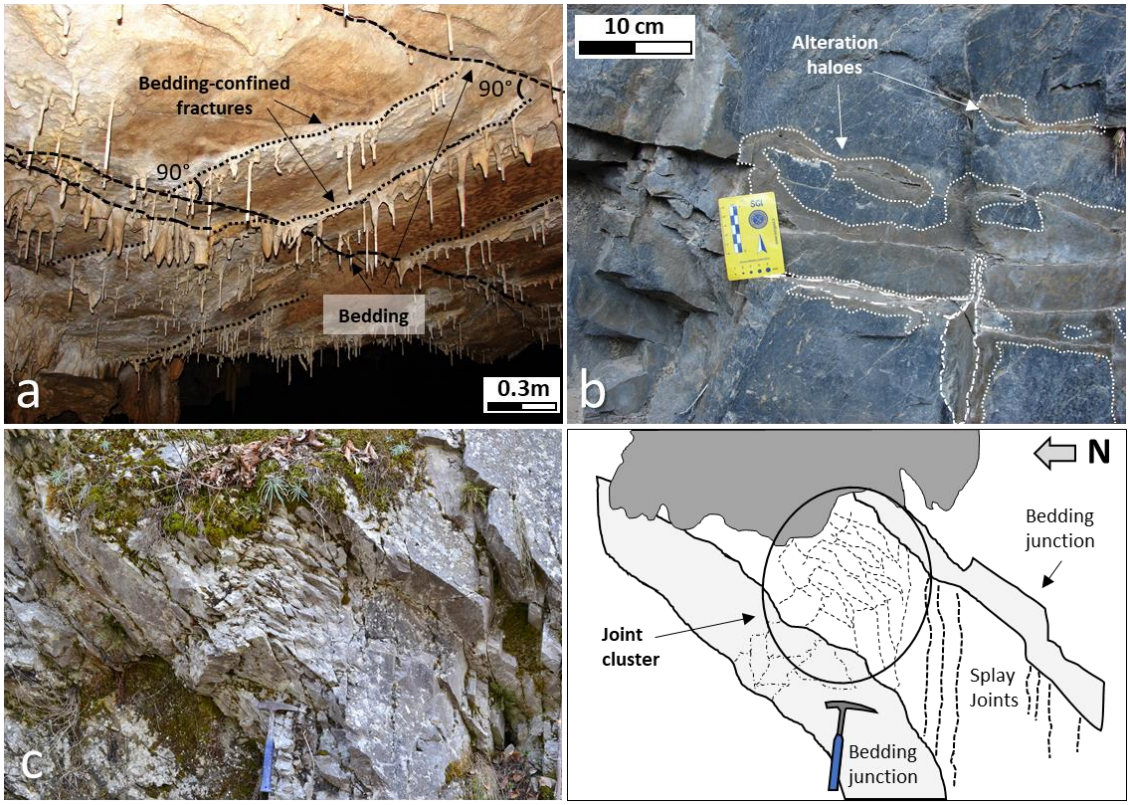

Fig. 2.11. Water-conductive structures. (a) Bed-confined joints with speleothems inside the *Bossea* cave. Bedding (dashed red lines) is steeply dipping. (b) Conductive joints with partial calcite fillings and alteration haloes (due to reactive diffusion of DO in the matrix from the fracture) (c) Joint cluster at the termination of the slipping patch of a bedding fault.

2.3.3.4. Joint clusters

Joint clusters are narrow zones (0.1 to 1 m wide) where joints have a small spacing (2 to 50 mm). Usually joint clusters cut across layering and may be up to several meters long. They have no uniform orientation but they tend to form an angle around 70° with the bedding surface. In many cases, joint clusters originate from the termination of a bedding surface where a parting surface or bedding parallel slip striae ends (Fig. 2.11c).

2.3.3.5. Stylolites

At the meso-scale, stylolites are not common in the carbonate sequence, although some are recognizable at both meso- and microscale (see the *Microstructures* section for details). The most apparent ones are along bedding surfaces where bedding is thinly layered (Fig. 2.10a). Stylolites are especially rare where the carbonate sequence is recrystallized into marble. Normal-to-bedding stylolites are short (1-5 cm) and fuzzy. Their microstructure is described in the microstructural results section.

2.3.3.6. Cleavage

Cleavage is well-developed within the meta-volcanics and in the black shales. In these rocks, cleavage planes formed by preferential recrystallization of chlorites, mica, and biotite. Cleavage in the meta-volcanics can be pervasive with spacing ranging from 2 to 20 centimeters. The highest frequency of cleavage (with spacing that could also be of 1-4 mm) is next to the disharmonic tectonic contact (Fig. 2.8b). Cleavage orientation is variable especially in the damage zone associated with the detachment. In the damage zone next to the major strike-slip faults, cleavage is preferentially oriented parallel to these bounding structures (E-W to ENE-WSW with subvertical dip angle, Fig. 2.10b).

2.3.3.7. Shear bands

Shear bands are present just below the tectonic detachment surface (Fig. 2.8b). The shear bands in Fig. 2.8 are localized in the core material of the detachment mostly made up of crushed cataclastic meta-volcanics rocks. The shear bands have a slip surface where striations are marked by reddish stains (iron oxides and hematite). Most shear bands are sub-parallel and at high angle to the shear zone boundaries and accommodate rotational deformation within the core. Offsets along the shear bands range from 0.02 to 0.5 m.

2.3.3.8. Small-scale folds

Mesoscopic-small-scale folds with wavelength from a few centimeters to a few meters were observed both in the marbles above the detachment surfaces and the meta-volcanics below the detachment surface. This kind of small-scale folds are mostly recumbent and tend to have their

axial surfaces sub-parallel to the detachment (Fig. 2.8c). The folds in the marble tend to have larger wavelengths (0.5 – 5 m) whereas those in the meta-volcanics are smaller (5 – 20 cm).

2.3.3.9. Deformed and crushed speleothems

Some speleothems are deformed in a brittle fashion by what appears uniaxial compression (Fig. 2.12). These structures are mostly located along the north and south sides of the cave, close to the junction between the roof and the floor. Other similar structures are placed in the southern side of the entry passage (Figs. 2.2 and 2.4a). Some of these speleothems seem to accommodate the deformation only in a localized part that is made of completely smashed redeposited calcite (Figs. 2.12c, d), whereas others show a highly deformed band coupled with open fractures (Figs. 2.12a, e, f).

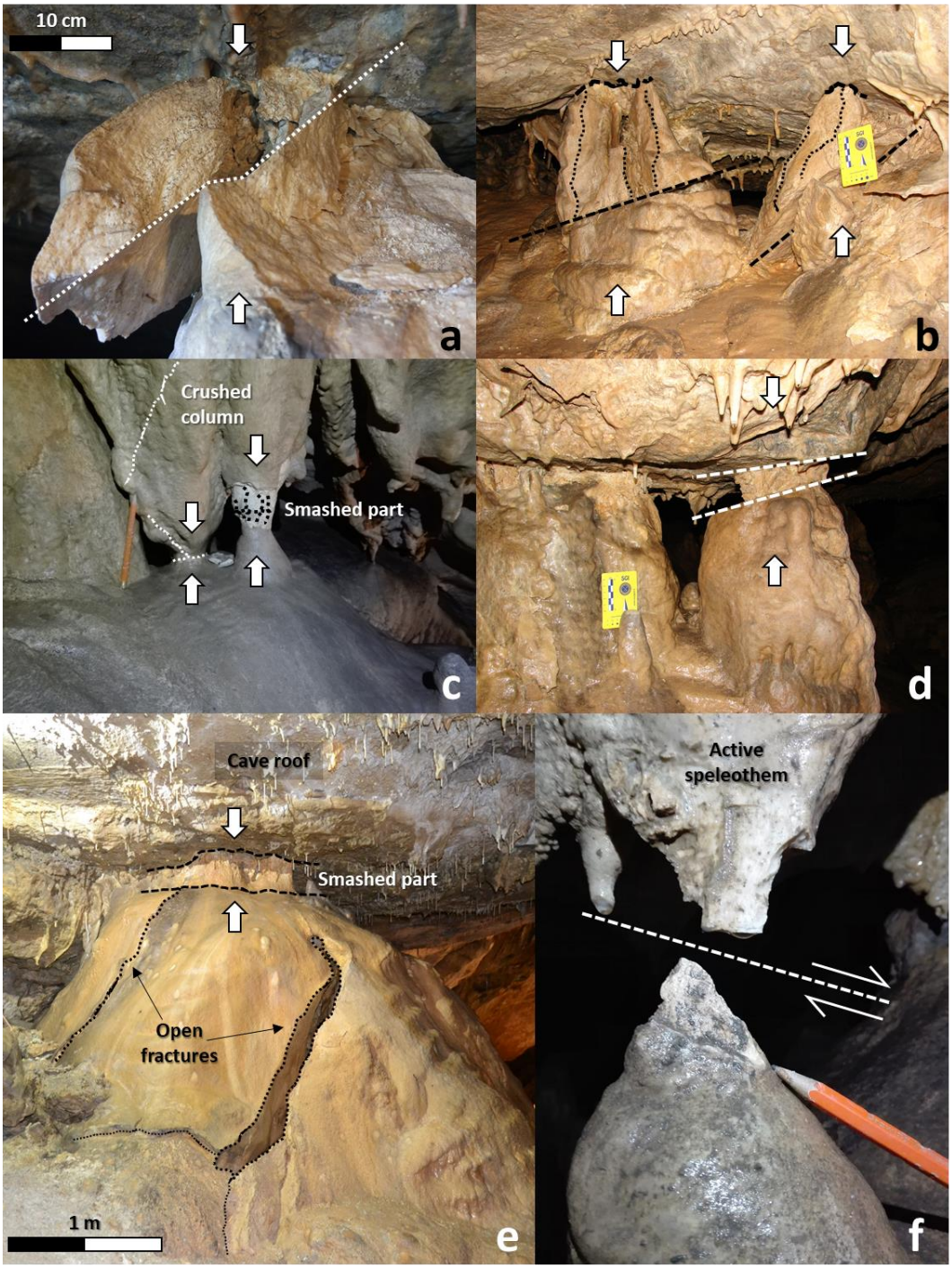

Fig. 2.12. Speleothems deformed in a brittle fashion in the *Bossea* cave; their position is reported in Figs. 2 and 4a. Generally, these structures are the result of uniaxial compression due to small roof movements (*a* to *d* and *f*); sometimes this process is coupled with unloading due to slope instability, the latter caused by *Mora* creek erosion at the base of the slope (expressed by open fractures in a deformed speleothem close to Milano drip site, *e*).

2.3.4. Microstructures

The microstructures observed in thin sections (Fig. 2.13) are important to define the porosity and to infer the fluid flow characteristics of the rocks associated to the *Bossea* karst system.

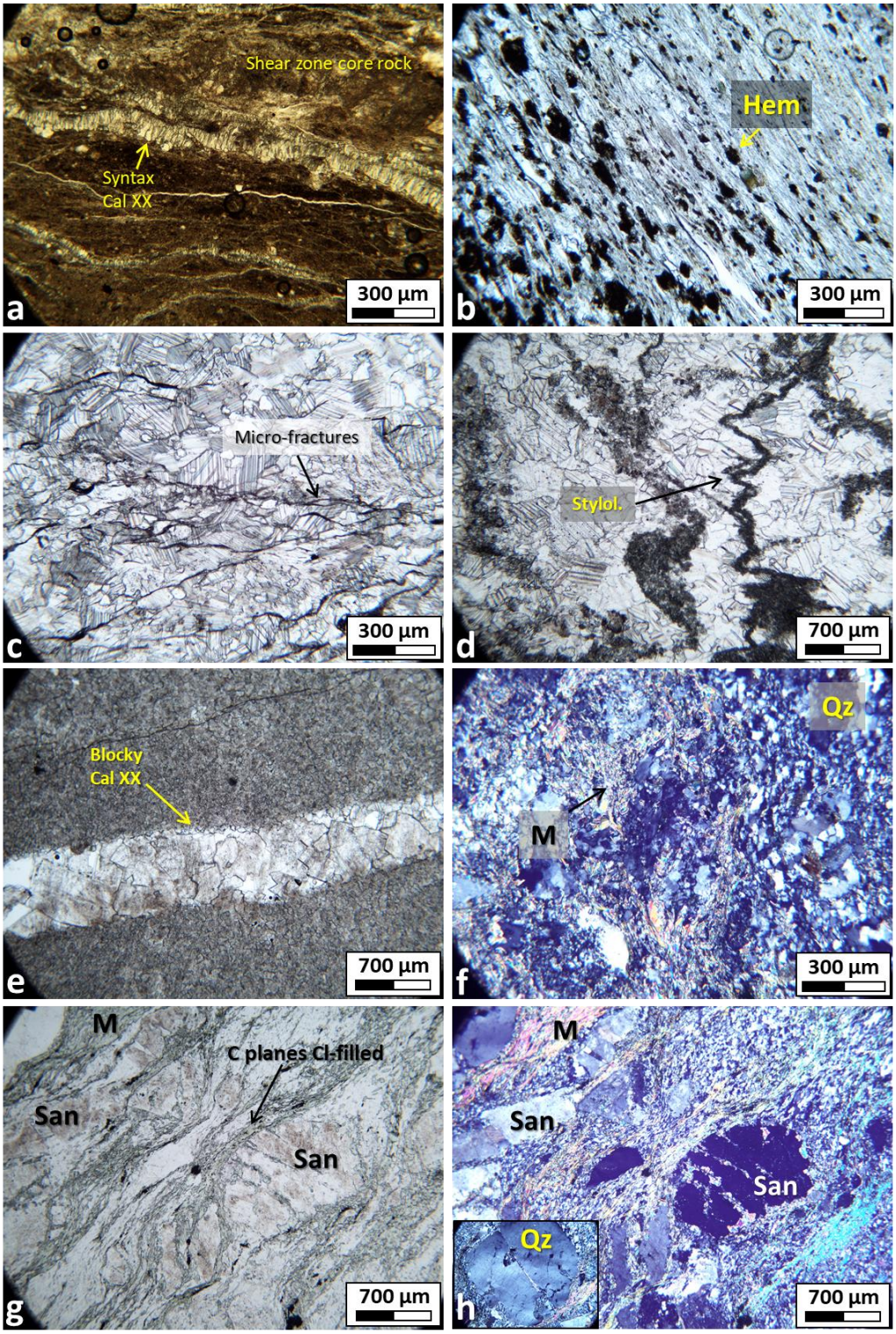

Fig. 2.13. Thin sections from the *Bossea* area. (a) Fault rock with veins and syntaxial calcite crystals. (b) Triassic dark shale: note the alignment of opaque minerals along the fabric of the sample. (c) Deformed crystalline Triassic marble with short intergranular and intragranular cracks. (d) Crystalline Triassic marble with stylolites. (e) Microcrystalline Triassic marble with veins and recrystallized blocky calcite crystals in the vein. (f) Deformed quartzite (crossed nicols). (g) Deformed meta-volcanics (polarized light). (h) Deformed meta-volcanics (same as (g) crossed nicols); the size of the small insert is 1,6 x 1,2 mm. The labels "San", "M", "Qz", "Hem" stand respectively for sanidine, micas, quartz and hematite crystals.

2.3.4.1. Detachment fault rock

The sample of fault zone in Fig. 2.13a is characterized by a fine cataclastic matrix of meta-volcanics and a few fragments of surviving feldspar phenocrysts. This sample originates from the meta-volcanic-rich portion of the detachment core. Very fine grains (silt and clay size) make up the framework of the fault rock. A dense network of anastomosing veins with a thickness from a few μm to 100 μm and a spacing ranging from 50 to 100 μm make up the structure of this fault rock. The veins contain syntaxial calcite crystals that are perpendicular to the vein wall. Single calcite crystals may span the entire thickness of the vein and have a width in the order of 5 to 20 μm. Besides fine-grained cataclastic material, the fault rock matrix contains clay minerals and chlorites. Effective porosity is essentially lacking in the fault rock.

2.3.4.2. Black shale

The thin section of a sample of Triassic black shale is shown in Fig. 2.13b. The framework of the sample is given by an alignment of chlorite and clay minerals parallel to bedding that gives a characteristic fabric to this rock. A considerable amount (20% of the rock composition) of opaque minerals (mostly hematite) is aligned in micro-layers parallel to the fabric of the chlorite and clay minerals. The opaque minerals are anisotropic with their longer axis parallel to the fabric of the sample and lengths ranging from 10 to 500 μm. No effective porosity is observed in the black shale.

2.3.4.3. Marbles

The marbles of the Triassic carbonate sequence have different characteristics according to their mineralogy and the presence of tectonic structures such as fractures and some sporadic stylolites. The crystalline massive marble beds contain clear or brownish recrystallized calcite crystals with a dimension of 50 to 500 μm (Figs. 2.13c, d). Many crystals show accentuated calcite twinning. Some short *en-echelon* intragranular and intergranular fractures with a length of 100 μm to a few mm form at the grain boundaries or cut across the grains taking advantage of the cleavage planes (Fig. 2.13c). Stylolites are rare but a dark insoluble material marks where they form; the insoluble material has a thickness in the order of 10 to 500 μm (Fig. 2.13d). Stylolites have column heights in the order of 50-800 μm and their wavelength ranges from 200 to 600 μm (Fig. 2.13d). Some marble samples are fine-grained (Fig. 2.13e) with a greenish-brown color probably due to the presence of clays and chlorites. In these latter samples, the

calcite crystals are 10-50 μm in diameter. Thick calcite veins (500 μm to 2 mm) are observed in both the fine-grained (Fig. 2.13e) and coarse-grained marble. The vein fills are blocky recrystallized calcite crystals of a diameter ranging between 20 and 200 μm (Figs. 2.13e). Very few veins show deformed syntaxial calcite crystals. Secondary porosity in the vein can be up to 15-20%. Primary porosity in the marble is not existent. Vein filling material in the marble can make up 30-40% of the rock volume (Fig. 2.13e).

2.3.4.4. Quartzite

Fig. 2.13f shows a deformed quartzite (sampled in the upper part of *Bossea* cave, in a tight isoclinally-folded sequence) that can be broadly divided in two portions: the right half is occupied predominantly by quartz crystals with uniform dimensions (10x10 μm up to 30x30 μm) weakly aligned along undulated bands. The left half of the section shows a more chaotic framework where quartz phenocrysts are deformed and surrounded by fine-grained white mica crystals (M in Fig. 2.13f). The micas define an undulated cleavage. The latter portion could be related to slip along the folded bedding surface, visible also at the mesoscale. There is no evidence of effective porosity.

2.3.4.5. Meta-volcanic rock

Figures 2.13g and 2.13h (polarized and cross nicols light) show the deformed meta-volcanic rock in the damage zone just below the detachment surface. Alignment of white mica and possibly chlorite crystals define the cleavage planes that here have a 100 μm to 2 mm spacing. Large deformed feldspar (and some quartz, see insert in Fig. 2.13h) phenocrysts have a diameter ranging from 0.5 to 4 mm. Many of these feldspar phenocrysts have an S-shape geometry due to deformation. The largest phenocrysts are broken by intragranular fractures that can have a spacing of 100-200 μm. In the upper left corner of the thin section, some feldspar grains are sheared by S-C structures (clockwise rotation in the shear zone).

2.4. Discussion

2.4.1. Structural geology and tectonic synthesis

The tectonic setting of *Bossea* is important for the development of its karst system. The geological map (Fig. 2.4) shows that the cave developed in the transpressional region between two major bounding left-lateral strike-slip faults. According to several authors (Vanossi, 1984;

Seno et al., 2005a; Piana et al., 2009; Bonini et al., 2010; d'Atri et al., 2016), transpressional tectonics started between late Eocene and early Oligocene and induced a NE–SW shortening together with significant left-lateral movements. This tectonic phase was followed by (late Oligocene–middle Miocene) right-lateral movements along E–W to SE–NW striking shear zones. The major bounding faults in *Bossea* do not show any signs of this latter reactivation and they preserve their early Oligocene tectonic structure. Transpression in the overlap region of the strike-slip faults caused a warping (due to buckling) of the meta-volcanic basement, which formed an ESE plunging antiform with a pervasive cleavage system. The marble carbonate sequence above the detachment surface and along the contact with the meta-volcanics is folded disharmonically by tight isoclinal folds (WNW-ESE direction) associated with bedding-parallel high angle reverse and strike slips faults. These faults represent the reactivation of bedding planes as a consequence of flexural slip folding. Generally, these structures started as bedding plane faults and then they eventually cut through the folded rock sequence. The detachment surface at the contact between the disharmonic folds in the marble and meta-volcanics is a complex structure where slabs of cataclastic material are embedded between carbonate rock duplexes (1 to 20 m in thickness) and shear zones developed in the disaggregated meta-volcanics and the strongly deformed quartzites. The detachment zone may have a width of a few meters to tens of meters. We propose that the detachment developed in the early Oligocene during the transpressional phase, and most of the deformation associated with this tectonic event developed under low-grade greenschist metamorphism where ductile and brittle structures might have coexisted (Messiga, 1987). This would account for the marbles, the isoclinal folds, and the bedding-parallel high angle reverse faults in the Triassic carbonate sequence (Figs. 2.4b, 2.7, 2.8). The brittle structures such as joint clusters at the tip of bedding parallel faults and the joints confined in the marble, quartzite, and meta-volcanic rocks might have formed in recent times in shallow burial conditions. Two major deformation events, in fact, are recorded in the Northern Apennines during the early Pliocene and the Pleistocene (*Gelasian*) and their effect might have reached the Western Alps in the *Bossea* area (Ghielmi et al., 2002, 2019; Vigna et al., 2010). Alternatively, there is the possibility that these brittle structures formed during the first Alpine tectonic event (D1) and then were reactivated during later deformational phases. The directions of compression during D1 and the following tectonic events are subparallel and we think that this is the cause of the arrangement of the brittle structures with respect to the local direction of compression. Regionally, the reactivation

of all generations of structures during the following tectonic phases is well documented (Piana et al., 2009; Bonini et al., 2010; d'Atri et al., 2016; Ghielmi et al., 2019) so it is highly probable that the brittle structures such as bedding-confined joints and fracture clusters were at least affected by the latest phases of deformations.

2.4.2. Pathways for water circulation

The rocks in the *Bossea* karst system have a low or inexistent primary porosity. Thin section observations showed that marbles have porosities ranging from zero to 1-4% and black shales, quartzite, and meta-volcanics have almost zero effective porosity.

Some of the deformation structures in the *Bossea* area are ductile (isoclinal folds, *boudinages*, pressure solution surfaces – stylolites, etc.) and are not associated with secondary porosity development. Cataclastic zones in the core of the detachment zone have also very low porosity and they probably act as barriers to water circulation as observed directly in the cave.

The most important structures for the formation of secondary porosity and for allowing fluid flow in the vadose karst zone are bedding surfaces, joint clusters associated with bedding parallel faults, and bed-confined joints (Figs. 2.9, 2.10, and 2.11).

Karstified zones often develop along and adjacent to bedding surfaces in the marbles of the carbonate sequence (Fig. 2.9). These zones facilitate water percolation along the steeply dipping layers of the tight isoclinal folds, so that water from the vadose zone can reach the underground *Bossea* flow system. The *Milano* drip, one of the most active water trickles from the vadose zone, is located along a karstified bedding surface. The *Bossea* karst springs along the *Corsaglia* River developed along bedding contacts (Figs. 2.9b and 2.9c), demonstrating that flow along these surfaces may be important also in the saturated zone.

Joint clusters often form at the termination of slipping bedding plane fault patches (Fig. 2.11c). Joint clusters are highly localized and represent fluid-conductive volumes of rock that allow water to flow across a layered sequence. They are especially important where the layered sequence has a very low hydraulic conductivity as for the marbles in the *Bossea* karst system (National Research Council, 1996; Aydin, 2000; Antonellini and Mollema, 2019, and references therein).

Bedding-confined joints are usually at high angle to the bedding surfaces and at *Bossea* they seem to be secondary structures for water flow. At the surface outcrop, these joints are associated with alteration halos (3-5 cm thick) that suggest they were open to flow and that

reactive species could move by diffusion from the fracture into the rock matrix (Fig. 2.11b) (Antonellini et al., 2017). In the cave, these joints are observed in roof exposure with steeply dipping bedding and are associated with small speleothems (soda straws; Fig. 2.11a). They are probably important to transmit water where bedding surfaces are closed or where a lack of joint clusters does not allow cross bedding flow.

Several authors already described the importance of bedding surfaces and joints to karst development and water flow in the vadose zone (Čar and Šebela, 1998, for a review see Klimchouk and Ford, 2000; Shanov and Kostov, 2015). Filipponi et al. (2009), for example, claim that bedding planes could be inception horizons particularly favorable to karstification by virtue of physical, lithological or chemical deviation from the predominant carbonate facies within the surrounding sequence. Possible reasons for such a higher karstification potential are (Lowe, 2000): (1) Higher primary porosity and permeability of the bedding plane respect to the surrounding rock mass; (2) bedding plane enclosing highly soluble minerals; (3) bedding planes with sulfide minerals that during water percolation may oxidize and produce sulfuric acid turning the solution into a highly corrosive one; (4) bedding planes in siliciclastic sequences such as shales or volcanic clays can be impervious and act as a low permeability "screen" along which water will flow preferentially.

Klimchouk and Ford (2000) claim that bedding planes and contacts most readily exploited by water include those with substantial depositional disconformities, planes with shale laminae or thicker partings such as pressure solution structures - stylolites (often with disseminated pyrite) and planes with nodules or sheets of chert. Furthermore, they also suggest that the most important bedding discontinuities are those that functioned as surfaces of differential slippage during tectonic events. A few centimeters slip and small amounts of breccia that enhance openings is enough to promote preferential fluid flow. This is more important in steeply tilted and intensely folded strata that often display differential slip.

According to Klimchouk and Ford (2000), when a rock is approaching the surface there is a stress relaxation due to the unloading of the overburden. This stress unloading changes the forces applied to existing discontinuities and allow them to extend or new fractures to form between them. This could be the origin of the bed-confined joints observed at *Bossea*. The timing for the formation of these joints might be placed during the recent tectonic uplift and unloading of the Pleistocene (Vigna et al., 2010; Ghielmi et al., 2019) or, alternatively, they

might have formed during the main phase of the Alpine orogenesis, being reactivated during a later phase.

2.4.3. Karst Development Model

In the *Bossea* karst system, both structural and lithological factors control speleogenesis (Fig. 2.14a). The important lithological elements are the soluble marbles of the Mesozoic sequence and the highly deformed rock in the damage and core zones of the detachment. The core zone of the detachment is made up of cataclastic meta-volcanics, quartzite, and black shale slivers that are easy to erode. The damage zone above the detachment is organized in pockets made of marble duplexes with intervening slip surfaces and meta-volcanic slivers. These pockets can be easily removed by erosion, enhancing gravitational instability of the cave roof that is facilitated along the slip surfaces limiting the duplexes.

The karst system started to develop by dissolution in the upper tightly-folded meta-carbonates-marbles and then worked its way down until it reached the detachment surface at the disharmonic contact between tightly folded marble above and meta-volcanics below (Fig. 2.14b, c, d). This process focused underground water movement along the crestal region and down plunge of the antiformal meta-volcanic structure. At this point speleogenesis progressed by erosion of the non-cohesive cataclastic rock in the damage and core zones (Fig. 2.14e). The antiformal structure is intensely deformed especially in its crestal region (multiple sets of pervasive cleavage planes). Marble block collapse in the damage zone above the detachment surface contributed to the evolution of the karst system by forming large halls (Inset Fig 2.14c and Fig. 2.14f). Fallen blocks were gradually eroded (chemical and mechanical erosion) and taken away by the underground water flow.

Tightly-folded and faulted (high-angle reverse faults) carbonate-marble rocks above the detachment allow, initially, to focus dissolution that is facilitated mostly along bedding contacts and secondarily by bedding-contained fracture networks and joint clusters (Figs. 2.14a, b, c). The karstified bedding discontinuities, bed-confined joint networks, and joint clusters that form at the termination of bedding-parallel slipping patches focus water flow circulation (Fig. 2.14d). The last phases of brittle deformation in the area (*Gelasiano* - Pleistocene; Vigna et al., 2010; Ghielmi et al., 2019) likely caused the formation and/or the reactivation of the brittle structures (joints and joint clusters) along which dissolution was more efficient.

To the best of our knowledge, a specific structural control on karst development such as the one observed in *Bossea* is not reported in the literature. Some authors, however, have mentioned the control of regional tectonic structures on karst evolution. Andrejchuk (1996) reports preferential karst development above an eroded anticline in gypsum rocks of the Pre-Ural Region (Russia). In the setting he described, carbonate rocks are at the core and sulfate rocks are at the top; it is possible that intense deformation at the core of the anticline aided speleogenesis. Šebela (2009) and Šebela and Liu (2014) proposed a structural control in the development of conduits for two karst systems in Slovenia and China. Pisani et al. (2019) report in detail the structural control on speleogenesis and underground passage morphologies in the epigenic gypsum caves near Bologna, Italy.

Tîrlă and Vijulie (2013), by means of a statistical analysis, related the karst corridors of Croatia to tectonics and structures (extensional faults) and they propose a "tectonogenetic" karst classification (orogenic and epi-orogenic karst) for these features. Tectonogenetic karst is particularly relevant in orogens and the model proposed for *Bossea* is a new contribution that may explain karst systems in many other orogens around the world.

Another factor influencing the development of the *Bossea* cave is the magnitude of erosion that the *Mora* creek caused to reach its base level (i.e. the *Corsaglia* River). There are evidences that the *Mora* creek (TM) has still not reached its equilibrium profile: the cave entrance passage and other smaller openings well above base level become active during strong precipitation events and floods, because the *Bossea* springs along the *Corsaglia* River are not able to drain the large volume of water collected by the karst system. The hydrological activation of this entrance passage is a recurring phenomenon that has been going on over many thousands of years, as highlighted by the thick sequence of flood deposits interlayered with cm-thick calcite flowstones. Furthermore, the *Corsaglia* River has not reached its equilibrium profile; the downcutting of the external river, which is related to the variable rate of tectonic uplift, drives the erosion occurring inside the cave (Fig. 2.14e, 2.14f). Overall, the downcutting of the *Corsaglia* River and the renewing of *Bossea* cave (roof collapses phase) are related to a series of uplift events and the subsequent fluvial dynamics during Pleistocene times: the uplift (up to 100 m or more) led to the *Tanaro* River diversion and consequently to the deepening of its entire drainage network, both primary and secondary tributaries included (Civita et al., 1990; Vigna et al., 2011; Ghielmi et al., 2019).

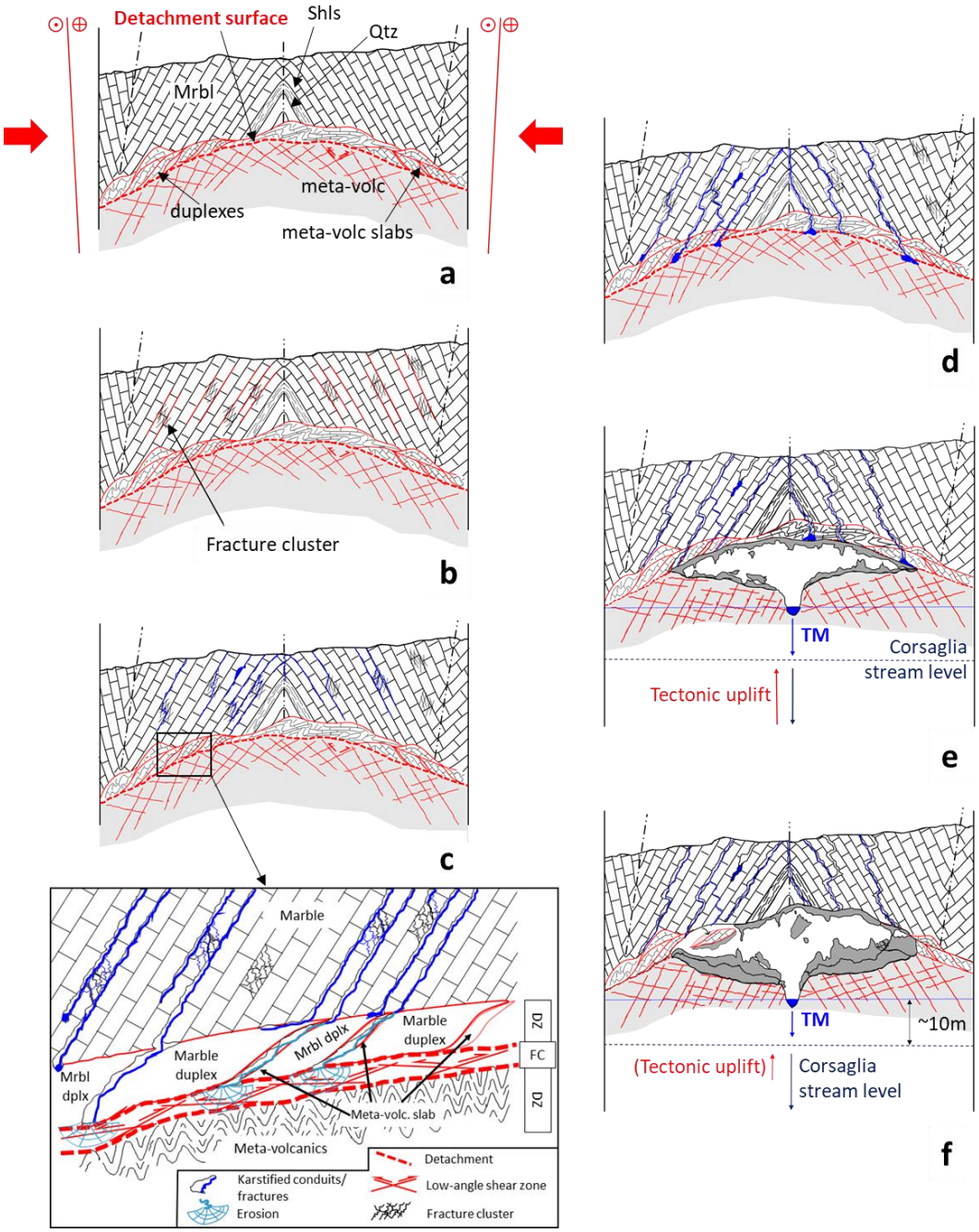

Fig. 2.14. Model for the development of the *Bossea* karst system. (a) Alpine main deformation phases (Early Oligocene); two left-lateral ESE-WNW strike-slip faults accommodate transpression and the development of disharmonic deformation (quartzite+shales+marbles vs. meta-volcanics) by ductile deformation; red arrows indicate shortening direction. (b) Late deformation phases (Pleistocene); development and/or reactivation of secondary brittle structures (e.g. fracture clusters and bed-confined joint networks). (c) Karstification takes advantage of pre-existing structural features; the most important flow paths are the bedding contacts in the marble sequence (no matrix permeability). Localized secondary fracture networks (joint clusters) provide intra-bedding connectivity. (d) Once the water reaches the highly deformed meta-volcanics of the detachment core, erosion starts. (e) The erosion process works faster than karstification and removes large volumes of meta-volcanics. The *Torrente Mora* (TM) continues to erode rocks to reach its base level (*Corsaglia* River). The *Corsaglia* River is also not in equilibrium due to tectonic uplift. (f) The downward erosion of the meta-volcanics causes gravitational instability of the cave roof, enhanced by the structural elements in the damage zone above the detachment surface (e.g. slip surfaces and slabs of meta-volcanics inserted between marble duplexes); development of giant halls.

At *Bossea*, the role of brittle structures in controlling fluid flow in the vadose zone is apparent. Shanov and Kostov (2015) stress the importance of fracturing and its relationship to stress, especially in rocks susceptible to karstification (limestones, dolomites, marbles, etc.). They claim that brittle fracturing is often the result of neotectonics or stress states that arise at shallow crustal depth such as during uplift and denudation of an orogenic belt (Shanov and Kostov, 2015). The presence of broken and/or deformed speleothems in a cave may be due to several causes: (1) Elastic deformation due to overburden loading. (2) Valley-ward sliding of rock slabs along slopes. (3) Gravitational instability due to underground flow erosion at the base of the karst system. (4) Differential subsidence. (5) Neotectonics (Forti and Postpischl, 1984; Gilli, 1986, 2004, 2005; Becker et al., 2006, 2012; Plan et al., 2010). Gilli (2005) argues that even in cases where active tectonics is the cause of speleothem deformation, it is difficult to evaluate whether the movement is due to a seismic event or to aseismic creep, regardless of the local level of seismicity. The deformed speleothems found in the *Bossea* cave are the result of uniaxial compression due to small displacements in the roof of the cave (Figs. 2.12). Whether these roof displacements are the result of neotectonics, differential unloading, or slope movements is still unclear. The effect of neotectonics, however, cannot be ruled out for the *Bossea* area which is characterized by low to moderate seismicity related to active tectonics in the adjacent sectors of the southwestern Alps, especially to that in the *Imperia-Sanremo* area (Sue et al., 2007; Molin et al., 2008; Larroque et al., 2009; Sanchez et al., 2010; Locati et al., 2016). Historical earthquakes in this latter alpine sector resulted in macroseismic intensity up to 6 in the Bossea area (1818 and 1887 earthquakes, Locati et al., 2016). More recent earthquakes occurred in western Liguria caused some damages in the study area and roof collapses were detected in *Bossea* cave (Vigna, personal communication). The position and the morphology of the deformed speleothems inside the cave exclude the effect of flow transport and sediment creep as genetic causes. All deformed speleothems, in fact, are found on the southern or northern side of the cave, far from the *Mora* creek, where the pavement and the ceiling of the cave are close. Previous surveys at the surface didn't highlight any sign of slope instability (Vigna, personal communication) so this mechanism can also be ruled out as possible cause.

In summary, the *Bossea* karst system formed by structural control first at deep crustal level (metamorphism, detachment, and folding of the marbles and meta-volcanics) and then by brittle fracturing (joints, joint clusters, bedding plane faults, etc.) at shallow crustal depth. Structural

control in speleogenesis, therefore, can be important both in the metamorphic ductile regime and at shallow depth in the brittle one.

2.5. Concluding remarks

The major objective of the structural investigation was to show that complex structures such as major strike-slip faults, disharmonic detachment contacts with associated damage zones, core zones, and folds play an important role in the development of karst systems such as *Bossea*. These processes include secondary dissolution, erosion, and collapse. Different structural elements control the development of each of these processes.

The structural setting of *Bossea*, at the boundary between the internal and external Briançonnaise units in the Western Alps, is dominated by transpression between major left-lateral vertical strike-slip faults. The different rheological behavior of the carbonate/marble sequence above the meta-volcanics causes the formation of a detachment surface where tight isoclinal disharmonic folding develops in the marbles and buckling, accommodated by pervasive cleavage and cataclasis, occurs in the basement meta-volcanics.

The *Bossea* karst system develops by taking advantage of this peculiar structural and metamorphic setting. In particular, there are two processes at work: (1) Layer-parallel dissolution in the tightly folded marble sequence, and (2) mechanical erosion at the boundary between marble and the meta-volcanics basement.

The karst development process consists of the following steps: (1) Dissolution occurs along bedding boundaries and other brittle structures (clustered joints and minor bedding-confined joints) in the subvertical folded tight Mesozoic marbles. (2) The dissolution phase or karstification *sensu strictu* is active in the upper part of the Bossea cave, which is fully developed in marbles. (3) Erosion starts when dissolution reaches the detachment surface and the associated damaged rock. Water circulation in the disaggregated rocks of the damage and core zones causes the removal of important meta-volcanic rock volumes. (4) Gravitational instability in the marble duplexes within the damage zone above the detachment causes roof collapse and the formation of large halls. Collapsed marble blocks are dissolved and eroded by the internal stream (*Mora* creek, TM).

Circulation of water through an open joint network system is possible only if the stress state allowed the formation and the preservation of such brittle structures. Recent tectonic phases

(Pleistocene) and neotectonic features in the cave and in outcrop suggest that this was possible at *Bossea*.

The mechanism of karst development described for *Bossea* may be at work in many other karst systems in the western Alps, which have similar structural settings and in many other orogenic contexts worldwide (Austria, Croatia, Turkey, etc.) where similar structural conditions exist.

Chapter 3: Hydrodynamics of Bossea karst system

3.1. Methods

Several parameters were monitored inside the cave as well as on the land surface to get insight on the flow dynamics of both the unsaturated zone and the main underground river. Regarding the meteorological parameters, hourly precipitation (P) and air temperature (T_{air}) data were measured at the *Borello* meteorological station (Fig. 3.1a), that is part of the monitoring network of the Piedmont regional agency for environmental protection (ARPA). This station is located about a kilometer south of the *Bossea* cave at an altitude of 1005 m a.s.l. and it is equipped with a PMB2/R – CAE heated pluviometer and a thermometer. This station experienced malfunctioning between August 2006 and May 2007 and from January to April 2009; for this reason, the meteorological data were taken from the *Chiusa Pesio* station (Fig. 3.1b) during these two intervals. The latter station is located about 12 km west to the studied cave, at an elevation of 935 m a.s.l.; it is equipped with the same instruments of *Borello*. Relative humidity and global solar radiation data were taken by the *Colle San Bernardo* meteorological station (Fig. 3.1c). This station is located about 15 km ESE of *Bossea*, at an elevation of 980 m a.s.l., and it is equipped with a thermo-hygrometer CAE-TU20 for relative humidity and a pyranometer HE20/K for solar radiation measurement. The acquisition from this latter station was necessary due to the absence of the proper sensors in *Borello* and the other nearby stations. The data from the three aforementioned stations were used to calculate potential evapotranspiration (ET_0) through the *Turc* formula (Turc, 1961):

$$ET_0(mm\ d^{-1}) = a \cdot C \cdot (R_G + b) \cdot \frac{T}{T+15} \tag{3.1}$$

Where

- a is an empirical constant equal to 0.31 ($m^2\ MJ^{-1}\ mm^{-1}$)
- b is an empirical constant equal to 2.094 ($MJ\ m^{-2}\ day^{-1}$)
- C is a parameter constrained by relative humidity RH (%) as follows:

$$C = 1 + \frac{50-RH}{70} \quad \text{if} \quad RH < 50\% \tag{3.2}$$

$$C = 1 \quad \text{if} \quad RH > 50\% \tag{3.3}$$

- R_G is the total radiation at the site ($MJ\ m^{-2}\ day^{-1}$)
- T is the mean daily temperature (°C).

There are several empirical formulas for the estimation of this parameter. *Turc* formula is one the energy-based methods, which apply the energy balance approach to estimate potential evapotranspiration (Zhao et al., 2013). The advantages of this formula are its simplicity and the requirement of a limited amount of climate data.

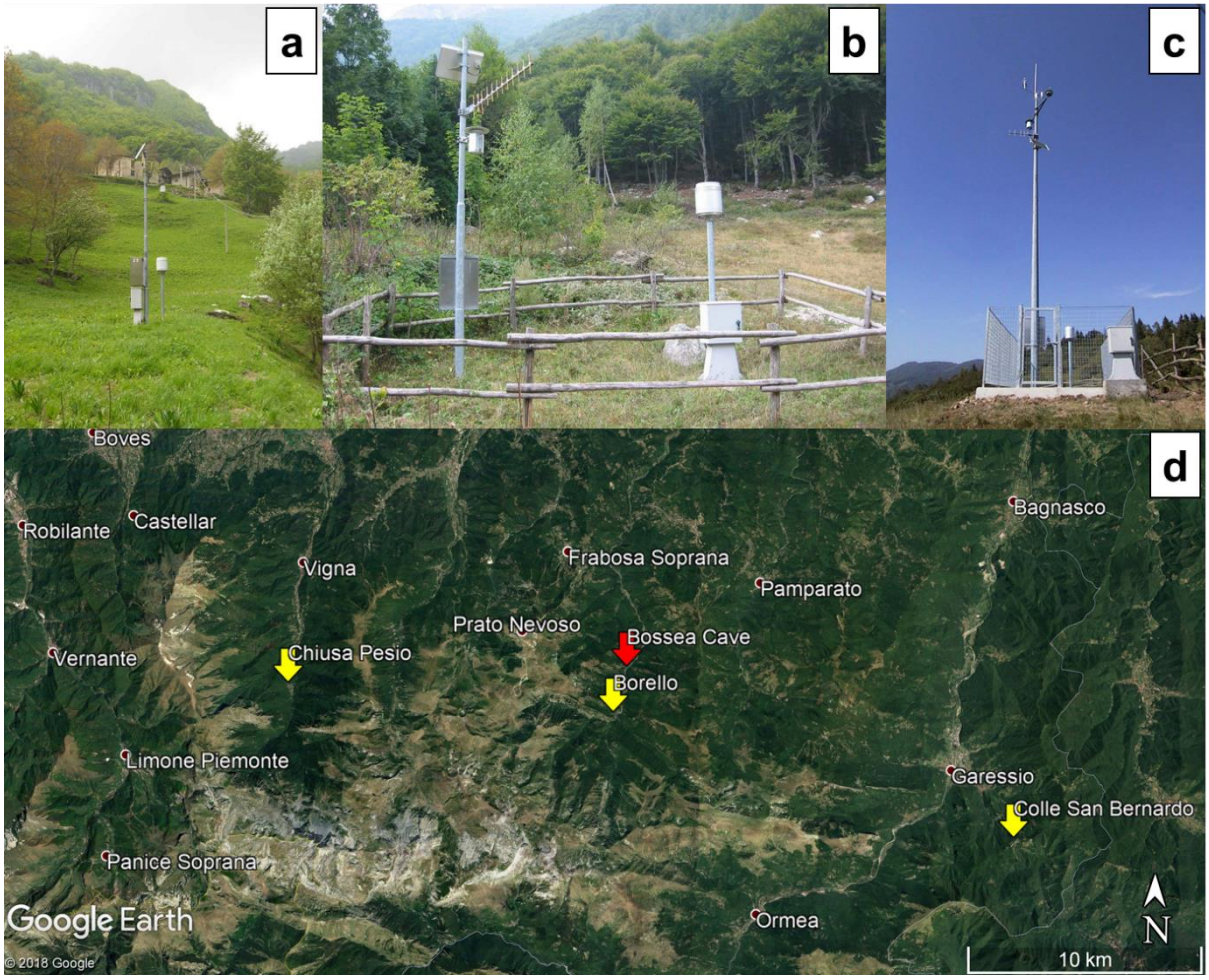

Fig. 3.1. Meteorological stations used for the present study: *Borello* (a), *Chiusa Pesio* (b) and *Colle San Bernardo* (c). Their positions are highlighted by the yellow arrows in (d) in which also the *Bossea* cave position is marked (red arrow.

Regarding the groundwater monitoring, two main types of outflow were investigated: the main underground river (*Mora* creek, TM) and its small tributaries that are represented by inflows from conductive fractures in the rock above the cave (Fig. 3.2). These secondary inflows can be further distinguished between those (locally called "*Polle*") discharging water along the detachment that separates the Permian volcanoclastics from the Mesozoic carbonates above, and those that percolate from fractures in the cave roof (drip site s.s.). *Polla delle anatre* (PA), *Polletta* (PTTA) and *Polla dell'orso* (PO) fall in the former sub-category whereas *Milano* (M),

Torre (TO), *Sacrestia* (SA), *Cancello* (CA), *Balena* (BA), *Onda* (ON) and *Laghi Pensili* (LP) fall in the latter one. The continuous monitoring of these sites was possible thanks to an underground scientific laboratory for karst hydrology research active for the last 40 years (Vigna et al., 2017b).

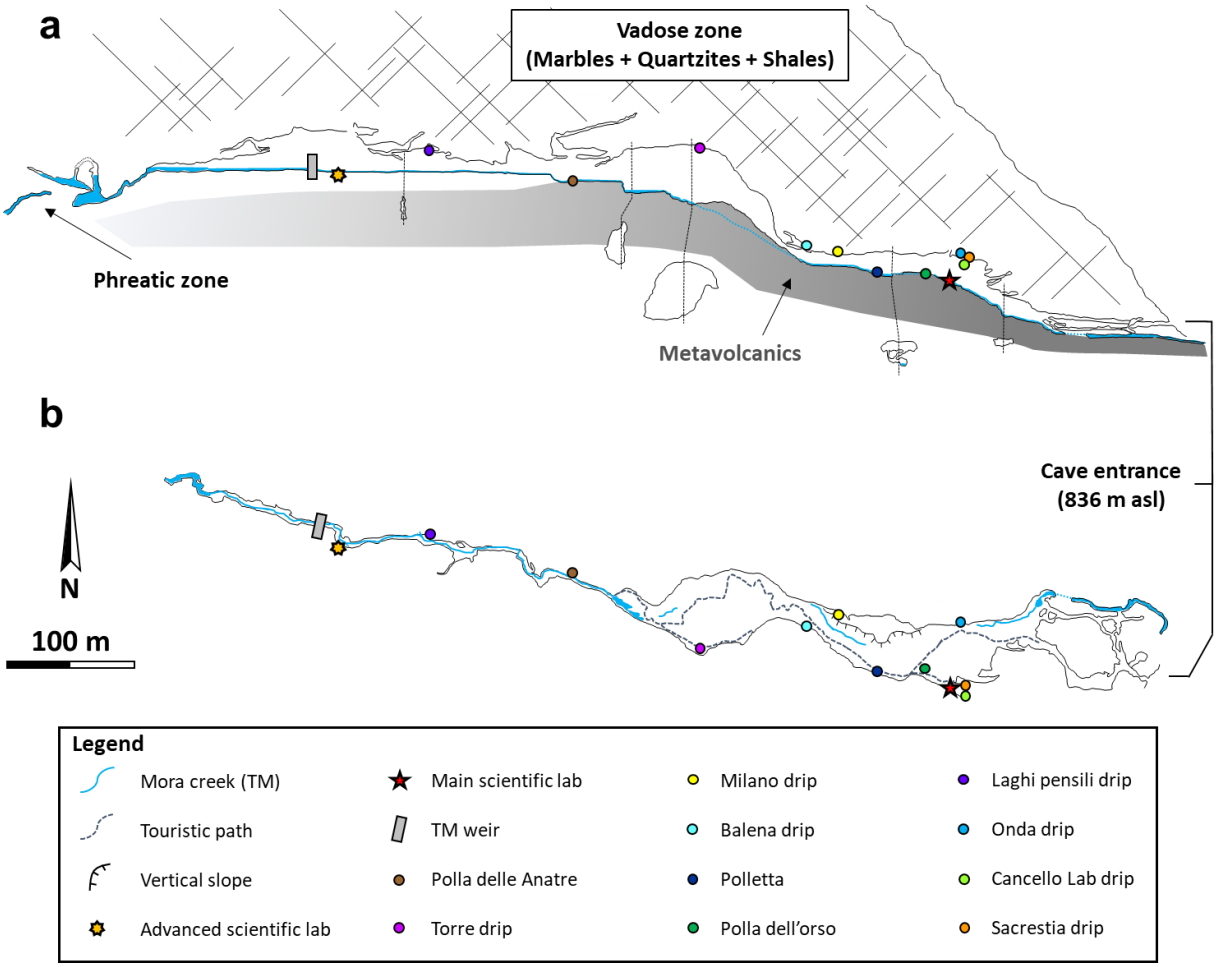

Fig. 3.2. Cross-section (a) and map view (b) of the *Bossea* cave. The positions of the underground river, the secondary inflows and the scientific facilities are reported.

The *Mora* creek and its secondary tributaries, which are characterized by relatively persistent flow, were monitored by means of multiparametric devices (Greenspan, STS, then substituted with OTTs) for water level (L), water temperature (T_{water}) and water electrical conductivity (EC). Concrete weirs were installed along the main tributary pathways and the multiparametric sensors were placed in the artificial pool created upstream of the weirs (Fig. 3.3a, b). Conversion from water level to water discharge was operated for five of these inflows. The

Bazin's formula for horizontal, sharp edged weirs was adopted for the *Milano* and *Torre* drips (Horton, 1907):

$$Q = 0.66 \cdot c \cdot B \cdot (2g)^{0.66} \cdot H^{1.5} \quad (3.4)$$

Where

- Q is the water flow rate ($m^3\ s^{-1}$)
- c is the discharge coefficient, average 0.62
- B is the weir width, equal to 0.01 m
- g is the gravitational constant, 9.81 ($m\ s^{-2}$)
- H is the height of the water over the weir measured behind the weir edge (m)

Polla delle anatre, *Polletta*, *Polla dell'Orso* water levels were converted to flow rate by means of the flow equation for triangular weirs (Henderson, 1966):

$$Q = \frac{8}{15} c \sqrt{2g} \tan\left(\frac{\theta}{2}\right) \cdot H^{5/2} \quad (3.5)$$

Where

- Q is the water flow rate ($m^3\ s^{-1}$)
- c is the discharge coefficient
- θ is the weir V-notch angle (equal to 30°, 60°,90° for *Polletta*, *Polla dell'orso* and *Polla delle anatre*, respectively)
- H is the height of the water over the weir measured behind the weir edge (m)

The inflows with the lowest discharges (*Sacrestia*, *Cancello*) were equipped with funnels and rain gauges (Fig. 3.3c).

A rectangular weir was built also for *Mora* creek in the canyon segment (Fig. 3.2 and Fig. 3.3d for its position and picture, respectively). The conversion formula calibrated for the underground river is the following:

$$Q = 0.385 \cdot B \cdot H \cdot \sqrt{2gH} \quad (3.6)$$

Where

- Q is the water flow rate ($l\ s^{-1}$)

- *B* is the weir width, equal to 12 dm
- *H* is the height of the water over the weir measured behind the weir edge (dm)
- *g* is the gravitational constant, 9.81 (m s^{-2})

The *Mora* creek has also been equipped with a turbidity sensor Solitax t-line sc coupled with a controller device, model Hach Lange sc 200. The system was installed at the beginning of 2018 and data acquisition lasted until May 2019, although some episodes of malfunctioning occurred.

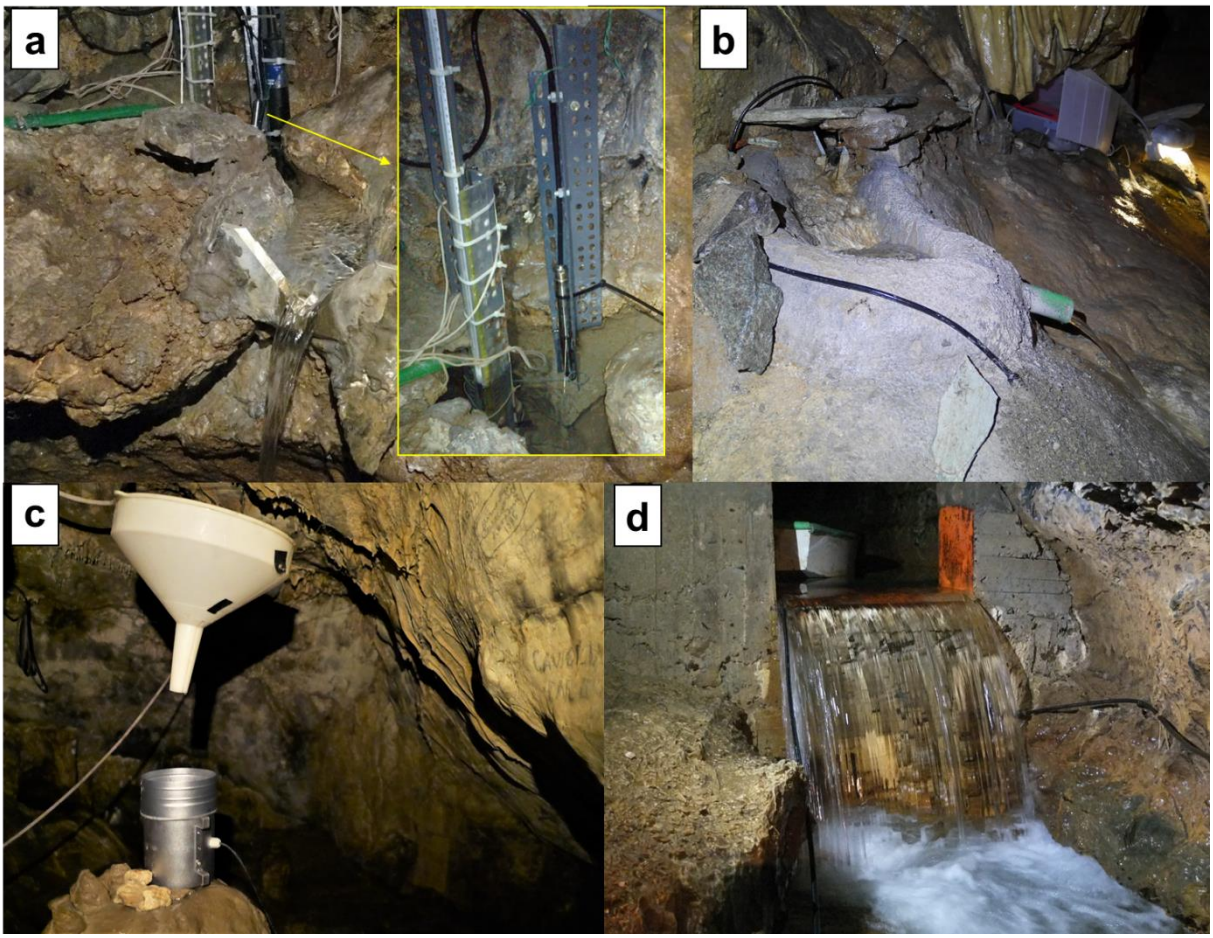

Fig. 3.3. Pictures showing the instruments used in Bossea cave for hydrologic monitoring. (a) *Polla delle anatre* inflows (the box shows a zoom on the multiparametric sensor installed). (b) *Polletta artificial* pool. (c) *Sacrestia* upper monitoring site, equipped with a funnel that collects dripping water and directs it to the rain gauge below. (d) *Mora* creek weir.

Finally, a few tracer tests were carried out for further studying the *Mora* creek and *Milano* drip hydrodynamics. Part of the results of these tests were published by Banzato et al. (2013) as examples for the application of the drainage index to a set of karst systems. In this thesis, all the tests are reported in order to obtain supplementary indications on flow dynamic in the *Bossea* karst system, in addition to the data collected with the hydrodynamic monitoring. Two

tracer tests were performed for the *Milano* drip site, one in October 2010 and the other one in July 2012. Both tests were carried out injecting the dye (uranine) in a fountain located on the slope over the cave (Fig. 3.4a). The injection point is located approximately 100 m higher than the drip site, the horizontal distance injection-arrival point being 150 m. Three tests were performed for the *Mora* creek, in May to mid-June 2007, May 2008 and May to mid-June 2015 respectively. The injection point was the same for all of them: the uranine was injected in the *Roccia Bianca* sinkhole (Fig. 3.4a, b) that is 480 m higher than the *Mora* creek and 3 km far from the measurement point inside the cave. A GGUN FL22 fluorometer was used for all tests. This device has an optical cell that measures the concentration of the fluorescent tracer in the water passing through a sampling chamber. The probe detection limit for uranine is 0.02 ppb (Schnegg and Bossy, 2001; Flynn et al., 2005). The sensor was inserted in a protective cylinder (Fig. 3.4c) and then it was installed either along *Mora* creek (Fig. 3.4d) or in the artificial pool underlying the *Milano* drip.

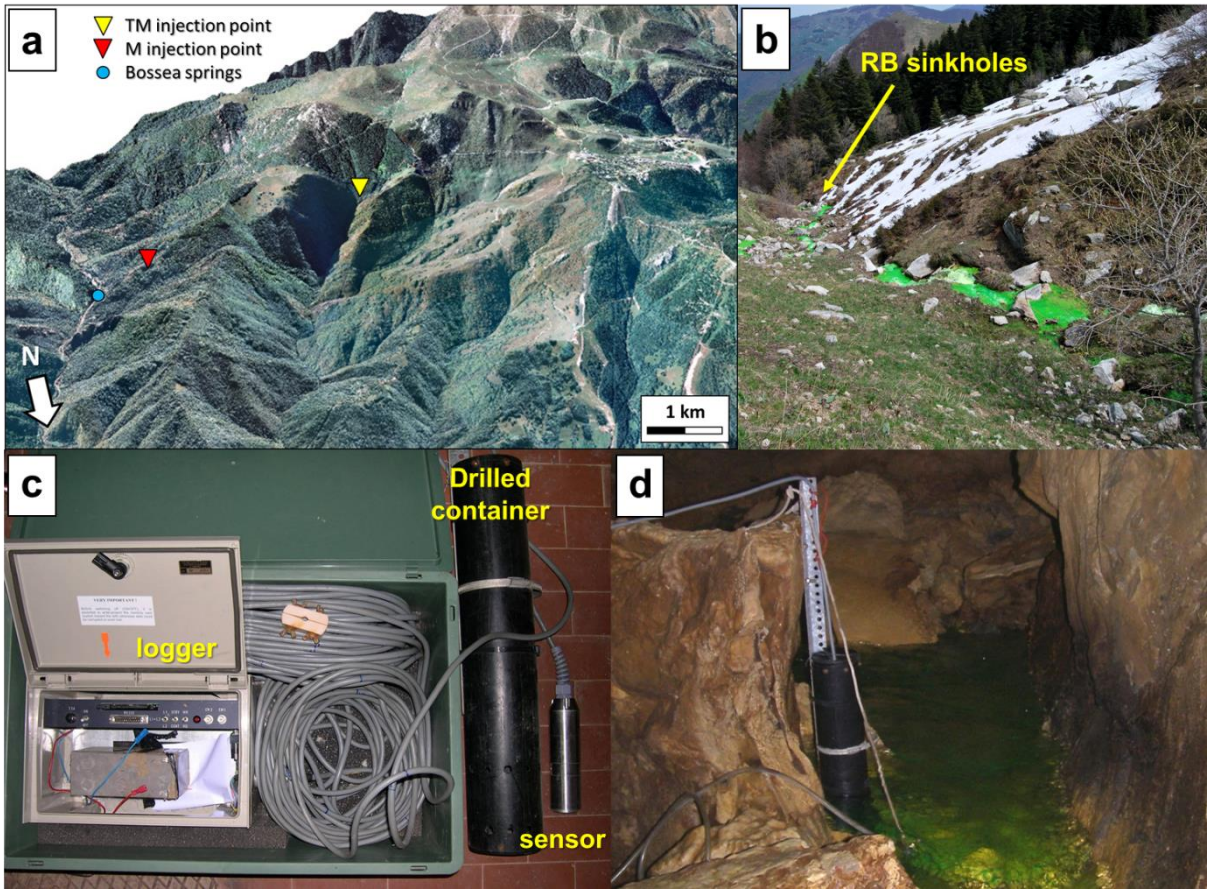

Fig. 3.4. (a) Position of the injection points for both *Mora* creek (yellow triangle) and *Milano* (red triangle). (b) Picture of the *Roccia Bianca* brook during one of TM tests. (c) Instrumentation used for the test and (d) pictures of the device installed along *Mora* creek.

3.2. Results

3.2.1. Climate regime and meteorological considerations

The complete dataset collected by the *Borello* meteorological station is reported in Appendix 1. The data reveal that the mean annual precipitations is about 1360 mm in the time interval 2000-2018, ranging from a minimum of 784.2 mm recorded in 2017 to the maximum of 2174 mm observed in 2002 (Tab. 3.1). Mean monthly precipitations measured between 2000 and 2019 show a bimodal distribution with two precipitation peaks, a first one in April and the highest value in November (up to 242.2 mm) whereas the lowest is found in July (56.0 mm). The highest variability in precipitation is found in October and November (from no precipitations to the highest ever recorded value) whereas the lowest variability of monthly precipitations corresponds to June and August.

	Monthly precipitations (mm)												total annual precipitation (mm)
	January	**February**	**March**	**April**	**May**	**June**	**July**	**August**	**September**	**October**	**November**	**December**	
2000	26.6	0.0	34.0	209.0	128.6	203.0	67.8	105.4	233.4	410.6	318.6	61.0	1798.0
2001	137.6	33.4	165.2	49.4	234.0	36.0	78.6	31.8	86.4	65.6	113.4	30.0	1061.4
2002	19.4	133.4	98.2	114.2	274.4	138.2	286.2	134.2	129.8	146.6	569.2	130.2	2174.0
2003	39.6	12.6	9.6	167.6	60.2	97.6	28.6	59.6	33.4	187.2	198.2	322.8	1217.0
2004	34.8	129.4	37.8	112.2	197.2	56.6	35.4	33.4	59.2	120.6	86.8	115.0	1018.4
2005	0.4	37.6	48.0	226.6	77.8	74.6	6.8	55.8	90.8	221.6	46.8	67.6	954.4
2006	21.6	85.0	15.6	44.2	37.0	35.6	65.6	**70.2**	**232.2**	**68.4**	**16.4**	**122.8**	814.6
2007	**24.6**	**18.8**	**118**	**104.8**	**99.2**	154.6	2.6	102.2	61.0	162.4	147.0	37.6	1032.8
2008	162.0	25.6	61.6	116.0	215.6	136.6	10.0	20.4	62.2	76.6	366.2	323.6	1576.4
2009	**85.8**	**105.6**	**158.6**	**385.8**	39.8	114.8	28.0	83.4	148.8	92.6	158.6	114.8	1516.6
2010	86.4	108.0	101.0	155.2	89.6	152.8	32.0	93.8	40.2	297.2	284.6	142.2	1583.0
2011	52.8	88.8	255.2	42.2	12.0	143.2	53.6	16.4	68.2	110.4	437.0	0.0	1279.8
2012	66.2	35.6	90.2	184.0	189.4	10.8	20.0	27.0	242.4	121.0	251.2	20.0	1257.8
2013	130.4	49.0	238.6	232.6	216.4	36.8	47.0	83.2	34.4	111.2	152.6	175.6	1507.8
2014	239.6	133.0	115.6	131.6	67.4	143.2	33.2	34.0	65.4	54.2	514.8	117.2	1649.2
2015	65.4	201.0	193.8	75.0	71.0	125.2	22.0	90.8	100.8	197.8	6.6	9.2	1158.6
2016	3.0	248.4	102.8	40.8	105.6	171.4	51.4	58.4	30.6	148.6	551.8	74.4	1587.2
2017	20.8	103.4	94.4	95.2	52.8	19.4	17.2	16.6	50.4	0.0	161.6	152.4	784.2
2018	199.0	101.4	192.4	163.2	325.6	128.4	59.8	50.2	35.6	355.8	220.8	23.4	1855.6
2019	16.2	71.8	5.2	241.6	204.0	39.0	175.0	49.2	-	-	-	-	**Mean annual P**
Mean Monthly precipitation	*71.6*	*86.1*	*106.8*	*144.6*	*134.9*	*100.9*	*56.0*	*60.8*	*95.0*	*155.2*	*242.2*	*107.4*	*1359.3*

bold values were obtained using data from Chiusa Pesio meteo station in missing data interval of Borello time serie

Tab. 3.1. Monthly precipitations data collected by *Borello* station. In case of missing data intervals, the gaps were filled with data taken from *Chiusa Pesio* station in order to obtain the monthly values (bold numbers).

Mean air temperature values measured between 2000 and 2019 show a unimodal distribution (Fig. 3.5) with the highest temperatures measured in the summer season (maximum of about 18 °C found in July) and the lowest ones in winter (the minimum mean value of -0.3°C was recorded in January). The mean annual temperature value is 8.7 °C. Regarding the data collected hourly, the absolute lowest value of air temperature is -16 °C (measured in February 2012) whereas the absolute highest air temperature (32.5 °C) was observed in August 2017.

The monthly data fit in the Köppen-Geiger climatic classes Dfb (Cold without a particularly dry season and with a warm summer) revised by Beck et al. (2018), who also propose this climate class for the alpine region in which the study area is located. Occasionally, the climatic class can shift to the Mediterranean class Csb due to the proximity of the study area to the Mediterranean Sea.

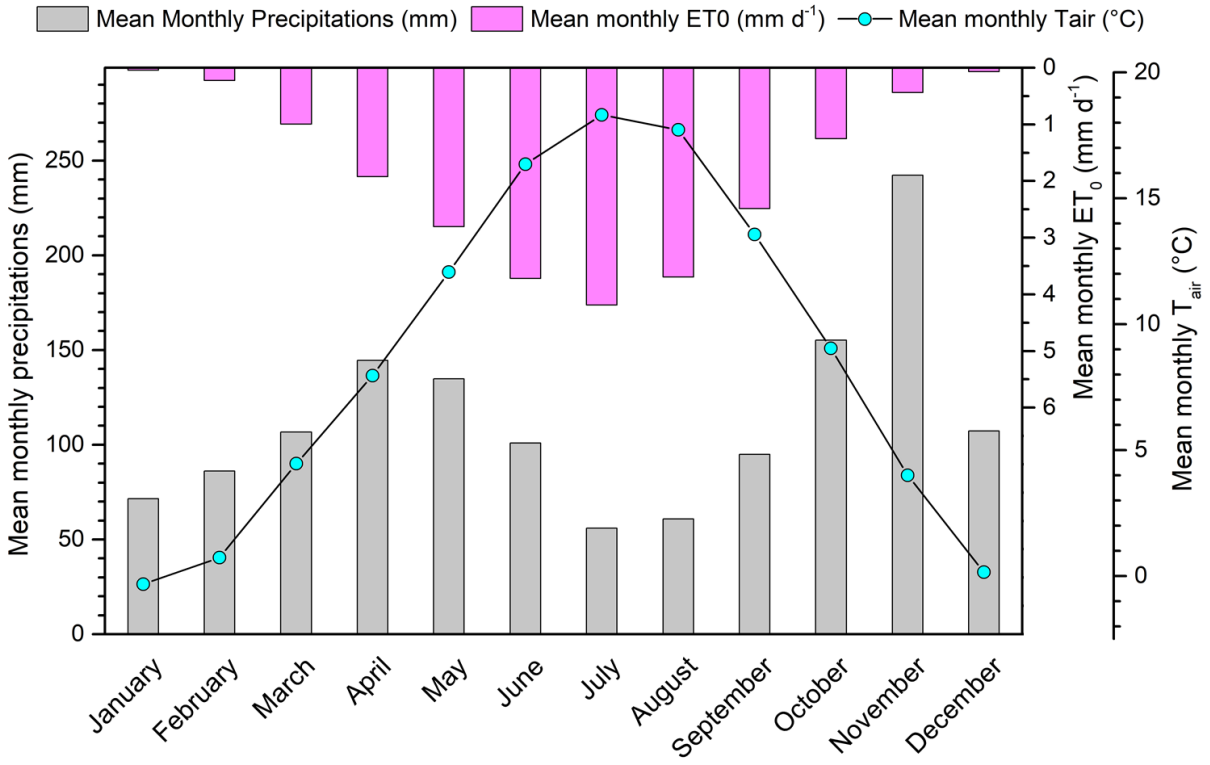

Fig. 3.5. Mean monthly precipitations distribution and mean monthly air temperature measured by *Borello* station in the time interval 2000-2018 and potential evapotranspiration (ET_0) calculated with the data collected by the meteorological stations described in the previous section, coupled with mean monthly air temperature measured by *Borello* station.

Potential evapotranspiration shows a unimodal distribution through the year that follows the trend of air temperature (Fig. 3.5). The highest values are found in summer months whereas the lowest ones correspond to winter months.

3.2.2. Hydrodynamic of the secondary inflows

The summary statistics of the hydrological and physicochemical parameters monitored for each inflow are reported in Tab. 3.2. As mentioned in the previous section, the *Mora* creek secondary tributaries can be subdivided in two main categories, depending on their position respect to the

structural setting: the so-called "*Polle"*, that discharge water along the tectonic contact between the *Impermeable Complex* and the carbonate sequence above, and the drip sites discharging from fractures in the cave roof. This latter category can be further split in drips discharging along bedding junctions and the others outflowing from secondary fractures. The hydrological characterization of each inflows is reported in the following subsections; some examples the hydrodynamic behavior during the recharge/discharge phases are reported for each inflow. The complete hydrographs and chemographs for each inflow are reported in Appendix 2. It should be noted that the definition of *Impermeable Complex* for the basement rocks is used in this thesis because it is the classical hydrogeological definition adopted for this rock sequence. In reality, these non-carbonate rocks should be defined as *low permeable complex* because evidences of (limited) flow circulation in the fractures of these rocks were recognized.

3.2.2.1. Polla delle anatre (PA)

This inflow discharges water from a point located along the detachment surface between the basement rocks and the Mesozoic carbonates. It is placed on the terminal part of the Mora creek upper sector, close to the point where the canyon ends abruptly with the *Ernestina*'s waterfall (Fig. 3.2). It is the secondary tributary of the underground river with the most constant flow rate. Its discharge has never reached zero in the monitored time interval, not even in case of severe dry periods. If discharge exceeds the threshold of 2.02 l/s, outflow occurs over the borders of the artificial pool that collects the water and that contains the monitoring sensors. Since *Polla delle Anatre* exceeded the threshold a few times, its maximum flow rate is over that value, but it is not possible to assess it precisely. The highest flow rates were recorded during the spring and autumn seasons whereas the lowest values were recorded at the end of summer.

	Polla delle Anatre (PA)			Polletta (PTTA)			Polla dell'Orso (PO)		
	Q	T	EC	Q	T	EC	Q	T	EC
	l/s	°C	µS/cm	l/s	°C	µS/cm	l/s	°C	µS/cm
Mean	0.03	9.96	275.1	0.01	9.45	340.7	0.07	9.35	417.1
Standard error	0.00	0.00	0.1	0.00	0.00	0.1	0.00	0.00	0.5
Median	0.00	9.95	270.0	0.00	9.35	340.0	0.00	9.38	421.0
Mode	0.00	9.95	269.0	0.00	9.25	339.0	0.00	9.40	438.0
Standard devation	0.11	0.05	15.5	0.04	0.32	29.0	0.14	0.07	28.1
Variance	0.01	0.00	239.8	0.00	0.10	843.8	0.02	0.01	787.4
Curtosis	111.19	129.57	2.1	14.57	-0.10	1.1	16.62	-1.01	0.2
Skewness	9.28	8.45	1.5	3.71	1.03	-0.1	3.53	-0.51	-0.7
Range	2.02	1.16	97.9	0.33	1.57	241.0	1.13	0.26	150.0
Minimum	<0.001	9.92	255.1	0.00	9.08	215.0	0.00	9.22	333.0
Maximum	2.02	11.08	353.0	0.33	10.65	456.0	1.13	9.48	483.0
CV	396%	0.5%	5.6%	279%	3.4%	8.5%	205%	0.8%	6.7%
time interval	2011-2019	2011-2019	2014-2019	2008-2019	2008-2019	20011-2019	2019	2019	2019

	Milano (MI)			Torre (TO)			Laghi Pensili (LP)		
	Q	T	EC	Q	T	EC	L	T	EC
	l/s	°C	µS/cm	l/min	°C	µS/cm	cm	°C	µS/cm
Mean	0.04	9.54	411.9	0.32	9.18	284.6	16.37	8.56	347.68
Standard error	0.00	0.00	0.1	0.00	0.00	0.1	0.00	0.00	0.09
Median	0.00	9.31	413.0	0.06	9.10	284.0	16.40	8.57	350.00
Mode	0.00	9.20	418.0	0.00	9.10	281.0	16.40	8.57	356.00
Standard devation	0.07	0.39	36.1	0.46	0.25	5.5	0.00	0.01	7.68
Variance	0.00	0.15	1305.0	0.22	0.06	30.4	0.00	0.00	58.96
Curtosis	6.78	-1.40	0.3	0.60	4.66	2.9	-0.34	-0.15	-1.05
Skewness	2.56	0.50	-0.1	1.41	1.56	1.0	0.05	-0.37	-0.53
Range	0.54	1.50	249.2	2.12	2.13	54.2	0.90	0.07	26.00
Minimum	0.00	9.10	286.8	0.00	8.90	258.0	16.00	8.54	331.00
Maximum	0.55	10.60	536.0	2.12	11.03	312.2	16.90	8.61	357.00
CV	187%	4.1%	8.8%	144%	2.7%	1.9%	1.1%	0.1%	2.2%
t interval	2003-2019	2003-2019	2003-2019	2002-2007	2/2004-2017	2005-2017	2019	2019	2019

	Sacrestia (SA)			Cancello Lab (CA)			Onda (ON)		
	L (upp)	L (low)	EC	L	T	EC	L	T	EC
	mm	mm	µS/cm	mm	°C	µS/cm	cm	°C	µS/cm
Mean	1.32	0.75	-	1.71	-	-	0.18	9.33	435.7
Standard error	0.04	0.01	-	0.03	-	-	0.01	0.00	0.6
Median	0.00	0.40	-	0.80	-	-	0.00	9.31	433.0
Mode	0.00	0.20	-	0.80	-	-	0.00	9.36	453.0
Standard devation	6.55	1.41	-	4.00	-	-	0.44	0.18	24.9
Variance	42.94	1.99	-	16.03	-	-	0.19	0.03	621.7
Curtosis	272.36	19.89	-	62.02	-	-	28.15	1.21	-0.1
Skewness	12.68	4.31	-	6.79	-	-	4.59	1.22	0.3
Range	236.20	14.60	-	56.20	-	-	4.90	0.87	147.0
Minimum	0.00	0.20	-	0.00	-	-	0.00	9.07	375.0
Maximum	236.20	14.80	-	56.20	-	-	4.90	9.94	522.0
CV	496%	188%	-	234%	-	-	238%	1.9%	5.7%
t interval	2011-2019	2019	-	2015-2018	-	-	2019	2019	2019

	Balena (BA)		
	L	T	EC
	cm	°C	µS/cm
Mean	-	9.57	324.98
Standard error	-	0.01	0.58
Median	-	9.33	306.50
Mode	-	9.07	300.50
Standard devation	-	0.58	29.02
Variance	-	0.33	842.24
Curtosis	-	-0.84	-1.52
Skewness	-	0.84	0.47
Range	-	1.89	88.80
Minimum	-	9.01	294.10
Maximum	-	10.90	382.90
CV	-	6.0%	8.9%
t interval	-	2018	2018

Tab. 3.2. Summary statistics of all the tributaries of Mora creek. Water level is reported instead of discharge when the conversion was not accurate.

The complete hydrograph and chemographs are reported in Appendix 2a. *Polla delle anatre* is the secondary tributary with the lowest mean electrical conductivity. During fall precipitations, *Polla delle anatre* showed sharp increases in flow rate (*Q*), water temperature (T_{water}) and electrical conductivity (*EC*. Fig. 3.6a). The peak values for all monitored parameters showed a delay respect to precipitation peaks of a few hours, never exceeding 24 hours. The maximum variation of water temperature and electrical conductivity during these peaks is about 1,2 °C and 90 µS/cm respectively. The maximum values for both T and EC were recorded during autumn events but not simultaneously (Appendix 2a). The example reported in Fig. 3.6 shows that overflow from the border of the artificial pool occurred during 3 over the 5 recorded flow peaks. The highest ever EC value for this inflow was recorded during the second peak whereas water temperature showed a maximum variation of 0,3 °C during the same peak flow. During springtime, *Polla delle Anatre* showed increases in flow rate that can be either sharp (fourth and fifth peaks in Fig. 3.6b) or smooth with several small oscillations (sixth Q increase, mid-April, Fig. 3.6b). Water temperature showed very sharp increases during the first type of flow increments whereas it did not vary during the smooth Q oscillations.

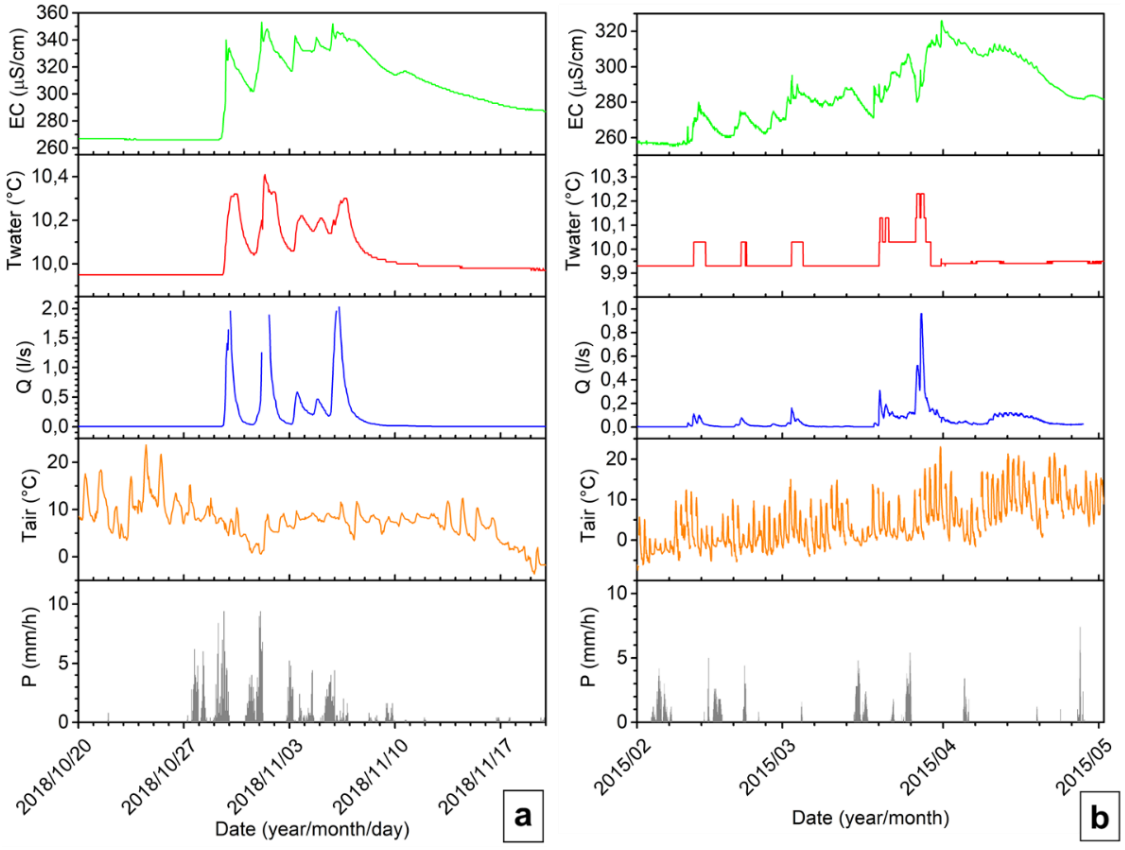

Fig. 3.6. Examples of *Polla delle anatre* behavior during precipitation events in different phases of the hydrological year: autumn (a) and spring (b). Precipitations and air temperature are reported for comparison.

Electrical conductivity, overall, increased during the subsequent flow increments in both fall and springtime (Fig. 3.6a, b), but its pulses are broader (i.e. they last longer) than those exhibited by discharge and temperature. Moreover, EC showed two sharp decreases during the two highest discharge (and temperature) pulses. This phenomenon occurred in a few other occasions through the time series in springtime and once during a strong flood event (see Chapter 6 for further information). Electrical conductivity mirrored Q during its oscillations in mid-April 2015. The matching oscillations in Q and EC can be found in other springtime intervals through the time series. All the monitored parameters showed no response to precipitations during summer (Fig. 3.7a) and winter seasons, with a couple of exceptions during winter, like the one presented in Fig. 3.7b. The latter event was characterized by sharp, positive peaks in discharge, water temperature and electrical conductivity. They rose simultaneously but EC pulse lasted more than the ones showed by the other parameters. This is also the only case of overflowing in wintertime through the whole monitoring interval.

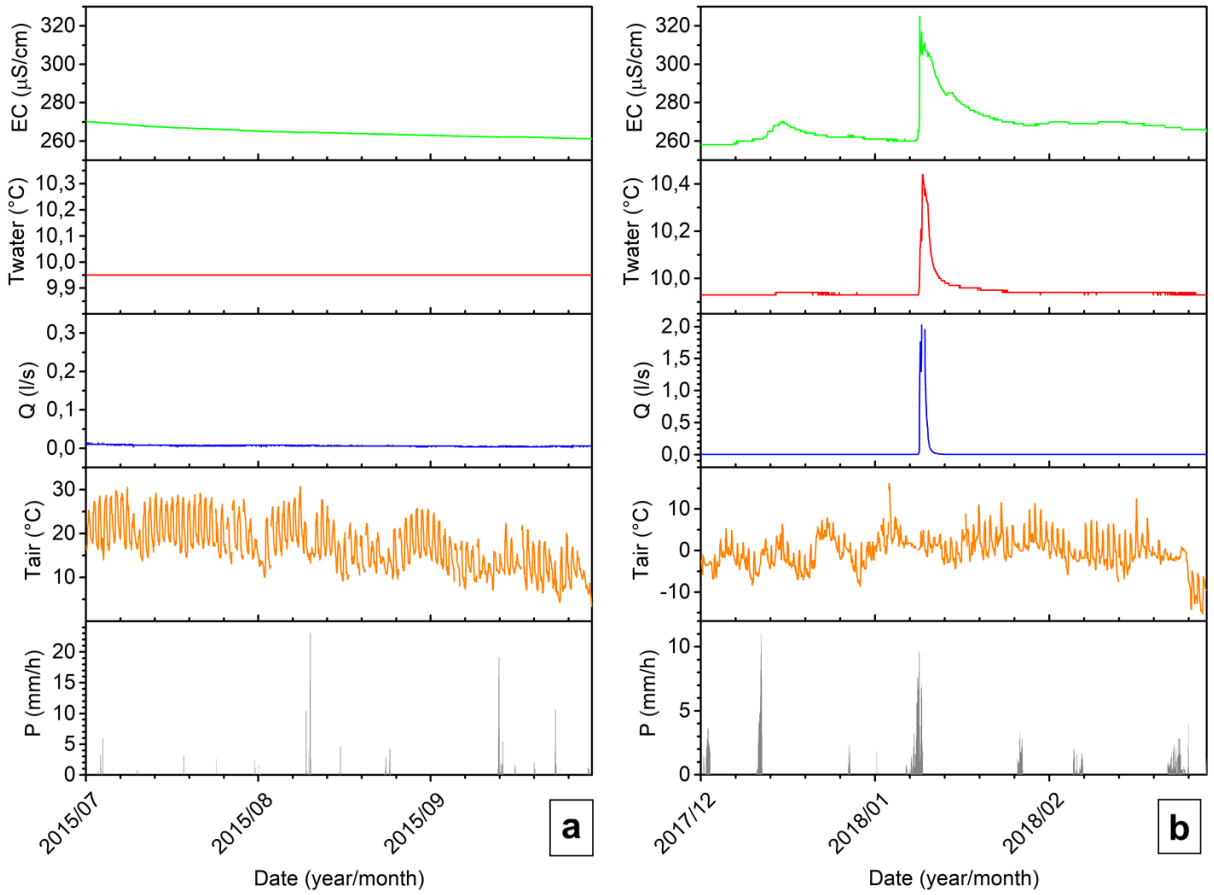

Fig. 3.7. Examples of *Polla delle anatre* behavior during summertime (a) and winter (b).

3.2.2.2. Polletta (PTTA)

Like *Polla delle Anatre*, *Polletta* outflow is placed on the detachment surface outcropping inside the cave. This inflow is located in one of the large rooms belonging to the bottom sector of the *Bossea* cave, along the touristic path (Fig. 3.2). It has a quite constant flow rate of about 0.01 l/s but it can reach zero during dry periods, especially at the end of the hydrological year (beginning of September). It has a maximum discharge significantly lower than that of *Polla delle anatre* but it has a higher mean mineralization. The complete dataset is reported in Appendix 2b. This inflow showed sharp increases of discharge and water temperature in response to precipitation events during the fall season, like in the interval reported in Fig. 3.8a. Electrical conductivity had a more complex behavior: it sharply decreased during the first flow peaks then it progressively followed the Q and T trends during the following late fall peaks. The time lag between precipitation and peak flow ranged between 6 hours to a day.

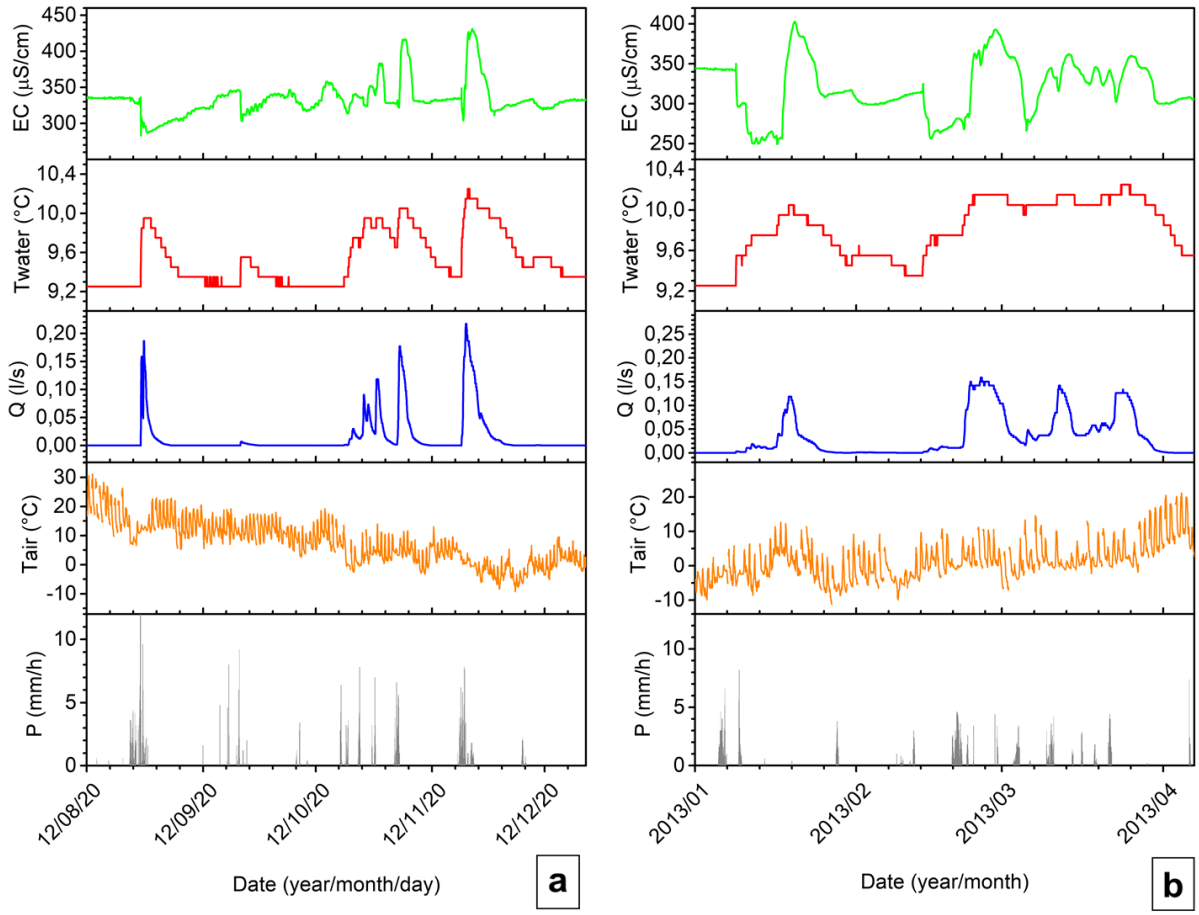

Fig. 3.8. Examples of *Polletta* hydrograph and chemographs during autumn (a) and spring (b).

The time interval represented in Fig. 3.8b is a typical example of the *Polletta* behavior during springtime: the rise in discharge can last for more than a week after the precipitation events and the lag time between precipitations and flow peak can be up to a week. Water temperature varied according to the discharge trend, but its pulses are more prolonged than those of flow rate. There is a positive temperature peak lasting almost two months from 2013/02/27 to 2013/04/21 in the considered example. This proposed example shows that water mineralization exhibited first a negative prolonged decrease (50 to 90 µS/cm less than the pre-peak values) followed by a sharp positive peak during the first two discharge peaks. The following EC oscillations are more irregular.

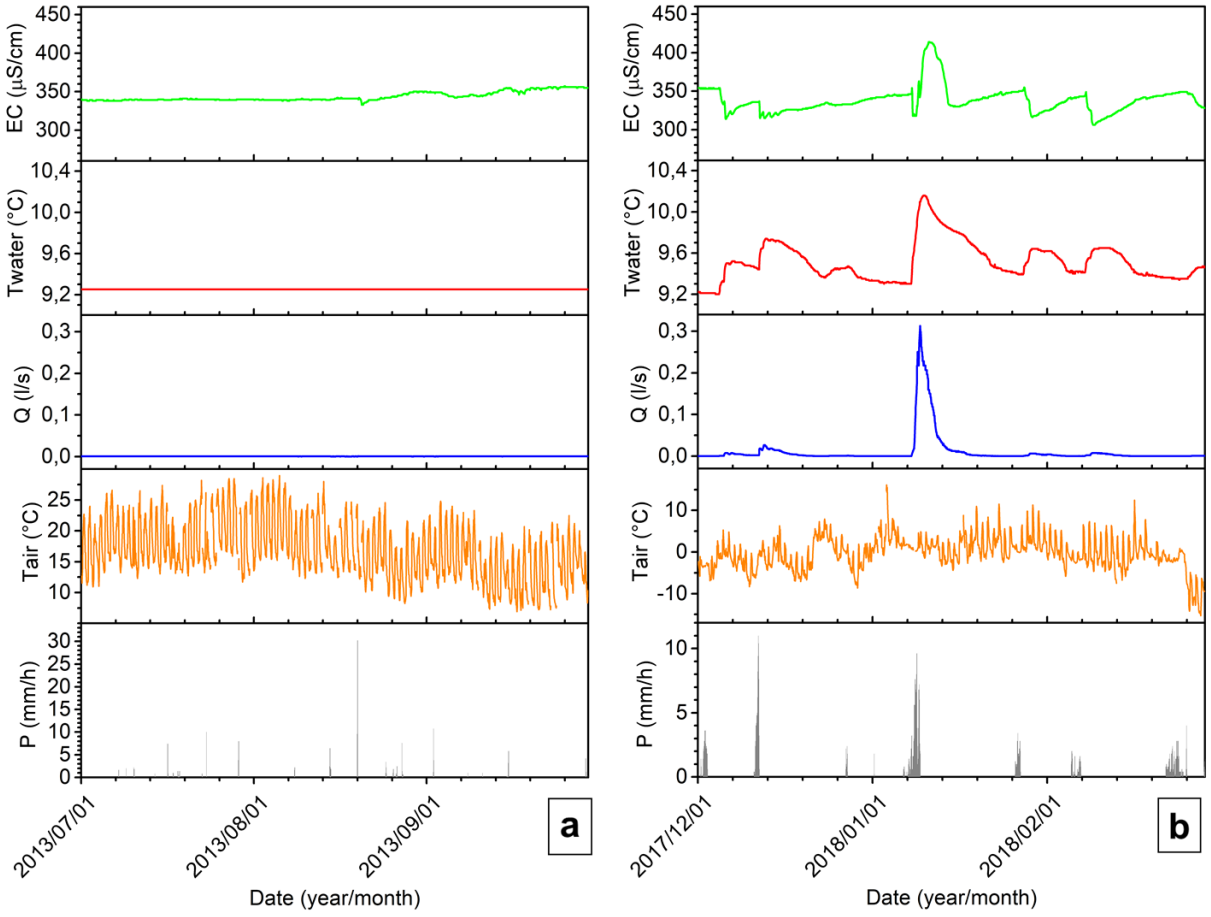

Fig. 3.9. Examples of *Polletta* hydrograph and chemographs during summer (a) and winter (b) seasons.

Polletta showed no response to summer precipitations (Fig. 3.9a) whereas it was more responsive to winter precipitations. This latter behavior can be observed in Fig. 3.9b: the inflow responded impulsively to all the precipitation events. Water temperature showed marked and prolonged increments during the consecutive precipitations whereas EC had a specular trend

respect to that of T. A negative EC peak corresponds to a positive T peak, the only exception being the flow peak occurred during the second week of January 2018: first EC decreased sharply but then a strong positive EC peak occurred. This event corresponds also to the second highest peak discharge observed in the whole monitoring interval.

3.2.2.3. Polla dell'Orso (PO)

This is the last monitored inflow that discharges along the tectonic contact outcropping in the cave. Like the previous one, it is found in the bottom part of the cave, close to the touristic path (Fig. 3.2). The reported data are for 2019 only, because of repeated malfunctioning in the previous years.

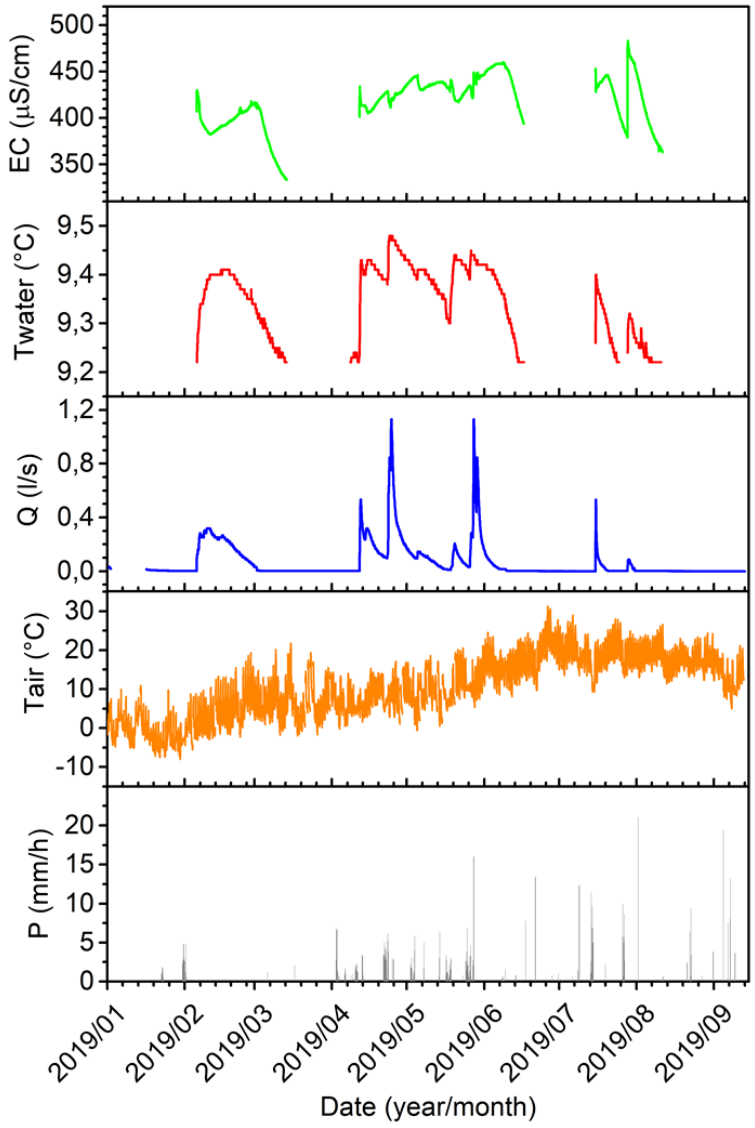

Fig. 3.10. *Polla dell'orso* monitoring data collected during 2019.

This inflow is characterized by a marked impulsive behavior: it was usually dry during periods of no precipitation whereas its discharge increased abruptly up to more than a liter per second when precipitation occurred. It has the most mineralized and coldest water among the so-called *"Polle"*. The hydrograph and the chemographs show that all parameters had a synchronous impulsive behavior during precipitation events occurred between February and July 2019 (Fig. 3.10). Water temperature showed positive increments that mirrored the flow peaks, with a range of variation not exceeding 0.3 °C. During each consecutive flow peak, water electrical conductivity showed first a negative peak (with a maximum decrement of 50 µS/cm but usually of about 10 µS/cm), then EC started to increase progressively during the discharge recession limb, until the next flow peak occurred. There was an exception to this trend during the last monitored peak flow: the last discharge peak occurred at the end of July 2019 after strong precipitations (up to 20 mm/h) and this small flow peak was accompanied only by a sharp increase of electrical conductivity (more than 100 µS/cm). After that, the rainfall events occurred in August and September didn't caused any response of *Polla dell'Orso*, no matter the precipitation intensity.

3.2.2.4. Milano drip site

This drip site is located at the end of the first large collapse room encountered from the cave entrance (Fig. 3.2). The *Milano* drip site discharges water from a bedding junction in the cave ceiling; there is also a secondary outflow from an adjacent bedding junction, but it is seldom active. Both fractures are covered by abundant speleothem deposits. This drip site is characterized by a constant flow rate that dries out only in case of extremely dry periods and it can exceed half a liter per second. It has a relatively high mineralization, surpassed only by *Polla dell'Orso*. During the monitoring period, water temperature ranged from 9.1 to 10.6 °C, which is the second highest variability range observed among all monitored inflows. The complete hydrograph and chemographs for the whole monitoring interval (2003-2019) are reported in Appendix 2d. Two examples of the behavior of this drip during autumn and snow melting phase, respectively, are reported in Fig. 11. The first rainfall event occurred in October 2012 did not caused a clear response of *Milano* discharge but remarkable increases in water temperature and electrical conductivity were indeed observed (Fig. 3.11a). The subsequent precipitations were followed by positive peaks of Q as well as of water temperature. Lag times between precipitation peaks and those of discharge varied from 4 hours to a day. Water

temperature showed a maximum increase of 1 °C and its positive peaks were broader than those showed by the flow rate. Electrical conductivity showed increments that mirrored the trend observed for Q. The maximum absolute variation of EC observed during this phase were around 150 µS/cm, and the relative variation between pre-peak and peak values ranged from 20 to 150 µS/cm. The highest EC relative variations were observed during the last two discharge peaks, when EC showed first a sharp, short drop followed by a strong increase. During the January to May 2013 interval, the *Milano* drip showed a slightly more irregular response to precipitations (Fig. 3.11b). Flow rate started to slowly increase after the first precipitation of January 2013, then it exhibited a strong, prolonged impulse that lasted for two weeks. Discharge oscillated during the whole March 2013, not always corresponding to precipitation inputs. Water temperature increased during the first discharge increase, and it remained higher than mean values until the last spring rainfall event (end of March 2013).

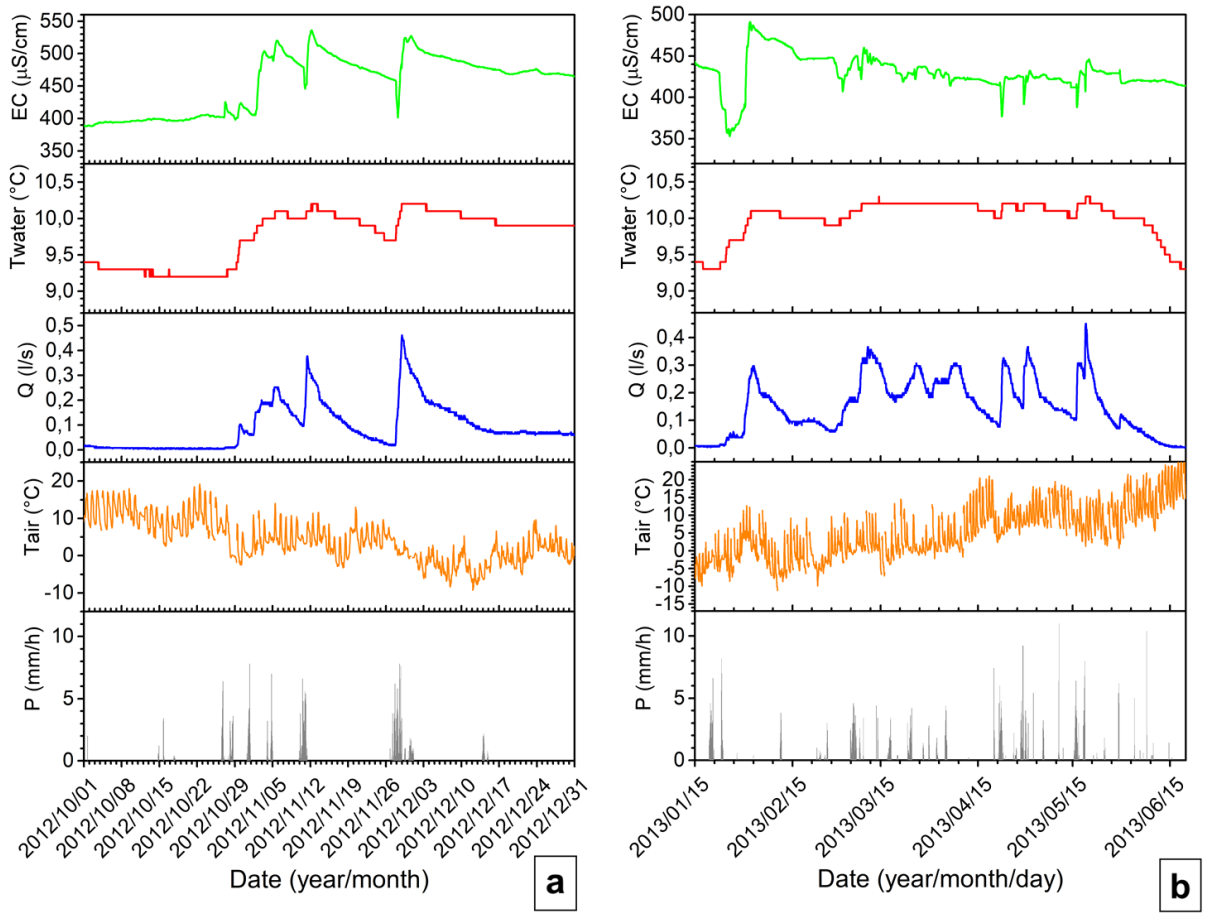

Fig. 3.11. Examples of *Milano* behavior during autumn (a) and winter to springtime (b).

Water electrical conductivity showed a strong, prolonged decrease followed by a marked increase during the first flow peak occurred in January 2013. From February to the beginning of June 2013, EC showed several fluctuations synchronous with the flow peaks, showing repeated alternations of negative and positive peaks. During summertime, this drip showed no response to precipitations (Fig. 3.12a) whereas it usually exhibited an impulsive response to winter precipitations, although the magnitude of these impulses was variable for all the three parameters considered, as shown by the hydrograph and chemograph of the December 2017 - February 2018 (Fig. 3.12b). Given a specific impulse, the shape of the peak was similar for the three variables, although EC exhibited small negative peaks preceding the positive ones during the January to February 2018 pulses. The maximum water temperature variation during these events was 0.5 °C, which was observed during the highest peak flow (January 9th), together with the strongest EC variation (100 µS/cm). Considering all three parameters, the other pulses were somewhat smoother and with a lower magnitude than the one occurred on January the 9th.

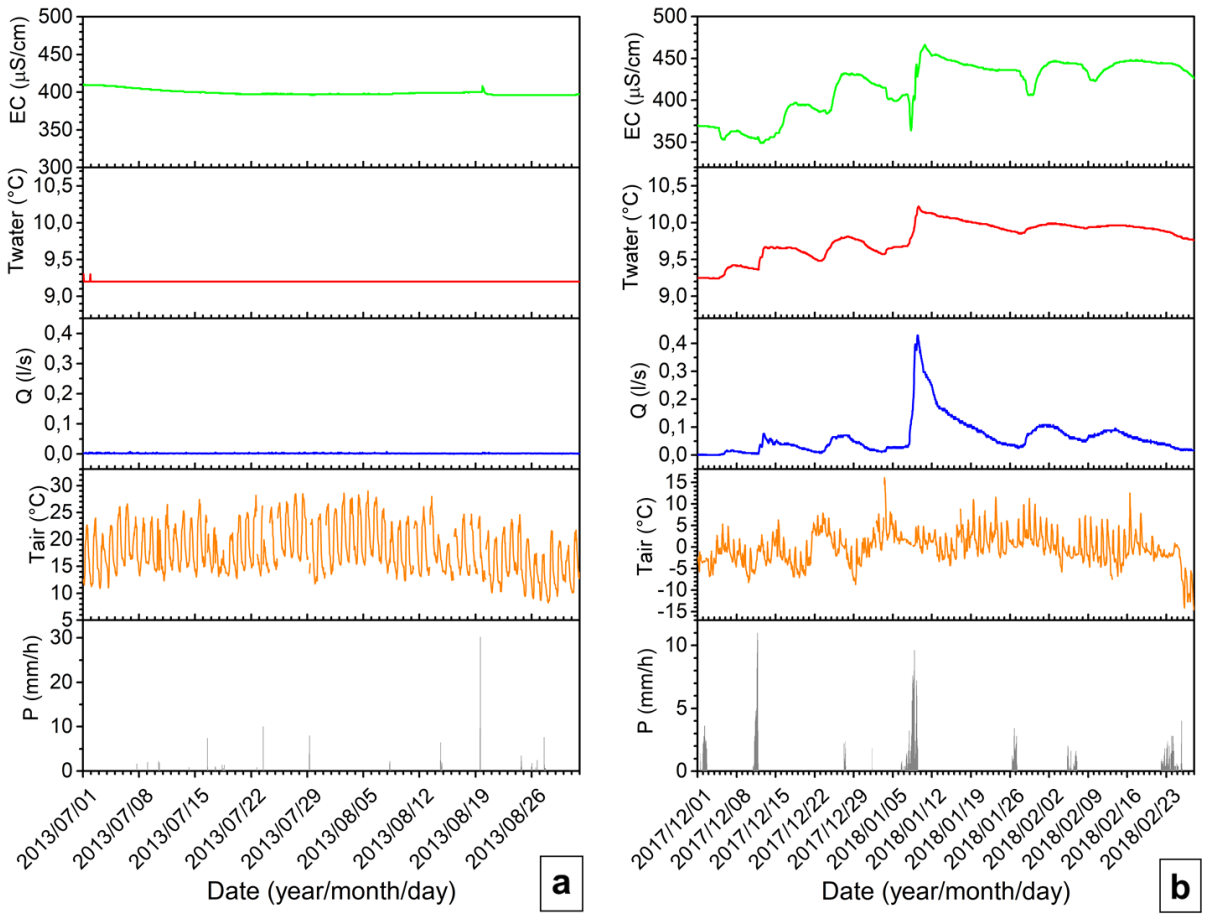

Fig. 3.12. Milano hydrograph and chemographs during summer (a) and wintertime (b).

3.2.2.5. Torre drip site (TO)

This drip site is located on the cave ceiling of the second large room in the lower sector of the show cave (Fig. 3.2). Few time intervals are reported due to several episodes of malfunctioning. The complete hydrograph is reported in Appendix 2e whereas the chemographs are shown in Appendix 2f. This drip is characterized by a medium discharge of 0.005 l/s which is significantly lower than those showed by the secondary tributaries previously described. Its discharge can reach zero during summer periods. The lag time between precipitation pulses and flow peaks ranged between 3 hours to a day. The highest discharge values were reached during springtime, but peak flows are usually similar during spring and autumn (Fig. 3.13a). Discharge was not responsive to summer precipitations, with the only exception of summer 2002 when heavy rainfall caused impulsive reaction of the drip. Its electrical conductivity varied between 258.0 and 312.2 µS/cm with a mean value of 284.5 µS/cm that makes Torre the second less mineralized *Mora* creek monitored inflows. Its water temperature fluctuated between 8.9 and 11.03 °C, which is the maximum temperature variability observed among the monitored inflows.

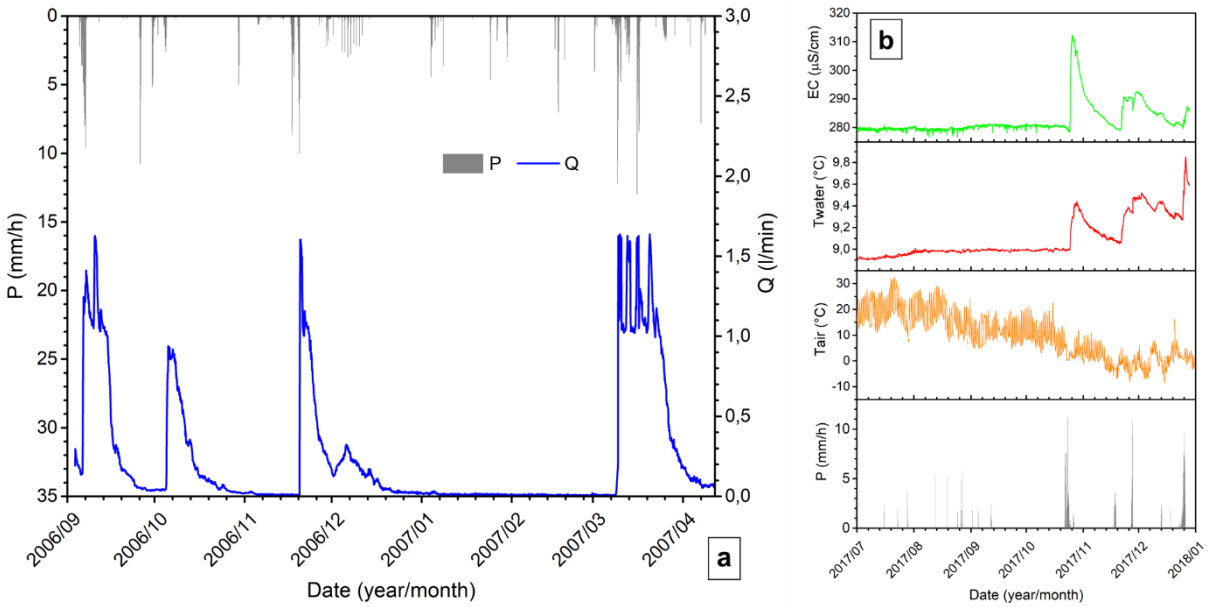

Fig. 3.13. Examples of the results of *Torre* drip site monitoring: 2006/09-2007/04 hydrograph (a) and 2017/07-2017/12 chemographs (b). Precipitations and air temperature are reported for comparison.

Water temperature always showed positive peaks immediately after precipitation events in autumn and spring; the maximum variation consequential to a precipitation event was 1 °C (occurred in November 2016, see Chapter 6 for further details). Electrical Conductivity has an

opposite behavior when considering different time intervals: it always showed an impulsive behavior following precipitations, but it exhibited sharp negative lows (synchronous to T positive peaks) in 2006 whereas it showed strong increases during autumn 2016 and 2017 (Fig. 3.13b). The variation range for EC during flow increases spanned from 10 to 50 µS/cm.

3.2.2.6. Balena (BA), Laghi Pensili (LP) and Onda (ON) drip sites

The results of the monitoring of these three drip sites are reported together due to the short time interval available (the monitoring of *Balena* and *Onda* started in 2018). Water level data were not available for *Balena*, so only the chemographs are reported (Fig. 3.14a). The *Balena* and *Onda* drips discharge water from fractures in the cave roof of the bottom large room (Fig. 3.2). These fractures are covered by abundant speleothem deposits. *Laghi Pensili* is located in the canyon sector of the *Bossea* cave (Fig. 3.2) and it drains water from a set of fractures in the carbonate sequence. The water percolates to a natural pool from which flow is directed to a smaller artificial pool. *Balena* exhibited a mean temperature of 9.56 °C and it varied between 9.01 and 10.9 °C during the monitoring interval. Electrical conductivity ranged between 294.1 and 382.9 µS/cm, with a mean value of 325.0 µS/cm. The two physicochemical parameters monitored for this drip showed rather similar impulsive behaviors during rainfall events with the only exception in the second half of June, when T and EC did not react to rainfalls (Fig. 3.14a). *Laghi Pensili* is characterized by a constant water level (that reflects a constant Q that should range approximately between 1.5 and 1.7 l/min) and water temperature, independently from precipitation events (Fig. 3.14b). The electrical conductivity showed a small variability (25 µS/cm as maximum variation), with a mean value of 347.7 µS/cm. The *Onda* drip had an impulsive response to precipitations, as shown by its hydrograph and chemographs (Fig. 3.14b). Water level fluctuated between zero (intervals in which EC and T are absent) and 4.5 cm, with the highest values measured during precipitation events. The time delay between peak precipitation and flow peaks ranged from an hour to 6 hours. After the last rainfall event of July 2019, the drip discharge did not react to precipitations occurred in August. This drip has a EC comprised between 375.0 and 522.0 µS/cm, with a mean EC of 435.7 µS/cm, making *Onda* the inflow with the highest EC among the all monitored. Electrical conductivity, like water temperature, exhibited pronounced positive peaks during flow increments

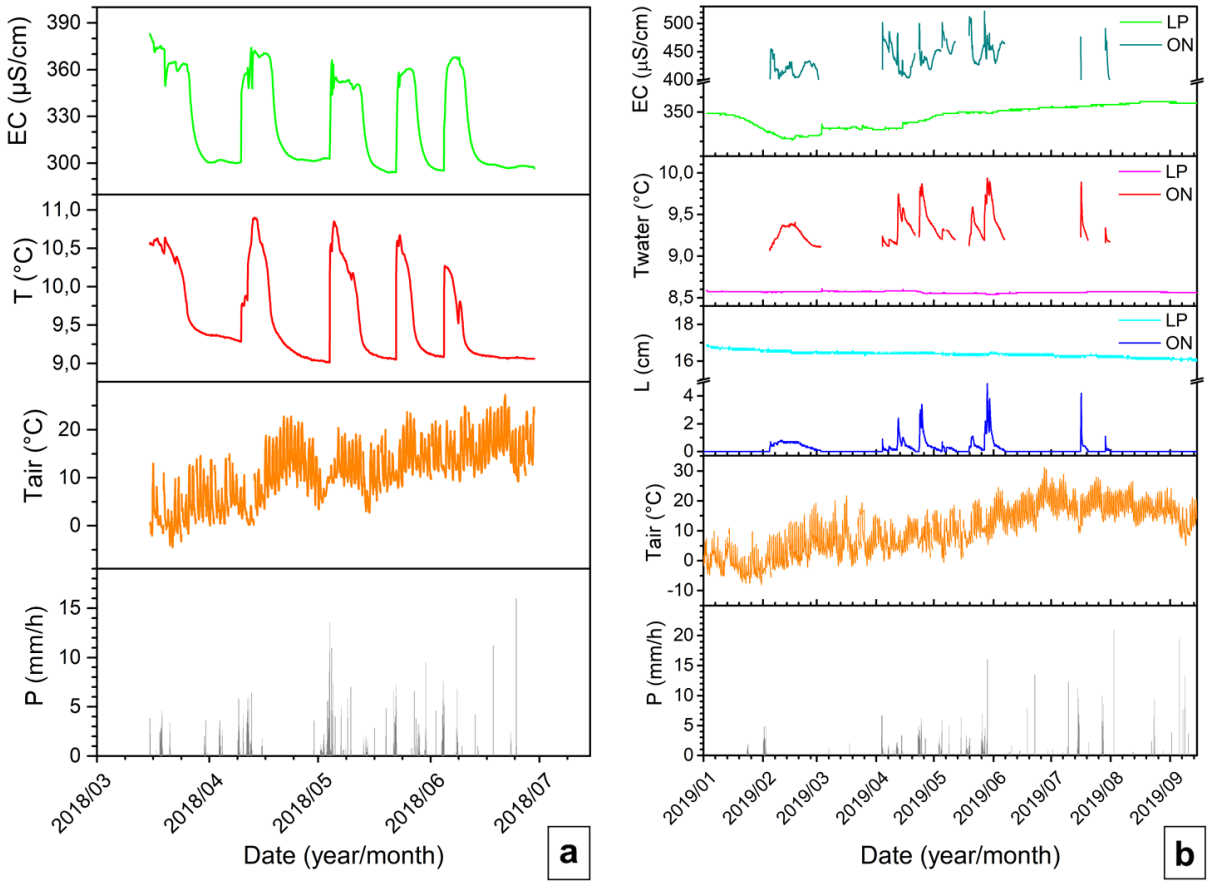

Fig. 3.14. *Balena* chemographs (a) and *Laghi Pensili* and *Onda* hydrographs and chemographs (b).

3.2.2.7. Sacrestia (SA) and Cancello (CA) drip sites

These two drip sites are located inside the underground scientific laboratory which is installed in the bottom large room (giant halls sector; Fig. 3.2). Both drips drain water from small fracture sets. The complete dataset of *Sacrestia* is presented in Appendix 2g and h whereas the dataset of *Cancello* is in Appendix 2i. Since no chemographs were available for *Sacrestia* and *Cancello*, some information on their physio-chemical parameters were taken from the spotted water samples collected during the last years. Further details on water chemistry are reported and discussed in Chapter 5. The discharge from the fractures drained by *Sacrestia* is monitored by means of two drip gauges placed a meter apart that are named *Sacrestia* bottom (SAlow in Tab. 3.2) and upper (SAupp in Tab 3.2. Fig. 3.15). *Sacrestia* is characterized by a water temperature ranging from 9.57 °C to 10.4 °C, with a mean of 9.93 °C. Electrical conductivity varied between 308 µS/cm and 444 µS/cm with 378.7 µS/cm as mean value. On average, the upper drip gauge showed a higher discharge than the bottom one (Tab. 3.2). An example of the behavior of the two *Sacrestia* drps from January to April 2019 is represented in Fig. 3.15. SA bottom showed

a weak response to the precipitations occurred in January and the increase in discharge started with a week of delay. The small rainfall events occurred during March did not cause any increase in discharge whereas the precipitation from mid-April caused first a small increment of flow rate and then a pronounced peak that progressively decreased for a week, followed by another small peak. SA upper drip displayed more pronounced impulsive responses to the subsequent meteorological events. During the precipitations occurred from March to April 2019, SA upper drip showed impulses almost simultaneous to each rainfall event.

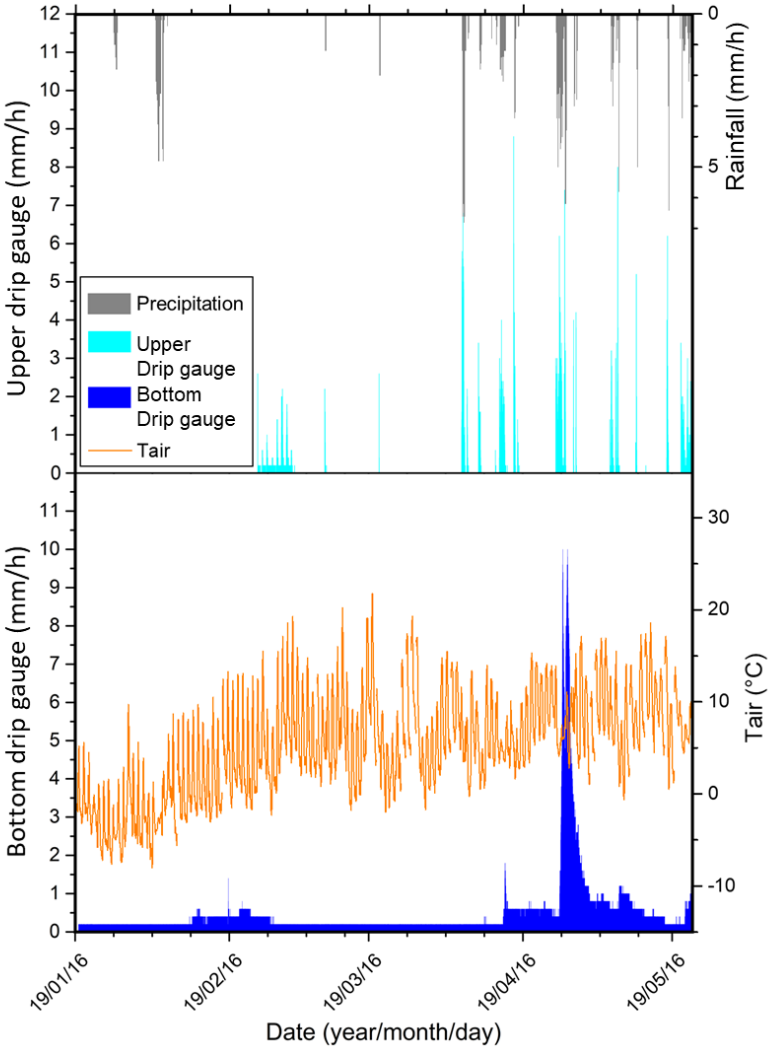

Fig. 3.15. Examples of *Sacrestia* bottom and upper behavior during some precipitations occurred between January and April 2019. Precipitations and air temperature are reported for comparison.

The *Cancello* drip typically showed no discharge in case of no precipitation whereas its flow rate strongly increased following rainfall events, as shown by the example in Fig. 3.16. In this example, the drip showed a marked increment of water amount (which is reported instead of

discharge) during each precipitation event occurred between March and mid-June 2018, with lag times varying from a few hours to a couple of days. After mid-June, further rainfall inputs were not followed by any discharge increment. The spotted water samples collected during the last 4 years show that CA water temperature ranged between 9.27°C and 9.9 °C, with a mean value of 9.64 °C. Electrical conductivity fluctuated between 271.0 µS/cm to 337.0 µS/cm with a mean value of 304.1 µS/cm.

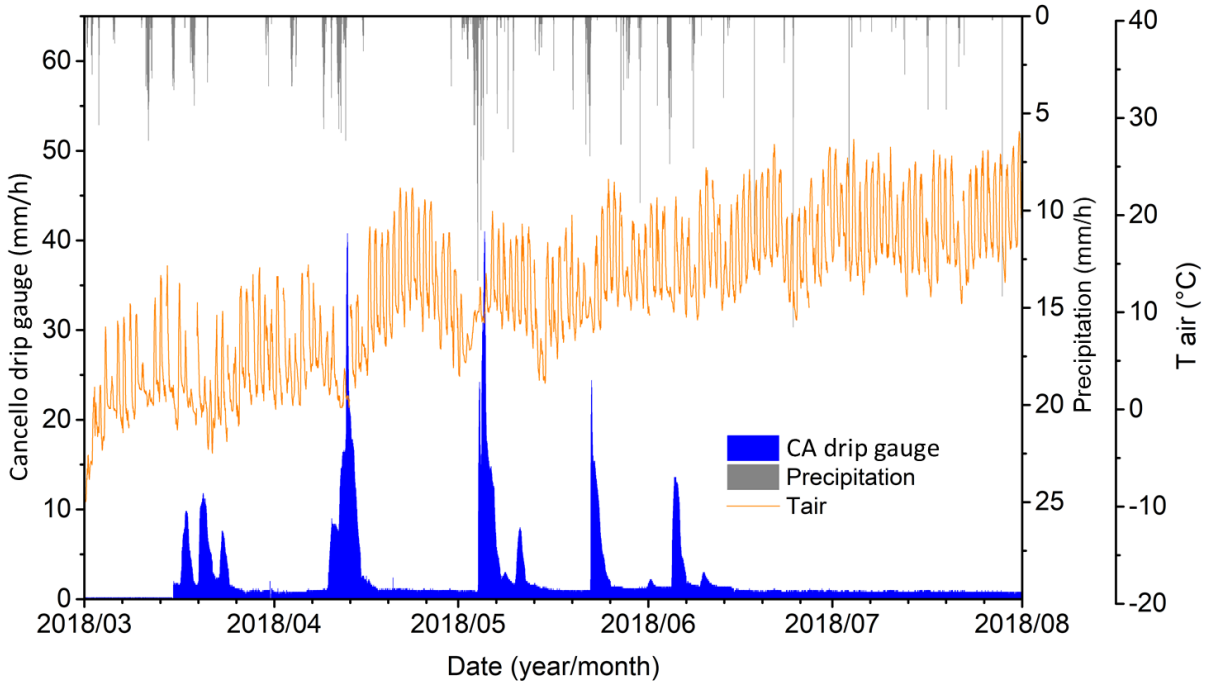

Fig. 3.16. Water amount discharged by *Cancello* drip from March to July 2018. Precipitations and air temperature measured by *Borello* station are also reported.

3.2.2. Mora creek hydrodynamic

A summary statistic is presented for the *Mora* creek water discharge (Q), water temperature (T), electrical conductivity (EC) and turbidity data collected in the last 10 years (Tab. 3.3). The complete hydrograph and chemographs are reported in Appendix 3. The *Mora* creek is characterized by a mean discharge of 177 l/s but its flow rate can be extremely variable: it can decrease to 45-50 l/s in periods of drought, like after the summer of 2012 (less than 60 mm measured from June to August) but it can also reach values close to 2000 l/s during strong rainfall events, such as the one occurred in November 2016 (see Chapter 6). Water temperature ranges between 6.74 °C to 7.92 °C pointing to a maximum variability of 1.2 °C. Electrical conductivity varied between slightly less than 200 µS/cm to 265 µS/cm.

	Mora Creek (TM)			
	Q	*T*	*EC*	*Turbidity*
	l/s	*°C*	*µS/cm*	*FNU*
Mean	177.34	7.53	219.6	9.35
Standard error	0.55	0.00	0.0	0.29
Median	124.67	7.55	218.0	5.89
Mode	73.64	7.55	217.0	2.11
Standard devation	150.19	0.18	7.2	25.22
Variance	22556.33	0.03	51.3	635.84
Curtosis	16.12	1.31	3.6	686.90
Skewness	3.22	-1.07	1.4	23.89
Range	1915.73	1.18	69.0	887.81
Minimum	44.50	6.74	196.0	2.06
Maximum	1960.23	7.92	265.0	889.87
CV	85%	2.4%	3.3%	269.6%
t interval	11/2008-2019	12/2009-2019	12/2009-2019	2018-2019

Tab. 3.3. *Mora* creek summary statistics for the monitored parameters.

Two examples of typical *Mora* creek hydrological year are presented in Fig. 3.17. The most recurrent case is characterized by maximum discharge occurring in springtime (Fig. 3.17a), when peak discharge varies between 900 and 1250 l/s. A second period of strong flow increase is during autumn, but peak flows are sensibly lower than those measured in spring. There are a few cases of hydrological years characterized by moderate peak flow in spring (250 l/s to 500 l/s) and high discharges in autumn, exceeding 1300 l/s (Fig. 3.17b). In both cases, two phases of low discharge can be distinguished, one during summer and the other one in winter. In both phases, precipitations are not necessarily followed by an increment in discharge. Water temperature usually decreases during discharge increases and the most pronounced decrements are commonly observed during the spring peak flow (the maximum decrement measured is 1 °C). Water electrical conductivity has a complex behavior outlined by more fluctuations than those observed for water temperature. Electrical conductivity, however, usually shows positive sharp peaks in concomitance of flow increases (Fig. 17a, b).

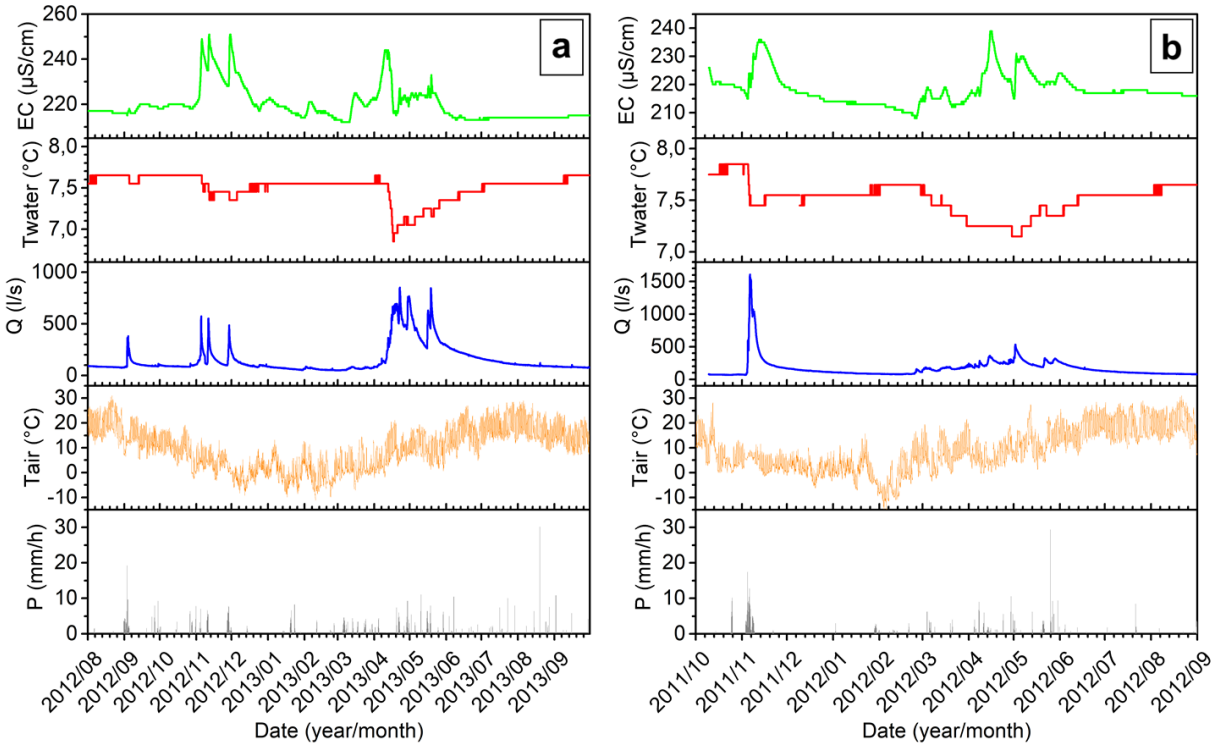

Fig. 3.17. Examples of possible hydrological years observed for *Mora* creek during the monitoring interval. (a) Typical hydrological year. (b) Infrequent hydrological year.

Water turbidity was monitored from February 2018 to May 2019, although there are some intervals of missing data. The observed values ranged from a minimum of 2.1 FNU to a maximum of 890 FNU, with a mean of 9.3 FNU. Strong increases in turbidity were observed during high flow phases, respectively from April to May 2018, November 2018 and to a smaller extent in April 2019 (Fig. 3.18). There was, however, an episode of remarkable increment of turbidity that followed the high flow stage occurred in November 2018. This event was characterized by a prolonged interval of high turbidity that took about one month to fade. This increase was not correlated with heavy recharge. The turbidity peak observed at the end of April 2018 had a magnitude more than ten times higher than those of the other measured increments. These latter increments ranged in fact between 40 to 90 FNU whereas the former event almost reached 900 FNU.

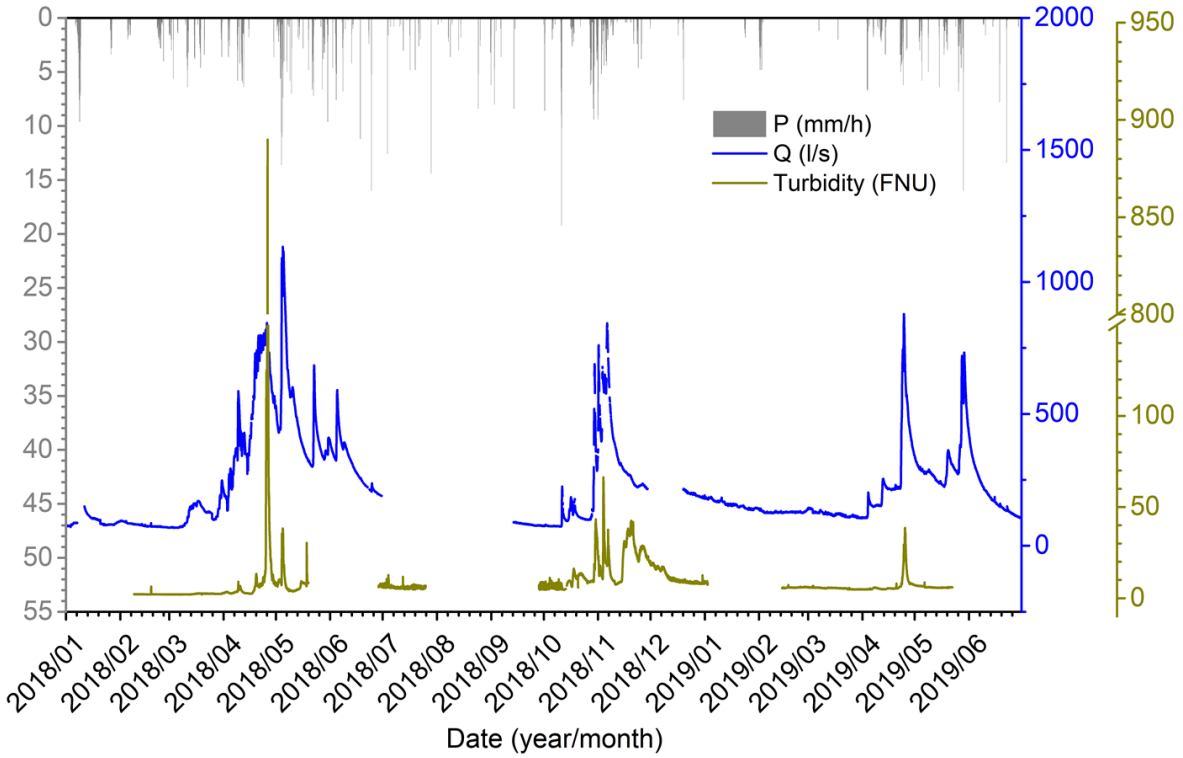

Fig. 3.18. *Mora* creek hydrograph and water turbidity trend observed from the beginning of 2018 to mid-2019.

3.2.3. Tracer tests results

3.2.3.1. Milano drip site

The two tracer tests at the *Milano* drip site were made in different hydrological conditions: the first one was carried out during a period disseminated by precipitation events (fall 2010. Fig. 3.19a) whereas the second one was carried out during summer 2012 when rainfall were scarce, so that they did not influence the drip discharge (Fig. 3.19b). The first test was heavily conditioned by consecutive rainfall events that determined multiple episodes of dye dilution, so that it was not possible to gain much information. However, the first arrival of the dye was recorded before the first increment of flow rate, which allowed to compute a maximum velocity of 66.7 m/day. The second tracer test showed a slow increase of the breakthrough curve (about 12 days from the first dye arrival to the peak concentration). The maximum velocity for this test was equal to 50 m/day and a dispersivity of 21 m was calculated. More details of the tracer tests are reported in Fig. 3.19c.

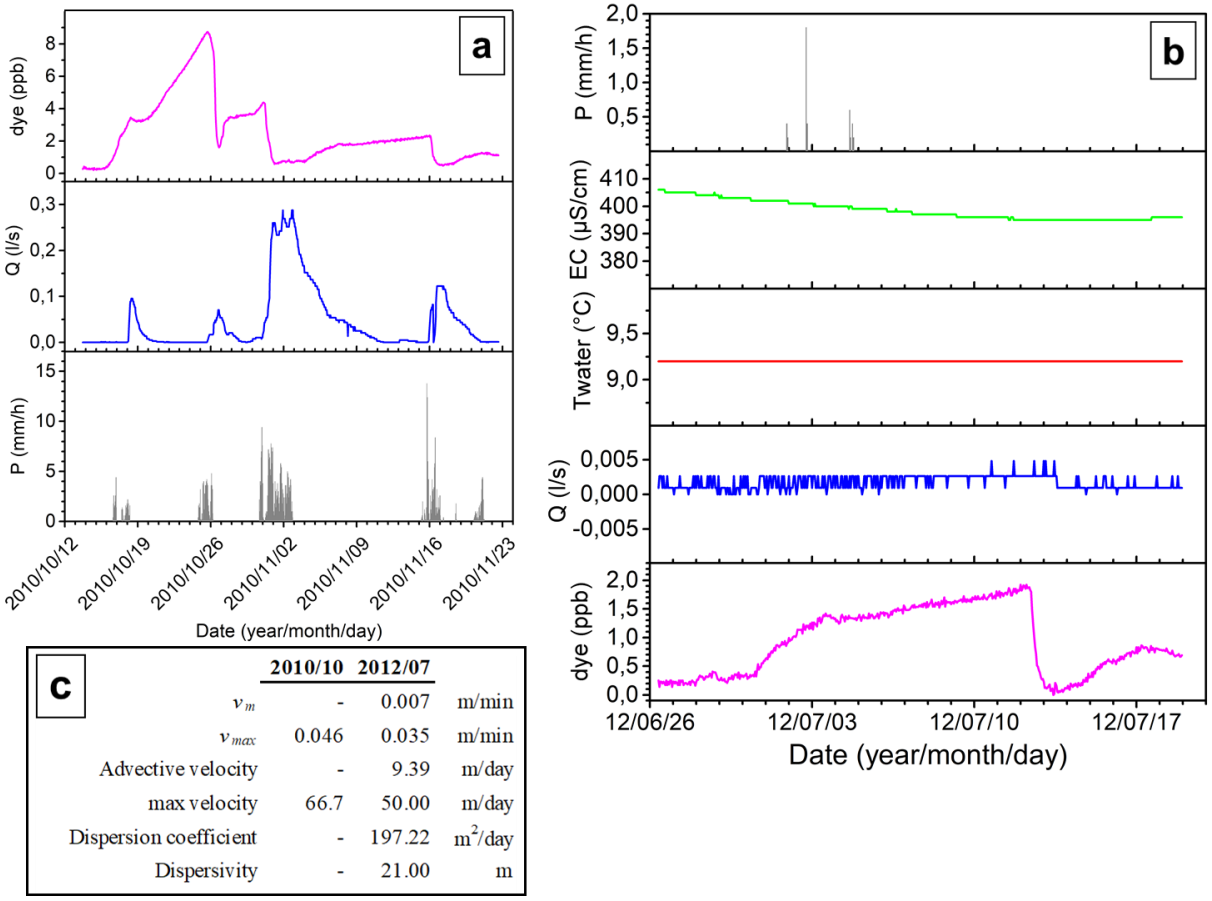

c

	2010/10	2012/07	
v_m	-	0.007	m/min
v_{max}	0.046	0.035	m/min
Advective velocity	-	9.39	m/day
max velocity	66.7	50.00	m/day
Dispersion coefficient	-	197.22	m^2/day
Dispersivity	-	21.00	m

Fig. 3.19. Breakthrough curve, hydrographs and chemographs of *Milano* drip site during the October 2010 (a) and July 2012 tracer tests (b). A table with the most relevant values obtained with the test is presented (c).

3.2.3.2. Mora creek tracer tests

The three tests on the *Mora* creek were carried out in different hydrodynamic conditions. The first one (2007/05/16 - 2007/06/17) was performed during moderate flow conditions (120 l/s on average) and it permitted to calculate a maximum velocity of 644.3 m/day and a dispersivity of 417 m. The second test (2008/05/05 – 2008/06/18) was carried out during high flow conditions (around 300 l/s) and it showed a maximum velocity of 2650 m/day and a dispersivity of 328 m. The last test (2015/05/28 – 2015/06/18) was performed during normal flow conditions (Vigna, personal communication). A maximum velocity of 1375 m/day was measured during the 2015 test. The value obtained for dispersivity was 268 m. The breakthrough curves and further details of these tests are reported in Fig. 3.20.

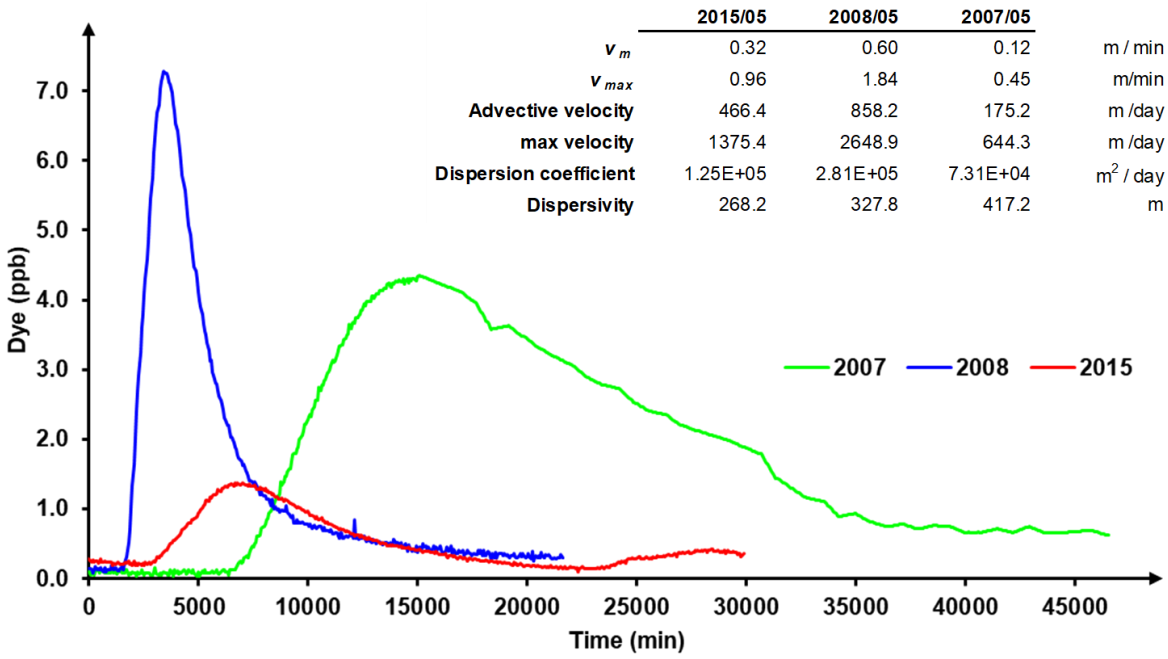

Fig. 3.20. *Mora* creek modeled breakthrough curves for each tracer test. The main characteristics obtained from the test are listed.

3.3. Discussion

3.3.1. Hydrological classification of the inflows

The data collected for each inflow revealed a complex architecture of the system, since each outlet display a characteristic hydrological behavior. A first method to classify the type of flow of cave inlets (unsaturated or supposedly so) was proposed first by Friedrich and Smart (1981) and it is based on the maximum discharge and the discharge coefficient of variation (CV). This classification was later updated by other authors (Smart and Friedrich, 1987; Baker et al., 1997; Genty and Deflandre, 1998). The discharge data were plotted on the discharge CV – maximum discharge graph (Fig. 3.21). *Laghi Pensili* fits the percolation stream box as expected, as it was expected that *Torre*, *Sacrestia* and *Cancello* fitted the seasonal drips area, since their lower discharges and high variability. This plot suggests also that the major hydrodynamic component for *Milano*, *Polletta*, *Polla dell'Orso* and *Onda* should be related to the subcutaneous flow, the most superficial component of karst unsaturated flow. However, some consideration should be addressed. First, subcutaneous flow is classically referred to topmost 20-30 m of the unsaturated zone where it is highly fissured (Baker et al., 1997), and this type is characterized by very intermittent flow. This latter characteristic is not compatible with the trends observed for the first three inlets whereas it could be correct for *Onda* drip site. However, the epikarst of *Bossea*

system is not well developed, so its storage capacity is very reduced if not absent. Second, it has been observed that a single inlet could exhibit intra-annual variations in flow behavior and consequently could fit in different categories of the plot depending on the considered hydrologic year (Baker et al., 1997; Genty and Deflandre, 1998). This is hardly the case for *Milano* and *Polletta* because, given their constant flow throughout the years, they do not fit in the subcutaneous flow area. Finally, *Polla delle anatre* does not fit in any category of the plot, having an extremely high CV. Smart and Friedrich (1987) suggested that this kind of behavior could be related either to the discharge of the inlet not being caused by percolation or to the existence of vertical inhomogeneities in the unsaturated zone. In order to better understand the hydrological behavior of the inlets, their chemographs and hydrograph will be more accurately discussed in the following sub-sections, contextualizing their behavior in the complex architecture of the *Bossea* karst system.

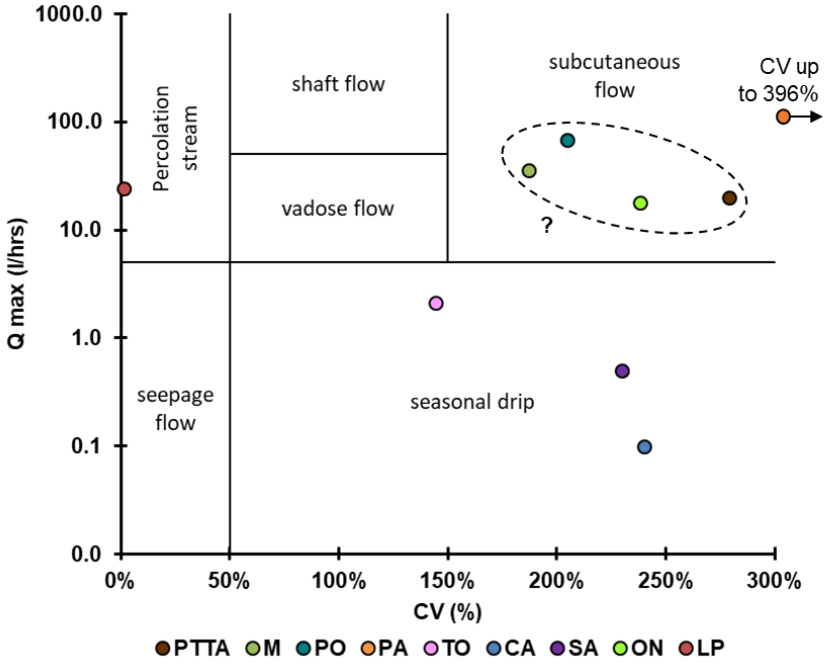

Fig. 3.21. Smart and Friedrich (1987) plot for cave inlet classification.

3.3.2. Polla delle Anatre, Polletta and Polla dell'Orso

Overall, these three inflows showed a piston flow behavior, so that inputs of precipitation were followed by the discharge from the *polle* of water already stored in the fractured aquifer. These inlets, however, show peculiar hydrological characteristics, especially comparing EC and T chemographs; there were impulsive episodes in which the discharged water was warm (i.e. T

positive peaks) but its EC was remarkably low. At the same time, air temperature was significantly lower than the water temperature at the inlets during the precipitation events that preceded the inflows pulses. This ruled out the possibility of freshwater arrival during such impulsive events, because it should have caused both dilution and cooling of the water. The observed trend should be related to the input of less mineralized water stored in the *Impermeable complex*. The water drained by the basement rocks is less mineralized because of their being less susceptible to chemical attack by percolating water respect to carbonate rocks. The drainage of this basement water is related to the position of the inlets in the structure of the cave: *polle* discharge water along the disharmonic contact between the carbonate sequence and the *Impermeable complex* below, here represented by deformed meta-volcanic rocks. The detachment surface and its related core and damage zones in the meta-volcanics represent a barrier to flow, however some evidences of flow circulation in the meta-volcanics were observed in the cave.

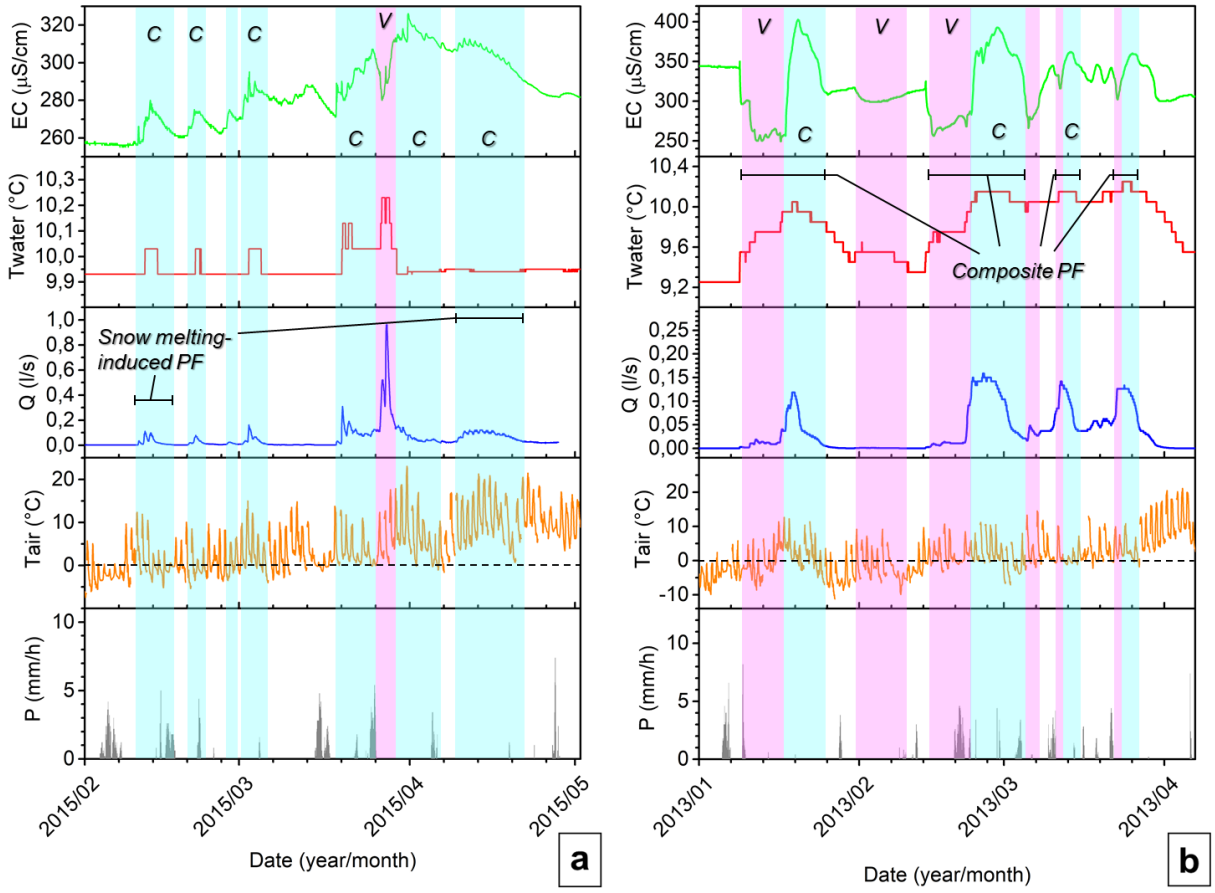

Fig. 3.22. Interpretation of *Polla delle anatre* (a) and *Polletta* (b) hydrographs and chemographs during snow melting episodes. V = meta-volcanic water, C = carbonate water, PF = piston flow.

This is not unexpected, given the speleogenesis of *Bossea*. This secondary circulation developed for erosion of the highly deformed rocks in the damage zone. Each *polla* showed different characteristics: negative lows are not frequent for *Polla delle anatre* (Fig. 3.22a) whereas *Polletta* showed either clear negative, positive, or composite EC peaks. During autumn recharge, this inlet usually showed first pulses of basement water only, then inputs of carbonate water (i.e. simultaneous positive EC and T water peaks). During springtime, for a given discharge pulse there were usually inputs first of meta-volcanic water, then those from the carbonate sequence resulting in a "composite" piston-flow (Fig. 3.22b). The shape of the Q, T and EC pulses are influenced by the type of precipitation for all inlets (Baker and Brunsdon, 2003): rainfall caused sharp impulsive response of the inlets whereas snowfall and consequent snow melting produced smoother pulses that sometimes showed oscillations related to diurnal fluctuation of snow melting (air temperature related). The freshwater infiltration (rain and snow) does not contribute to discharge but it transmits efficiently the hydraulic pressure wave. Considering the structural setting, the water that percolates from the unsaturated zone and reaches the detachment zone should flow laterally, away from the cave walls, so that flow through the outcropping contact should be limited or absent.

Therefore, the continuous discharge observed for these two inlets and their physico-chemical characteristics suggest the presence of a saturated zone developed in the fractures of the bottom part of the carbonate sequence and in a restricted portion of the less permeable damage zone in the meta-volcanics. This saturated reservoir probably controls the base flow of the considered *polla* whereas unsaturated flow feeds the saturated reservoir and it plays a fundamental role in overflow dynamics during strong infiltration events (Fig. 3.23). This arrangement can also explain *Polletta* hydrodynamics: the first water drained has a chemical composition strongly controlled by the meta-volcanics, then the pressure wave propagation from the unsaturated zone brings more proper carbonate water into the small, fractured saturated reservoir, rising water level in the fractures and determining impulsive outflow events (Fig. 3.23b). *Polla delle anatre* did not show this marked distinction between carbonate and non-carbonate piston flow (with a few exception, see Chapter 6) probably because its hydrodynamic and hydrochemistry is more controlled by a bigger meta-volcanic reservoir rather than by the input from the unsaturated zone, as demonstrated by its low mean mineralization. The latter compartment still regulates hydraulic pressure transmission to the saturated reservoir, but the overall chemistry is more "volcanic", so the piston flow episodes highlights only the arrival of carbonate water. *Polla*

dell'Orso has probably a similar reservoir but it is activated only in case of strong infiltration events that are capable of transmit more efficiently hydraulic pressure. The intermittent nature of this inlet can be related to a stronger heterogeneity in the fractured rock volume that feeds it and/or to the smaller dimension of its saturated reservoir.

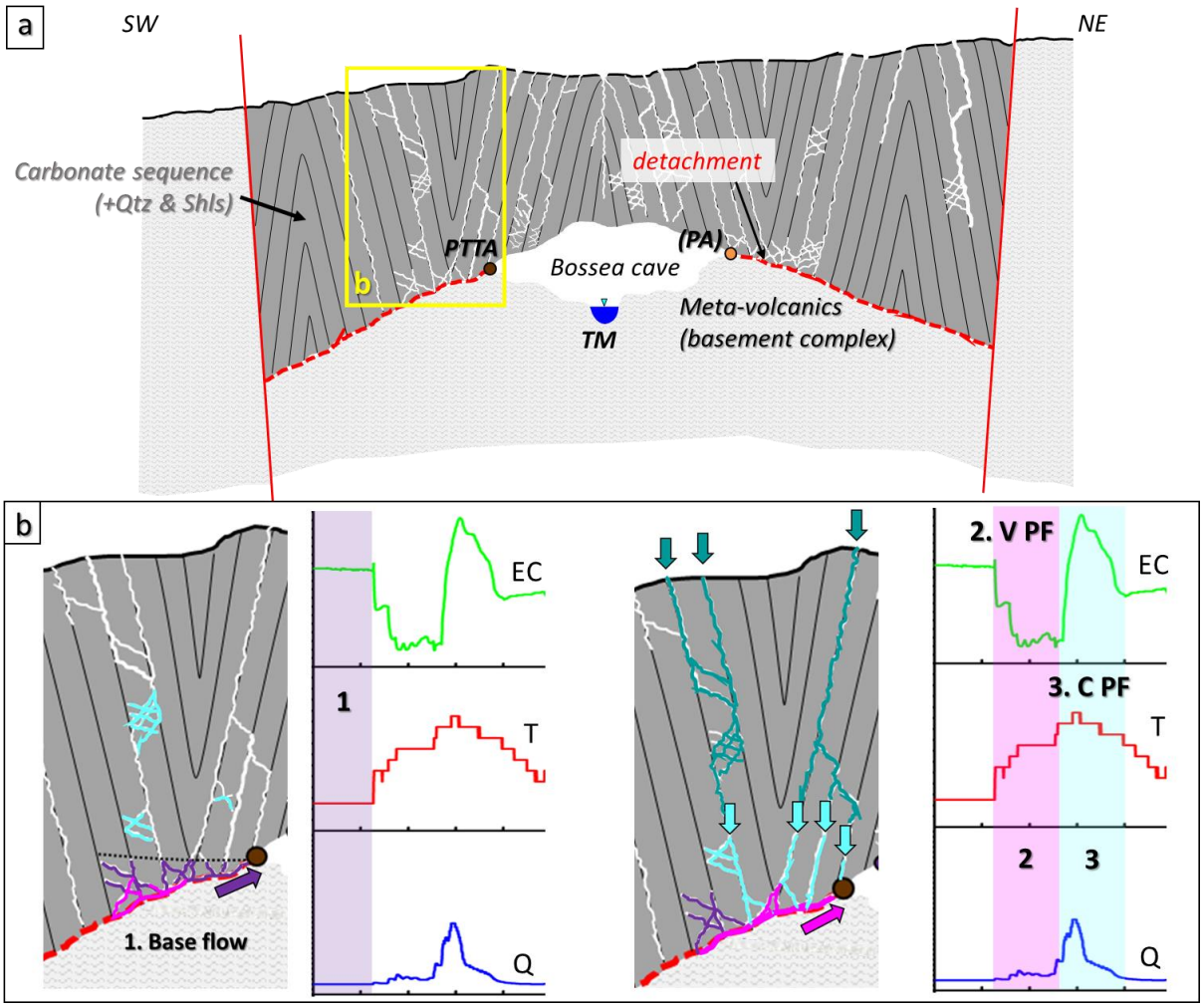

Fig. 3.23. (a) Bossea cross-section and (b) flow dynamics model in the detachment zone that hypnotizes the presence of a saturated zone that regulates baseflow (1) and is influenced by the unsaturated zone (2 = metavolcanic water Piston Flow; 3 = Carbonate water Piston Flow). Pink and purple arrows show the discharge of metavolcanics water and mixed water (carbonate and metavolcanics), respectively, that are stored in the perched aquifer in the detachment zone. *Polla delle anatre* position is reported in brackets because its real position is along the contact but in the upper sector of the cave, not in the large rooms part.

3.3.3. Unsaturated flow: dripsites

The various monitored drips showed different characteristics regarding their hydrological behavior. Most of them showed a piston flow behavior throughout the hydrological years, *Laghi Pensili* being the only exception. Among the drip sites, *Milano* and *Torre* showed some variable inputs of water from the *Impermeable Complex* that are dependent on the specific architecture

of the fracture networks drained by each drip. It seems that for *Milano*, for instance, these non-carbonate contributions are more relevant during the winter/spring snow melting whereas they are absent or reduced during autumn (Fig. 3.24a). The input of non-carbonate water for *Milano* is confirmed also by the tracer tests: these were carried out injecting the dye from a fountain that is fed by water drained by the *Impermeable complex* (Banzato et al., 2013). The *Torre* drip showed relevant input from the non-carbonate rocks during some monitored time intervals whereas these contributions were not observed in recent years. The non-carbonate inputs for this drip could be related to the local structural setting. As explained in Chapter 2, the carbonate sequence, the quartzites, and shales detached together from the originally underlying meta-volcanic sequence and they were tightly folded. Some examples of tight, isoclinal folds with shales and quartzites in the hinge zone outcrop in the upper terminal part of the large rooms sector (see Fig. 2.5b), close to the *Torre* drip. Other drip sites such as *Onda*, and *Balena* showed mineralization increments during flow peaks and they should be related to drainage of fracture networks that developed only in the carbonate sequence.

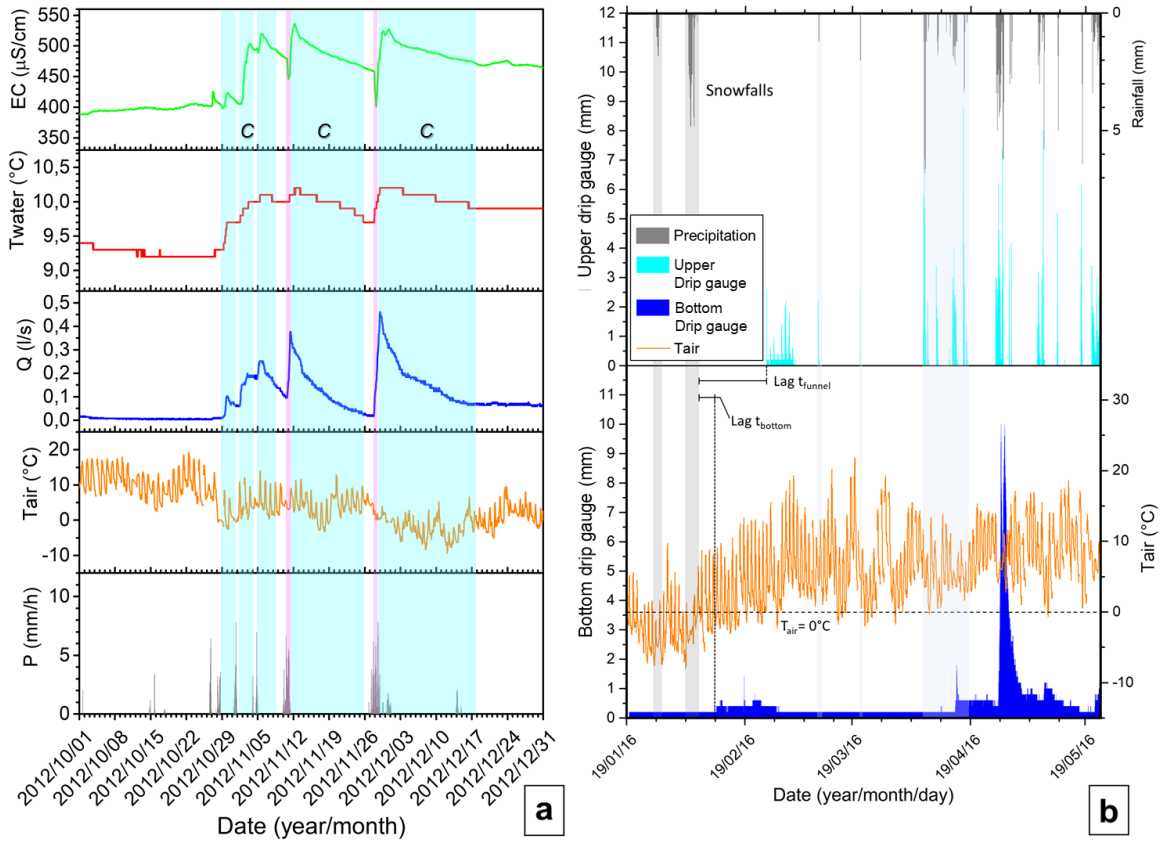

Fig. 3.24. Examples of interpretations of hydrographs and chemographs of *Milano* (a) and *Sacrestia* (b) drip sites. C = carbonate input.

The *Sacrestia* and *Cancello* drip sites are good examples of flow through fractures with low permeability. They should be fed by small perched aquifer made up of fracture networks that are characterized by very low permeability. As a consequence, the two drip sites are able to discharge only in case of relatively strong infiltration events that are capable to transmit a certain hydraulic pressure.They are indeed seasonal drips that are active only in case of precipitations. The low permeability and the spatial heterogeneity of their drainage system is evident comparing the two *Sacrestia* drip gauges (Fig. 3.24b): they are only a few meters apart but their responses to infiltration are different, although both impulsive. The bottom gauge showed a reaction to snow melt infiltration faster than the upper one, but the latter exhibited a more pronounced peak. On the contrary, during later rainfall infiltrations, the upper point responded faster than the bottom one, but the discharge increments of the former are short-lived whereas the latter showed a slow recession phase. The *Cancello* drip showed a behavior similar to the *Sacrestia* bottom pluviometer: an impulsive response to infiltration that slowly recedes to zero discharge. The difference with the previous drip is the lag time between peak precipitation and flow peak: *Cancello* generally shows a shorter delay than *Sacrestia* during both snow melting processes and rainfall infiltration (Fig. 3.25). Again, it should be noted that these two drips are just a few meters away, but the strong heterogeneity of the fractured rock volume is decisive in controlling the hydrodynamic behavior of the inflows (Baldini et al., 2006).

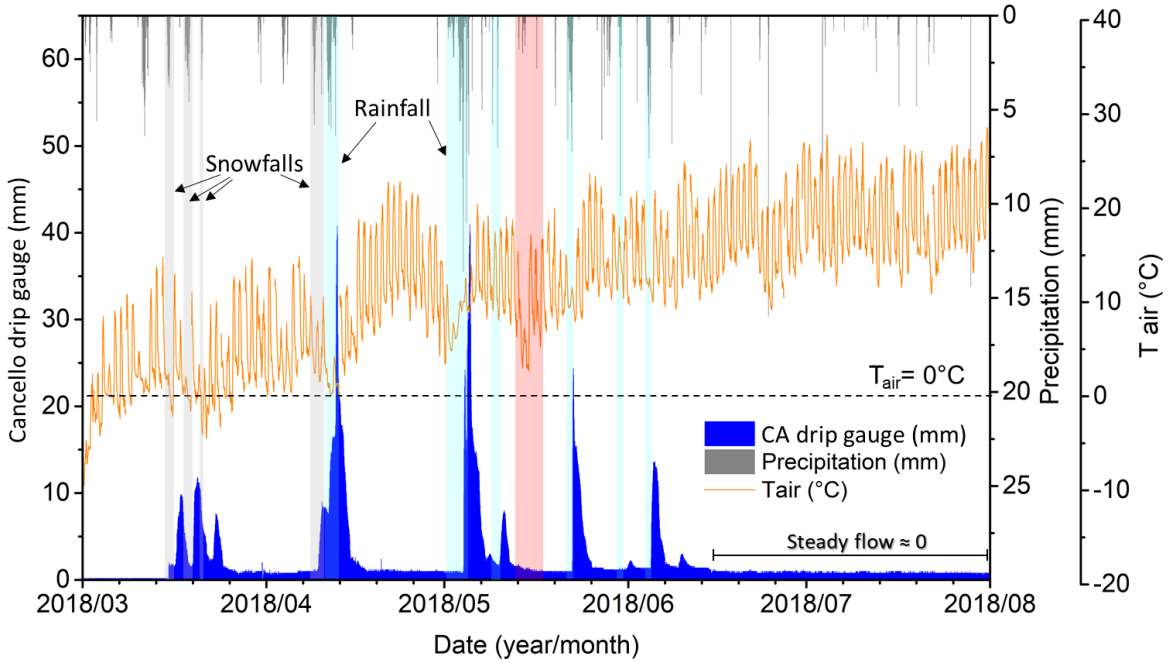

Fig. 3.25. Interpretation of Cancello hydrograph.

3.3.4. Fracture flow architecture in Bossea cave

As discussed in the previous sections, the monitoring of the *Mora* creek secondary tributaries revealed a complex organization of water circulation. The primary forcing factor turned out to be the structural setting, as already evident from the structural investigations presented in the previous chapter. Consequently, fracture distribution and properties exert control on flow. In particular, there are domains in the fractured rock volume in which the fractures are saturated due to very low permeability. These can be seen as perched aquifer spatially delimited only by the permeability of their fracture networks. The drips with the lowest discharge appear to be fed only by networks of small fractures whereas the drips with the highest discharge developed along bedding junctions and their perched reservoirs should be made up by fracture networks of variable dimensions. The disharmonic surface played a fundamental role in the organization of flow: it acts as an impermeable barrier, but it locally permitted the development of a flow circulation network along the lower damage zone (see the picture in Fig. 3.26).

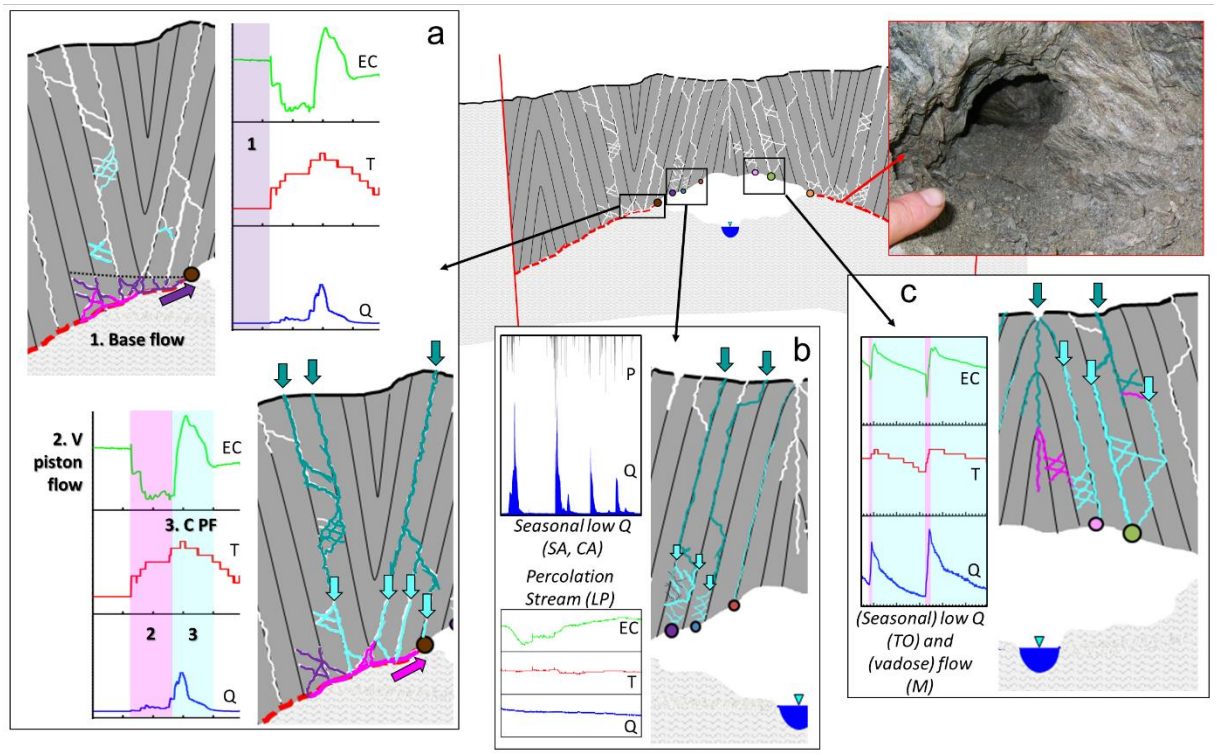

Fig. 3.26. Organization of fracture flow in *Bossea* cave. The picture on the top right shows and example of circulation pathway developed in the bottom damage zone (meta-volcanics) related to the detachment surface. (a) *Polle* hydrodynamic behavior: during infiltration events, this outflow discharges first the "volcanic" water that flowed in the damage zone (2, V piston flow), then water stored in fractures of the carbonate sequence is discharged (3, carbonate piston flow). (b) examples of perennial drips fed by very low permeable fracture networks. (c) Examples of high discharge drips that developed along bedding surfaces.

The heterogeneity in the fractured carbonate sequence and its structural arrangement (i.e subvertical bedding surfaces), coupled with the presence of the detachment, led to the development of small water reservoirs that feed the so-called *Polle*. The reservoir characteristics regulate the base flow whereas the unsaturated zone dynamics controls the high flow phases. Other important factors are the climate regime and the evapotranspiration. The former parameter is fundamental in regulating fracture flow during summer: all the inlet, in fact, showed no response to rainfall input during the hottest and driest months, unless heavy storms occurred (like the one happened at the end of August 2012). The dynamic of snow melting is also decisive in controlling hydrodynamic behavior of the inlets during the spring discharge phase. In some cases, the influence of diurnal oscillations of snow melting can be recognized in the inlet hydrographs and chemographs (EC).

3.3.5. Conduit flow: Mora creek hydrodynamics

The dominant mechanism that regulates the underground river during infiltration events is piston-flow and this phenomenon can be observed during both autumn and spring high-flow stages. Episodes of dilution are infrequent and observed only in springtime. The recognized episodes are either restricted to a short phase of peak flow (Fig. 3.27a) or, rarely, protracted for most of the snow melting infiltration phase (Fig. 3.28b). The diminishing of water temperature during flow peaks cannot be considered an index of freshwater infiltration (i.e. dilution), because it is usually associated to a specular increase in EC. The water temperature decrease can be related either to a major contribution of water drained from the *Impermeable Complex* and/or to the drainage of a larger portion of the system.

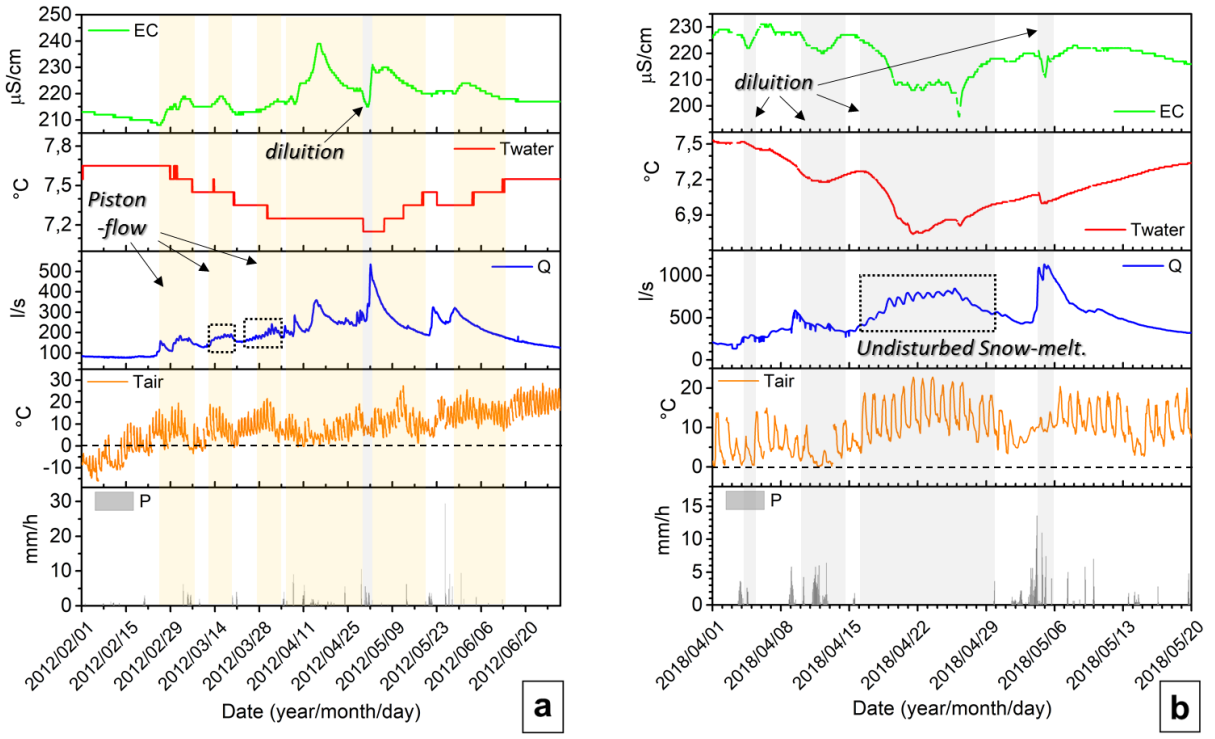

Fig. 3.27. Examples of piston-flow dominated (a) and dilution-dominated (b) spring discharge of Mora creek. The Q intervals comprised in the dotted rectangles represent examples of flow rate fluctuations controlled by snow melting diurnal oscillations not influenced by precipitations (undisturbed).

Water turbidity showed interesting oscillations in relation to flow. Turbidity peaks can either follow flow peaks, like the ones observed during the discharge increases in October - beginning of November 2018, or they could show no apparent correlation with discharge, like the increments observed at the end of November 2018 (red rectangle in Fig. 3.28a). The latter increments and even more so the anomalous turbidity peak occurred at the end of April 2018 (Fig. 3.28b) should be related to massive remobilization of fine sediments volumes that were accumulated in the phreatic conduits upstream of the *Bossea* cave.

The anomalous peak at the end of April 2018 could have been caused by partial obstruction of the conduits that, due to the high flow condition, was suddenly removed at the end of the unperturbed snow melting-induced peak flow. This is a small replicate of the phenomenon occurred in October 1996, when the total obstruction of the phreatic conduits provoked a destructive flood in the *Bossea* cave (Civita et al., 2005; Peano et al., 2005).

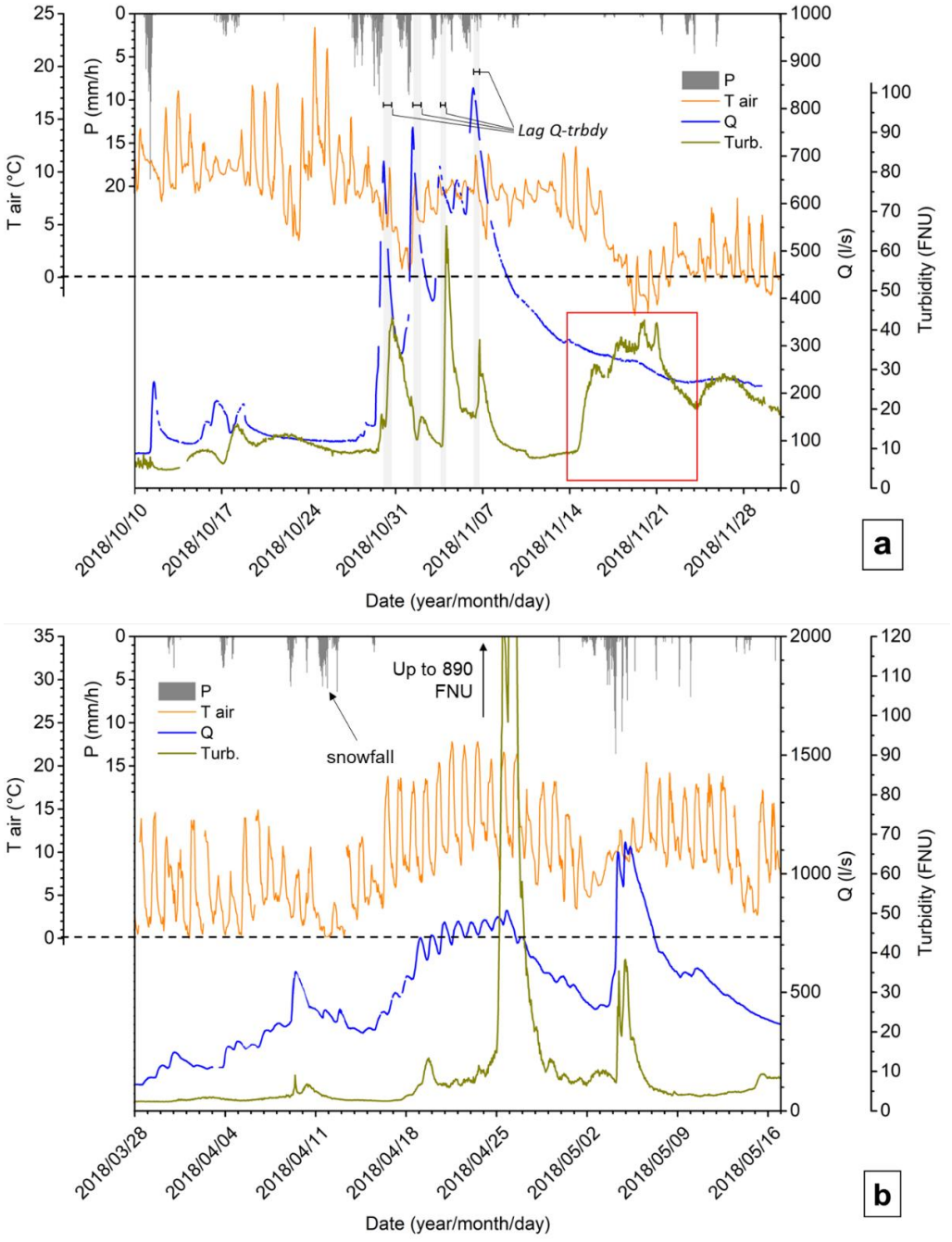

Fig. 3.28. Comparison of turbidity and flow rate measured in *Mora* creek during autumn 2018 (a) and spring 2018 (b).

The tracer tests revealed that flow velocities are extremely variable, ranging from 644.3 m/day in low flow conditions to 2650 m/day in high flow conditions. Moreover, the analysis of the breakthrough curve revealed that the highest dispersion corresponds to normal flow conditions whereas the lowest one was found during low flow conditions. These values of velocity and dispersion are by far much higher than the values observed for the *Milano* drip site, which are characteristic of a dispersion-dominated circulation system. As pointed out by Banzato et al.

(2013), the *Bossea* karst system has a complex architecture that falls between an interconnected conduit system type (with phreatic conduits) and a dominant conduit system type, so that its response to recharge is complicate. The interconnected conduit component is highlighted by the recurrent piston flow behavior, whereas the most prominent features of the dominant conduit component are the low karstification level and the not so well-developed phreatic zone.

3.4. Concluding remarks

The monitoring of the hydrodynamic behavior of *Mora* creek and some of its secondary tributaries permitted to infer the organization of flow circulation in the karst system and to shed some light on the relationships between the unsaturated zone hydrodynamics and the complex structural setting. The latter played a fundamental role in the speleogenetic evolution of the system by controlling and focusing flow along preferential pathways and creating flow barriers. The most prominent features for water flow are the detachment surface and bedding junction arrangements. The interplay between these two factors determined the development of the *Polle* whereas fracture organization (bedding and joints) and climatic factors control flow in the unsaturated zone. The *Polle* are also influenced by the dynamic in the unsaturated rock volume that feeds them. Fracture permeability is fundamental for the development of spatially limited saturated domain in the unsaturated zone. These fractured perched aquifers control the baseflow of the perennial drip sites, granting water discharge also during prolonged dry period. These portions of saturated rock volume are probably characterized by fractures with very low permeability that allows prolonged water storage. The existence of these saturated domains in the unsaturated zone is fundamental for flow regulation in this portion of the aquifer, particularly because *Bossea* system does not have a well-developed epikarst to retain water. These perched aquifers could hence be important for the storage in the unsaturated zone of other karst system characterized by the absence of the epikarst, like those that underwent glacial erosion. The dominant mechanism for both fracture and conduit flow is piston flow, although each monitored inlet/spring has its peculiar hydrodynamic behavior and drains a specific portion of the aquifer, receiving inputs from both carbonate and non-carbonate compartments.

Chapter 4: Recession and fracture analyses as tools for fracture architecture and permeability estimation

4.1. Theoretical basis of the methodology

The Milano drip site was selected for the investigation of fracture permeability in a portion of the unsaturated zone. The summary statistics of discharge, water temperature, and electrical conductivity for this drip site are reported in the previous Chapter (Tab. 3.2), together with the meteorological parameters (Tab. 3.1 and Fig. 3.5). The complete hydrograph and chemographs for the whole monitoring interval are in the Appendix 2. The work reported in the following sections was focused on this specific drip site, because of the availability of a long discharge time series that permitted to select the most appropriate storm events for recession analysis. Another reason for selecting this inflow was its position: the water is discharged along a bedding surface (plus a bedding surface that is seldom inactive) in the unsaturated zone of the carbonate sequence (Fig. 4.1). For this reason, it is representative of the main circulation pathways inside the vadose zone of this karst system, as explained in Chapter 2.

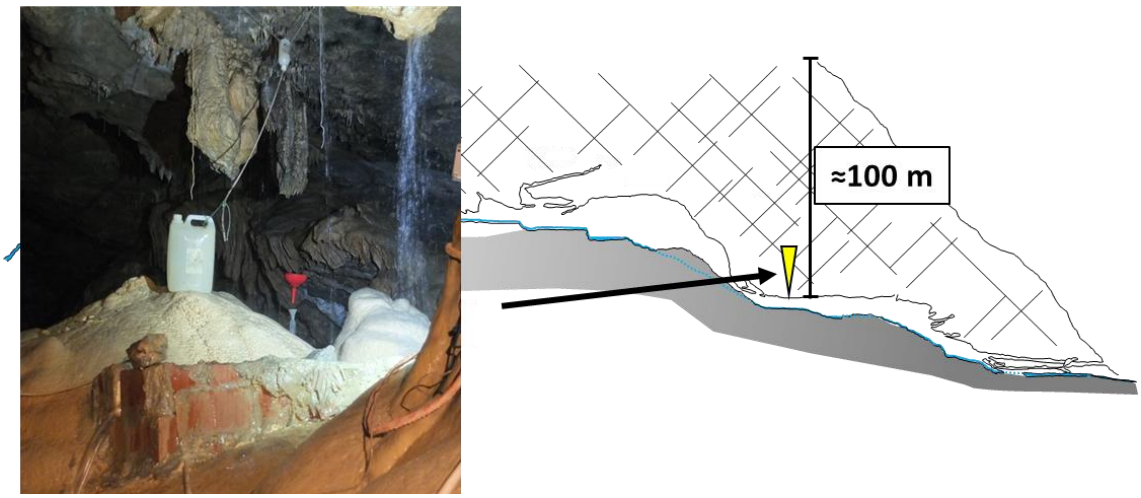

Fig. 4.1. Milano drip position inside the *Bossea* cave. The approximate thickness of the unsaturated zone above the drip is reported.

4.1.1. Recession analysis

The variation of a spring or drip site discharge over time is represented by its hydrograph. The hydrograph shape is the consequence of all processes that transform recharge (precipitations) to flow in the drainage system down to the outlet point of discharge (Bonacci, 1993; Kresic,

2007). Hydrograph analysis, and in particular its response to precipitation events, gives useful insights on aquifer characteristics such as storage and transmissivity (Dewandel et al., 2003). A storm hydrograph corresponds to a discharge increase occurring as a consequence to a precipitation event. The storm hydrograph can be subdivided in two portions (Fig. 4.2): a time interval where discharge increases up to the peak flow (the "rising limb") and the following recession limb during which discharge returns progressively to pre-storm values (Amit et al., 2002; Kresic, 2007; Fiorillo, 2014).

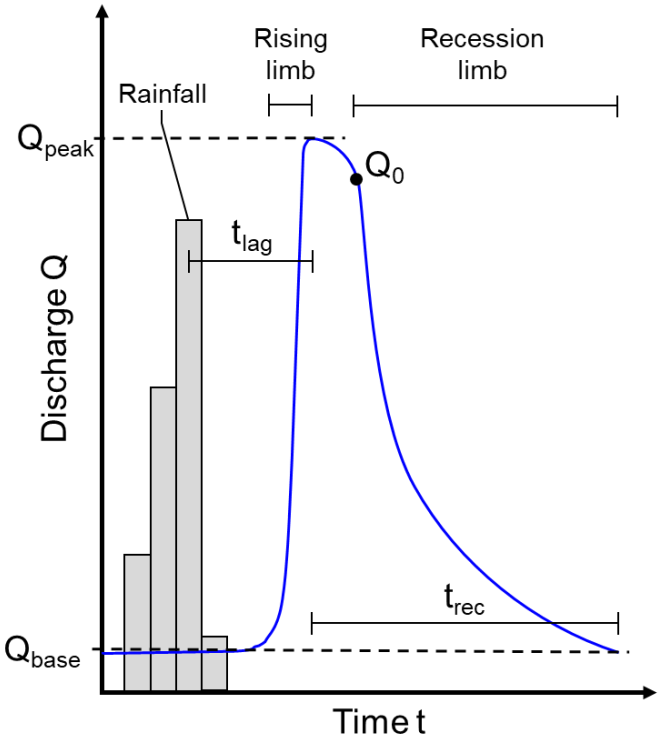

Fig. 4.2. Schematic representation of a storm hydrograph and its components (modified after Fiorillo, 2014).

This latter part is the one investigated with recession analysis, a method first developed for porous aquifers and later adopted for karst aquifers (Schoeller, 1948; Mijatovic, 1974; Mangin, 1975; Atkinson, 1977; Bonacci, 1993; Padilla et al., 1994; Shevenell, 1996). Recession analysis is based on the fitting of the recession curve with appropriate models. The most common methods are the quadratic (Boussinesq, 1903) and the exponential (Maillet, 1905) formulas. Dewandel et al. (2003) pointed out that the quadratic form better represents karst spring recession where horizontal flow is dominant whereas the exponential fits better the recession curve where flow has an important vertical component. For the purpose of this study, only the exponential model was applied. The Maillet exponential model describes the discharge as a function of the stored water volume using the following simple relation:

$$Q_t = Q_0 e^{-\alpha t} \tag{4.1}$$

Where

- Q_t is the discharge at time t (m^3s^{-1})
- Q_0 is the initial discharge at t_0, the beginning of the recession (m^3s^{-1})
- e is the base of the Napierian logarithms
- α is the recession coefficient (s^{-1})

This model is based on the assumption of a porous, free, homogeneous and isotropic aquifer. The recession coefficient represents the slope of the recession in a semi-logarithmic plot and depends only on the aquifer hydraulic system. Since this formula can be applied only to the last part of the recession curve (i.e. the most distant in time from the last precipitation) and semi-logarithmic plots of karst spring recession usually exhibit two or more segments, multiple exponential reservoirs models were developed to describe the spring recession curve by fitting a series of exponential sub-curves to different hydrograph segments (Forkasiewicz and Paloc, 1967; Torbarov, 1976; Petras, 1986; Jeannin and Sauter, 1998):

$$Q_t = \sum_{i=1}^{n} Q_{0_i} e^{-\alpha_i t} \tag{4.2}$$

Where n is the total number of reservoirs and α_i is the slope of the i-th component of the recession curve on a semi-logarithmic Q-t graph. It is possible to calculate the total volume drained during the recession from the volumes of each segment of the recession (Fig. 4.3) as follows:

$$V_t = \int_0^t Q(t)dt = \sum_{i=1}^{n} \frac{Q_i}{\alpha_i} \tag{4.3}$$

The recession curves were selected in order to apply the multiple exponential model to storm hydrographs with recession limbs that are as undisturbed as possible, so that the decreasing discharge is not perturbed by precipitation events following the one that caused the peak flow.

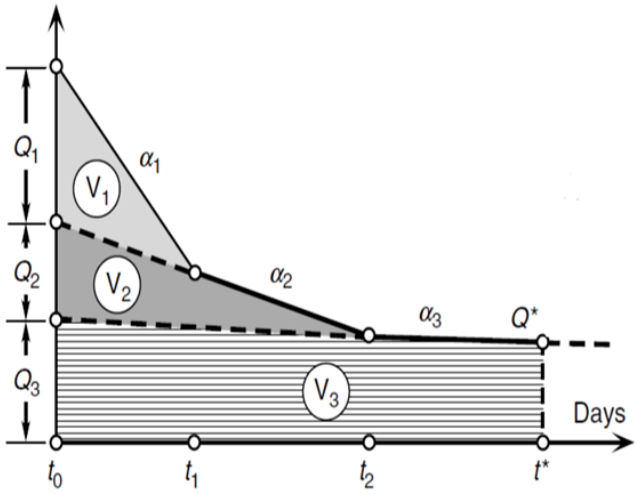

Fig. 4.3. Representation of the multiple exponential recession model (modified from Kresic and Stevanovic, 2009).

4.1.2. Fracture aperture: the cubic law and fractal analysis

The two methods that were used for fracture analysis are based on the hypothesis that a saturated flow regime exists in the fracture network connected to the Milano drip site during a storm event, the recession and the base flow periods. This is a fair assumption because of the occurrence of piston flow during storm events, as already discussed in Chapter 3. The first method used to infer fracture aperture was the inversion of the cubic law using the data obtained with the recession analysis. In case of laminar flow conditions, the flow rate from a single fracture of unit length can be modelled with the cubic law as follows (National Research Council, 1996; Ford and Williams, 2007):

$$Q = \frac{\rho g b^3 c}{12\mu} \cdot \frac{dh}{dl} \tag{4.4}$$

Where

- Q is the flow rate (m^3/s)
- ρ is water density (kg/m^3)
- g is the gravitational acceleration (m/s^2)
- b is the fracture aperture (m)
- c is the fracture width (m)
- μ is water viscosity (kg/m·s)
- dh/dl is the hydraulic gradient

This formulation of fluid flow through fractures simplifies to that of parallel plates with uniform aperture (Fig. 4.4) and it assumes laminar, incompressible flow, and impermeable fracture walls. It is one of the solution of the Navier-Stokes equations (Klimczak et al., 2010) and it is valid in open or closed fractures (Whitherspoon et al., 1980).

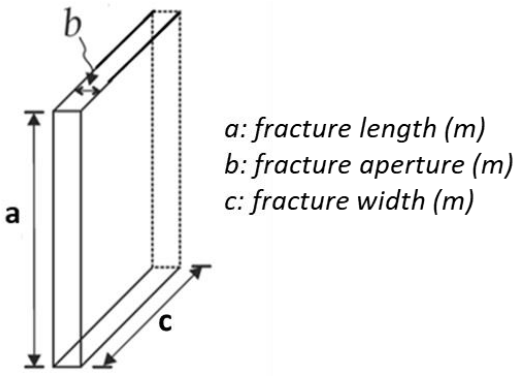

Fig. 4.4. Schematic representation of fracture geometry visualized as two parallel plates.

As pointed out by Phillips (2009), a rock fracture plane should be considered as a planar network of intersecting ribbon-shaped fluid pathways around areas of close rock contacts rather than a uniform gap between two parallel rock surfaces. The total area covered by the ribbon pathways in the fracture plane per unit volume of the medium is represented by λ (m^{-1}). If the volume is envisioned as a stack of slices, then λ approximates the total length of the intersections of the ribbon pathway network per unit area in any slice of the medium (active aperture length). Using this formulation, the cubic law can be then rewritten as follows:

$$Q = \frac{\rho g b^3 \lambda}{12\mu} \cdot \frac{dh}{dl} \tag{4.5}$$

Its inversion permits to calculate *b*:

$$b = \sqrt[3]{\frac{12\mu Q}{\rho g \lambda \frac{dh}{dl}}} \tag{4.6}$$

In order to calculate *b* for the fracture sets involved in each step of the recession curves, it is necessary to assume a specific λ for each segment of the recession. This is possible using field observations and the formula that relates λ to the geometric parameters of the fractures. It is also assumed that each step of the recession curve corresponds to the drainage of fracture networks with specific dimensional ranges. λ and the geometric parameters are calculated by iteration, finding the highest correlation between the volumes obtained from the recession analysis and those obtained by the inversion of the following formula:

$$\lambda = \frac{(a \cdot b \cdot c) \cdot n}{V} \quad (4.7)$$

Where *a*,*b* and *c* represent fracture height, aperture, and width, respectively and *n* stands for the number of hypothetic fractures for each dimensional class. The hydraulic gradient is taken constant and the dimensions of the first class of fractures (i.e. the biggest ones, namely the bedding planes where dripping occurs) are directly taken from field data, the only unknown being fracture height *a*: *Milano* drip drains water from two fractures so that *n* equals 2, their aperture is 0.005 m and their width is 0.2 m.

The second approach used to calculate the geometric parameters of the fractures is fractal scaling, assuming the distribution of fracture sizes as scale invariant, a property widely recognized for fractures in rocks, at least over certain ranges of scale (La Pointe, 1988; Chelidze and Gueguen, 1990; Bonnet et al., 2001; Kruhl, 2013). A fractal distribution requires that the number of objects larger or smaller than a certain size has a power-law dependence on the size (Turcotte, 1997):

$$N_i = \frac{C}{r_i^D} \quad (4.8)$$

Where

- N_i is the number of objects (fractures) having dimensions lower than a specific linear dimension r_i
- *C* is a proportionality constant
- r_i is the characteristic linear dimension
- *D* is the fractal dimension (constant, equals to 1.6)

The geometric fracture parameters *a* (length), *b* (aperture), and *c* (width) calculated with fractal analysis were used to calculate again λ as follows:

$$\lambda = \frac{(a \cdot b \cdot c) \cdot n}{V} \quad (4.9)$$

This time the hypothetic volume is 100 m^3 for every dimension class, which it is a rough estimate of the rock volume above *Milano* drip site, which is interested by the fracture network. Field observations permitted to recognize that the number of fractures *n* equals 2 in the largest class size of aperture, length, and width. Using this information, it is possible to generate the number of fractures in all other class sizes ranges for aperture, length, and width. The fractal λ, *a,* and *b* were applied again in the cubic law with the same procedure discussed above.

Finally, the values of fracture aperture and λ obtained respectively with the cubic law, the fractal analysis, and the cubic law with fractal parameters were used to estimate permeability using the relationships (Phillips, 2009):

$$k = b^3\lambda \tag{4.10}$$

4.2. Results

4.2.1. Recession analysis

Five flood hydrographs were selected in the whole dataset; the summary statistics of the selected recession limbs and the corresponding recession parameters obtained with the multi-exponential model are listed in Table 4.1. These hydrographs were selected because their recession limbs were not perturbed by later precipitations, moreover these storms happened in one of the most important phase of the hydrological year, namely the end of baseflow – beginning of recharge, so they could potentially give insights on the recharge dynamics.

	Recession				Maillet model					Recession interval		
	Q_{90}	Q_{10}	Q_{max}	Q_{min}	Q_{90}	Q_{10}	Q_{max}	Q_{min}	R^2	Start Date	End Date	Duration
	(l/s)				(l/s)					(yy/mm/dd hh:mm)	(yy/mm/dd hh:mm)	(hrs)
Recession 1	0.034	0.003	0.102	0.003	0.036	0.002	0.102	0.002	0.994	2009/10/23 16:00	2009/11/02 08:00	232
Recession 2	0.017	0.000	0.109	0.000	0.018	0.000	0.109	0.000	0.997	2010/08/15 01:00	2010/08/23 08:00	199
Recession 3	0.029	0.000	0.100	0.000	0.028	0.000	0.100	0.000	0.994	2010/10/18 12:00	2010/10/25 14:00	170
Recession 4	0.070	0.003	0.279	0.003	0.070	0.004	0.279	0.004	0.992	2012/09/04 05:00	2012/09/20 12:00	480
Recession 5	0.083	0.007	0.199	0.007	0.084	0.012	0.199	0.012	0.995	2015/10/04 13:00	2015/10/13 03:00	206

Q_{90}, Q_{10} = 90^{th}/10^{th} percentiles

	α_1	α_2	α_3	α_4	V_1	V_2	V_3	V_{base}	V_{tot}	P_{tot}*	P_{48}**	P_{36}**	P_{24}**	P_{12}**
	hrs^{-1}				m^3					mm				
Recession 1	0.00079	0.00067	0.00030	0.00013	0.014	0.095	0.058	0.06	0.227	91	79	8.8	7.2	0
Recession 2	0.0015	0.0007	0.0005	0.0003	0.044	0.03	0.03	0.017	0.122	57.4	48.6	47.2	46.2	42.2
Recession 3	0.0012	0.0011	0.001	0.0003	0.003	0.014	0.074	0.006	0.098	38.8	38.8	20.6	19.4	9.6
Recession 4	0.0005	0.0004	0.0003	5E-05	0.051	0.235	0.593	0.311	1.190	201.8	123.8	122	96.4	28.8
Recession 5	0.0009	0.0007	5E-05	-	0.046	0.181	-	0.109	0.337	130.6	68.4	41.8	41.6	0

* *P_{tot} represents the cumulative precipitations registered in the time interval between the considered flow peak and the previous one*

** *each index stands for cumulative precipitations collected during the 48, 36, 24 and 12 hours antecedent to the flow peak, respectively*

Tab. 4.1. Summary statistics for the recession intervals for each analyzed storm hydrograph and cumulative precipitations in the time intervals preceding the recession limb.

The storm hydrographs that we considered occurred during August (Recession 2, Fig. 4.5b), September (Recession 4, Fig. 4.5d) and October to November (Recessions 1,3 and 5, Fig. 4.5a, c, e). Recession 4 had the longest duration and the highest peak flow whereas the shortest recession limb and the lowest peak flow characterized Recession 3. The coefficient of determination (R^2), calculated between the monitored flow rate values and those calculated with the exponential model, shows that the *Maillet* model replicates well the observed outcomes (Tab. 4.1). The highest recession coefficients for each segment of the recession limb were found in Recessions 2 and 3, whereas Recession 4 showed the lowest ones.

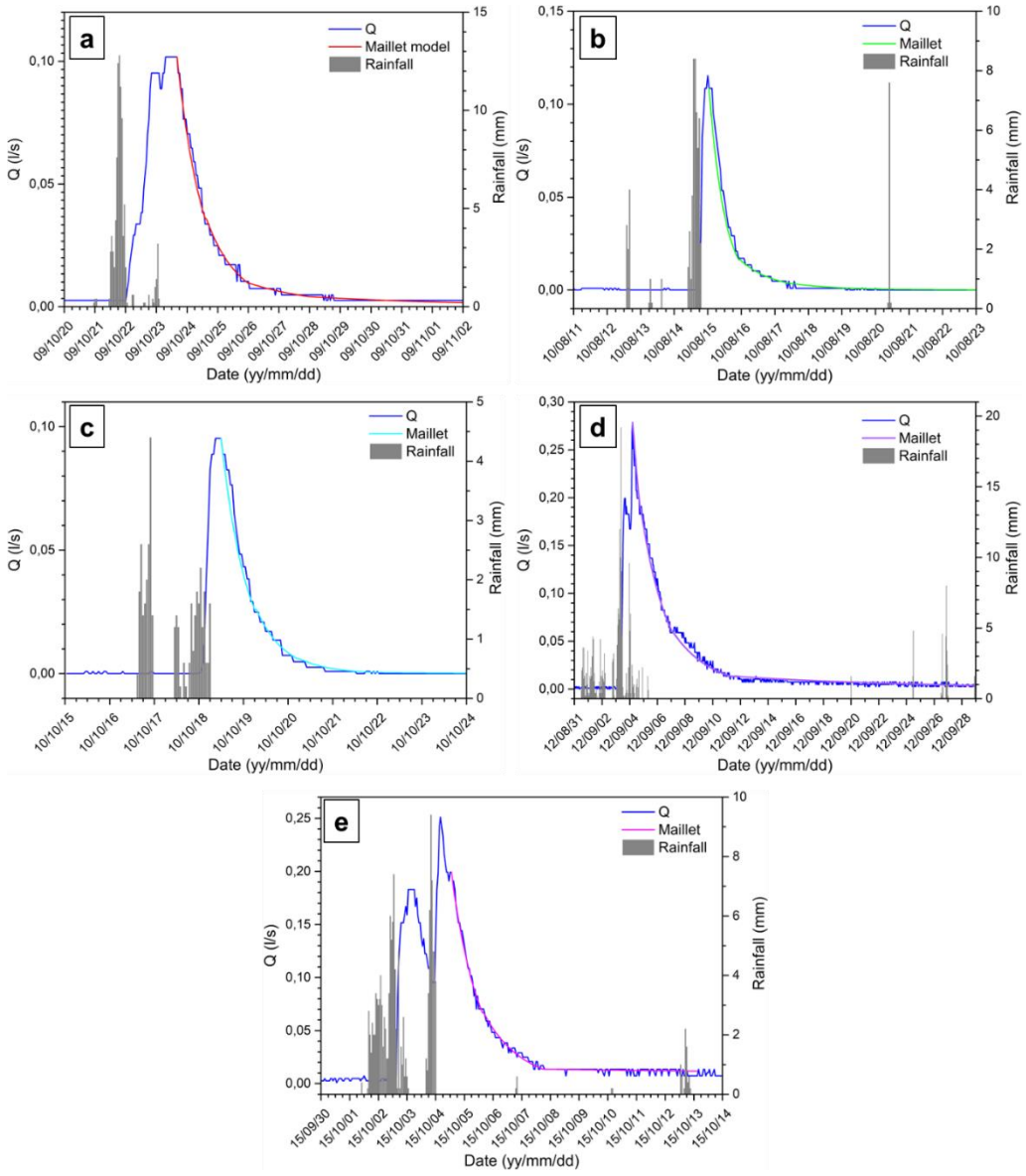

Fig. 4.5. Storm hydrographs investigated with recession analysis. (a) Recession 1, (b) Recession 2, (c) Recession 3, (d) Recession 4, (e) Recession 5. See Tab. 4.1 for details on each recession.

4.2.2. Fracture geometry

The summary results of fracture analysis by means of the cubic-law inversion are shown in Tab. 4.2. In particular, Table 4.2 reports average flow rate values for each recession segment in all storm hydrographs considered, the number of fractures contributing to each segment of the recession and the fracture geometry parameters.

a

Parameters used for fracture aperture calculation by means of cubic law inversion

recession segment	Recession 1 l/s	Recession 2 l/s	Recession 3 l/s	Recession 4 l/s	Recession 5 l/s	λ m^{-1}
Q_1	0.1018	0.1085	0.0952	0.2786	0.1749	0.002
Q_2	0.0904	0.0418	0.0913	0.2531	0.1335	0.1
Q_3	0.0266	0.0208	0.0758	0.1708	0.0066	0.4
Q_4	0.0093	0.0056	0.0018	0.0225	-	25
Q_{base}	0.0015	0.0001	0.0001	0.0036	0.0012	30

μ at 20°C (kg $m^{-1}s^{-1}$)	dh/dl	g (m s^{-2})	ρH_2O (kg m^{-3})
0.001	0.5	9.81	1000

b

Fracture aperture for each recession segment obtained from the cubic law inversion.

recession segment	Recession 1 *b* (m)	Recession 2 *b* (m)	Recession 3 *b* (m)	Recession 4 *b* (m)	Recession 5 *b* (m)
Q_1	0.00499	0.00510	0.00488	0.00698	0.00598
Q_2	0.00130	0.00101	0.00131	0.00184	0.00148
Q_3	0.00055	0.00050	0.00077	0.00101	0.00034
Q_4	0.00010	0.00008	0.00006	0.00013	-
Q_{base}	0.00005	0.00002	0.00002	0.00007	0.00005

c

Volumes calculated with recession analysis

recession segment	Recession 1 m^3	Recession 2 m^3	Recession 3 m^3	Recession 4 m^3	Recession 5 m^3
Q_1	0.014	0.044	0.003	0.051	0.046
Q_2	0.095	0.030	0.014	0.235	0.181
Q_3	0.058	0.030	0.074	0.593	0.109
Q_4	0.060	0.017	0.006	0.380	-
Q_{base}	0.012	0.000	0.001	0.071	0.024

d

	Volumes calculated from cubic law inversion					*hypothesized fracture geometry*		
recession segment	Recession 1 m^3	Recession 2 m^3	Recession 3 m^3	Recession 4 m^3	Recession 5 m^3	*n*	*c* m	*a* m
Q_1	0.016	0.016	0.016	0.022	0.019	2	0.20	8.00
Q_2	0.096	0.074	0.096	0.135	0.109	160	0.12	4.00
Q_3	0.057	0.052	0.080	0.106	0.036	16000	0.05	0.13
Q_4	0.048	0.041	0.028	0.065	-	500000	0.01	0.10
Q_{base}	0.001	0.001	0.001	0.002	0.001	120000	0.005	0.04
correlation*	0.99	0.37	0.62	0.65	0.97			

** correlation between the volumes obtained with recession analysis and the ones calculated with cubic law inversion*

Tab. 4.2. Results of the fracture analysis with cubic law inversion. (a) values of discharge (Q), water viscosity (μ), and density (ρ), hydraulic gradient (dh/dl) used for the cubic law inversion. (b) values of fracture aperture (*b*) obtained from the cubic law inversion. (c) and (d) show the drained volumes obtained with recession and cubic law inversion, respectively.

There is a general good correspondence between the volumes obtained from recession analysis and the ones from cubic law inversion, although R^2 is not as good for every recession (see the correlation values in the bottom of Tab. 4.2d). It is worth to mention, however, that, for a given recession segment, the volumes have the same order of magnitude comparing in every recession, moreover the trends from the first segment to the last are remarkably similar for 4 over 5 recessions.

The results of fractal analysis are reported in Tab. 4.3. As expected from the model, the fractures with smallest size are the most abundant, whereas the largest fractures are scarce in number.

	N_i	r_i	C	D
Width parameters	2	0.01	0.001262	1.6
Length parameters	2	100	3169.79	1.6
Aperture parameters	2	0.0001	0.000001	1.6

Fractal calculation results			
Length	**Width**	**Aperture**	**Number of fractures**
100	0.01	0.005	2.8
50	0.005	0.003	126
20	0.002	0.001	1450
10	0.001	0.0005	11800
5	0.0005	0.0001	42000

Tab. 4.3. Fracture geometry parameters obtained with fractal analysis.

The geometric parameters of fractures calculated with fractal analysis were then applied in the calculation of fracture aperture *b* using cubic law inversion. In this way, a hydraulic gradient progressively increasing through the recession segments was calculated by iteration. Again, the comparison between the volumes calculated by recession analysis with those obtained with the latter procedure shows similar values and trends from a recession segment to the following one. The values of fracture aperture *b* progressively decrease from the first section of the recession limb to the following ones in all examined recessions (Tab. 4.4).

a

Parameters used for fracture aperture calculation by cubic law inversion with fractal values

recession segment	Recession 1 l/s	Recession 2 l/s	Recession 3 l/s	Recession 4 l/s	Recession 5 l/s	λ m^{-1}	dh/dl
Q_1	0.1018	0.1085	0.0952	0.2786	0.1749	0.056	0.009
Q_2	0.0904	0.0418	0.0913	0.2531	0.1335	0.63	0.01
Q_3	0.0266	0.0208	0.0758	0.1708	0.0066	1.16	0.05
Q_4	0.0093	0.0056	0.0018	0.0225	-	2.36	0.2
Q_{base}	0.0015	0.0001	0.0001	0.0036	0.0012	2.1	1.5

μ at 20°C (kg $m^{-1}s^{-1}$)	g (m s^{-2})	ρH_2O (kg m^{-3})
0.001	9.81	1000

b

Fracture aperture for each recession segment obtained from the cubic law inversion.

recession segment	Recession 1 *b* (m)	Recession 2 *b* (m)	Recession 3 *b* (m)	Recession 4 *b* (m)	Recession 5 *b* (m)
Q_1	0.00627	0.00641	0.00614	0.00878	0.00752
Q_2	0.00260	0.00201	0.00261	0.00366	0.00296
Q_3	0.00082	0.00076	0.00117	0.00153	0.00052
Q_4	0.00029	0.00024	0.00017	0.00039	
Q_{base}	0.00008	0.00004	0.00004	0.00011	0.00008

c

Volumes calculated with recession analysis

recession segment	Recession 1 m^3	Recession 2 m^3	Recession 3 m^3	Recession 4 m^3	Recession 5 m^3
Q_1	0.014	0.044	0.003	0.051	0.046
Q_2	0.095	0.030	0.014	0.235	0.181
Q_3	0.058	0.030	0.074	0.593	0.109
Q_4	0.060	0.017	0.006	0.380	-
Q_{base}	0.012	0.000	0.001	0.071	0.024

d

Volumes calculated from cubic law inversion | *fracture geometry from fractal analysis*

recession segment	Recession 1 m^3	Recession 2 m^3	Recession 3 m^3	Recession 4 m^3	Recession 5 m^3	*n*	*c* m	*a* m
Q_1	0.018	0.018	0.017	0.025	0.021	2.8	0.010	100
Q_2	0.082	0.063	0.082	0.115	0.093	126	0.005	50
Q_3	0.048	0.044	0.068	0.089	0.030	1450	0.002	20
Q_4	0.034	0.029	0.020	0.046	-	11800	0.001	10
Q_{base}	0.009	0.004	0.004	0.012	0.008	42000	0.001	5
correlation*	0.96	0.43	0.61	0.58	0.95			

** correlation between the volumes obtained with recession analysis and the ones calculated with cubic law inversion*

Tab. 4.4. Results of the fracture analysis by cubic law inversion with geometric parameters and λ calculated with fractal analysis. Table (a) reports the values of discharge (Q), water viscosity (μ), and density (ρ), hydraulic gradient (dh/dl) used for the cubic law inversion with fractal geometric parameters. This time dh/dl was obtained by iteration. (b) shows the values of fracture aperture (*b*) obtained from the cubic law inversion. (c) and (d) show the drained volumes obtained with recession and fractal-cubic law inversion, respectively.

Finally, the permeability of the watershed portion drained by the *Milano* drip site was compared among all models (cubic law, fractal analysis, fractal cubic law) with equation (4.10). The obtained *k* values are reported in Fig. 4.6.

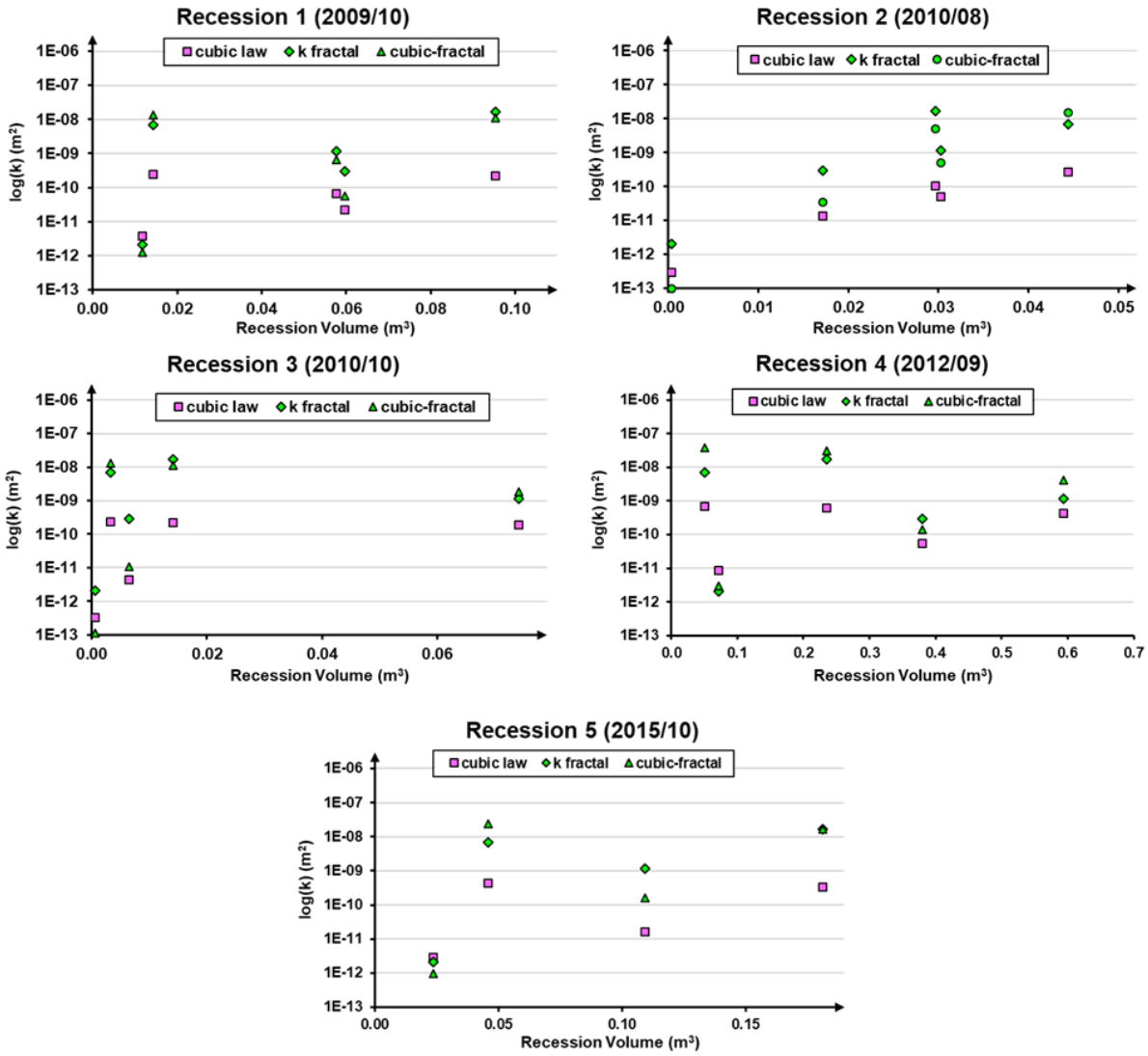

Fig. 4.6. Permeability for the volumes drained during each segment of the recession curves, calculated with the different models

It is apparent from the comparison that the permeabilities modelled with the different approaches are similar for a given volume, since they do not differ more than two orders of magnitude.

4.3. Discussion

As already discussed in the previous Chapter, the *Milano* drip site has a piston flow behavior and its hydrodynamic response to recharge is dependent on evapotranspiration at a seasonal scale. The influence of evapotranspiration is particularly relevant during summer when it can

prevent flow increases after precipitation events, unless such events are protracted for enough time to reach the minimum threshold for water deep percolation (difference between precipitation and evapotranspiration). The degree of saturation in different volumes of the system regulates the response to infiltration. Moreover, flow connectivity through the fracture system is fundamental in controlling the drip response to infiltration. It reaches its maximum during the recharge phase (mid-Autumn to Spring), when it determines the fastest flow response to rainfall, whereas saturation lowest levels are related to the discharge phase in the dry season (Summer to mid-Autumn) when the relationship rainfall-flow is not straightforward. The storm hydrographs analyzed with recession analysis are useful to unravel the mechanisms involved in the transition from baseflow to the onset of recharge, because they were recorded between August and the beginning of November. The five recessions analyzed can be subdivided in two categories: those perturbed by multiple rainfall impulses, which are characterized by an irregular rising limb (recession 1, 4 and 5, Fig. 4.5a, d, e) and those undisturbed (recession 2 and 3, Fig. 4.5b, c), which have normal rising limbs. The different response to rainfall are related to the water content before the beginning of precipitations (Arbel et al., 2008; Tritz et al., 2011). It is also interesting to note, however, that the Maillet models for the unperturbed recessions are characterized by the highest recession coefficient α_1 (an order of magnitude higher than those of the perturbed recessions, see Tab. 4.1) and the shortest recession intervals (Fig. 4.7).

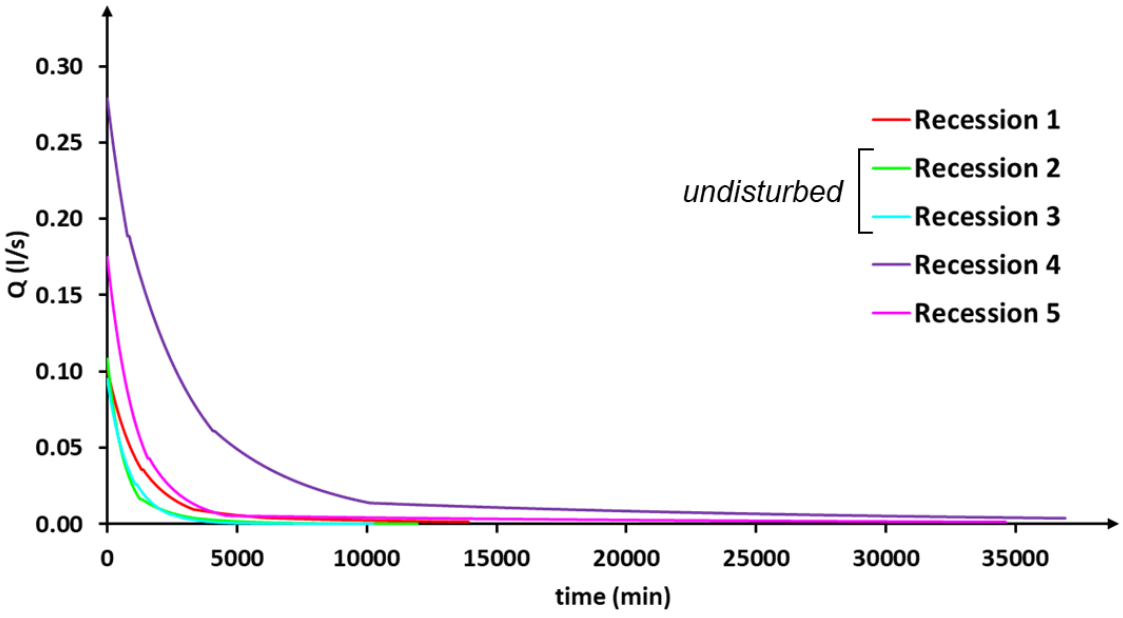

Fig. 4.7. Maillet recession models for the 5 storm hydrographs considered.

The recession coefficient α is related to the connectivity of the system flow path, so it depends on the structure of the unsaturated zone at the local scale (Arbel et al., 2008; Liu et al., 2016). The decrease of α during the recession is a consequence of the heterogeneity of the fractures drained by the *Milano* drip and it is an indicator of the sequential involvement of fracture networks with different hydraulic conductivity (Petras, 1986; Bonacci, 1993; Pronk et al., 2008; Poulain et al., 2018). This should also reflect an increasing hydraulic gradient through the recession because the contributing fractures are progressively smaller, so that flow occurs locally. The good match between the volumes obtained with the cubic law simple inversion and the ones obtained with the cubic law inversion with fractal parameters and a progressively increasing hydraulic gradient could be a confirmation of the involvement of progressively smaller fractures. The different slopes observed for the two groups of recessions is related to the activation of distinct fracture networks, so that the unperturbed recessions represent drainage form secondary (i.e. smaller) fractures. Furthermore, the water volumes measured during these recessions are smaller than those that are drained by the disturbed ones; this happens also as a result of the smaller cumulative amount of rainfall that fell before the unperturbed recessions with respect to the perturbed ones. A positive correlation between the total amount of rainfall and the total volume is demonstrated by the R^2 values reported in Tab. 4.5 (see also Tab. 4.1 for volume and rainfall values for each event).

	R^2 recession volumes - cumulative rainfall				
(m^3)	**P_{tot}**	**P_{48}**	**P_{36}**	**P_{24}**	**P_{12}**
V_1	0.672	0.517	0.734	0.795	0.504
V_2	0.979	0.882	0.715	0.695	-0.111
V_3	0.949	0.889	0.930	0.888	0.251
V_{base}	0.971	0.950	0.900	0.859	0.174
V_{tot}	0.936	0.937	0.923	0.877	0.251

Tab. 4.5. Coefficient of determination between the volumes drained during each recession segment and the cumulative rainfall in different time intervals (48, 36, 24 and 12 hours before peak flow).

The volumes of drained water that have the lowest correlation with the total amount of precipitation are those drained during the first segment of the recession limb. It appears that the recession coefficients α_1 are inversely correlated with the recession duration, pointing to a progressive decrease of hydraulic conductivity with time. There are two possible explanations:

1. Following the model proposed by Pronk et al. (2008), the transmission of the pressure wave in the unsaturated zone leads first to the saturation of the smallest fractures, then the major fractures are saturated and this permits to activate the small fracture networks that were not initially activated and which are characterized by very low hydraulic conductivity. Once precipitations cease, the hydraulic gradient starts to decrease, provoking the deactivation of the biggest fractures so that flow is regulated exclusively by smaller fractures.
2. The perturbed recessions exhibit lower α due to the fast activation of the largest fractures during the perturbed phase of the storm hydrograph (Fig. 4.8a); this is shown by the positive correlation between the recession coefficient and the hydraulic conductivity. These large fractures are rapidly deactivated after the start of the recession, so that fracture networks that have a lower hydraulic conductivity and that are more abundant in the rock volume (Fig. 4.8b to e) control the following phases of the recession. The higher recession coefficients of Recessions 2 and 3 represent the activation of the fractures with largest aperture that, due to antecedent scarce precipitations and their low water storage capacity, do not provoke the activation of smaller fractures, leading to shorter recession intervals (Fig. 4.8a to b or c).

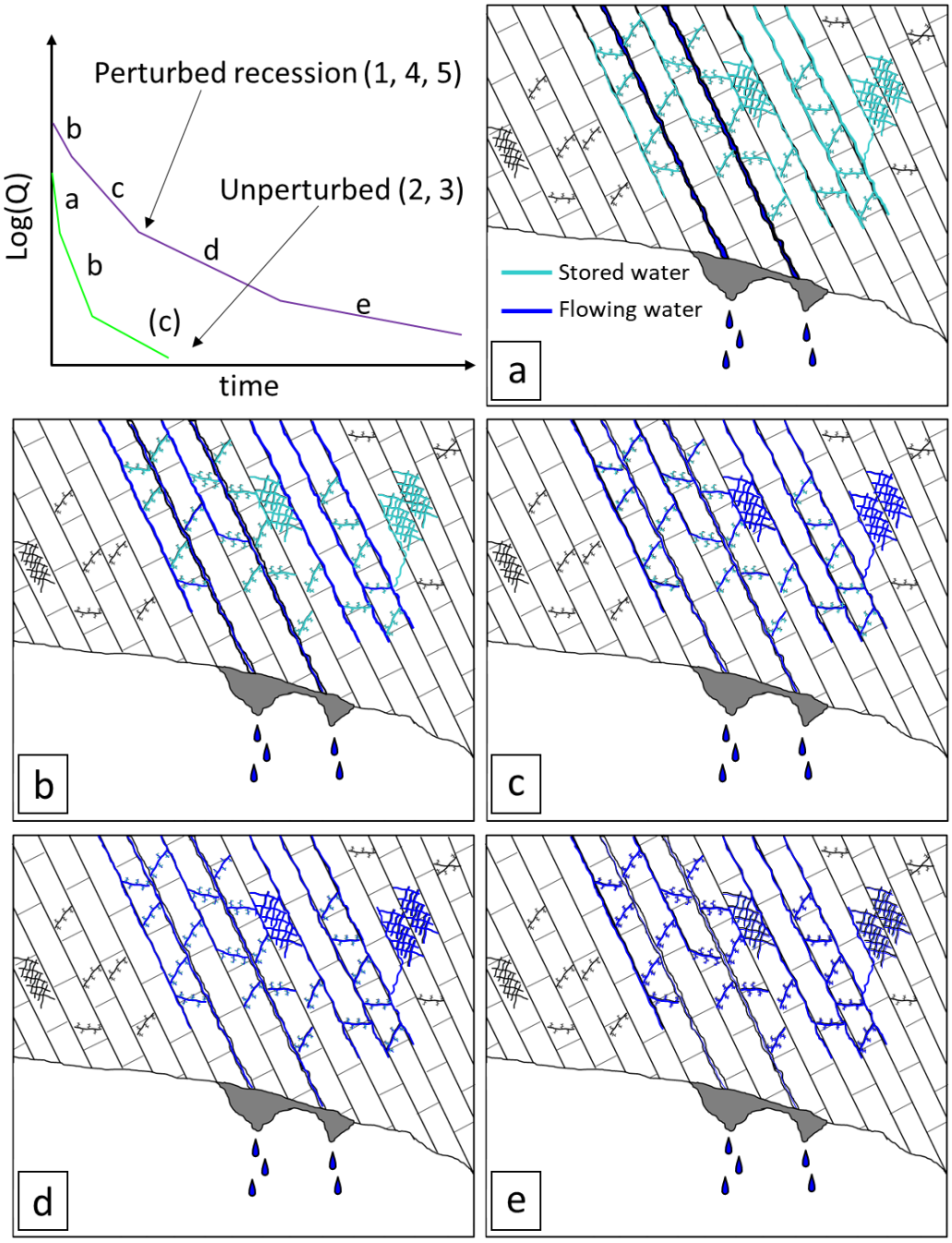

Fig. 4.8. Evolution of the drainage system during the recession limb. The boxes *a* to *e* correspond to the recession segment in the top left log(Q) – t plot labelled with the same letter. Each box shows the fracture networks activated (marked in blue, "flowing water") during the corresponding recession segments.

This latter interpretation is confirmed by the geometric and fractal modeling: the recession segments with the highest slopes correspond to the drainage of the most open fractures, independently from the method used to calculate the aperture of the fractures. The volumes calculated for the recessions with the highest α (Recessions 2 and 3) are, in fact, smaller than

those calculated for the perturbed recessions, because the largest fractures are less abundant than the smaller ones (Fig. 4.9).

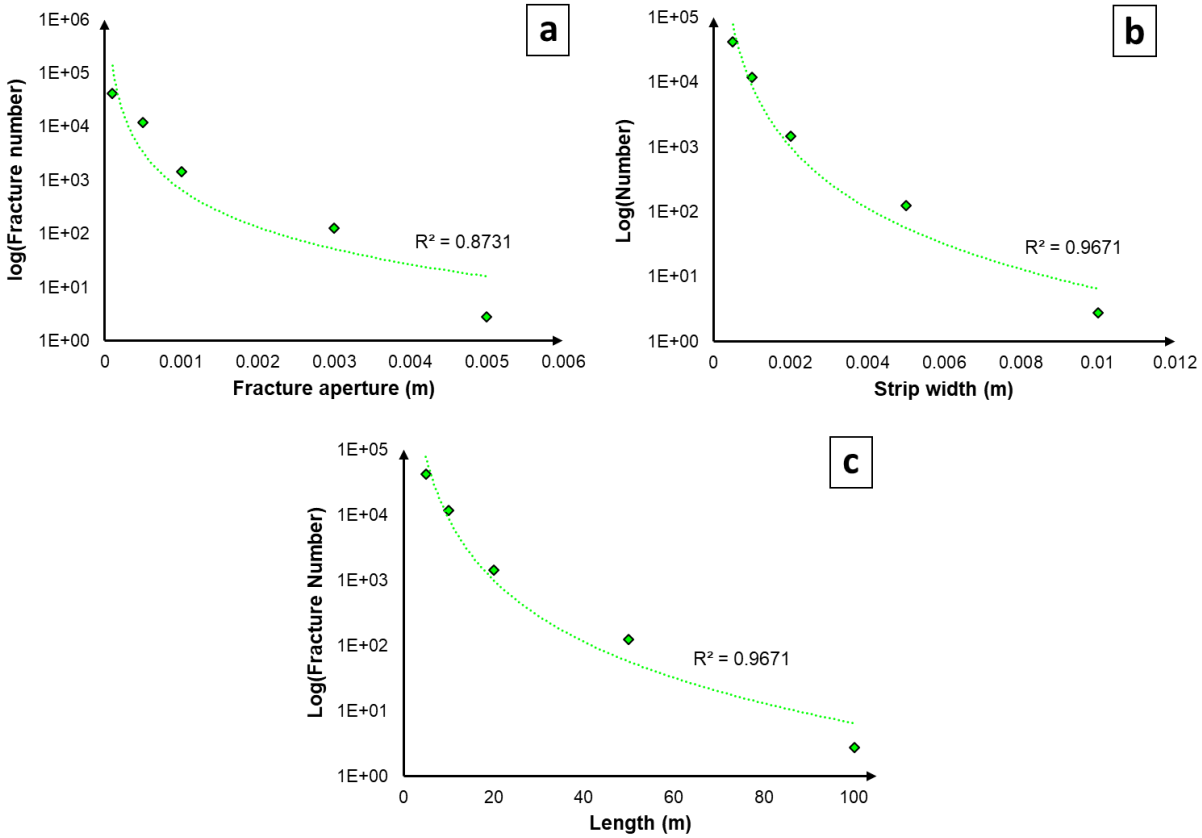

Fig. 4.9. Distribution of the classes of fracture dimensions. The classes for each geometric parameter are plotted against the number of fractures pertaining to each class. (a) Fracture aperture vs number of fractures. (b) Fracture ribbon width vs number of fractures. (c) Fracture length vs number of fractures.

The small fractures represent a reservoir that can store more water than the water contained in the largest fractures. After modest amounts of rainfall, the hydraulic pressure wave does not activate the small fractures, which store most water. Under these conditions, only the largest fractures (i.e. the bedding surfaces with the most continuous active surfaces) are drained. In case of prolonged rainfall and/or a long recharge interval, the smaller fracture networks are activated and the piston flow phenomenon is more efficient. This results in a progressive decrease of hydraulic conductivity through the recession limb due to the drainage of much less permeable fracture networks.

4.4. Concluding remarks

The coupling of recession and fracture analysis is a powerful approach to infer the architecture of the unsaturated volume drained by *Milano* drip site. The geometry inferred is complex and characterized by several size classes of fractures. The arrangement of the fracture classes resembles a fractal distribution, as demonstrated by the results of all models applied. Drainage is controlled by the largest aperture fractures (i.e. bedding junction planes) whereas storage is regulated by the smaller fractures, possibly bedding-confined joints and small fracture clusters. Water residence time in the unsaturated reservoir depends upon the efficiency in the transmission of hydraulic pressure waves during infiltration events. This efficiency is, in turn, controlled by the interplay between precipitation rate and cumulative amount as well as saturation conditions in the fractures. This study, therefore, has provided new knowledge and insights on the relationship between the hydrodynamic behavior and the geometric characteristics of the fracture networks in the *Milano* reservoir and the *Bossea* karst system. The implications are important for the functioning of unsaturated flow in similar karst systems around the world, where vadose zone inflows developed along bedding junctions, which are preferential flow paths.

Chapter 5: Hydrochemistry

5.1. Materials and methods

Several samples were taken over the past 10-15 years in order to characterize the water chemistry of the underground river and the secondary tributaries described in Chapter 3. During every sampling campaign, two water samples were collected for each inflow, one was taken in a 500-ml bottle for major ion content, the other one in a 100-ml bottle. This latter sample was acidified in situ with HNO_3 (65%) and sent to the lab for the determination of metals and lanthanides. Each sample was sealed and kept refrigerated. Sample temperature, pH, and EC were measured in situ with portable probes. The water samples were brought to the Department of Environment, Land, and Infrastructure Engineering (DIATI), Polytechnic University of Turin (Italy). The determination of Ca^{2+}, Mg^{2+} was carried out by means of ion-selective electrode, HCO_3^- was determined by acid-base titration with instrumental control of pH. Anion concentrations were determined by ion chromatography (Metrohm 881bIC Pro). Na^+ and K^+ were determined by Atomic Absorption Spectroscopy (AAS, Shimadzu); NH_4^+ was analyzed by UV-VIS spectrophotometry. An X Series 2 ICP-MS (Thermo Scientific) was employed for metal and lanthanide determination. The detection limit for ion chromatography and titration is 0.1 mg/l, whereas it is 0.05 mg/l for AAS. The detection limit is 2 ppb for metals and 5 ppt for the lanthanides. The analytical error for the chemical analyses were below 5%. The lanthanide concentrations were normalized to the Post Archean Australian Shale (*PAAS*, McLennan, 1989). The hydrochemical composition of a nearby spring was taken as reference of the non-carbonate water drained from the Impermeable Complex (*Sorgente dei Matti* spring, SdM; Fig. 5.1). Calcite and dolomite saturation indexes (*SI*) were calculated when water pH data were available. Their calculation is based on the estimation of the activity coefficient by means of the Debye-Hückel equation (Clark, 2015). Regarding water stable isotopes (^{18}O and ^{2}H), samples were collected on an irregular basis during 2016 and 2017, whereas seasonal samplings were performed between 2018 and 2019 for *Mora* creek and its secondary tributaries. An aliquot of 4 ml was collected in an amber glass vial for each investigated spot, then 2 ml of the sample were transferred in 2 ml glass vials for isotopes determination. All the samples were kept refrigerated to inhibit evaporation. Moreover, four monitoring surveys of stable isotope composition of Milano drip site were carried out during consecutive rainfall events in autumn 2018 and spring 2019. This was achieved thanks to an automatic water sampler (ISCO model

2900 sampler, ISCO Inc.) that was set to collect water at specific sampling frequencies: a sample every 6 hours was collected during the first (2018/10/08 22:00 to 2018/10/14 16:00) and the second (2018/10/15 11:00 to 2018/10/21 11:00) rainfall events. The sampling frequency adopted during the third survey (2018/10/25 16:30 to 2018/11/02 16:30) was 8 hours, whereas the sampling frequency adopted for last monitored rainfall events (2019/04/10 22:00 to 2019/04/16 16:00) was again 6 hours.

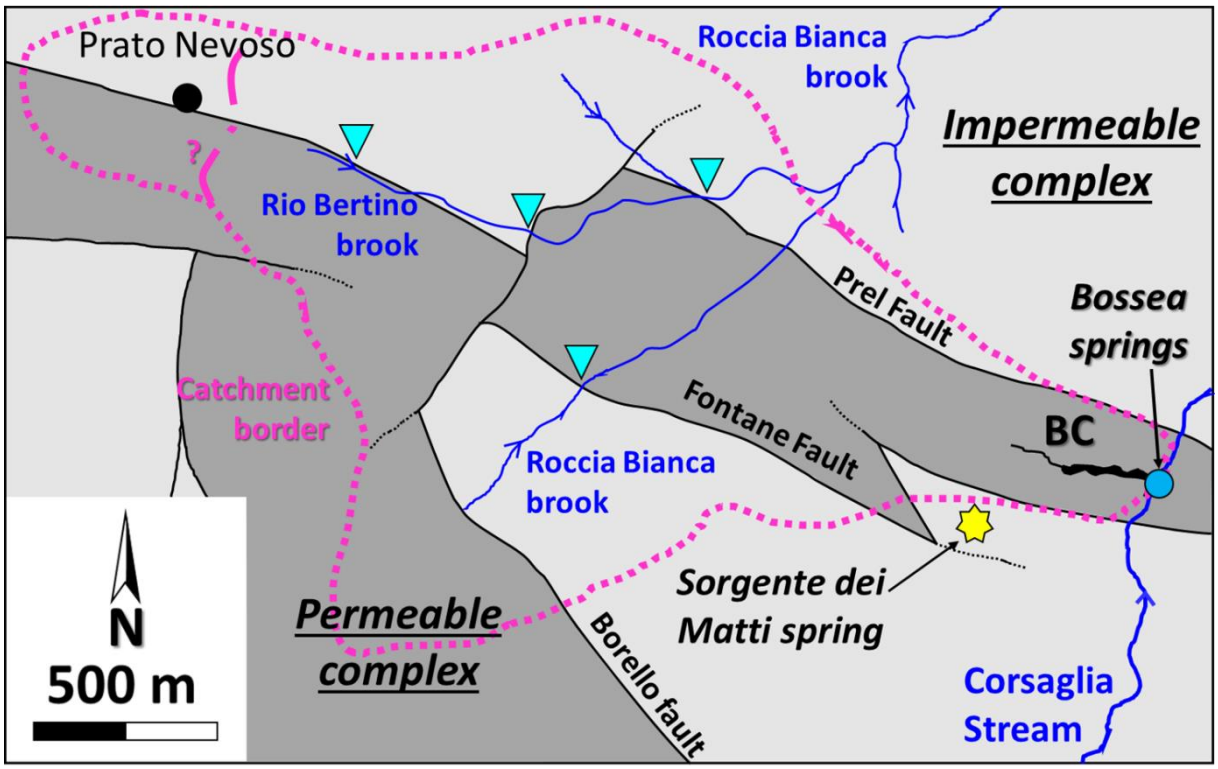

Fig. 5.1. Simplified hydro-geological map of the study area in which the position of *Sorgente dei Matti* spring is reported (BC = Bossea Cave, reversed triangles represents sinkholes).

The samples were collected by the automatic sampler with 500 ml bottles; again, 2 ml of water were taken from each bottle and transferred to glass vials for the same purpose of the aforementioned seasonal samplings. At the ending of each precipitation event, a rainfall sample was collected on the slope over *Bossea* cave by means of a rain gauge. The instrument collected water for most of the duration of each meteorological event. The rainfall collected was transferred in 2 ml glass vials immediately after the ending of precipitation to avoid evaporation. The analyses of $\delta^{18}O$ and $\delta^{2}H$ were carried out at the Institute of Geology of Innsbruck University (Austria), by means of a Picarro Cavity RingDown Spectrometer L2140-*i* coupled with a vaporization module and an autosampler. All the analyses were performed in

high precision mode and the post-run correction procedure implemented by van Geldern and Barth (2012) was adopted to maximize precision and accuracy of the analyses. Precision is better than 1‰ for $\delta^{2}H$ (1σ) and better than 0.1‰ for $\delta^{18}O$ (1σ).

5.2. Results

5.2.1. Major components and trace elements

The results of the chemical analyses performed on the *Bossea* samples revealed an overall calcium-bicarbonate to calcium-magnesian bicarbonate hydrochemical facies for all the monitored outlets (Fig. 5.2). However, the hydrochemical composition of each monitored discharging point (*Mora* creek, *Polle* and drip sites) are plotted in Schoeller diagrams to observe the characteristics of each outlet that cannot be recognized nor on a piper nor on a Langelier-Ludwig diagram. The normalized concentrations of the rare earth elements (REEs) are reported in spider diagrams for each flow, the only exception being *Onda* and *Balena* drip sites for which REEs data are not available.

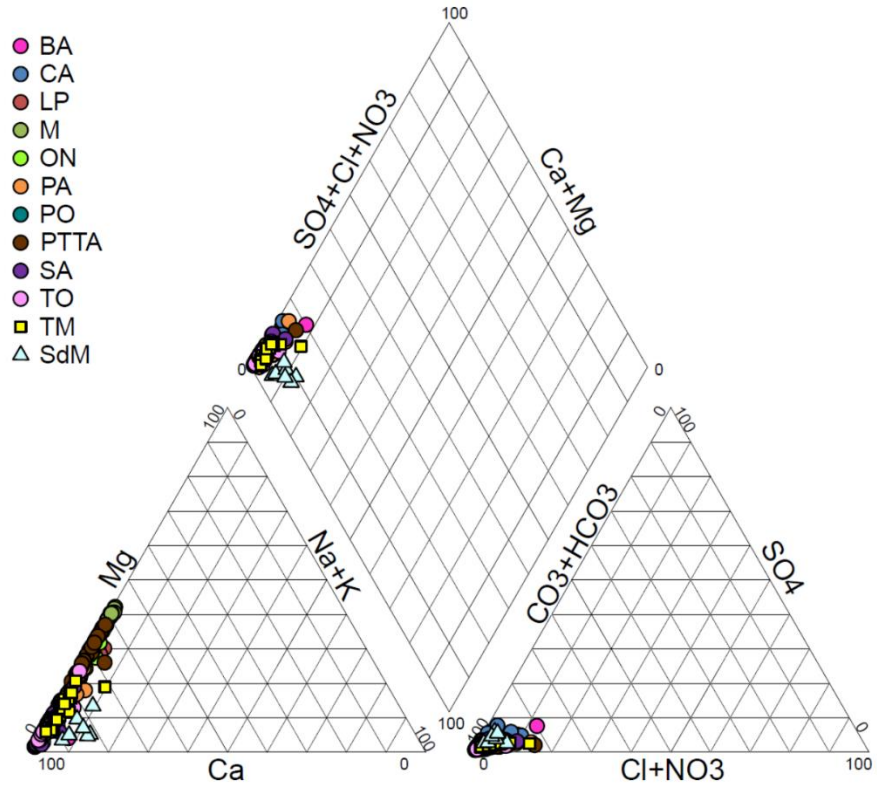

Fig. 5.2. Piper diagram of all the samples collected in *Bossea* cave, distinguished by the discharging point: BA = Balena; CA = Cancello; LP = Laghi Pensili; M = Milano; ON = Onda; PA = Polla delle Anatre; PO = Polla dell'Orso; PTTA = Polletta; SA = Sacrestia; TO = Torre; TM = Mora creek; SdM = Sorgente dei Matti spring.

The compositional data measured for the collected water samples are reported in Appendix 4 (major ion chemistry, expressed in milliequivalents per liter, meq/l) and Appendix 5 (Rb, Sr, Ba and lanthanides). A statistic summary for major chemistry and for the concentrations of the relevant trace elements (Rubidium, Strontium and Barium) measured in each monitored outlet is reported in Appendix 6. Following the results and related discussion of Chapter 3, the results of the investigation on the outlets' hydrochemistry are ordered in function of their position in the cave system respect to the structural setting and in relation to their hydrological classification: first, the so-called *Polle*, then the drip sites and finally the underground river and the spring draining the non-carbonate rocks, not hydrologically connected to *Bossea* system (*Sorgente dei Matti* spring, SdM).

5.2.1.1. Polla delle Anatre, Polla dell'orso and Polletta

Polla delle anatre showed a calcium-bicarbonate hydrochemical facies in all the analyzed samples. The most variable components were, in order, the alkali ions (sodium and potassium), chloride and the nitrate anions, the dominant components were in turn very stable (Appendix 6). This inflow showed a highly variable ratio between alkali and chloride, ranging from the unit to much higher values (i.e. a larger proportion of alkali respect to chloride), depending on the considered sample (up to 6.9; Fig. 5.3a). *Polla delle anatre* exhibited also variations in the normalized REE values and in the shape of the resultant spider diagrams. There are samples that showed flat REE normalized patterns, those that presented negative Cerium anomaly coupled with positive Europium anomaly and those that presented positive trends (i.e. positive slope of the overall spider diagram) going from the light REEs to the heavy REEs (Fig. 5.3b).

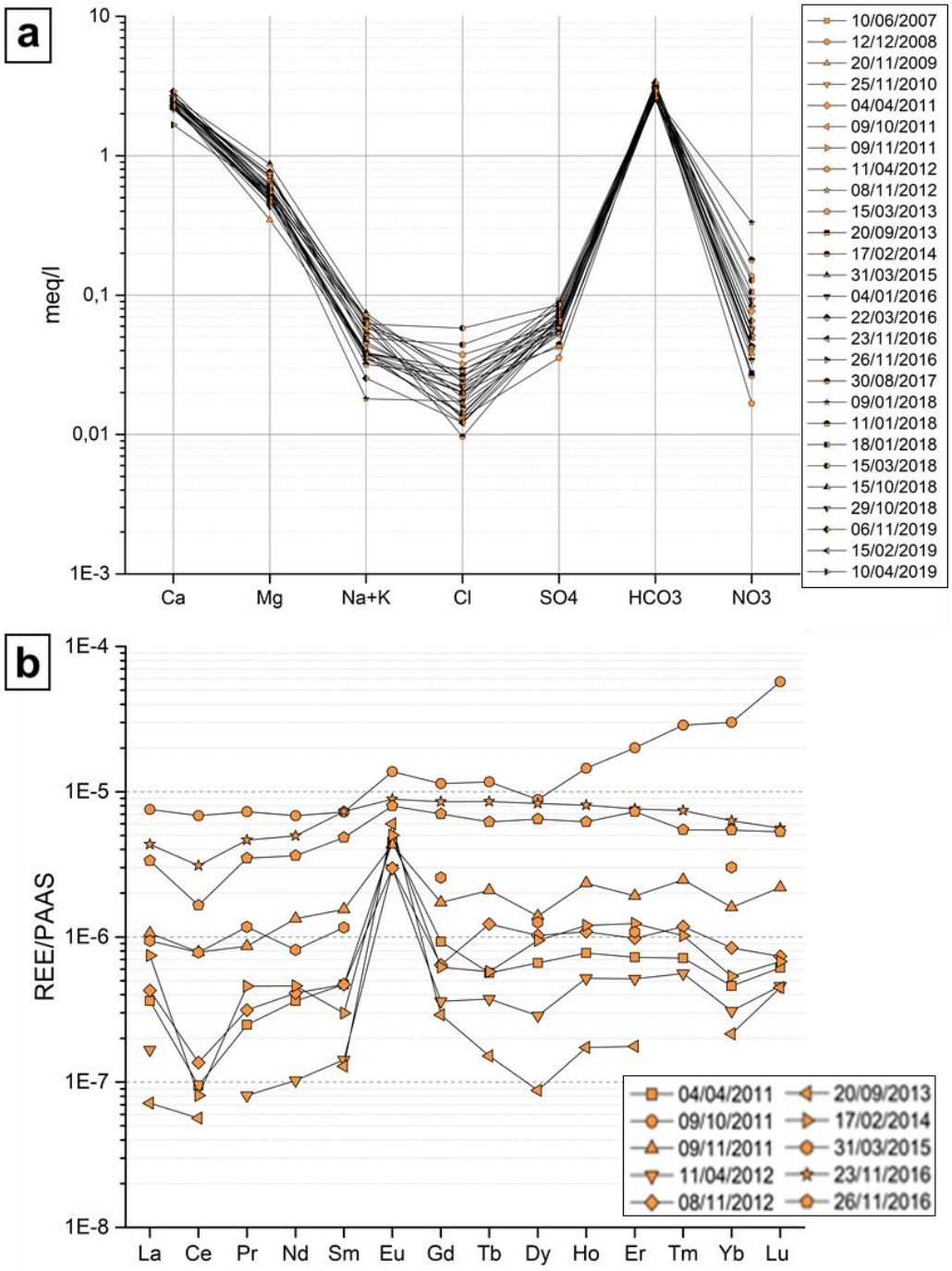

Fig. 5.3. *Polla delle Anatre* Schoeller diagram for major components chemistry (a) and Spide diagram for REE concentrations normalized to the *Post Archean Australian Shale* (b).

Polla dell'Orso exhibited a calcium-bicarbonate hydrochemical facies for all samples. It showed a relatively high variability in magnesium, alkali, chloride and, above all, in nitrate content (Fig. 5.4a; Appendix 6). Even this inlet showed a highly variable alkali to chloride ratio, depending on the sample (range of the ratio: 0.8-2.4). Its spider diagram shows that *Polla dell'Orso* is usually characterized by the presence of a negative Ce anomaly and a positive Eu

anomaly, however there are also a few examples of flatter patterns with weaker Ce and Eu anomalies (Fig. 5.4b). It is the *Polla* with the highest concentrations of Strontium (Appendix 6).

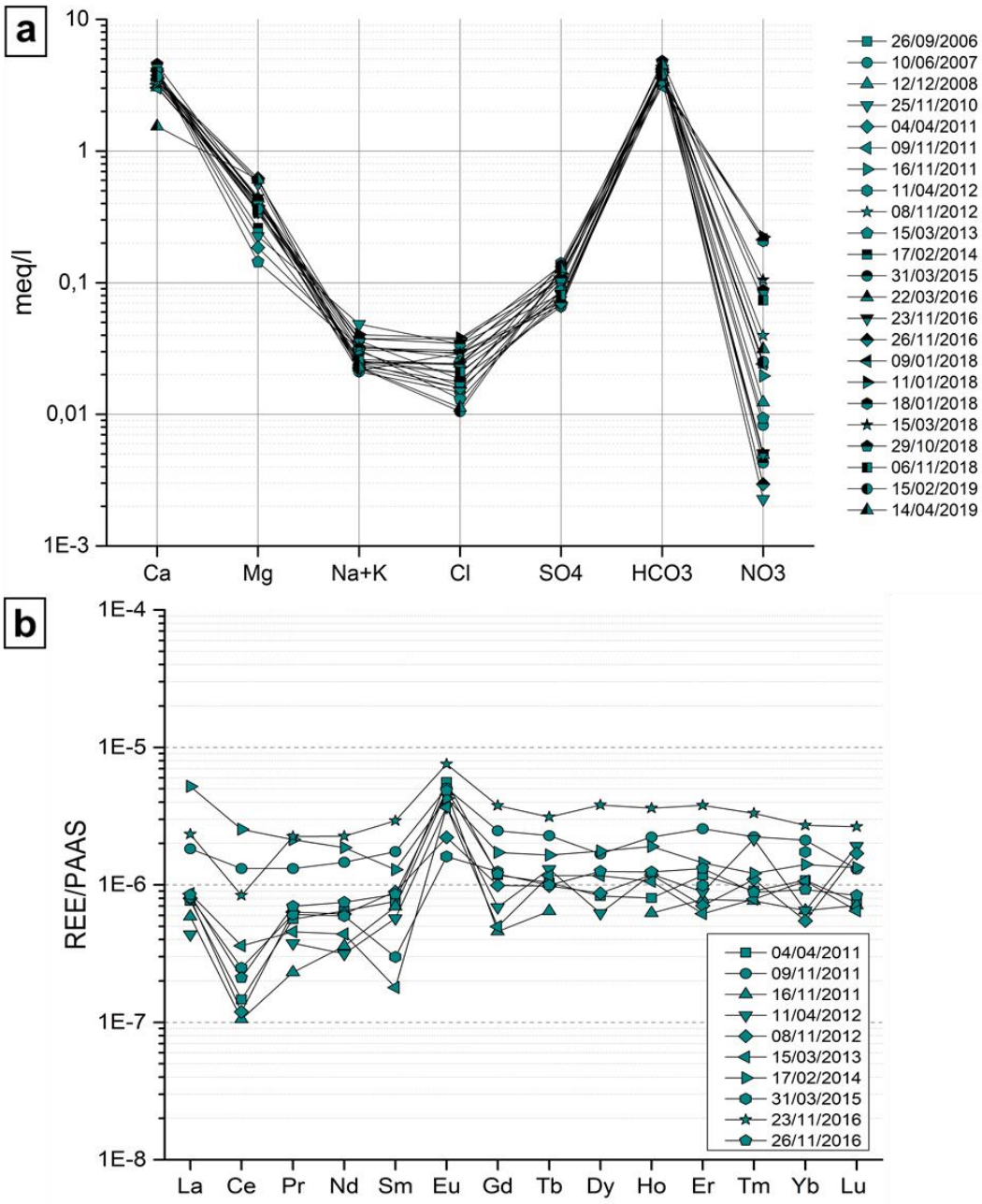

Fig. 5.4. *Polla dell'orso* Schoeller diagram for major components chemistry (a) and spider diagram for REEs normalized concentrations (b).

Among the so-called *polle*, *Polletta* is the only one that is characterized by a bicarbonate-calcium-magnesian hydrochemical facies (Fig. 5.5a). It exhibited high variability in all the less abundant major components (Appendix 6) but, among them, it had a remarkable variability in

nitrate, which varied of more than an order of magnitude. It showed a variable alkali to chloride ratio that assumed values in the interval 1.00-2.03, but its oscillation was lower than that of the other *polle*.

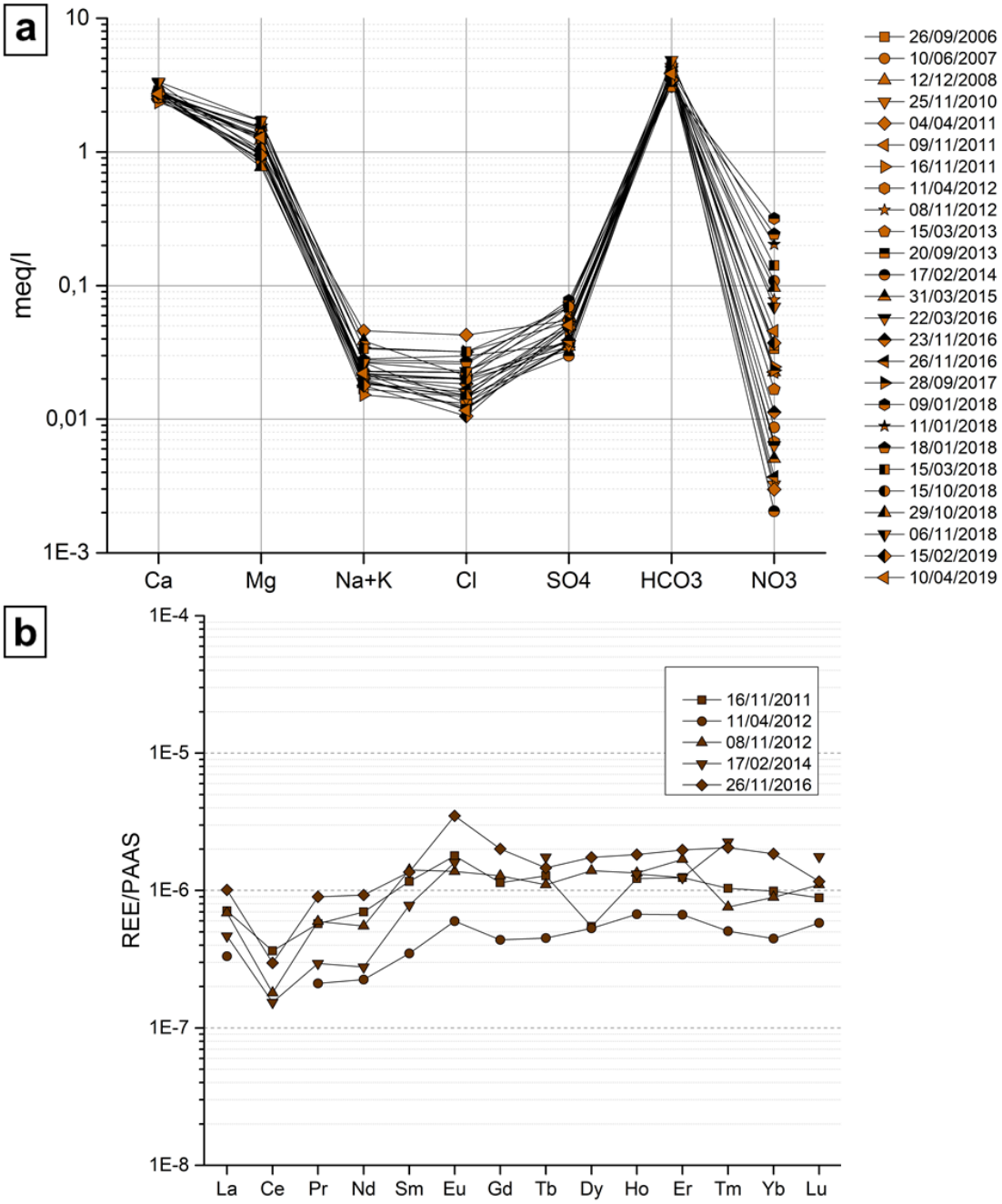

Fig. 5.5. *Polletta* schoeller diagram for major chemistry (a) and spider diagram for REE normalized concentration (b).

It is also the *polla* with the lower content of trace elements (Appendix 6). The shape of its REE normalized concentrations showed a negative Ce anomaly in most samples but the Europium

anomaly was usually absent, and the overall shape of the patterns showed a slight positive slope towards the heavy REE.

5.2.1.2. Drip sites hydrochemistry

Milano drip site is characterized by a calcium-magnesian carbonate hydrochemical facies (Fig. 5.6a; Appendix 6). It showed saturation in both calcite and dolomite, and both indexes never diminished to values close to zero. Also, the saturation condition of water discharged by this drip site is testified by the abundant speleothem deposits covering the outlet. Like the previous outlets, even *Milano* exhibited a marked variability in chloride and nitrates. The variable contents of Cl determined the oscillation of the alkali to chloride ratio from a sample to another (Fig. 5.6a), with values ranging from 1.0 to 3.3. Trace elements such as Rb and Ba were not abundant, whereas Sr is remarkably higher than the two previous trace elements. The shape of the patterns reported in Fig.5.6b is variable but it usually presented a positive Europium anomaly and a negative Cerium anomaly of variable strength. There are a few cases of slight flat patterns and there is one that presents a positive, progressive increment (i.e. positive slope) from light REEs to heavy REEs.

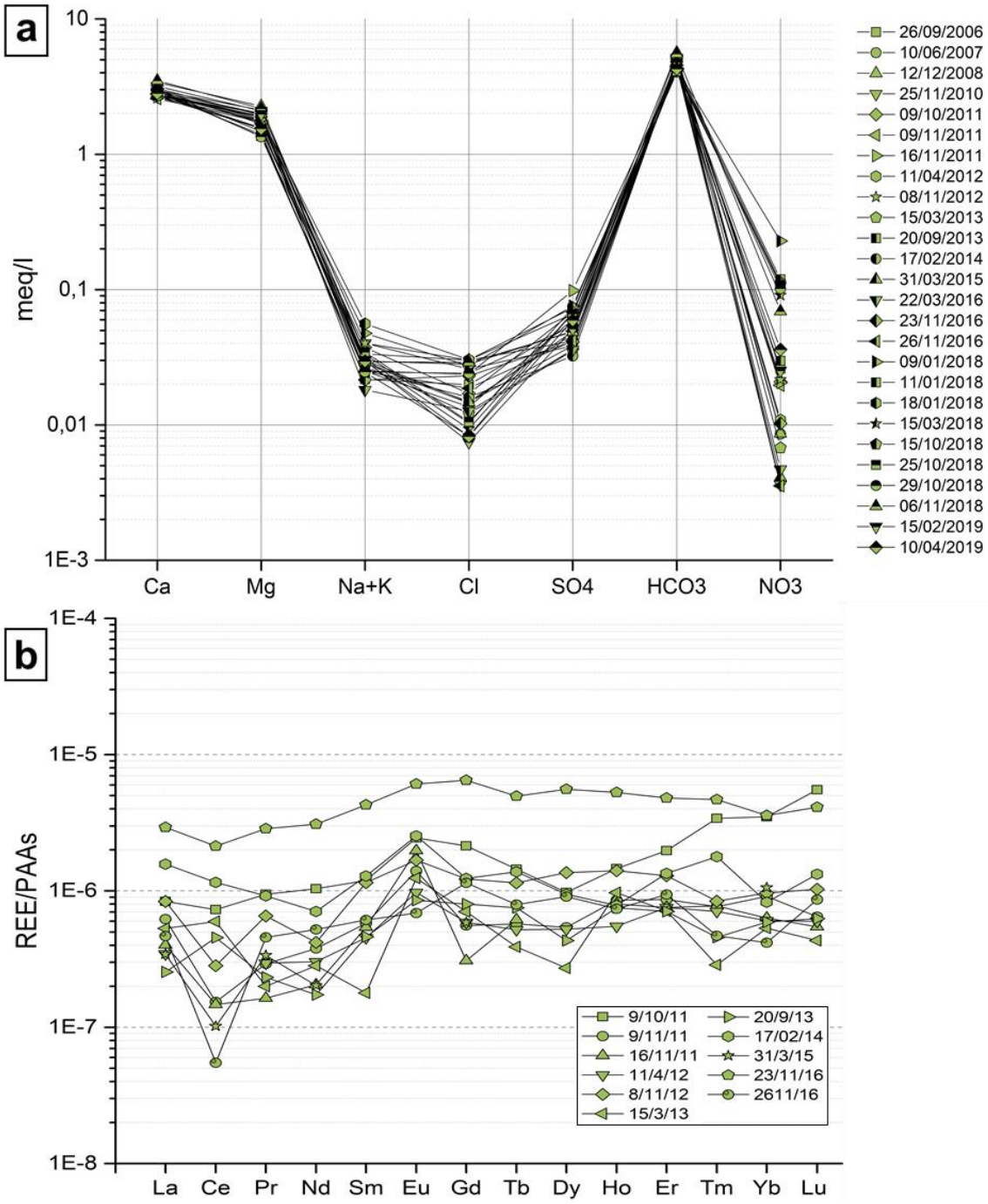

Fig. 5.6. *Milano* drip major chemistry represented in a Schoeller diagram (a) and its spider diagram (b).

The water samples collected in *Torre* drip site revealed a calcium-carbonate hydrochemical facies for this outlet. magnesium, alkali, chloride and nitrate showed a high variability, especially the last two components (Fig. 5.7a; Appendix 6). The alkali to chloride ratio varied depending on the considered sample from close to 1.0 to 1.9. Trace element concentrations are slightly lower than those observed for *Milano* and for *Polletta*. All samples exhibited

oversaturation with respect to calcite whereas they can be either saturated or undersaturated respect to dolomite. REEs normalized patterns are generally flat with a variable Cerium negative anomaly (Fig. 5.7b)

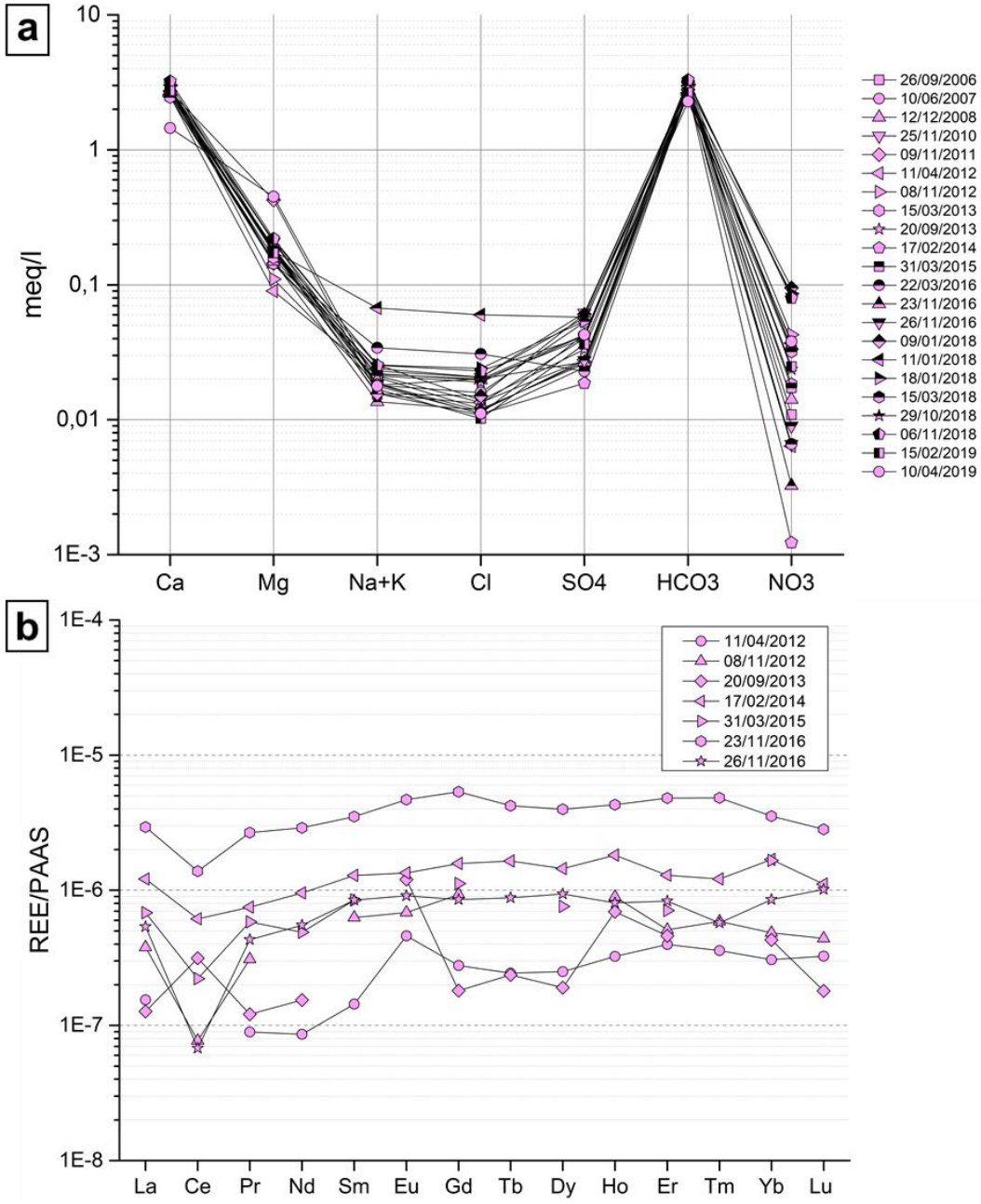

Fig. 5.7. Schoeller (a) and spider diagram (b) for *Torre* water samples.

The following three drips are described together due to the limited number of samples for these outflows (the hydrochemical monitoring program started only last year). The *Balena* drip site exhibited a calcium-magnesium carbonate hydrochemical facies. It showed a certain range of

variability for calcium, chloride and nitrate (Appendix 6; Fig. 5.8a). Like the previous outflows, the alkali to chloride ratios varied among the samples, from below one to some exceeding one. Nitrate had a range of variation lower respect to the previous investigated outflows, although it is still the most variable major compound. The *Onda* drip waters belong to the calcium-magnesium carbonate hydrochemical facies. Again, the most variable compounds are chloride and nitrate (Fig. 5.8b; Appendix 6). The *Laghi Pensili* has calcium-magnesium carbonate hydrochemical facies as well. The few samples collected showed pronounced variations of both alkali and chloride, but their ratio barely exceeded 1 (Fig. 5.8c).

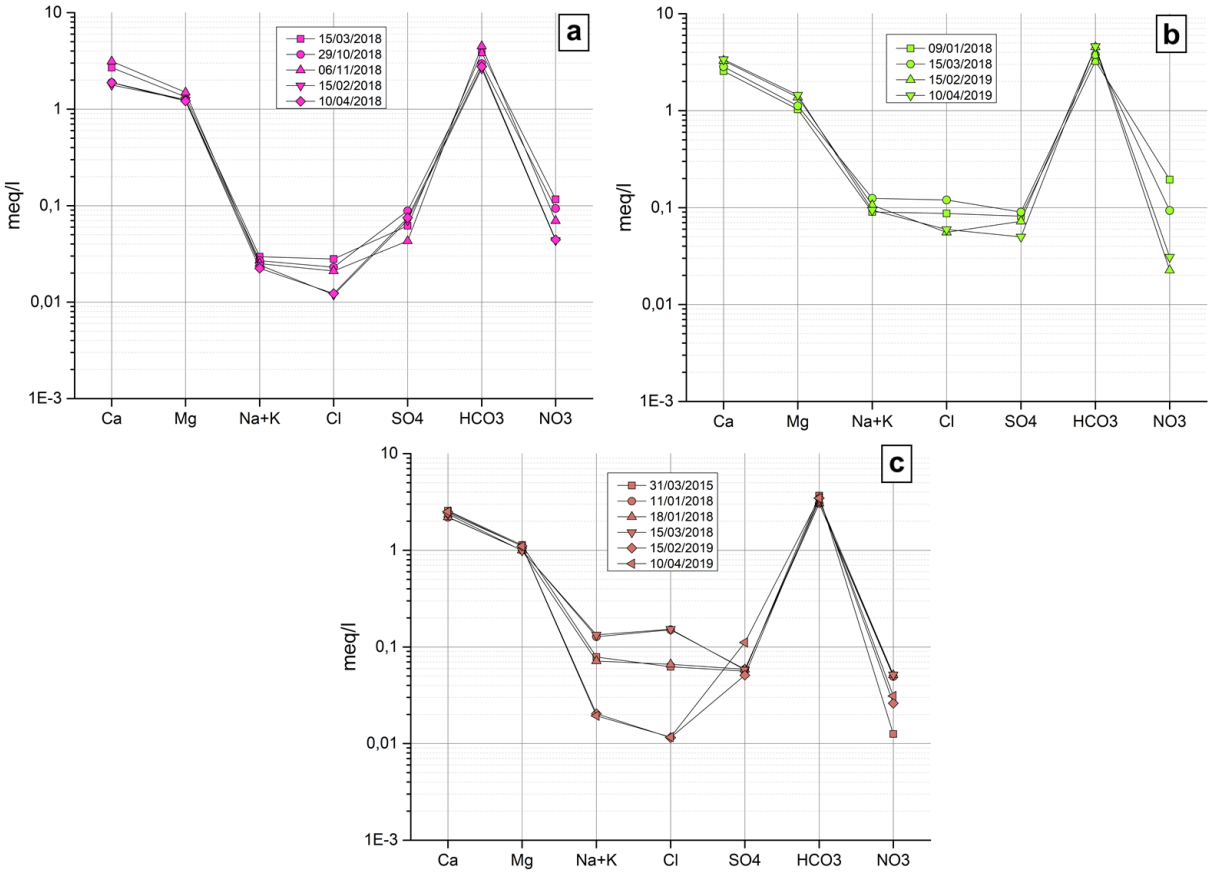

Fig. 5.8. Schoeller diagrams for *Balena* (a), *Onda* (b) and *Laghi Pensili* (c) drip sites.

The *Sacrestia* showed a calcium carbonate hydrochemical facies and it was characterized by high variability in magnesium and in all the less abundant compounds (alkali, chloride and nitrate; Fig. 5.9a; Appendix 6). The nitrates, in particular, showed a high variability, similarly to what observed for *Polletta*. This drip site exhibited also the maximum fluctuation for magnesium among all studied outflows. The alkali to chloride ratio varied between 0.9 and 2.5 but it was close to 1.0 for most samples. *Sacrestia* is also the second outflow with the highest

mean trace element concentration (greater only in *Polla dell'orso*). The pattern of REEs normalized concentrations plotted in a spider diagram show that most of the samples had a negative Cerium anomaly and an Europium positive anomaly. Some samples showed patterns with no Europium anomaly, a less pronounced Cerium negative anomaly and positive trend from La to Eu, whereas the trends are flat to slightly inclined (with negative slopes) from the medium to heavy REEs (Fig. 5.9b).

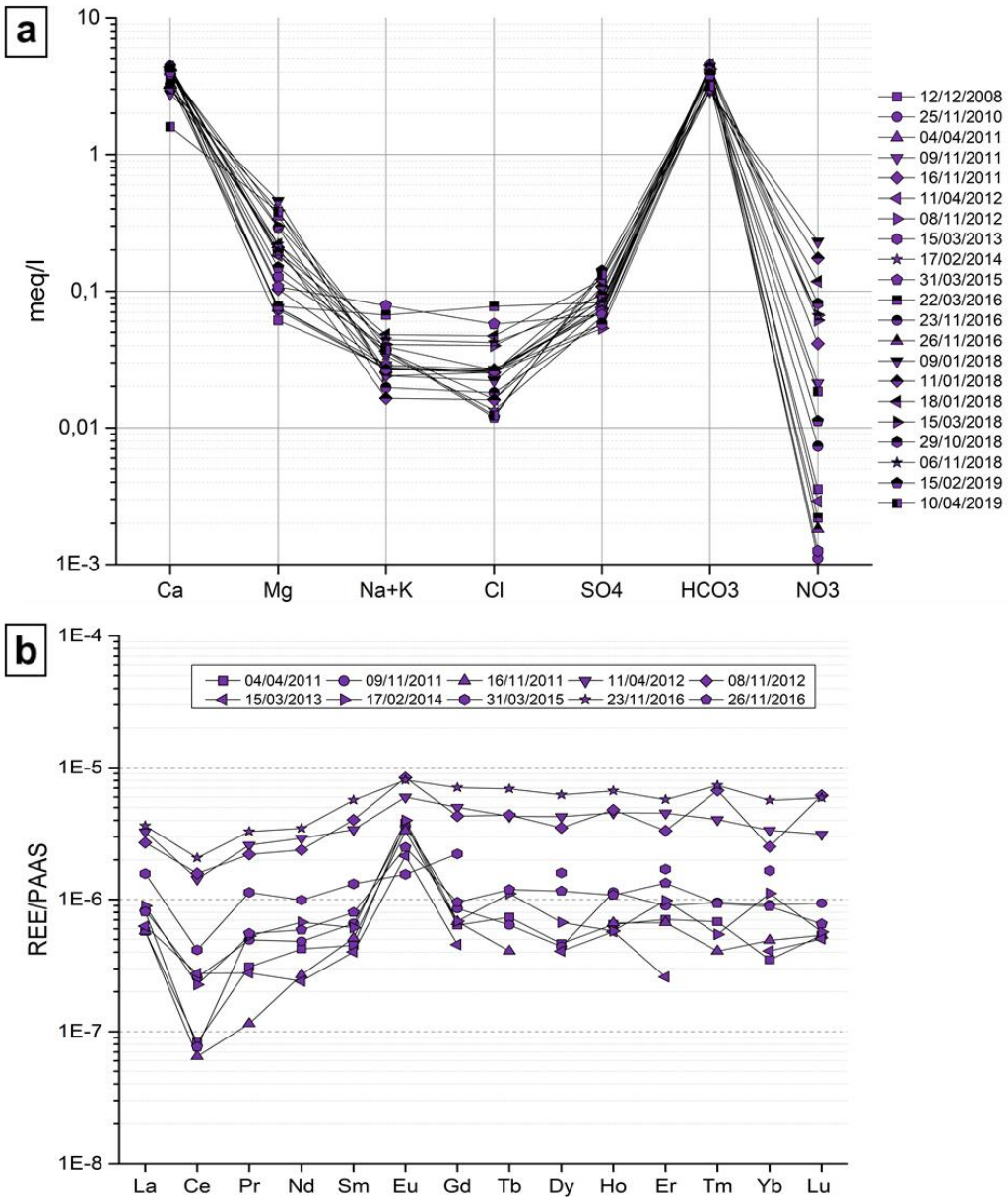

Fig. 5.9. *Sacrestia* schoeller diagram for major chemistry (a) and spider diagram for REE normalized concentration (b).

Cancello drip site showed a calcium-carbonate hydrochemical facies and highly variable amounts of magnesium, alkali, chloride and nitrate (Fig. 5.10a; Appendix 6). The alkali to chloride ratio varied between 0.8 and 2.7, with most of the values exceeding 1.5. All water samples showed saturation for calcite and a fluctuating undersaturation for dolomite (Appendix 6).

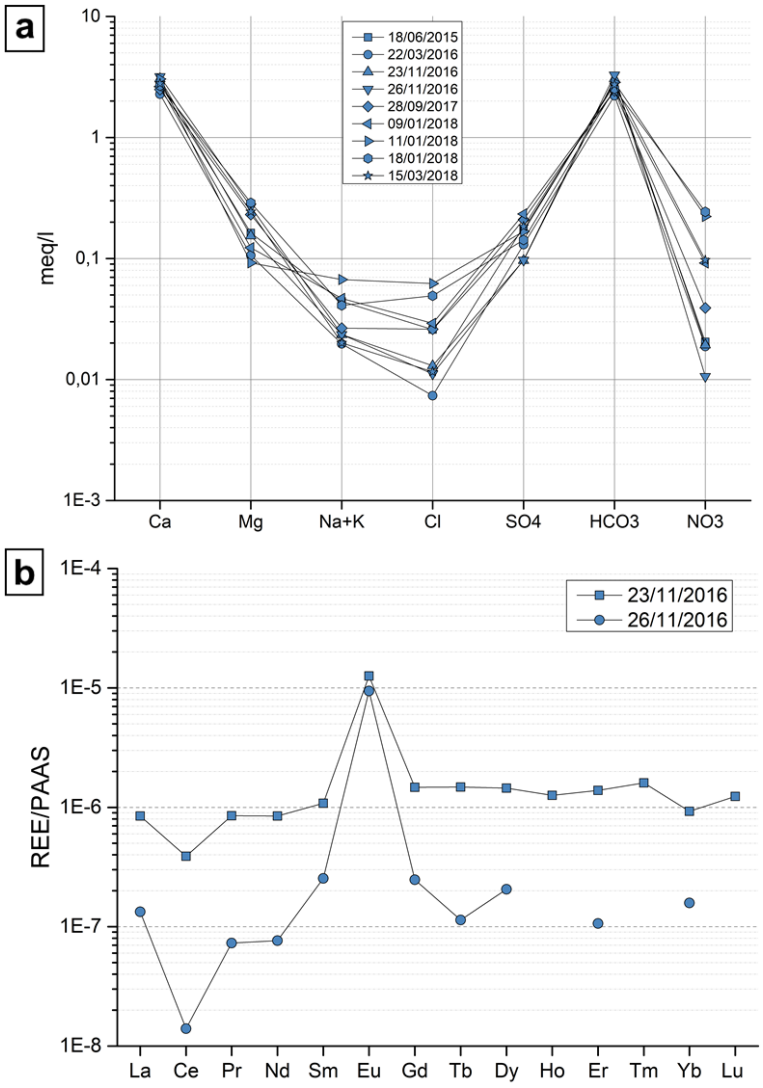

Fig. 5.10. *Cancello* major chemistry plotted in a Schoeller diagram (a) and REEs normalized concentrations plotted in a spider diagram (b).

The only two samples analyzed for REE content showed both a negative Cerium anomaly and a positive Europium anomaly in the patterns of normalized concentrations (Fig. 5.10b); the difference between the two samples is the magnitude of the Ce and Eu anomalies and the total amount of REE.

5.2.1.3. Mora creek and Sorgente dei Matti spring

The main underground river exhibited a calcium-carbonate hydrochemical facies for all the analyzed samples. It is characterized by a more diluted solute concentration respect to the other studied outflows (*polle* and drip sites). All the less abundant major components showed a much larger variability than calcium and bicarbonate, in particular magnesium, chloride and nitrate (Fig. 5.11a ; Appendix 6). *Mora* creek showed a variable saturation degree respect to calcite but its mean value corresponds to saturated waters. Saturation in dolomite is much more fluctuating but overall is lower than that of calcite. Mean total contents of trace elements were similar to the values observed in other studied outflows. The underground river, however, exhibited the mean highest contents of Rubidium and Barium. The alkali to chloride ratio varied from 1.0 to 4.1 depending on the considered sample, with a mean value of 1.2. Normalized rare earth element concentrations were plotted on a spider diagram for each sample; the sample patterns showed a variable Cerium negative anomaly and positive Europium anomaly (Fig. 5.11b). Some sparse cases of different patterns exist: a sample showed both Ce and Eu anomalies but also a progressive increase of normalized values from the medium to heavy REE. There is also the case of a sample with a slight progressive increase of normalized values from light to medium REEs, whereas the pattern is flat going from the medium to the heavy REE.

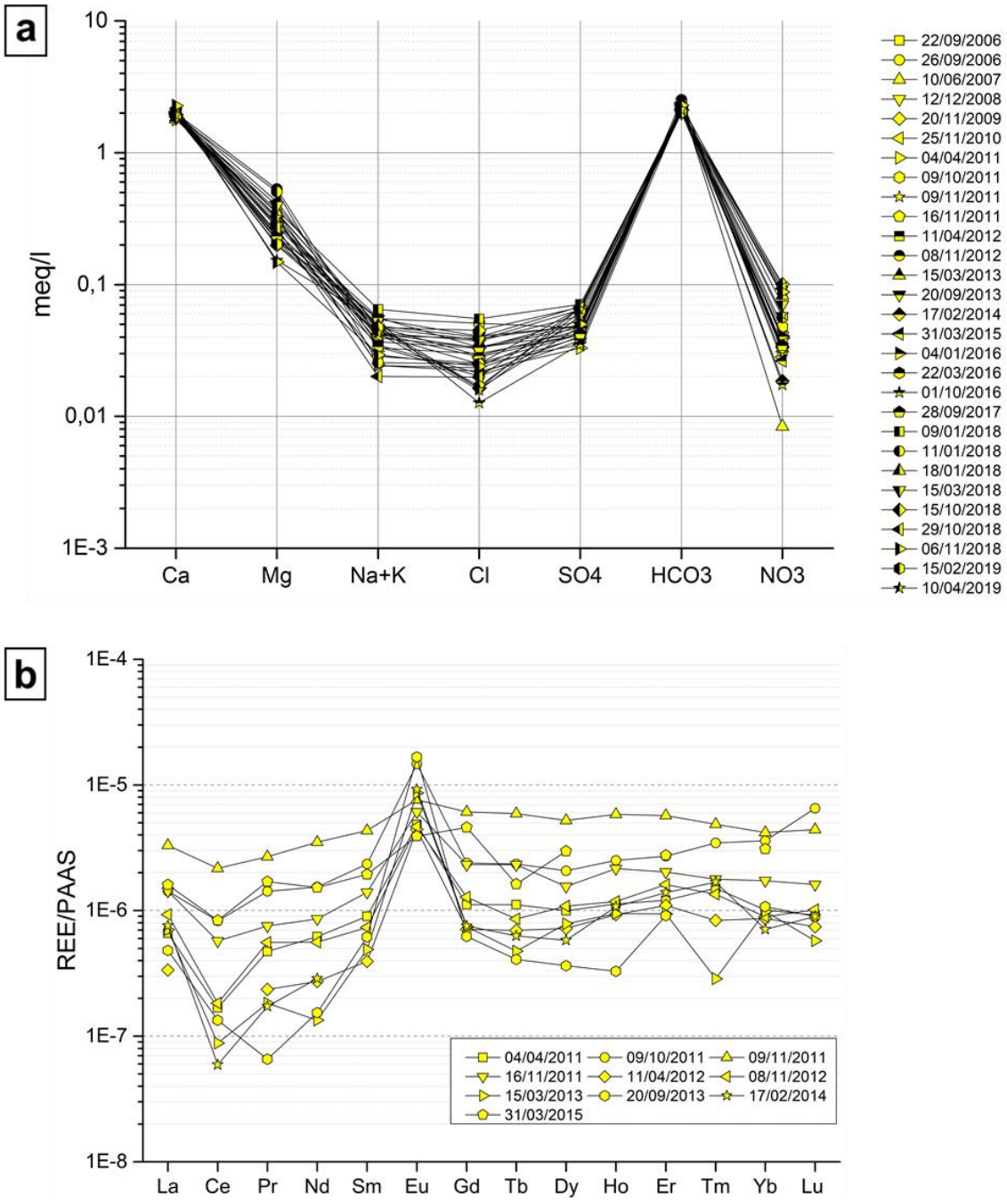

Fig. 5.11. *Mora* creek major component chemistry (a) and REE normalized values (b).

The *Sorgente dei Matti* spring showed a calcium-carbonate hydrochemical facies but it presented also relatively high concentrations of alkali that are of the same order of magnitude found for magnesium. Its medium value of solutes concentration is lower than any value observed in all Bossea outflows. The major components that exhibited the highest variability were magnesium, alkali, chloride and nitrate (Appendix 6). The most peculiar characteristic of this spring is the alkali to chloride ratio (Fig. 5.12).

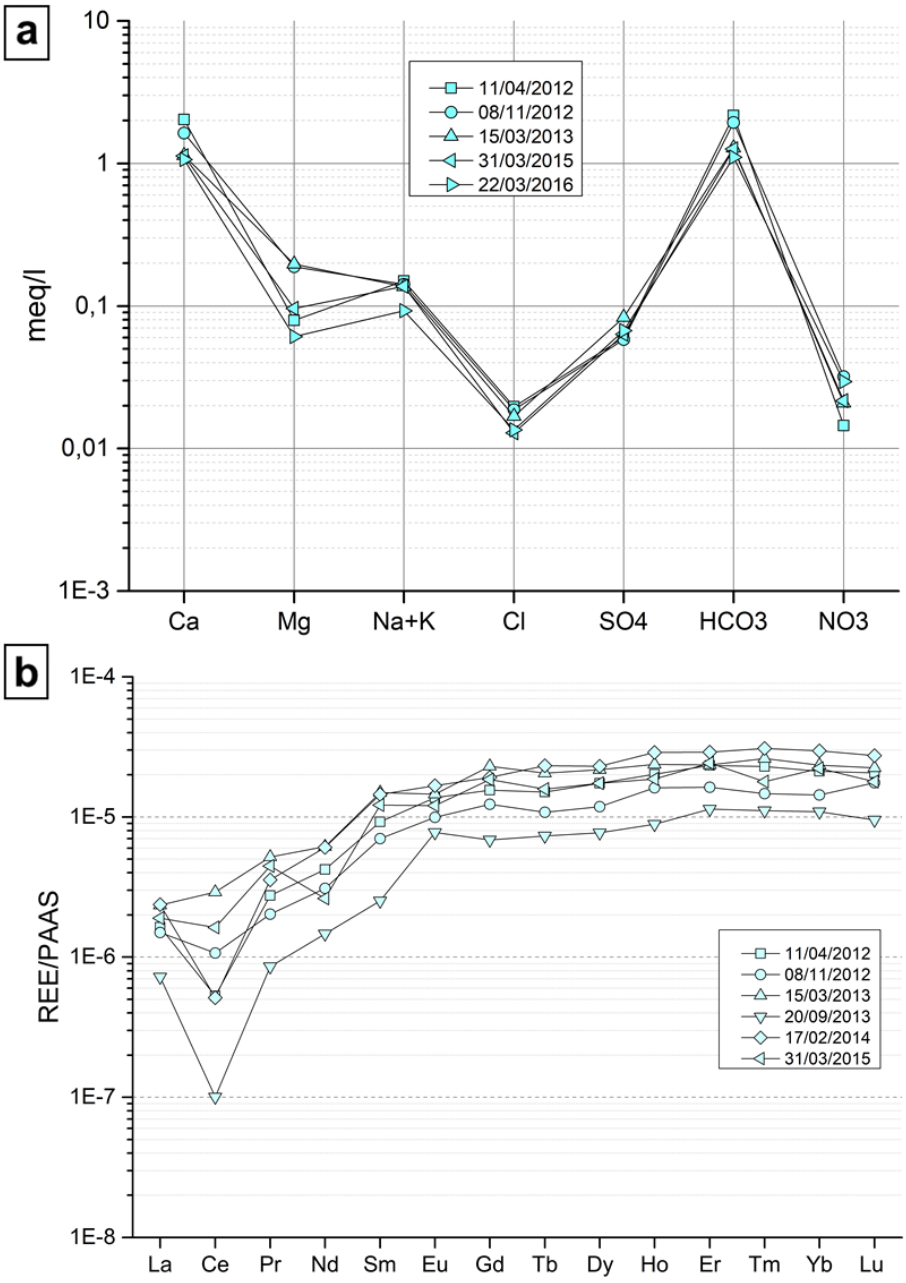

Fig. 5.12. Schoeller diagram (a) and spider diagram (b) reporting the composition of *Sorgente dei Matti* spring.

This ratio varied between 1.9 to 10.7 with a mean value of 7.6 that is significantly much higher than any other mean value observed in *Bossea* outflows. This high ratio is common to all the analyzed samples (Fig. 5.12a). Its trace elements content is similar to that measured in *Mora* creek and *polle* samples. Most samples are saturated in calcite whereas they can be either unsaturated or saturated respect to dolomite. The normalized rare earth elements patterns are characterized by a variable cerium negative anomaly and by the absence of a europium anomaly. The shape of the patterns shows a positive trend going from light rare earth elements

to Europium, after which the trends can be alternatively flat or with a slight positive slope going towards the heavy rare earth elements (Fig. 5.12b).

5.2.2. Water stable isotopes (^{18}O and ^{2}H)

Stable isotope analyses were performed on samples collected for all Bossea cave outflows that were described in Chapter 3, plus some rainfall samples. Overall, Bossea underground outflows showed isotopic composition ranging between -8.0 ‰ and -13.5 ‰ for $\delta^{18}O$ (V-SMOW), and between -55 ‰ and -93 ‰ for $\delta^{2}H$ (V-SMOW). However, each outflow exhibited its own stable isotope composition (Figs. 5.13, 5.14). The complete dataset of stable isotope analyses is reported in Appendix 7, whereas a statistical overview of the isotopic composition of the outflows and rainfall is reported in Appendix 8.

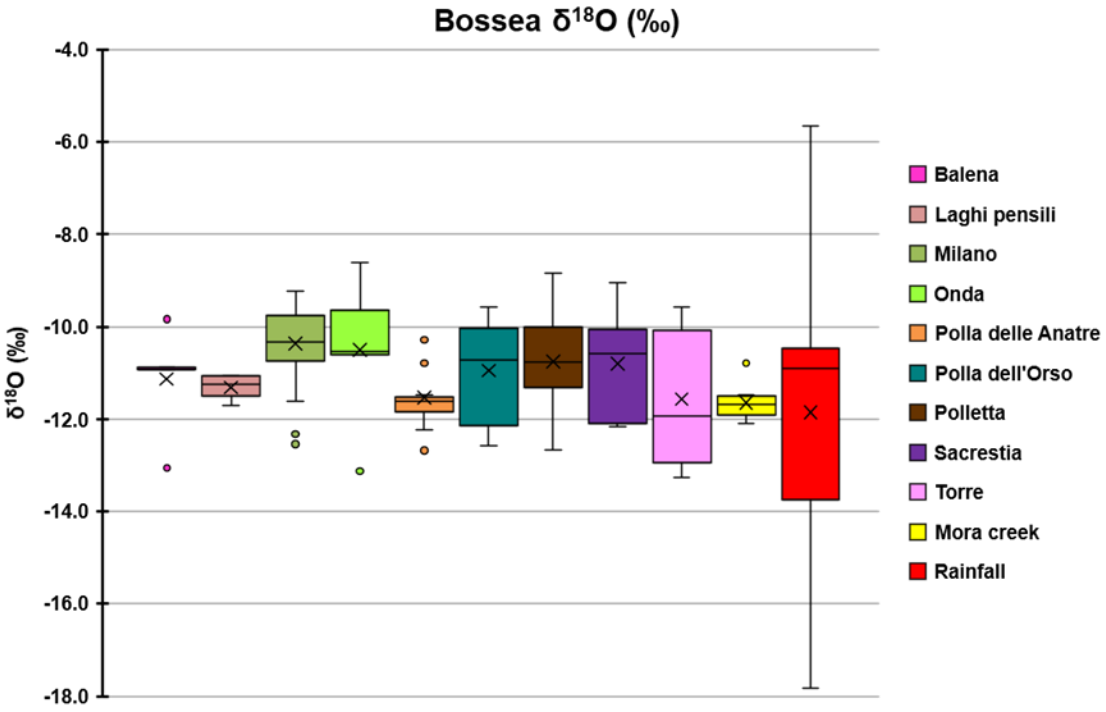

Fig. 5.13. Box plot reporting the results of $\delta^{18}O$ for all the monitored underground outflow of Bossea and of rainfall.

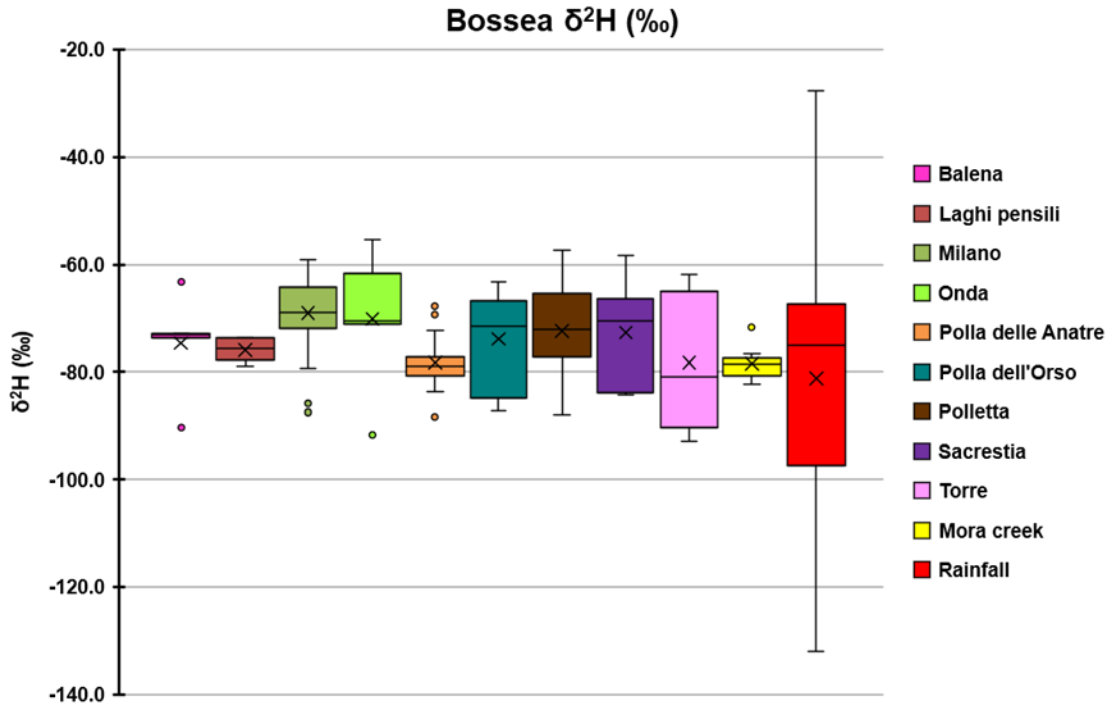

Fig. 5.14. Box plot with the results of δ^2H for all the monitored underground outflows of Bossea and of rainfall.

5.3. Discussion

5.3.1. Water chemistry and hydrodynamics

The sampling carried out in Bossea cave revealed a high heterogeneity in the system: each investigated underground outflow exhibited its own specific chemistry, although the general chemical composition is clearly calcium to calcium-magnesium bicarbonate. There are several factors that point to this heterogeneity: each outflow has its proper chemical signature, with specific proportion of major chemical compounds. Among the major chemical components, magnesium, alkali, chloride, sulfate and nitrate are extremely variable among the different inflows (Fig. 5.15). Magnesium is the first parameter to discriminate the outflows between calcium carbonate (*Polla delle anatre*, *Polla dell'orso*, *Sacrestia*, *Cancello* and *Mora* creek) and calcium-magnesium carbonate (*Milano*, *Balena*, *Laghi Pensili*, *Onda*, *Polletta*). The ratio of alkali over chloride is another useful parameter to make the distinction between the different outflows and for inferring contributions of water from different compartments of the system. A high value of this parameter can be explained by the arrival of water drained by fractures in the basement rocks (so from its -low- permeable portions), as testified by the chemical composition of *Sorgente dei Matti* spring: this spring can be considered as the compositional end member for "basement" water since its aquifer developed in the fractured portions of these rocks.

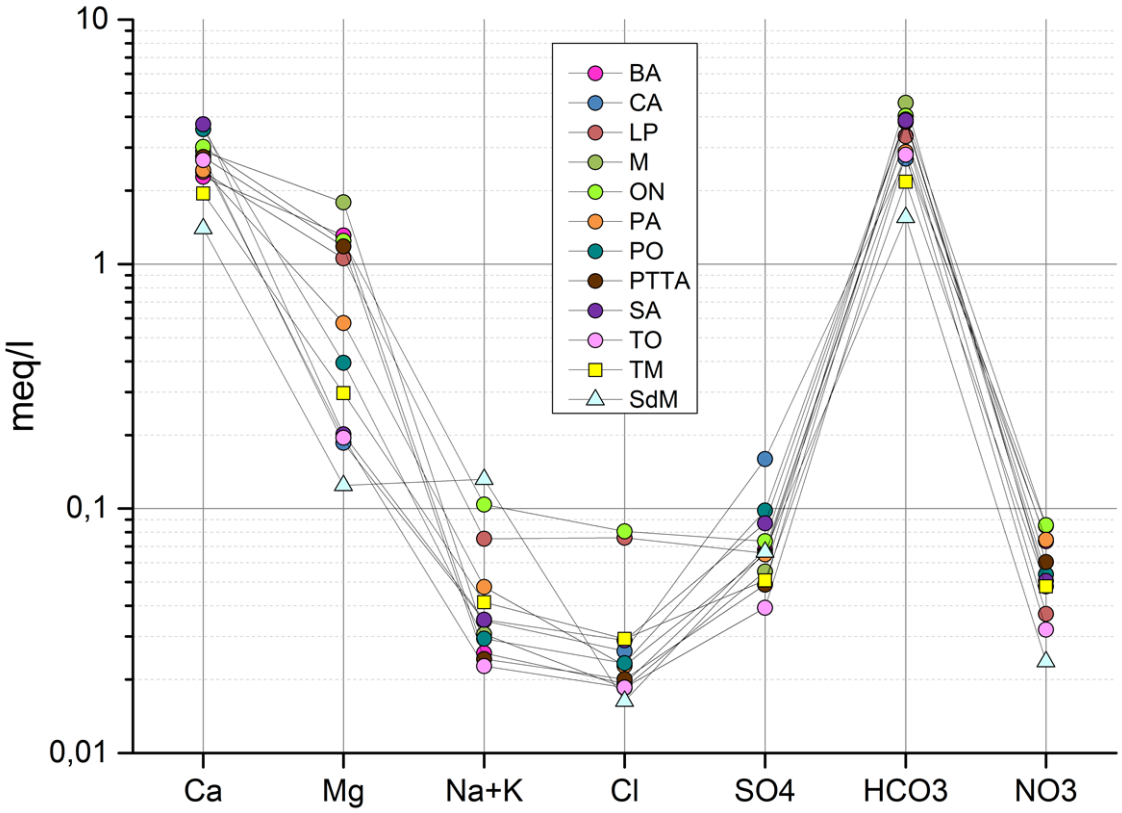

Fig. 5.15. Schoeller diagram that reports the mean composition of each investigated outflow.

The most peculiar feature of this hydrochemical end member is the very high value of the alkali to chloride ratio, representing a useful parameter for recognize inputs from the basement. Henceforth, it is not surprising that *Polla delle anatre* has, on average, the highest value for this ratio among the outflows monitored in Bossea cave. This inflow drains water from a perched aquifer that is partially developed in the bottom damage zone (i.e. in the metavolcanics of the basement) of the detachment described in the previous chapters, so it is expected that a clear basement signature is present in the *Polla delle anatre* water samples. It is instead unexpected that this basement signature is not that strong, on average, for *Polla dell'orso* and *Polletta*, although the mean value of this ratio is higher than the unit for both of them. Probably, the reduced metavolcanic signal is due to the small dimension of their recharge areas, so that the mixing with water percolated from the unsaturated zone is more efficient in masking the metavolcanics signal. The analysis of individual samples for each studied outflow revealed the occurrence of "basement" water input even in some of the outflows that are not placed near the detachment, although the magnitudes of these basement inputs are highly variable and overall lower than those observed for *Polla delle anatre*, at least looking only at the alkali/chloride

ratio. *Milano* drip site shows examples of inputs from the basement as demonstrated by the samples with high alkali/chloride and by the negative electrical conductivity peaks discussed in Chapter 3, in which this behavior was explained by the hypothesis that this drip site should have some connections with the so-called *Impermeable Complex*. The inputs from the *Impermeable Complex* are recognizable also in some water samples of *Torre* drip site. Again, as already discussed in Chapter 3, this drip should receive water also from the detached portions of basement rocks that outcrop in the cave sector where this drip is located, so the occurrence of non-carbonate inputs is not unexpected. Basement water inputs are possible also for other drip sites, although with a lower recurrence. The underground river receives non-carbonate inputs as well and this is confirmed by the alkali/chloride ratio of many samples (see also Chapter 6 for an example). The normalized pattern of the rare earth elements are also useful to infer the chemical signature of the discharged waters (Banks et al., 1999; Biddau et al., 2009; Gill et al., 2018). The spider diagram of the mean normalized REE concentrations to PAAS confirms that each outflow has its specific chemical composition that should be related to the drainage of different fracture networks in different portions of the system (Fig. 5.16). Most of the outflows present a carbonate mean composition but *Polletta* and *Torre* show mean patterns that partially resemble the one of *Sorgente dei Matti* spring. *Polla delle anatre* presents a carbonate pattern in which the basement fingerprint could be represented by the positive slope of the overall trend (Fig. 5.16). Again, an examination of all the patterns of a specific outflow confirms that there are inputs from the non-carbonate lithologies for most of the studied outflows with different timing and frequency from one site to another.

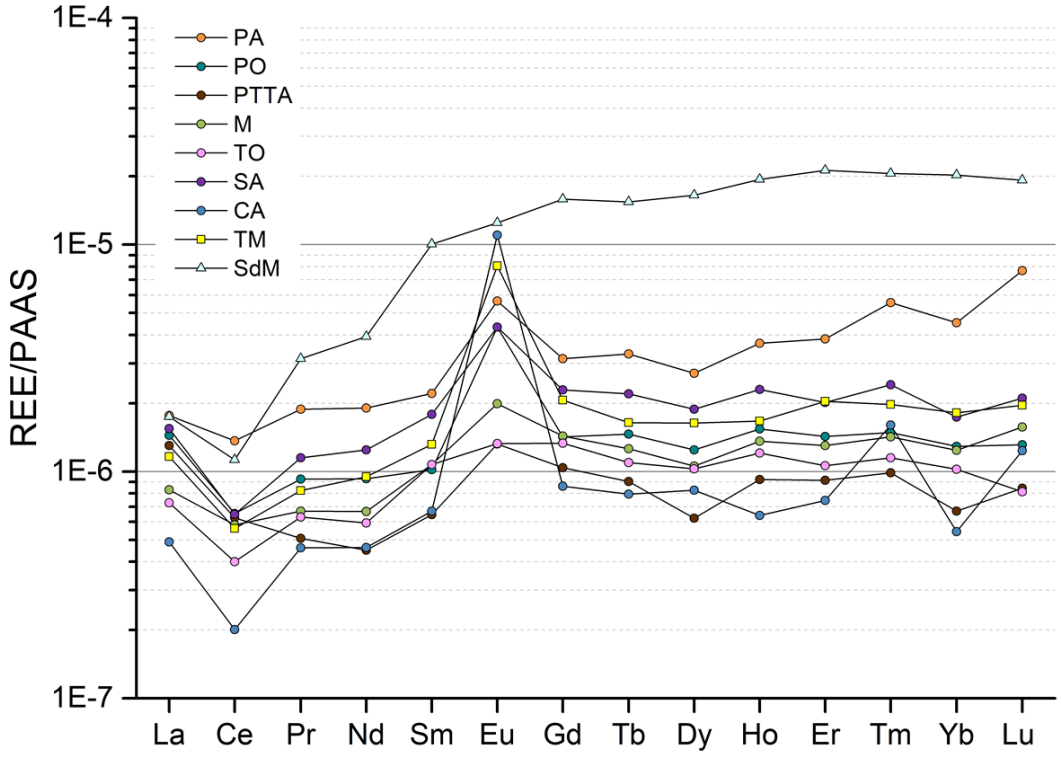

Fig. 5.16. Mean REE normalized patterns for each studied outflow.

The heterogeneities of the system and the variable contribution of different compartments of the feeding system to each outflow seems to be evident also comparing the ratio between some trace elements such as Barium and Strontium, and Calcium (Fig. 5.17). *Mora* creek tributaries seem to align on a certain trend ("trib. Trend"; Fig. 5.17) whereas the underground river samples seem to depict another trend ("TM trend"), with *Polla delle anatre* lying somewhat mid-way between the two trends. Each outflow sample tends to cluster in their own specific section of the trend (although with some interpositions), but it is interesting to observe the behavior of *Mora* creek samples. The samples labelled "TM 11/2016 prPF/trPF/PF/pPF" represent the different time intervals of a flood event, respectively, the interval before peak flow, the transition to peak flow, the peak flow and finally the post peak flow situation (recession limb). The first two phases are aligned on the *Mora* creek trend, then the composition tends to progressively cluster close to the trend of the tributaries. This could be an indication of an enhanced contribution of the fractured unsaturated zone to TM flow during the recession phase (see Chapter 6 for a detailed analysis of said flood event).

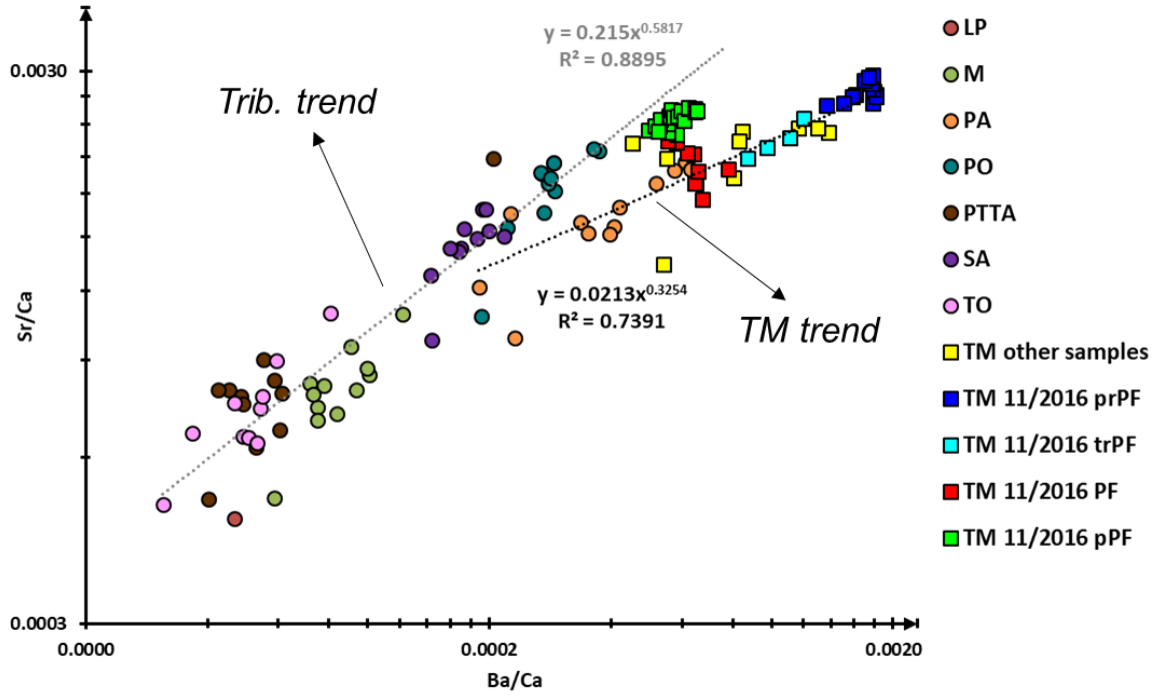

Fig. 5.17. Barium to calcium ratio against strontium to calcium ratio for some of the studied outflows. The secondary tributaries were selected according to the number of sample available (i.e. those with zero to 2 data were not considered because not statistically relevant).

Finally, the heterogeneities of the system and the fact that each outflow drains a different fracture network is highlighted also by the comparison of calcite and dolomite saturation indexes (Fig. 5.18). Initially the data were plotted together, ignoring the distinction between the outflows, and the outcome was a poor correlation between the two saturation indexes. Conversely, once the data were plotted separating samples of different outflows, the correlation between the two indices is good for almost all the studied outflows, the only exception being *Sacrestia* drip site (Fig. 5.18).

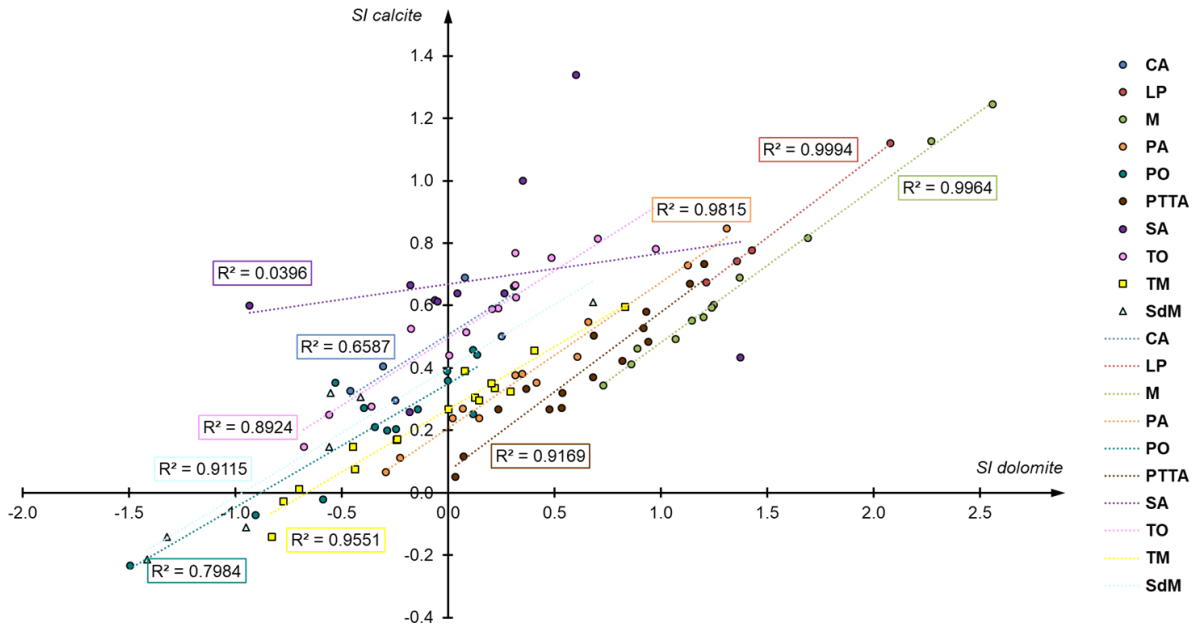

Fig. 5.18. Comparison of calcite and dolomite saturation indexes for each studied outflow. The dotted lines represent the correlation line for each group of samples with the corresponding R^2 reported.

5.3.2. Stable isotopes and discharge dynamics

The stable isotope data collected in the outflows of Bossea cave (underground river and its tributaries) and rainfall data collected on the slope above Bossea cave were plotted on the δ^2H-$\delta^{18}O$ plot. All samples fit well with the *Western Mediterranean Meteoric Water Line* (Celle, 2000), pointing to the Western Mediterranean Sea as principal source of the moisture that originated the rainfall infiltrating in the karst system. The influence of air masses of Mediterranean origin have been recognized by other authors (Bortolami et al., 1979; Celle-Jeanton et al., 2001; Longinelli and Selmo, 2003). The underground outflows show a relatively low variability in the $\delta^{18}O$ composition (range of variation broadly of 3 ‰), whereas rainfall isotopic composition is much more variable, even considering samples collected in the same month (a 16 ‰ of variability range was observed). This points to a homogenization effect of the unsaturated zone on the rainfall signal. This phenomenon has been recognized in many karst systems (Lachniet, 2009). However, it is still possible to recognize a seasonality in the fluctuations of the isotopic composition for all the studied sites (Fig. 5.20). It is interesting to note that the underground river is, together with *Balena* drip the most constant outflow in terms of isotopic signal, followed by *Polla delle anatre* and *Laghi pensili*. The other secondary tributaries show a relatively higher variability. The lower variability of *Mora* creek isotopic

signal could be related to the fact that this underground river collects input from the whole catchment so an efficient mixing of all the inflows can be expected.

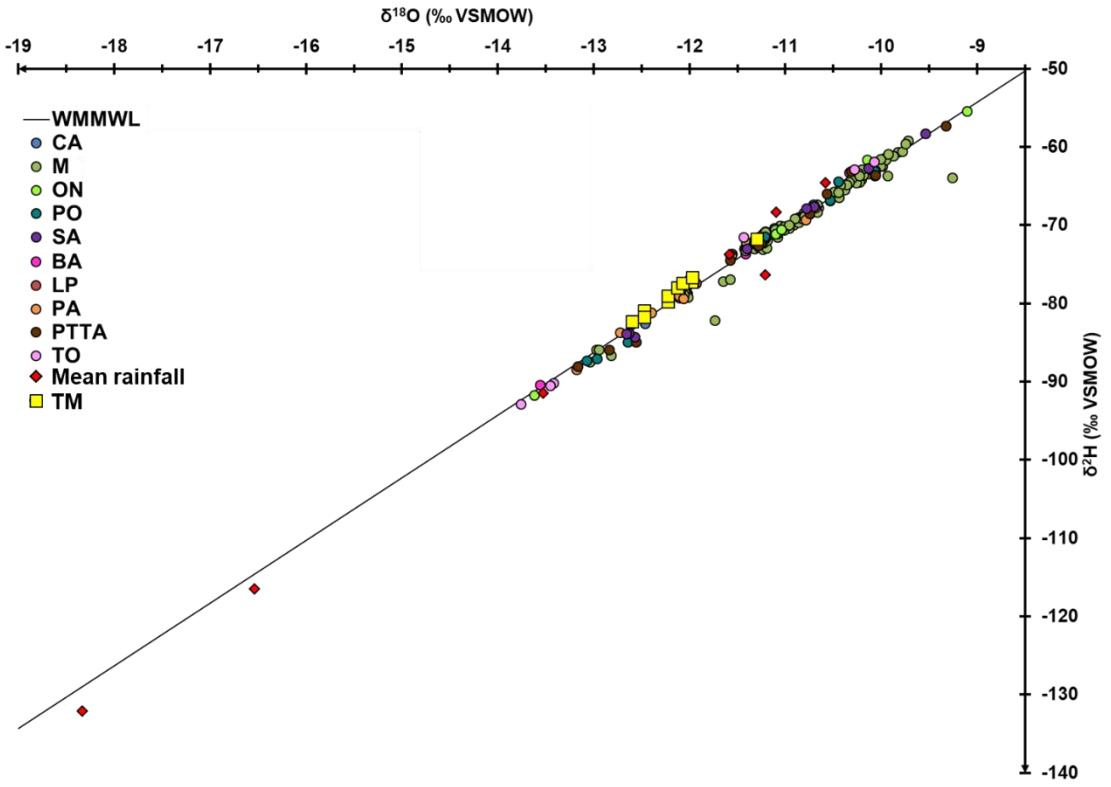

Fig. 5.19. $\delta^{18}O$ vs $\delta^{2}H$ data for Bossea and rainfall samples.

The comparison of the isotopic composition observed in *Milano* drip site during the 2018 Fall and the 2019 Spring discrete monitoring with the compositions found for the other outflows highlight the non-linearity in the hydrodynamic behavior of *Milano* drip: it showed an impulsive response of the isotopic signal to three consecutive precipitation events and the variability of $\delta^{18}O$ during these three events is almost of the same magnitude of the overall range of composition for the whole dataset. On the contrary, the compositional range found during Spring 2019 for *Milano* was reduced to less than 0.5 ‰. Moreover, *Milano* Spring 2019 composition is heavier than the values observed for the same drip site during the previous spring season (Fig. 5.20). The heavier composition in Spring 2019 than that of Spring 2018 should be simply related to the normal seasonal fluctuations of the isotopic input signal (i.e. precipitations), since this difference is observed for all the monitored outflows. The unresponsive behavior of the isotopes during the Spring 2019 monitoring interval (Fig. 5.21b) could be explained by a good homogenization of the input signal after the heavy precipitations of November to December 2018. On the contrary, the isotopic composition mirrored perfectly

the discharge trend of *Milano* during Fall 2018 (Fig. 5.21a), a perfect example of drip non-linearity, like the ones described by Doctor et al. (2015).

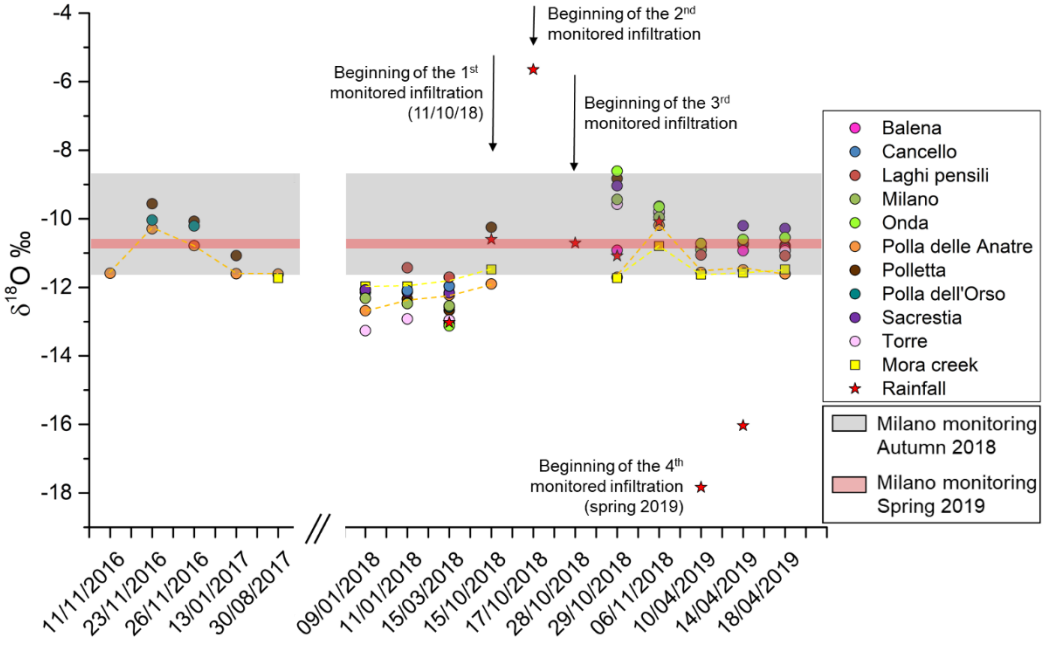

Fig. 5.20. $\delta^{18}O$ variation through the samplings carried out. The compositional ranges of variation of Milano Fall 2018 and Spring 2019 are reported as well.

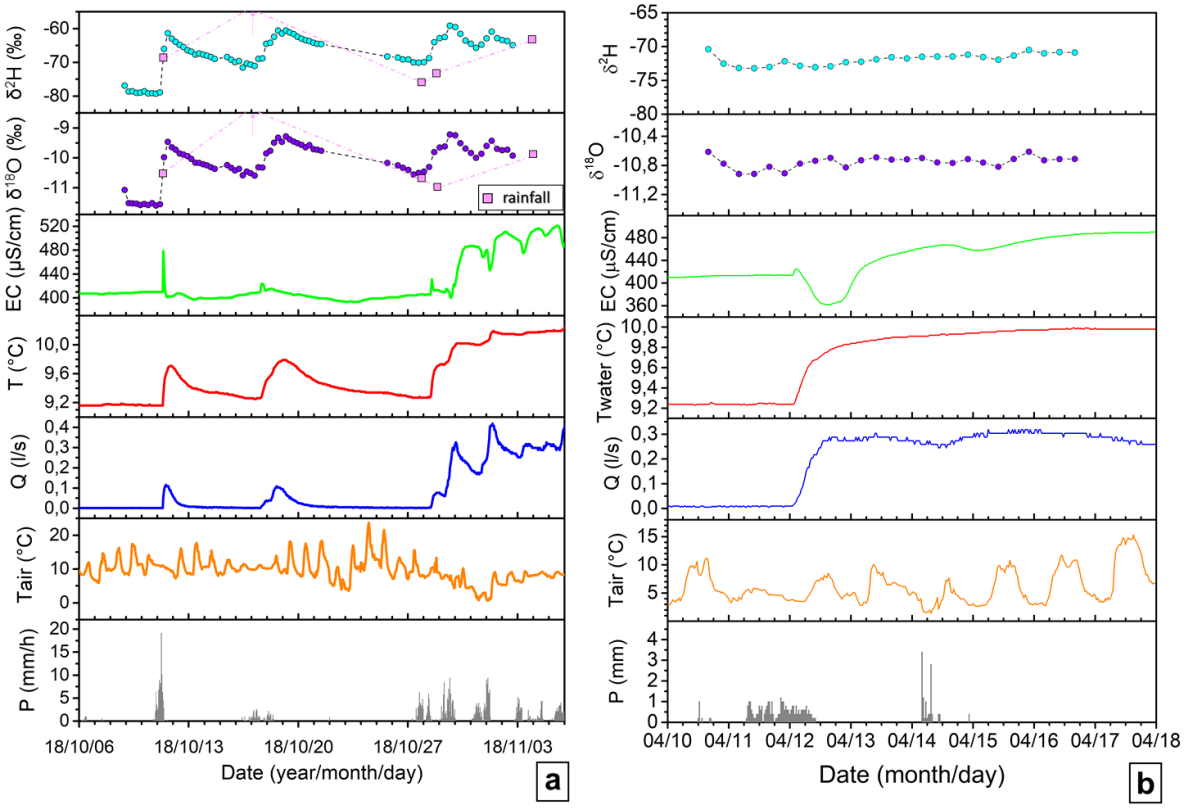

Fig. 5.21. *Milano* automatic monitoring during Fall 2018 (a) and Spring 2019 (b).

5.4. Concluding remarks

The hydrochemical investigations carried out in *Bossea* confirmed the complexity of the system discovered with the hydrological monitoring reported in Chapter 3. The major chemistry analysis was helpful for distinguishing the hydrochemical facies of each outflow (thanks to the Mg/Ca ratio) but also for recognizing the episodic inputs of non-carbonate water in most of the studied sites. Lanthanides helped as well to recognize the contribution of "basement" water to each outflow. These chemical analyses suggest a spatial (from a discharge point to another) and temporal variation (for each outflow) that, coupled with the saturation indices points to a strong system heterogeneity and complexity.

The stable isotopes showed that despite the homogenization effect of the unsaturated zone, a seasonal oscillation is observed in all outflows, although the underground river is more stable than the other sites. The semi-continuous monitoring of *Milano* drip site revealed a bimodal behavior, at least for the specific hydrological year: strong, impulsive response to precipitations in Fall, and unresponsive in Spring.

Further investigations on the hydrochemistry of *Bossea* system unsaturated zone could focus on the application of multivariate statistical analysis such as Hierarchical Cluster Analysis (HCA) and Principal Component Analysis (PCA). These methods are frequently used to study water quality and solute transport in both stream water and groundwater (Vega et al., 1998; Güler et al., 2002; Helstrup et al., 2007; Belkhiri et al., 2011; Wu et al., 2014). Recently, HCA and PCA were successfully applied together to identify and rank the processes associated to the hydrochemical variability of different flow outlets from the unsaturated zone of a karst system (Barbel-Périneau et al., 2019). A clear influence of the hydrodynamic behavior on the hydrochemical signature of each studied outflow was evidenced. A similar approach could be hence useful in a system such as *Bossea*'s, where the heterogeneity of flow in the unsaturated zone is evident.

Chapter 6: Effects of an extreme flood event on Bossea karst system

6.1. Objectives

The main goal of this chapter is to unravel the hydrodynamic behavior of a structurally complex karst system such as *Bossea Cave* during an extreme precipitation event like the one happened in November 2016, and to recognize the different contributions to unsaturated flow and to the main underground river from the distinct hydrogeological compartments of the catchment. The investigation was carried out by means of continuous and discrete hydrological and hydrochemical monitoring of some of *Mora* creek secondary tributaries described in Chapter 3 (drip sites and spill points) and of the main underground river itself.

6.2. The November 2016 flood event and previous floods

On 21st-25th November 2016 western and southern Piedmont were affected by strong precipitations. Heavy rainfall struck the southern Piedmont first (November 22nd-23rd) and then reached the western sectors of the Italian region. A mean value of 357 mm of precipitation was recorded in the *Tanaro* basin (*Corsaglia* river being one of its tributaries). The highest precipitation value (632.6 mm) was recorded in the uppermost section of *Tanaro* valley and it corresponds to more than 50% of the average yearly rainfall. Precipitation events of this magnitude have a recurrence interval of 200 years in Southern Piedmont (Arpa Piemonte and Regione Piemonte, 2018). Several floods and related landslides occurred, the strongest events of which were located in the *Tanaro* tributary valleys. The *Corsaglia* river flooded at several points along its pathway, causing several landslides and destroying the valley's main road. This event also caused one of the strongest flood events in the *Bossea* cave, similar to the one happened in October 1996. This latter event was caused by the obstruction of the syphons by fine sediments that started to accumulate in the system due to a building site in the recharge area (Peano et al., 2005).

Corsaglia valley major precipitation events

	1994/11	1996/10	1997/11	2011/11	2016/11
duration (days)	4	2	2	6	5
total rainfall (mm)	216.8	208.2	190	424.4	501
max daily rainfall (mm)	166.8	122.6	160.6	118.8	**246.4**

Storm 2011/11 daily rainfall

day	**03/11/2011**	**04/11/2011**	**05/11/2011**	**06/11/2011**	**07/11/2011**	**08/11/2011**
mm	33.20	98.60	118.80	101.20	21.40	51.20

Flood 2016/11 daily rainfall

day	**21/11/2016**	**22/11/2016**	**23/11/2016**	**24/11/2016**	**25/11/2016**
mm	109.6	38.0	79.8	246.4	27.2

	2011	**2016**	
total yearly rainfall	1279.8	1587.2	mm
total november rainfall	437.0	551.8	mm
Mean total rainfall per year	1409.5		mm

Tab 6.1. Overview of the major precipitation events occurred in *Corsaglia* valley recorded by *Borello* meteorological station (1,5 km S to the cave).

During the 2016 exceptional event the highest daily total amount of rainfall was registered (Tab. 6.1) and it represents 16% of the 2016 total amount of rainfall whereas the total amount of rainfall fallen during the flood constitutes one third of the 2016 rainfall.

The storm of November 2011 was characterized by about 425 mm of total amount of rainfall, less (but similar) than the one registered during the flood of 2016; however, the precipitation event lasted longer and, more importantly, the daily rainfall amount was less than half the one recorded in November 2016 and was lower than the ones recorded during other floods in the *Corsaglia* valley (Tab. 6.1. Arpa Piemonte, 2011).

6.3 Materials and methods

Monitoring devices were placed below some inflows and along the main underground river to monitor their hydrological behavior (Fig. 6.1). The main underground river (*Torrente Mora*, TM) was equipped with multiparametric devices and data loggers for water level (L), temperature (T) and electrical conductivity (EC). Three water samples were collected for hydrochemical analyses before, during and after the November 2011 storm event, respectively. An automatic water sampler (ISCO model 2900 sampler, ISCO Inc.) was installed during the 2016 flood event for hydrochemical monitoring. A time step of 6 hours was selected as

sampling frequency; the sampling started on 20th of November and ended on 2nd of December (the flood peak happened on the fourth sampling day and ended the following day).

One of the brooks that feed the karst system (*Roccia Bianca*, RB) was monitored during the 2016 flood. Water level and temperature were recorded by means of a multiparametric sensor. The secondary tributaries that have the highest discharges (up to 2 l/s) were equipped with concrete weirs and multiparametric loggers for water level (L), Temperature (T) and Electrical Conductivity (EC) were placed in the pools created upstream of the weirs. The loggers record 1 to 4 measurements per hour. *Milano* (M), *Polletta* (PTTA) and *Sacrestia* (SA) dripsites were monitored during both the 2011 and 2016 events whereas *Polla delle Anatre* (PA), *Torre* (TO) and *Cancello* (CA) dripsites were monitored only during the November 2016 flood. Because of their low discharge (less than 1 l/min), water height (R) is the only parameter monitored for CA and SA by means of drip gauges placed below funnels that collected water from the small dripping points. Water samples were collected for hydrochemical analysis from the drip sites before, during and after the 2011 storm and the 2016 flood events. Two water samples were collected for each inflow, one was taken in a 500-ml bottle for major ion content, the other one contained 100 ml of water that was acidified in situ with HNO_3 (65%) for the determination of metals and lanthanides contents. Each sample was sealed and kept refrigerated. Sample temperature, pH and EC were measured in situ with a multiparametric device. The samples collected by the automatic sampler used 500 ml bottles and 100 ml were taken from each bottle and acidified with the same procedure and purpose for the 100 ml drip water sample. The first 24 samples were taken from the automatic sampler after six days of sampling and the following 24 samples were collected at the end of the monitoring. The water samples were brought to the Department of Environment, Land and Infrastructure Engineering (DIATI), Polytechnic of Turin (Italy). The determination of Ca^{2+}, Mg^{2+} was carried out by means of ion-selective electrode, HCO_3^- was determined by acid-base titration with instrumental control of pH. Anion concentrations were determined by ion chromatography (Metrohm 881bIC Pro). Na^+ and K^+ were determined by Atomic Absorption Spectroscopy (AAS Shimadzu); NH_4^+ was analyzed by UV-VIS spectrophotometry. An X Series 2 ICP-MS (Thermo Scientific) was employed for metal and lanthanide determination. The detection limit for ion chromatography and titration is 0.1 mg/l, whereas it is 0.05 mg/l for AAS. The detection limit is 2 ppb for metals and 5 ppt for the lanthanides. The analytical error for the chemical analyses were below 5%. The lanthanide concentrations were normalized to the Post Archean Australian Shale (PAAS, McLennan,

1989). The hydrochemical composition of a nearby spring was taken as reference of the non-carbonatic water drained from the impermeable complex (*Sorgente dei Matti* spring, SdM). Rainfall amount and air temperature data were collected by the *Borello* meteorological station of the Piedmont Regional Agency for Environmental Protection (ARPA). This meteorological station is located a km and half away from the cave at an altitude of 1005 m asl. It is equipped with a rain gauge PMB2/R – CAE.

The choice of the inflows to investigate was made in function of the whole dataset available for each inflow and depending on their location: *Polla delle Anatre* and *Polletta* spill points developed along the detachment between the Mesozoic carbonate sequence and the underlying Permian metavolcanics, *Milano* and *Torre* drip discharge along bedding surfaces in the carbonate sequence, whereas *Sacrestia* and *Cancello* are fed by small clusters of fractures in the Mesozoic sequence.

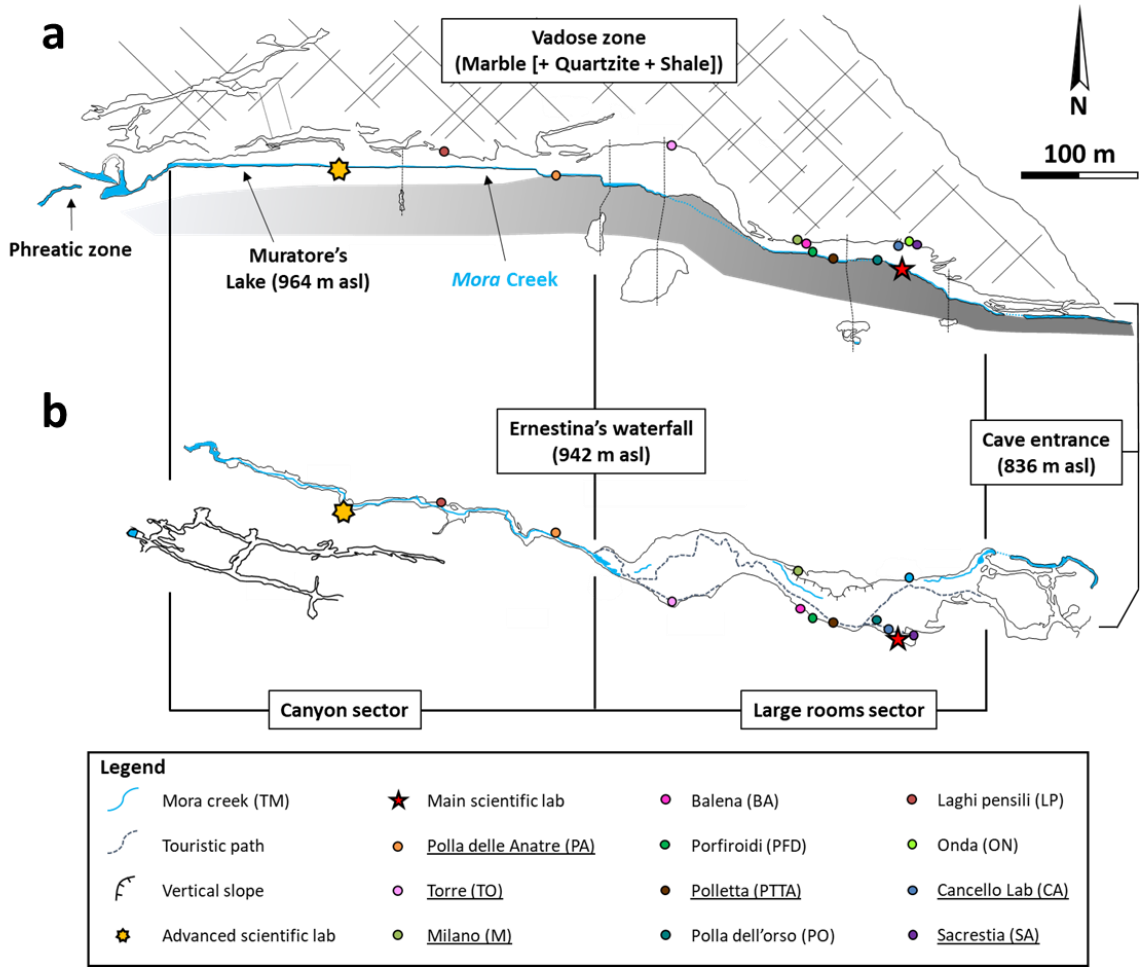

Fig. 6.1. Cross-section (a) and plan view (b) of the *Bossea* show cave. The colored dots mark the position of the secondary tributaries. The name of the inflows investigated in this study are underlined.

6.4. Results

6.4.1 Mora creek 2011 and 2016 monitoring

The results of the monitoring of *Mora* creek and *Roccia Bianca* brook are summarized in Tab. 6.2, whereas the hydrographs and the chemographs of physico-chemical parameters are reported in Fig. 6.2. Major ion chemistry results are represented in a Schoeller diagram for both events (Fig. 6.3) but, for better clarity, the range of variability for each major ion is represented in the diagram instead of each individual composition (48 samples) for the 2016 flood.

	TM			RB†		
	Q*	T**	EC**	L	T	
	l/s	°C	µS/cm	cm	°C	
Mean	177.9	7.53	219.6	18.9	8.53	**mean**
Median	124.7	7.55	218.0	15.8	8.50	
Min	33.8	6.74	196.0	11.5	5.20	
Max	1960.2	7.92	265.0	129.8	13.80	
Mean	263.8	7.62	220.8	-	-	**2011**
Range	1541.7	0.40	22.0	-	-	
Min	66.6	7.45	214.0	-	-	
Max (Flood peak)	1608.3	7.85	236.0	-	-	
Mean	280.9	7.5	225.2	22.7	9.13	**2016**
Range	1877.4	0.3	23.0	117.1	4.40	
Min	82.9	7.4	217.0	12.7	7.50	
Max (Flood peak)	1960.2	7.7	240.0	129.8	11.90	

time intervals for mean values calulations: * 1982 - 2019; ** 2008 - 2019

† hydrological year 2016-2017

Tab. 6.2. Statistical summary of *Mora* creek and *Roccia Bianca* brook hydrological and physico-chemical monitoring during the floods. Mean values of each parameter for the two streams are reported for comparison.

The 2011 storm event started on the 3rd of November and ended five days later, with highest daily amount of rain recorded on November 5th. The underground river (Fig. 6.2a) reached its peak flow on the morning of November 6th, approximately one day and a half after the peak of hourly precipitation (17,4 mm on November 4th late afternoon). After the peak flow, the recession limb of the hydrograph was perturbed by precipitation (November 8th-9th), then the flow returned to normal values in approximately 8 days. Water temperature started to decrease when water flow began to rise. After the peak flow, T rose continuously but slowly, and it didn't return to pre-storm values for more than 3 months. Electrical conductivity showed first a sharp decrease during the rising limb of flow, then it started to increase to reach its maximum on November 13th, returning to pre-storm values 2 weeks after.

The maximum hourly rainfall amount of November 2016 was recorded on the morning of the 24th that is also the day during which the highest precipitation amount fell. TM discharge showed a first flow peak an hour after the maximum hourly rainfall and reached its maximum peak flow 14 hours later (2016/11/24 23:00, Fig. 6.2b). The discharge returned to low-flow values approximately a week after the maximum flood peak. Water temperature decreased immediately with the beginning of flow increase, then it showed a small positive peak during the two flow peaks. It reached its minimum in the middle of the hydrograph recession limb, then started to slowly increase and it almost returned to pre-flood values at the beginning of February 2017. Electrical conductivity varied in a more complex way during the flood. It first increased sharply, reaching its maximum 16 hours before the first flood peak, then it showed a pronounced negative peak simultaneously to the maximum flood peak. It increased again during the hydrograph recession limb but slower than the antecedent peaks, reaching almost the same value occurred during the hydrograph rising limb, then it slowly decreased and came back to pre-flood values at the end of December 2016.

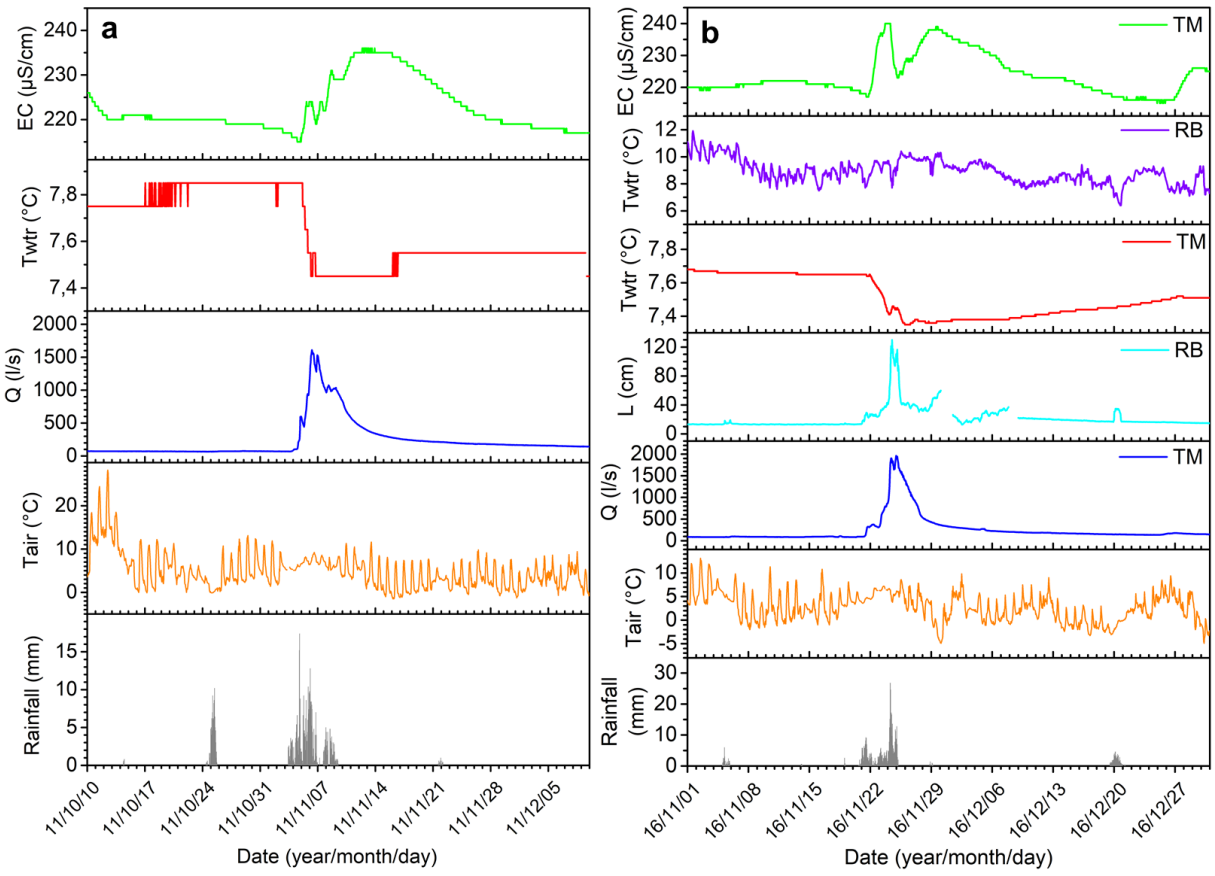

Fig. 6.2. (a) *Mora* creek hydrograph and chemographs (T, EC) during November 2011 monitoring. (b) *Mora* creek (TM) and *Roccia Bianca* brook (RB) hydrographs and chemographs during the November 2016 flood. Rainfall and air temperature measured by *Borello* meteorological station are reported for both precipitation events.

Roccia Bianca (RB, Fig. 6.2b) water level started to increase simultaneously to the onset of precipitation and reached its maximum on November 24th morning, 4 hours after the precipitation maximum. Water level then started to decrease but it rose again to a secondary level peak during the last abundant rainfall occurred in the first hours of November 25th. Then, water level sharply decreased until November 29th when some weak snow precipitation occurred and determined an increase of RB level. Water temperature fluctuation matched those of water level and air temperature: it sharply decreased during flow peaks and air temperature minimum, while it rose in concomitance of T air maximum and water level decreases.

The chemical analyses revealed that the *Mora* creek water samples is overall of the bicarbonate-calcic type for both the studied events (Fig. 6.3). The highest variability is presented by magnesium cation and even more by the less abundant ions (alkali, chloride, sulfate and nitrate ions).

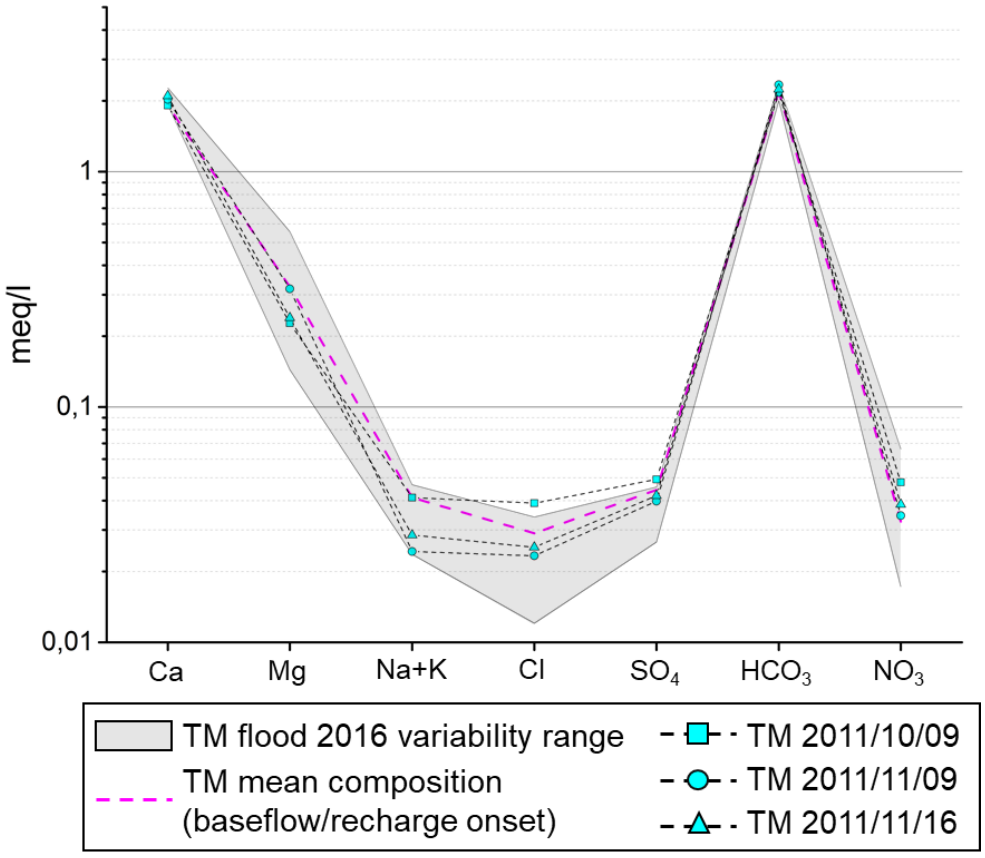

Fig. 6.3. Schoeller diagram of *Mora* creek hydrochemical composition during the 2011 and 2016 flood events. The composition of each individual sampling for 2016 monitoring is replaced by the range of variability of each major ion.

The summary statistics of the concentration of the most relevant trace elements (Al, Mn, Fe, Rb, Sr and Ba) and lanthanides is reported in Tab. 6.3. The data collected in 2011 shows much less variability than the 2016 ones but they fit in the same range of composition.

	2011					2016				
	min	max	mean	median	range	min	max	mean	median	range
Al	5.31	16.37	10.60	10.13	11.06	0.69	57.11	13.68	6.1	56.4
Mn	0.78	4.91	2.31	1.25	4.14	0.14	14.25	2.54	0.7	14.1
Fe	0.00	4.03	1.34	0.00	4.03	0.00	48.04	6.29	0.6	48.0
Rb	0.34	0.86	0.52	0.37	0.52	0.26	0.85	0.48	0.4	0.6
Sr	90.01	105.50	96.23	93.17	15.49	68.64	113.80	101.29	106.0	45.2
Ba	18.34	68.60	37.14	24.48	50.26	22.09	70.67	35.94	26.0	48.6
La	54.56	126.20	78.48	54.68	71.64	37.31	790.50	178.69	98.6	753.2
Ce	45.57	172.90	94.81	65.95	127.33	41.05	753.70	161.83	80.0	712.7
Pr	6.65	23.67	14.29	12.54	17.02	8.20	175.20	40.45	23.0	167.0
Nd	29.09	119.00	66.77	52.23	89.91	32.97	729.80	167.86	95.5	696.8
Sm	7.76	24.04	14.95	13.06	16.28	5.47	156.60	36.13	20.3	151.1
Eu	6.59	15.84	10.23	8.25	9.25	4.64	39.16	12.46	9.7	34.5
Gd	10.81	28.48	16.82	11.17	17.67	5.63	180.40	39.21	20.3	174.8
Tb	1.79	4.58	2.73	1.82	2.79	0.68	29.16	5.82	2.6	28.5
Dy	7.29	24.43	13.81	9.73	17.14	5.87	153.00	35.45	17.6	147.1
Ho	2.14	5.79	3.47	2.49	3.65	1.43	30.73	7.04	3.4	29.3
Er	5.77	16.29	9.92	7.71	10.52	4.72	93.01	20.60	10.5	88.3
Tm	0.72	1.97	1.37	1.40	1.25	0.75	11.61	2.99	1.6	10.9
Yb	4.87	11.82	8.94	10.14	6.95	3.86	69.30	16.17	8.6	65.4
Lu	0.70	2.83	1.81	1.91	2.13	0.36	9.40	2.31	1.3	9.0
ΣREE	184.44	569.33	338.41	261.46	384.90	170.47	3221.57	726.99	385.7	3051.1

Tab. 6.3. Summary statistics of trace element concentrations during the 2011 storm and 2016 flood. Al, Mn, Fe, Rb, Sr and Ba are reported in ppb, lanthanides in ppt.

6.4.2 Secondary inflows hydrologic and hydrochemical monitoring

The summary statistics of the hydrological and physico-chemical parameters of the inltes monitored during the two recharge events are reported in Table 6.4. Mean values for each inflow are reported for comparison and these average values were calculated with data collected in the last 10 years, except for *Torre* drip site (TO) for which different time intervals were considered. The hydrographs and the chemographs of each drip monitored in the 2011 storm and 2016 flood are reported in Fig. 6.4. Each secondary inflow showed a specific range of variability for all the considered parameters.

Milano drip (M, Tab.6.4, Fig. 6.4a, b) reached its highest ever values for discharge and water temperature during the November 2016 flood but its mineralization was in the standard range of variability characteristic for this drip.

Hydrologic summary															
	M			PA			PTTA			TO			CA	SA	
	Q	T	EC	Q	T	EC	Q	T	EC	Q*	T**	EC**	R	R	
	l/s	°C	µS/cm	l/s	°C	µS/cm	l/s	°C	µS/cm	l/min	°C	µS/cm	mm	mm	
Mean	0.04	9.55	411.1	0.029	9.97	275.2	0.01	9.46	338.5	0.3	9.18	284.6	1.71	1.3	**mean**
Median	0.005	9.33	411.0	0.002	9.95	270.0	$<10^{-4}$	9.35	339.0	0.1	9.10	284.0	0.80	0.0	
Min	0.00	9.10	286.8	0.000	9.92	255.1	0.00	9.09	215.0	0.0	8.90	258.0	0.00	0.0	
Max	0.54	10.60	536.0	1.89	11.08	353.0	0.33	10.65	456.0	2.1	11.03	312.2	56.2	236.2	
Mean	0.003	9.43	391.88	-	-	-	0.02	9.45	-	-	-	-	-	1.6	**2011**
Range	0.16	1.30	101.00	-	-	-	0.33	1.50	-	-	-	-	-	23.2	
Min	0.00	9.10	321.00	-	-	-	0.00	9.15	-	-	-	-	-	0.0	
Flood peak	0.16	10.40	422.00	-	-	-	0.33	10.65	-	-	-	-	-	23.2	
Mean	0.09	9.66	405.35	0.06	10.02	272.8	0.01	9.49	334.1	-	9.27	289.69	6.8	9.5	**2016**
Range	0.54	1.40	127.00	1.89	1.13	66.0	0.13	0.79	133.0	-	0.94	22.80	56.2	236.2	
Min	0.0003	9.20	345.00	0.0003	9.95	257.0	0.00	9.22	266.0	-	9.00	284.60	0.0	0.0	
Flood peak	0.54	10.60	472.00	1.89	11.08	323.0	0.13	10.01	399.0	-	9.94	307.40	56.2	236.2	

* mean summary statistics calculated for the time interval 2002 - 2007

** mean summary statistics calculated for the time interval 2005 - 2017

Tab. 6.4. Statistics of the hydrological and physico-chemical parameters of the secondary tributaries monitored during the two infiltration events.

During the 2011 storm it showed a lower variability compared to the 2016 flood in all the parameters, especially in water discharge. There was a lag time between rainfall pulses and peak discharges, going from an hour to 11 h during 2011 and 2 to 5 h for the 2016 flood, with the shortest lags measured for maximum flow peak for both 2011 and 2016 events.

Polletta (PTTA, Tab.6.4, Fig. 6.4a, b) showed a broader variability during the 2011 storm than during the 2016 flood. In November 2011, it reached the maximum discharge ever registered for this inflow and its highest water temperature. The lag time between each rainfall pulse and the corresponding discharge peak is comprised between 2 and 6 hours for the 2011 storm whereas it is about 2 weeks for the 2016 flood.

Sacrestia drip (SA, Tab. 6.4, Fig. 6.4a, b) showed a different range of variability during the two events. It passed from no flow to about 23 mm of water percolated during the 2011 storm, whereas it went from zero discharge to about 230 mm of water during the 2016 flood, an order of magnitude higher than the 2011 storm. The lag time spanned from 8 to 15 hours during the 2011 storm and it ranged between 2 and 14 h during the 2016 flood, the shortest ones were measured for the highest peak flows in both events.

Polla delle Anatre (PA, Tab. 6.4, Fig. 6.4b) was monitored only during the 2016 flood because of device failure during the 2011 storm. From the comparison with the average values calculated for the last 10 years, it appears that this inflow reached its highest discharge values during the flood 2016, although it was not possible to observe its exact values because overflow from the weir borders occurred during the flood. Water temperature maximum was also

registered during this flood. It was possible to observe only the lag time between the first precipitation pulse and the first (minor) peak flow and its value is 5 h.

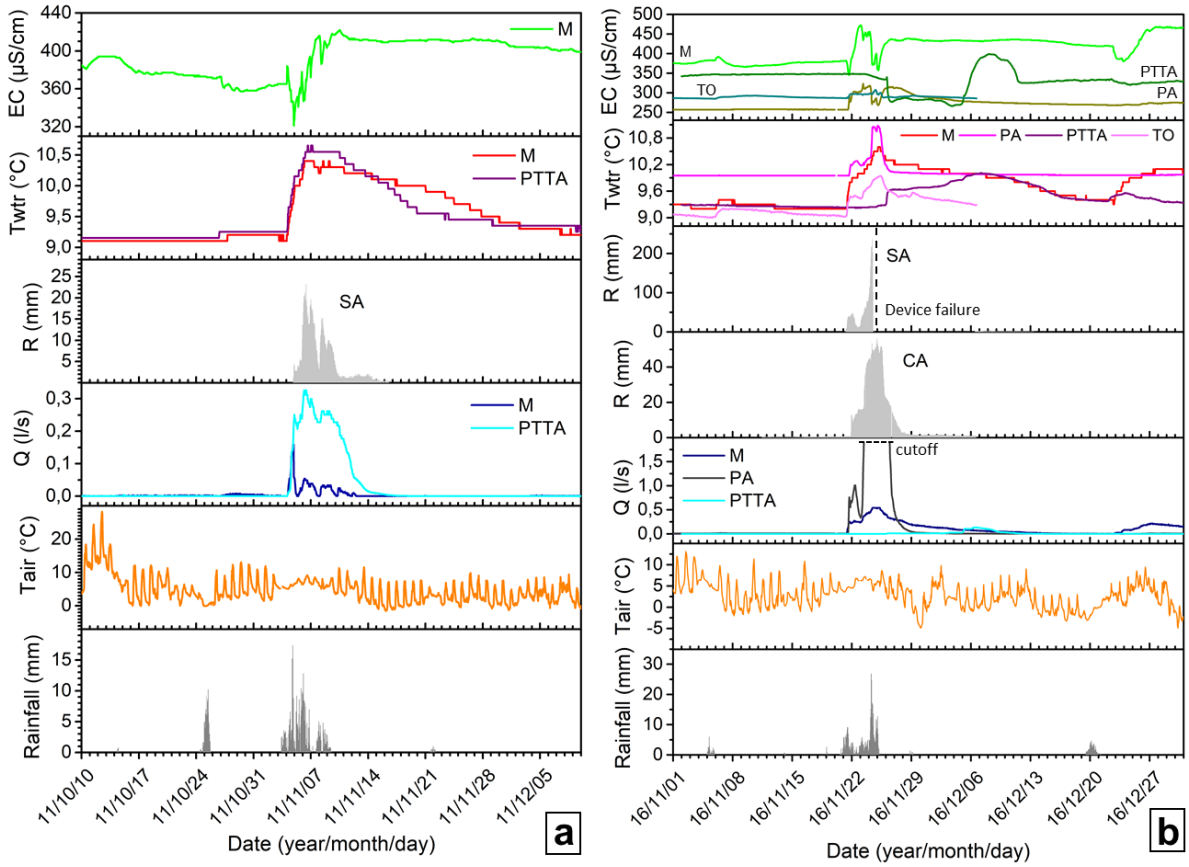

Fig. 6.4. Hydrographs and chemographs of the monitored drip sites during the November 2011 storm (a) and November 2016 flood (b).

Torre drip (TO, Tab.6.4, Fig. 6.4b) water T showed a first increase approximately one day after the first rainfall pulse of November 2016 flood and the highest peak appeared after one day and a half after the strongest precipitation pulse. EC increased sharply after 6 h from the first peak flow, it remained stable for 2 days then it reached its maximum for this event. The ranges of variability of the two previous parameters fit the standard values normally observed for this drip site.

Cancello drip (CA, Tab.6.4, Fig. 6.4b) exhibited its highest ever measured discharge during 2016 flood. The drip response to the onset of the heavy rainfall was about 9 hours. The lag time measured between the strongest rainfall pulse and the peak discharge is 15 hours.

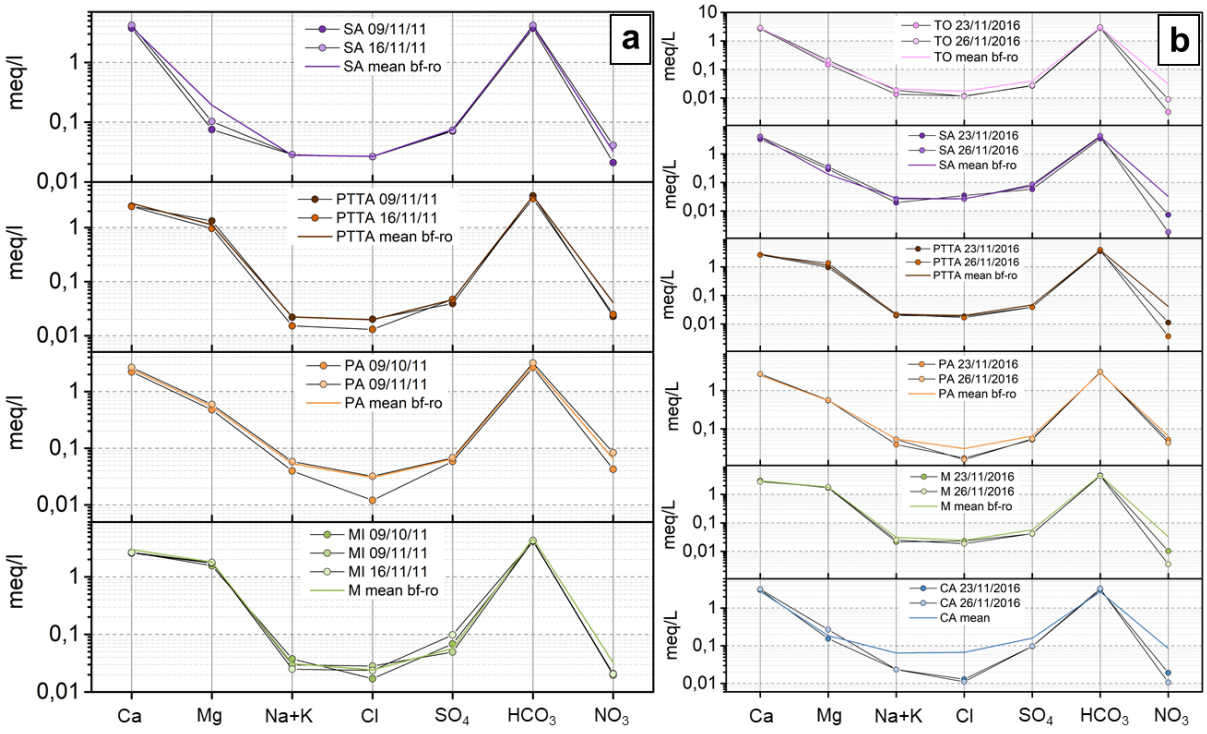

Fig. 6.5. Schoeller diagrams for the studied drip sites during the November 2011 storm (a) and November 2016 flood (b).

The chemical composition of the inflows is reported in the Schoeller diagrams of Fig. 6.5. The mean composition (labelled "[drip code] mean bf-ro") for each site taken from the database of the Bossea underground scientific lab are also reported for comparison and they are calculated with samples collected during the transition from base flow to the onset of the autumnal recharge phase (September to November). The only exception is represented by the mean CA composition that is measured over the whole available dataset because fewer chemical data were collected for this drip. Overall the vadose inflows have a bicarbonate-calcic (CA, SA, PA, TO) to calcic-magnesian (M and PTTA) hydrochemical composition. Like TM, the chemical components that exhibited the highest variability are the alkali, chloride, sulfate and nitrate ions but magnesium is less variable, depending on the considered drip. Each inflow displayed its characteristic chemical composition and its own degree of mineralization and, as a whole, all drips are more mineralized respect to TM.

Sample code and date	Al	Mn	Fe	Rb	Sr	Ba	La	Ce	Pr	Nd	Sm	Eu	Gd	Tb	Dy	Ho	Er	Tm	Yb	Lu
	ppb						ppt													
November 2016 flood																				
CA 23/11/16	2.1	0.7	3.2	0.7	3.2	66.4	32.3	30.9	7.5	28.7	6.0	13.6	6.9	1.1	6.8	nd	4.0	nd	2.6	nd
CA 26/11/16	1.6	0.0	1.7	0.0	1.7	71.9	5.1	1.1	0.6	2.6	1.4	10.2	1.2	0.1	1.0	0.0	0.3	0.0	0.4	0.0
MI 23/11/16	33.2	5.3	25.0	5.3	25.0	7.3	111.9	169.4	25.3	104.7	23.7	6.6	30.3	3.8	26.1	5.2	13.7	1.9	10.1	1.8
MI 26/11/16	3.9	0.0	0.3	0.0	0.3	5.1	17.9	4.4	4.0	17.7	3.4	0.7	5.3	0.6	4.3	0.7	2.7	0.2	1.2	0.4
PA 23/11/16	37.3	6.4	13.8	6.4	13.8	10.2	166.0	247.2	41.0	168.6	40.7	9.6	39.7	6.6	38.8	8.0	21.7	3.0	17.8	2.4
PA 26/11/16	25.3	2.8	6.2	2.8	6.2	14.7	128.0	131.7	30.8	123.3	26.9	8.6	32.8	4.8	30.3	6.1	20.7	2.2	15.4	2.3
PTTA 23/11/16	0.0	0.5	0.0	0.1	47.6	2.9	nd	nd	nd	nd	nd	nd	nd	nd	nd	nd	nd	nd	nd	nd
PTTA 26/11/16	6.6	9.6	7.9	9.6	7.9	10.7	38.7	23.7	8.0	31.5	7.6	3.8	9.3	1.1	8.2	1.8	5.6	0.8	5.2	0.5
SA 23/11/16	23.5	3.4	13.7	3.4	13.7	13.1	138.8	165.0	29.0	118.0	31.6	8.7	33.0	5.4	29.1	6.6	16.4	3.0	16.0	2.6
SA 26/11/16	1.6	0.0	1.2	0.0	1.2	15.9	30.8	6.1	4.9	20.0	4.4	2.7	4.5	0.9	5.4	1.1	3.8	0.4	2.5	0.3
TO 23/11/16	21.6	3.6	15.1	3.6	15.1	4.4	112.1	110.3	23.6	98.3	19.5	5.1	25.0	3.3	18.6	4.3	13.7	2.0	10.0	1.2
TO 26/11/16	3.0	0.0	1.1	0.0	1.1	3.4	20.6	5.4	3.8	18.7	4.7	1.0	4.0	0.7	4.4	0.8	2.4	0.2	2.4	0.4
November 2011 storm																				
MI 09/10/11	9.5	0.9	0.0	0.3	43.0	4.1	32.0	58.2	8.4	35.3	6.6	2.6	10.0	1.1	4.6	1.4	5.6	1.4	9.9	2.4
MI 09/11/11	1.9	0.6	0.0	0.1	42.2	3.7	23.7	12.2	2.6	12.8	3.2	1.5	2.6	0.4	2.5	0.9	2.5	0.3	2.6	0.3
MI 16/11/11	1.4	0.3	0.0	0.2	39.2	4.0	15.3	11.7	1.4	7.0	3.0	2.1	1.4	0.5	0.3	0.8	2.2	0.3	1.8	0.2
PA 09/10/11	5.0	0.1	0.0	0.4	91.4	27.1	288.8	544.8	64.5	232.3	40.4	14.9	52.9	9.0	41.4	14.4	57.1	11.7	84.7	24.7
PA 09/11/11	8.1	1.7	0.0	0.6	88.2	12.0	40.6	62.5	7.6	45.3	8.6	4.7	8.0	1.6	6.5	2.3	5.5	1.0	4.5	0.9
PTTA 09/11/11	2.3	0.2	0.0	0.1	38.7	2.4	20.0	13.6	1.7	9.2	3.4	1.3	nd	0.5	nd	1.0	2.3	nd	nd	0.3
PTTA 16/11/11	1.8	0.2	0.0	0.1	39.0	2.2	27.2	29.0	5.1	23.7	6.5	1.9	5.3	1.0	2.6	1.2	3.5	0.4	2.8	0.4
SA 09/11/11	2.9	0.4	0.0	0.1	116.1	13.0	31.7	20.4	4.4	16.4	3.7	3.9	4.0	0.5	2.1	1.1	2.6	0.4	2.6	0.4
SA 16/11/11	1.5	0.1	0.0	0.1	108.0	12.0	22.0	5.1	1.0	9.1	2.8	3.6	3.2	0.3	nd	0.7	1.9	0.2	1.4	0.2

Tab. 6.5. Trace element contents of the drip sites for the 2011 and 2016 events.

The most abundant trace elements and the lanthanide concentrations are reported in Tab. 6.5. During 2011, the concentration of the lanthanides decreased from the first sample to the last one, with PTTA being the only exception (its REEs content doubled from the first to the second sampling). The only noticeable variations in the content of metals are the progressive decrease in M and the increment in PA from the first to the last sample. The other trace elements didn't show relevant variations. The concentration of all the trace elements considered (Al, Mn, Fe, Rb, Ba, Sr and REEs) showed a decrease from the first sample to the second one during the 2016 flood, excluding PTTA that exhibited strong increases of metals (Al, Mn and Fe).

6.5. Discussion

6.5.1 Mora creek response to flooding: recognition of the different sources

The main underground river showed a complex behavior during the exceptional flood occurred in November 2016. This complexity can be related to the contribution to flood flow from different compartments of the catchment. As mentioned in Chapter 3, *Bossea* karst system has a complex architecture where several lithologies concur to the storage of the water that feeds the system. The REEs concentrations were normalized to the *Post Archean Australian Shale* for each sample collected by the automatic sampler. The purpose of the normalization was to

infer the host rocks that were drained during the flood, since it has been successfully used elsewhere (Gill et al., 2018; Berglund et al., 2019). Based upon the shape of the normalized REEs patterns and the sampling time, four different flow stages were distinguished (Fig. 6.6):

1. A pre-peak flow phase (prPF, mid 2016/11/20 to the beginning of 11/23, samples nr. 1-11), characterized by a marked Eu_n positive anomaly and a rising trend in Heavy Rare Earth Elements (HREE).
2. A transition to peak flow phase (trPF, 11/23 to the beginning of 11/24, samples nr. 12-15) that shows a less pronounced Eu_n positive anomaly and an inversion of the HREE trend, now decreasing from Gd to Lu. The whole REEs concentration is higher than that of the previous phase.
3. A peak flow stage (PF, from 11/24 early morning to 11/26 early morning, samples nr. 16-24) characterized by the disappearance of the Eu_n anomaly and a HREE trend similar to that observed in the previous phase. Another characteristic is the much higher REEs total concentration with respect to the precedent stages.
4. A final post peak flow phase (pPF, from 11/26 mid-morning to the end of the sampling, samples nr. 25-48). During this phase, a slight positive Eu_n anomaly reappeared but the HREE trend was still like the previous phase. The mean total REEs concentration is comprised between prPF and trPF values but closer to the former.

The distinction based on the normalized REE was than applied to the major hydrochemical compositions of each individual sample. If the samples are chronologically ordered and then grouped with respect to the stages recognized by the normalized REEs patterns and plotted on a Schoeller diagram (Fig. 6.7), some observations can be done. The concentration of magnesium fluctuated during the first three phases, then it decreased to its minimum values during the post-peak flow stage. Alkali, Chloride, sulfate and nitrate ions decreased from the first stage to the PF phase then they increased again during pPF stage but with different magnitudes, depending on the ion considered. Overall, the first stage is characterized by the lowest mean mineralization, but it displayed a high variability, lower only than that showed by the PF flow stage.

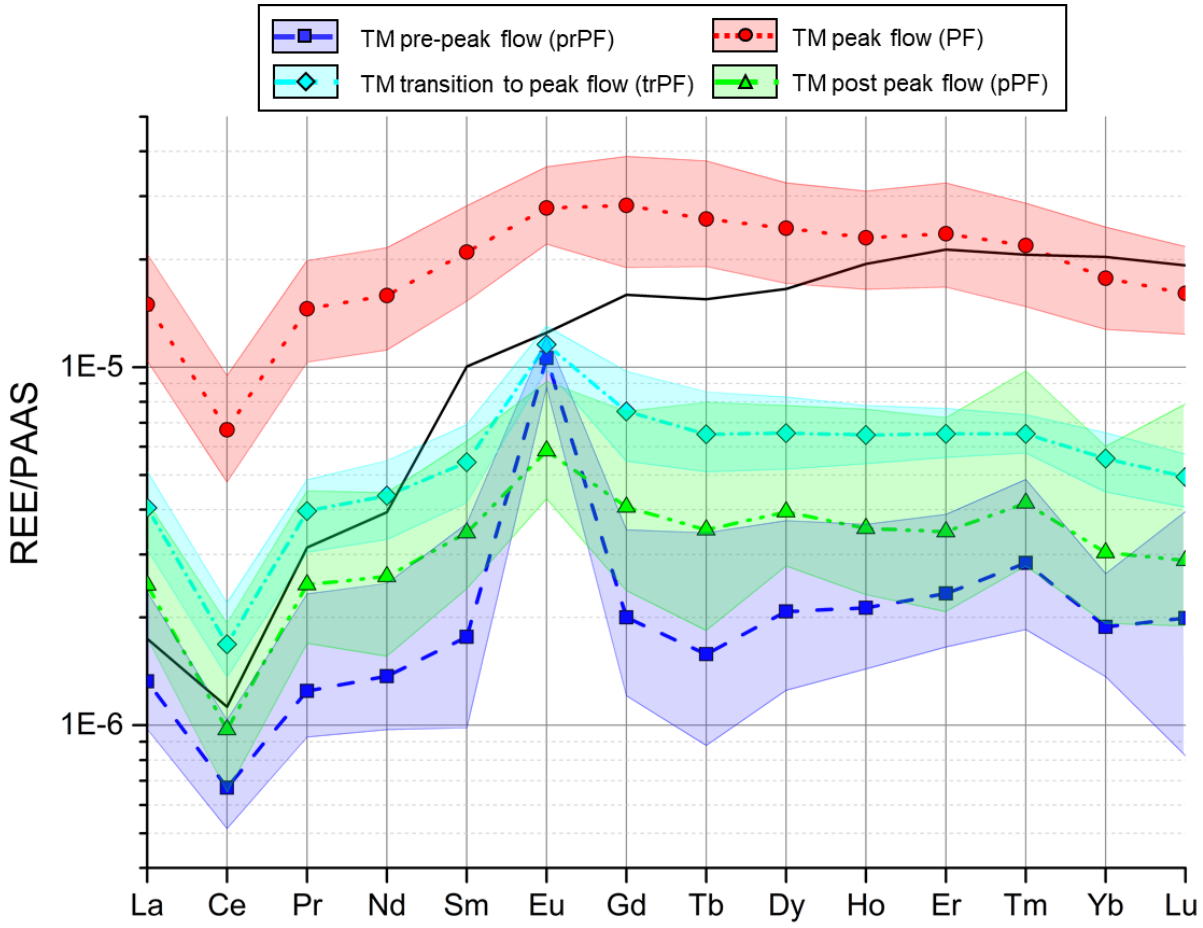

Fig. 6.6. Spider diagram of REEs concentrations normalized to PAAS. The patterns for each sample are grouped according to their shape and temporal disposition. The range of variability (and the mean value, lines + points pattern) for each group is plotted instead of every individual sample pattern for better clarity. *Sorgente dei Matti* (SdM) mean REE pattern in reported for comparison (black line).

The second stage (trPF) showed the highest mineralization. Moreover, the most important assessments can be carried out if the ratios between some of the major components are considered. The alkali to chloride ratio is a good marker for non-carbonate water, as highlighted by *Sorgente dei Matti* spring: this spring is fed by water from the meta-volcanic rocks of the impermeable complex so it can be used as impermeable end member for water chemistry (Fiorucci et al., 2015). It is possible to recognize an increase in contribution from the impermeable complex from prPF to PF.

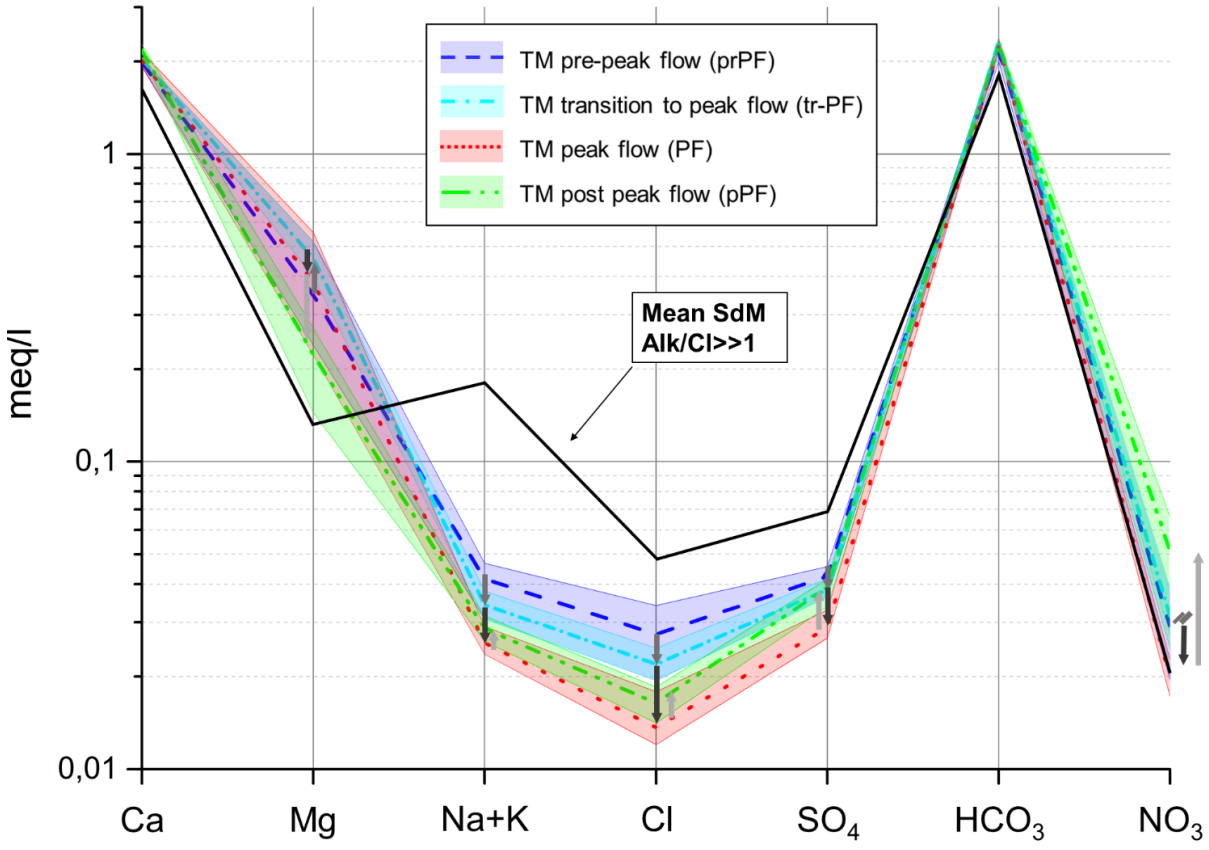

Fig. 6.7. Schoeller diagram reporting *Mora* creek chemical composition during the 2016 flood, separated according to the stages defined with the REEs spider diagram. The dashed, dash-dot-dash, dotted and dash-double dot lines represent the mean compositions for each stage. The black line represents *Sorgente dei Matti* mean composition (SdM). The dark grey, black and grey arrows highlight the evolution of the HREE trend from prPF to trPF, trPF to PF and from PF to pPF, respectively.

This increasing contribution from the impermeable complex is more evident comparing *Mora* creek hydrograph with the chemographs of its physico-chemical parameters, those of some major component ratios and the trace element ones (Fig. 6.8). Rb chemograph is not presented because it has the same shape of the one of Barium. Data from the monitoring of this event as well as any other TM sampling revealed a very good correlation between these two elements so they will be treated together henceforth. Al, Fe and Mn showed a very good correlation with ΣREE trend so their chemograph is not reported. It seems possible also to make some assessments on the contribution of the distinct "secondary" lithologies putting together the data from major chemistry with trace elements, stated that the overall dominant hydrochemical composition is calcium-carbonate in each stage (even the waters draining the non-carbonate reservoirs, see SdM mean composition in Fig. 6.7):

1. Pre-Peak Flow stage: during this stage, the discharged water was mainly from the calcium carbonate rocks, with some inflows from the shales as suggested by the HREE

trend (Fig. 6.8) and by the sulfate to bicarbonate ratio chemograph. The progressive decrease of the calcium to bicarbonate ratio was due to the increasing contribution of magnesium that reached its apex in the following stage. In fact, calcium concentration alone mirrored the electrical conductivity trend. Ba (and Rb) started to decrease slowly during this stage.

2. Transition to Peak Flow stage: the sustained precipitations led to a more pronounced increase of discharge; the discharged water had a more magnesium-calcic signature. Ba and Rb continued to decrease, probably because they are related to the carbonate lithologies. Although Rb and Ba should be much more abundant in the non-carbonate rocks (quartzites and meta-volcanics, respectively) than in the carbonates, their concentrations and trends appear to be related to the rate of water-rock interaction rather than to the lithology: the dissolution of non-carbonate lithologies such as quartzite is much slower than for carbonate rocks (Wray and Sauro, 2017).
3. Peak Flow stage (PF): this phase comprises the peak discharge and the following initial part of the recession stage. The strongest contribution from the non-carbonate lithologies happened during this phase, as suggested by the alkali to chloride ratio and electrical conductivity chemographs. A sharp decrease in mineralization marked this stage, however this negative EC peak cannot be ascribed to neo-infiltration water, as demonstrated also by the small positive water temperature peak: air temperature during the precipitations can be used as indicator of rainfall temperature, so because the highest air T registered during the flood (7,2 °C) was lower than *Mora* Creek's, an input of neo-infiltrating water would have caused a decrease in water temperature. For comparison, the *Roccia Bianca* brook T chemograph is clearly influenced by the diurnal and meteorological oscillations (rainfall and snowfall precipitation) of air temperature, as expected for a surface stream. The flood pulse activated a wider drainage area of the system that could have led to a small decrease in T. The lower mineralization is caused by the host rocks drained during this phase. There could be a major contribution first from the quartzite drainage system over the meta-volcanics, showed by the maximum REEs concentration during the first peak flow, then the meta-volcanic component overruled the quartzite one, as suggested by the relative decrease of ΣREE simultaneous to the highest values for the alkali to chloride ratio. Alternatively, the total REEs concentration and its good correlation with Fe, Al and Mn could also be related to the

suspended sediment concentration, as suggested by other authors (Ingri et al., 2000; Berglund et al., 2019). Flattened shale normalized patterns were associated to neo-infiltrating water (storm water) carrying high quantities of suspended sediments that derived either from homogeneous recharge through weathered sediments (Willis and Johannesson, 2011) or from specific sectors of the recharge area (Filippini et al., 2018; Berglund et al., 2019). However, this should not be the case for Bossea: the other parameters monitored during the flood (as well as during normal infiltration events, Fiorucci et al., 2015) suggest a piston-flow behavior, so the storm pulse transmits water stored in the system. Both parameters and REE normalized PF-patterns could also be related to a major contribution from quartzite compartments of the system, since the REEs normalized pattern of the PF samples has a shape similar to the quartzite sampled in the study area rather than a flattened shape; said lithology has also the highest REEs and metals contents. Another possibility is the remobilization of huge volumes of sediments (possibly with a quartzite-like chemistry) in the main sumps upstream during the flood; the accumulation of sediments in this part of the system was reported by cave divers and they seem to play a key-role in the activation of flood events not related to strong precipitations (Peano et al., 2005), but their chemical composition is still unknown. Whatever the source of REE and trace elements, the input from non-carbonate rocks is confirmed by the alkali to chloride ratio.

4. Post-Peak Flow Peak (pPF): this phase represents the attempt of the system to recover from the flood perturbation. The mineralization started to increase again and the chemograph analysis suggests that this portion of the hydrograph is fed by calcium-carbonate waters and secondarily by the meta-volcanic reservoir (the alkali/chloride ratio decreased but not to pre-flood values), whereas the shale contribution doesn't seem relevant (HREE trend inversion and SO_4/HCO_3 ratio lower than pre-flood levels). Considering the EC trend, the interval of recovery to pre-flood values is about a month.

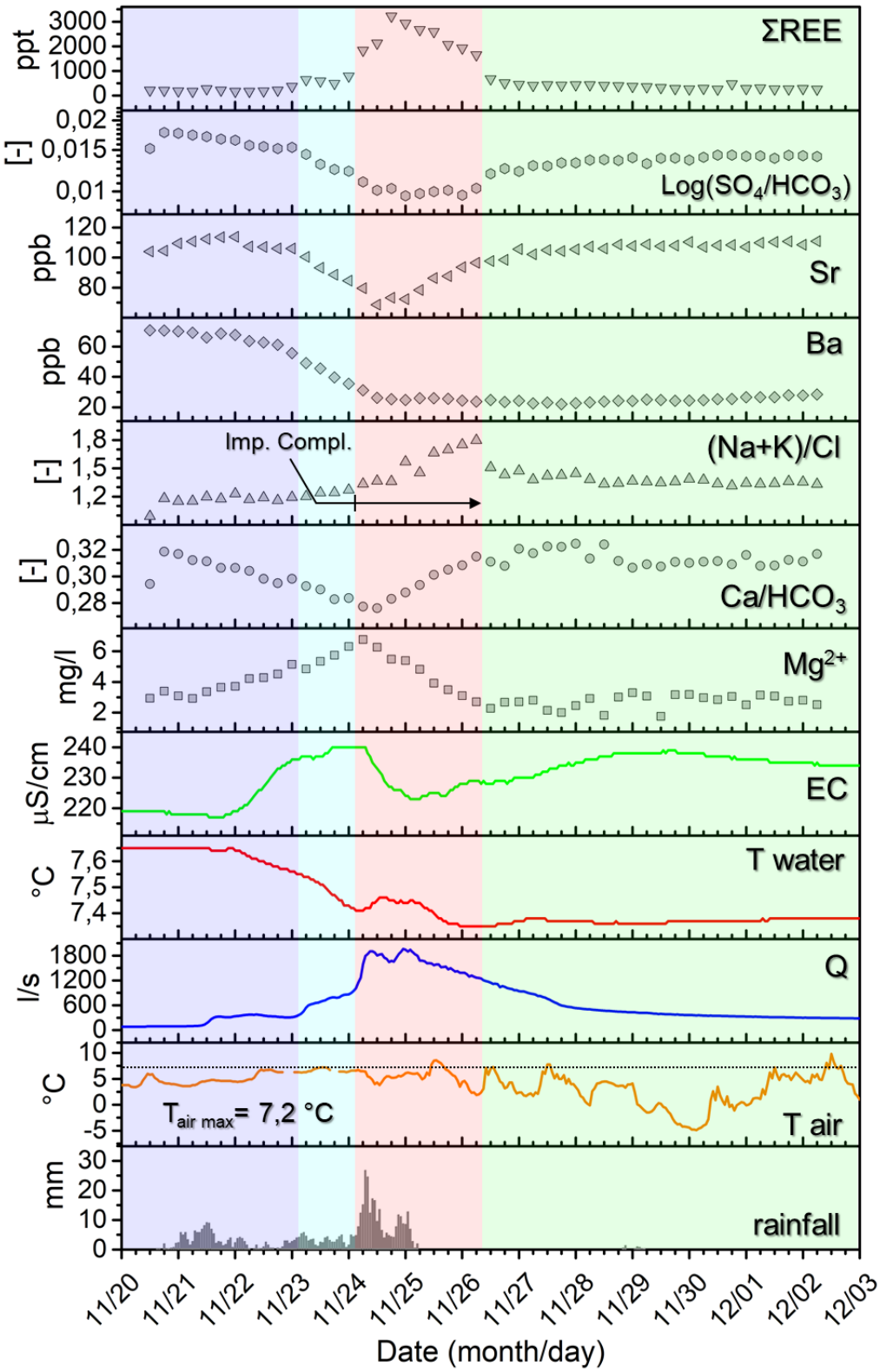

Fig. 6.8. Meteorological time series (precipitation and air T), TM hydrograph and chemographs for the November 2016 flood. The ratio between the ions are calculated with meq/l input data.

The hydrodynamics and hydrochemical behavior of the underground river during the 2016 flood appears complex and it showed some uncommon features if compared to normal infiltration events or to storms having magnitude (in terms of daily amounts of rainfall) lower than the 2016 event. The monitoring of the November 2011 rainfall event shows that strong precipitations homogeneously distributed over a larger time interval trigger an impulsive response of the karst system but with contributions possibly more restricted to the carbonate reservoir, so more spatially limited (Fig. 6.9). Again, the low-flow phase preceding the storm pulse was characterized by a prevalent contribution of the calcium carbonate host rock, with maybe a minor contribution from drainage networks developed in the shales (blue squares spider diagram in the Fig. 6.9 box). The decrease of water temperature (about 0.4 °C) is again caused by a wider drainage area rather than the infiltration of rainfall. The hydrograph and chemograph phase separation cannot be done as for the 2016 flood because there are not enough REEs nor major ions data. However, flow stages can be distinguished based upon the chemographs of the physico-chemical parameters, combined with the spotted chemical samplings. The principal phase of the storm discharge (rising limb, peak flow and recession onset) is characterized by a general increase of mineralization but with some small negative peaks. A sampling was carried out during the last "negative" EC peak and the corresponding REEs normalized pattern show a signature that correlates to the one of the *Impermeable Complex*, although the alkali to chloride ratio is approximately around the unit. This discrepancy with the behavior observed during the flood could be explained with a less relevant contribution from the impermeable complex, enough to perturb the chemical signal but to a much lower extent or, alternatively the REE pattern could be related to the remobilization of small volumes of sediments in the sumps. The total concentration of REEs showed an increase during the storm but no data are available for the peak flow. It is possible that their concentrations mirrored the EC trend, however the comparison in the same interval of the 2011 and 2016 hydrographs (onset to mid-recession limb, transition from peak flow to post peak flow) of ΣREE highlights the different magnitude of the non-carbonate reservoirs or sediment contribution during the two infiltration events (569,3 against 1650,7 ppt). The maximum mineralization was reached during the recession phase (pPF), approximately a week after the end of the storm. The recovery time for EC to return to pre-storm values was about 2 weeks after the peak flow, about half the time required by the underground river to return to normal values during the 2016 flood.

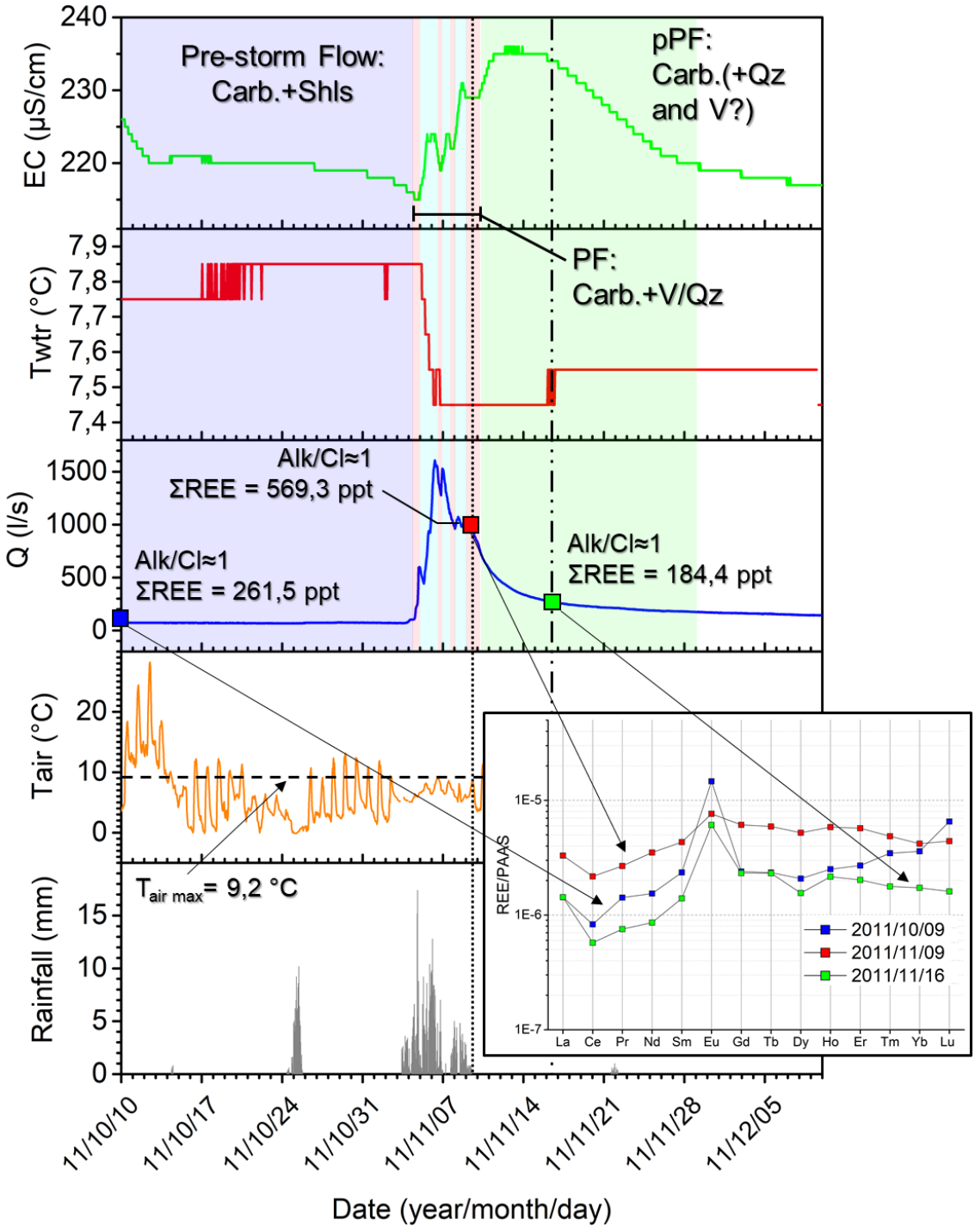

Fig. 6.9. TM hydrograph and chemographs during the November 2011 storm event. The box reports the spider diagrams of the samples collected 3 weeks before (blue rectangles), 4 days after (red rectangles) and 9 days after (green rectangles) the storm event.

As pointed out by Civita et al. (2005), it appears that Bossea karst system is not able to drain the whole amount of rainfall that occurs during strong to exceptional storm events, also in case of exceptional values of daily rainfall or total precipitation. The external morphology of the

karst system, characterized by steep slopes of carbonates bordered by impermeable rocks, limits the infiltration of water from both the surface stream runoff (developed mostly along the tectonic contact between permeable and impermeable complexes) and direct recharge on the carbonate surface. The system did not drain a lot of rainfall neither during the strongest natural antecedent flood event occurred in 1994 (maximum discharge of 1500 l/s), nor during the anthropic induced one occurred in 1996 (maximum discharge over 4000 l/s). These floods were caused by storms that had values of maximum daily rainfall almost half the value recorded during the one happened in 2016 (see Tab. 6.1 for details), yet they were destructive and were estimated to have recurrence times of 50 to a hundred of years (Regione Piemonte and Assessorato Ambiente, 1998; Luino, 1999). However, *Mora* creek peak discharge during the 1994 flood was just slightly above the peak discharges observed in the spring season. The anomalous flood occurred in October 1996 caused the severe damages inside the cave and it was determined by the concomitance of extreme precipitations (104 mm/day as mean daily value) and the effects of a building site in the drainage area above the cave (Peano et al., 2005). The causes and the effects on the karst system cannot be compared to the 2016 flood, however they share a similar extreme mean daily rainfall amount (100 mm/day for the 2016 flood). Therefore, the November 2016 event exhibited the most extreme characteristics in both meteorological and hydrodynamic conditions if we consider the "natural" floods: highest maximum daily precipitation, average daily value and total amount of rainfall, and the highest discharge. Even during this flood, the system showed its inability to completely drain the precipitation (not exceeding 2000 l/s despite the exceptional storm), confirmed also by the predominance of runoff over infiltration that led to *Roccia Bianca* flood peak. The chemical and hydrological monitoring confirmed the impulsive, piston-flow behavior of the system already recognized during previous floods.

6.5.2 The unsaturated zone response to strong precipitation events

The following sections discuss the response of each drip site to the infiltration events examined in this study. Overall, the unsaturated zone showed a piston-flow behavior during both events, but there are strong differences in the timing and in the drainage systems involved (due to the structural setting) for each investigated inflow. The sections are arranged in order to compare: a) the response of different secondary tributaries to the two storms, b) the behavior of the most

constant inflow against a seasonal drip and, c) the response of two intermittent low discharge drips to strong infiltration events.

6.5.2.1. Milano and Polletta: comparison of two hydrologically and structurally different inflows during the two floods

The two secondary tributaries are characterized by quite constant discharges that decrease to zero only in case of extremely dry summer seasons. *Milano* drip site has higher median and peak discharges with respect to *Polletta*. The former drip showed a piston-flow behavior during both events but it displayed peculiar characteristics specific for the event considered. The comparison between the chemographs of the physico-chemical parameters and air temperature (indicator of rainfall temperature) reveals that all the water drained during both events was relatively old stored water pushed down by pressure propagation, but the characteristics of the two precipitation events led to different timing of activation for each fracture network. Pre-flood water (prF, Fig. 6.10a) had an alkali to chloride ratio slightly higher than one and a positive $HREE_{norm}$ trend (increasing concentration from Dy to Lu) that could be indicative of contribution from shale host rock, similarly to what observed for TM pre-2011 storm flow. It is possible to distinguish two sub-phases of the piston flow during both events: a carbonate (PsFl C-d) and a non-carbonate dominated (PsFl nC-d, Fig. 6.10) one. The assumption on defining a dominant source rather than a distinct source for each sub-phase is done on the idea that different fractures, fed by different host rocks, contribute to drainage determining the observed EC fluctuation. The non-carbonate dominated sub-phase preceded the carbonate one during the 2011 storm (Fig. 6.10a). During the 2016 flood, the sub-phases order is reversed (Fig. 6.10b): the first part of the impulsive response is carbonate-dominated, followed by the nC-d. It seems that the timing of the non-carbonate sub-phase is related to the highest discharge pulses of both floods: in November 2011, the maximum discharge is reached during the first pulse of the storm whereas the peak flow of the 2016 was reached in the late phase of the rainfall event. We can conclude that the intrinsic characteristics of the meteorological event played a key role on *Milano* infiltration dynamics when comparing two events that share similar hydrodynamic conditions in the karst system. The possibility that non-carbonate water could feed this dripsite was confirmed also by some tracer tests performed in 2007. The injection point chosen for *Milano* tests was a fountain that drains water from the impermeable complex (Banzato et al., 2013). After the flood pulse, the drip is fed mainly by the Ca-Mg-carbonates

(recovery phase, “Rec. Crbn” in Fig. 6.10), as demonstrated by the Schoeller diagrams and the EC trend in both floods.

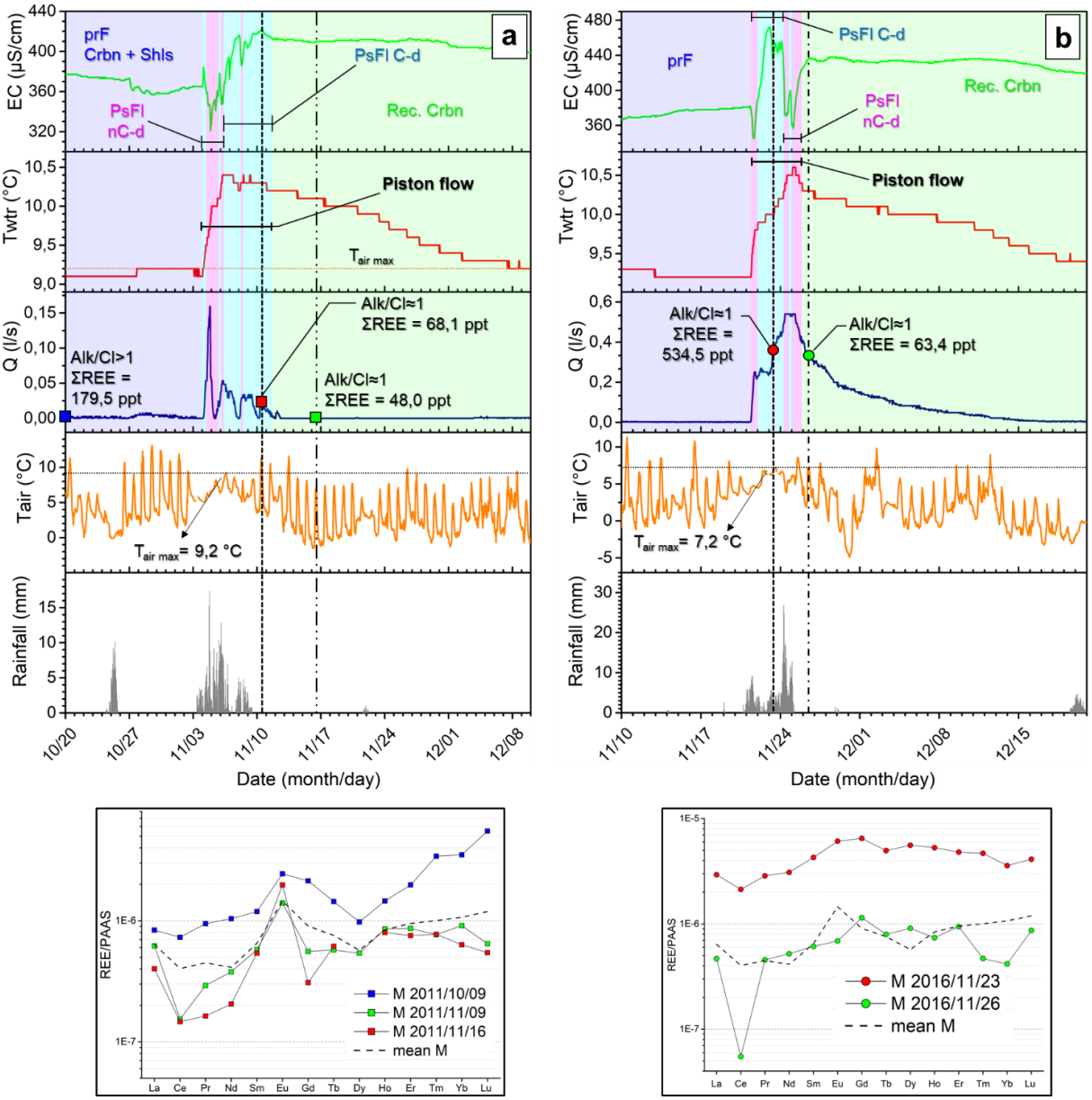

Fig. 6.10. Milano drip hydrograph, chemographs and REE spider diagram during the 2011 storm (a) and 2016 flood (b).

Like *Milano*, *Polletta* showed an impulsive, piston-flow behavior during both events (Fig. 6.11) but again, the monitored parameters showed peculiar trends for each storm. No EC data are available for the 2011 event, so the only information on water mineralization comes from the total dissolved solids (TDS, mg/l) of the two collected water samples. TDS, alkali/chloride ratio and the REE spider diagram point to the drainage of water from the carbonate reservoir, at least

during the second half of the storm peak and for the post-storm phase (Fig. 6.11a). Usually during autumn recharge, this spill point shows impulsive response to precipitations and the mineralization reveals a strong contribution from the impermeable complex (negative EC peaks) followed by a variable amount of water from the carbonate complex (positive peaks in mineralization). This could be the case also for the first part of the 2011 event but there are not enough evidences to confirm this. Differently to *Milano*, this inflow responded sharply to the precipitation, showing a single pronounced discharge peak that reached the highest value ever for *Polletta*; on the contrary, *Milano* attained its maximum during the 2016 flood and it had an intermittent impulsive response to each individual precipitation pulse of the 2011 event. *Polletta* response to the November 2016 flood is extremely peculiar: the water discharge started to increase slightly 2 days after the strongest rainfall input but then it remained stable for almost two weeks, when a strong impulse of water was discharged (Fig. 6.11b). Water temperature and electrical conductivity together showed a prolonged piston-flow episode that is characterized by two sub-phases. Nonetheless, these two parts of the impulse are quite different from the ones registered at *Milano*, where the arrivals from the non-carbonate rocks are intermittent. Here, there was first a well-defined input of less mineralized water from the impermeable complex (non-carbonate piston flow, nC-PsFl, Fig. 6.11b), then a sharp increase of EC marked the transition to an equally clear carbonate contribution (C-PsFl). It is interesting to note that the recovery time required by *Milano* drip to restore pre-storm values of the physico-chemical parameters is quite similar for both floods (about 3 weeks after the piston-flow onset) but the time lag between rainfall pulse and peak flow is completely different during the two events. Moreover, PTTA did not get even close to its maximum discharge values during the 2016 flood. This kind of impulsive response to precipitation is not common for *Polletta*, especially in the considered phase of the hydrological year (autumn recharge), while it is relatively more common during the beginning of spring snow-melting phase. However, the maximum lag time between the precipitation and peak flow was registered during this flood.

It is evident that the drainage system architecture of the two inflows played a key-role in the response to the examined storms, although the meteorological characteristics of the precipitation events, together with the overall structure of the unsaturated zone, also had a strong influence on the hydrological behavior of the inflows.

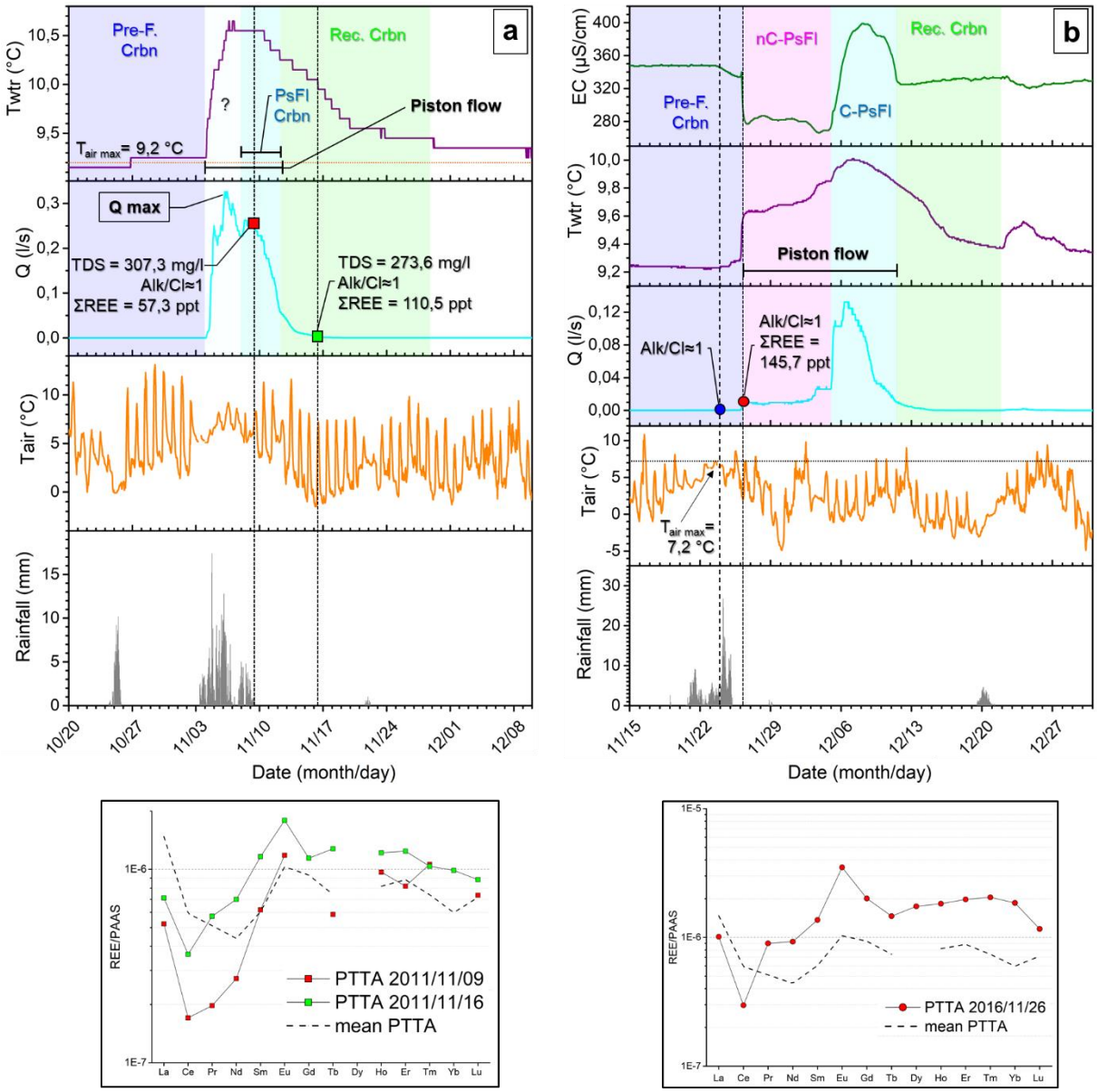

Fig. 6.11. *Polletta* hydrology during the November 2011 (a) and November 2016 (b) floods.

Milano drainage system developed predominantly in the carbonate compartments of *Bossea* system and the impermeable inputs represent exceptions. On the contrary, *Polletta* drains much more water from the less permeable basement rocks: it discharges along the contact between the metavolcanics and the Mesozoic carbonate sequence and its discharge is the result of a piston flow first of the water in the small aquifer developed in the damage zone of the detachment, then the water coming from the carbonate unsaturated zone.

6.5.2.2. Polla delle Anatre and Torre: perennial vs seasonal inflow response to flood

Polla delle Anatre is the secondary tributary characterized by the most constant and highest discharge monitored in the *Bossea* cave. It overflowed during the November 2016 flood so its peak discharge is unknown. It is also the less mineralized monitored inflow, as a consequence of the amount of water drained from the impermeable complex. During the 2016 flood, it showed a carbonate-dominated piston-flow phase first (C-d PsFl, Fig. 6.12a), followed during peak flow by a sub-phase regulated by inputs from the impermeable complex (nC-d PsFl). The sharp decrease of mineralization was followed by the input of carbonate water in the recovery interval (Rec. Crbn). *Torre* drip showed instead an unusual behavior during the flood. Looking only at the physico-chemographs it seems that it responded quickly to the storm, but the EC behaved strangely (Fig.6.12b): it increased sharply together with water temperature and then it remained stable for 2 days. The mineralization started to fluctuate with small, sharp positive peaks during the strongest rainfall pulses. A day after the end of the storm, EC sharply decreased while water T started to diminish gentler than mineralization. The recovery phase was perturbed by a small late rainfall event that made the physico-chemical parameters increase slightly but, overall, EC seemed to return to pre-storm values much faster than T. The high EC pulse can be explained by a drainage system developed in the carbonate succession characterized by low to very low permeability, that is capable of activating the less permeable fractures only during the strongest pulses of extreme precipitations. *Torre* typically responds quickly to rainfall events, even to the very small ones (see the perturbation during the recession phase by the rainfall event occurred on November 29th) once enough hydraulic pressure is transmitted to its drainage network. The occurrence of three consecutive rainfall events before the flood allowed the activation of the drip site after the summer season. The duration and the intensity of the 2016 event could explain the plateau shape of the first part of the impulsive response while the heaviest rainfall peaks permitted a more efficient transmission of hydraulic pressure in the whole fracture network. The spotted samplings suggest some quick input from the impermeable rocks as also observed for other seasonal samplings. However, the hydrodynamic conditions in the system antecedent to the flood did not lead to extreme variations in the drainage system, in the sense that an exceptional meteorological event was not capable to provoke the maximum oscillation observed for the physico-chemical parameters (see Tab. 6.4 for the ranges of variability). In comparison, the flood was more "disturbing" for a constant inflow such as *Polla delle Anatre* rather than for a seasonal drip like *Torre*, in terms of variability.

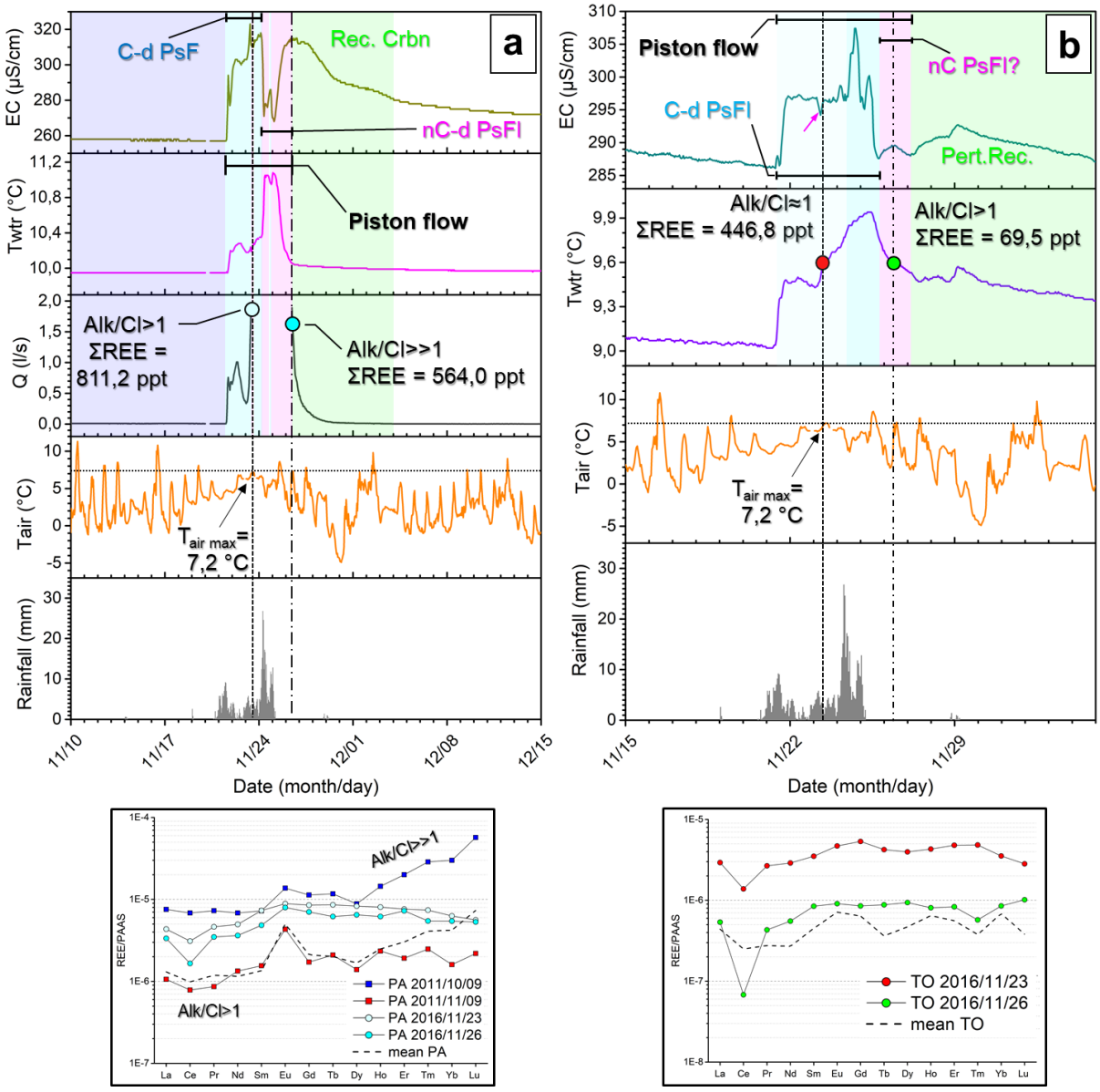

Fig. 6.12. *Polla delle Anatre* hydrograph and chemographs (a) and *Torre* chemographs (b) recorded during the November 2016 flood.

6.5.2.3. Sacrestia and Cancello drip sites: hydrological behavior of intermittent inflows during extreme precipitations

The available data on these two intermittent drips (discharge and spotted samplings) revealed a similar reaction to the storm for both drip sites. Both reached their maximum discharge during the 2016 flood and they responded almost instantaneously to precipitation. *Sacrestia* exhibited a carbonate REE signature during the recession phase for both storms (Fig. 16a, b), while a non-carbonate contribution was observed before the peak discharge of the 2016 event. *Cancello*

hydrochemistry points to a carbonate signature but the alkali to chloride ratio suggest also the possible contribution of water from the impermeable complex (Fig. 16c).

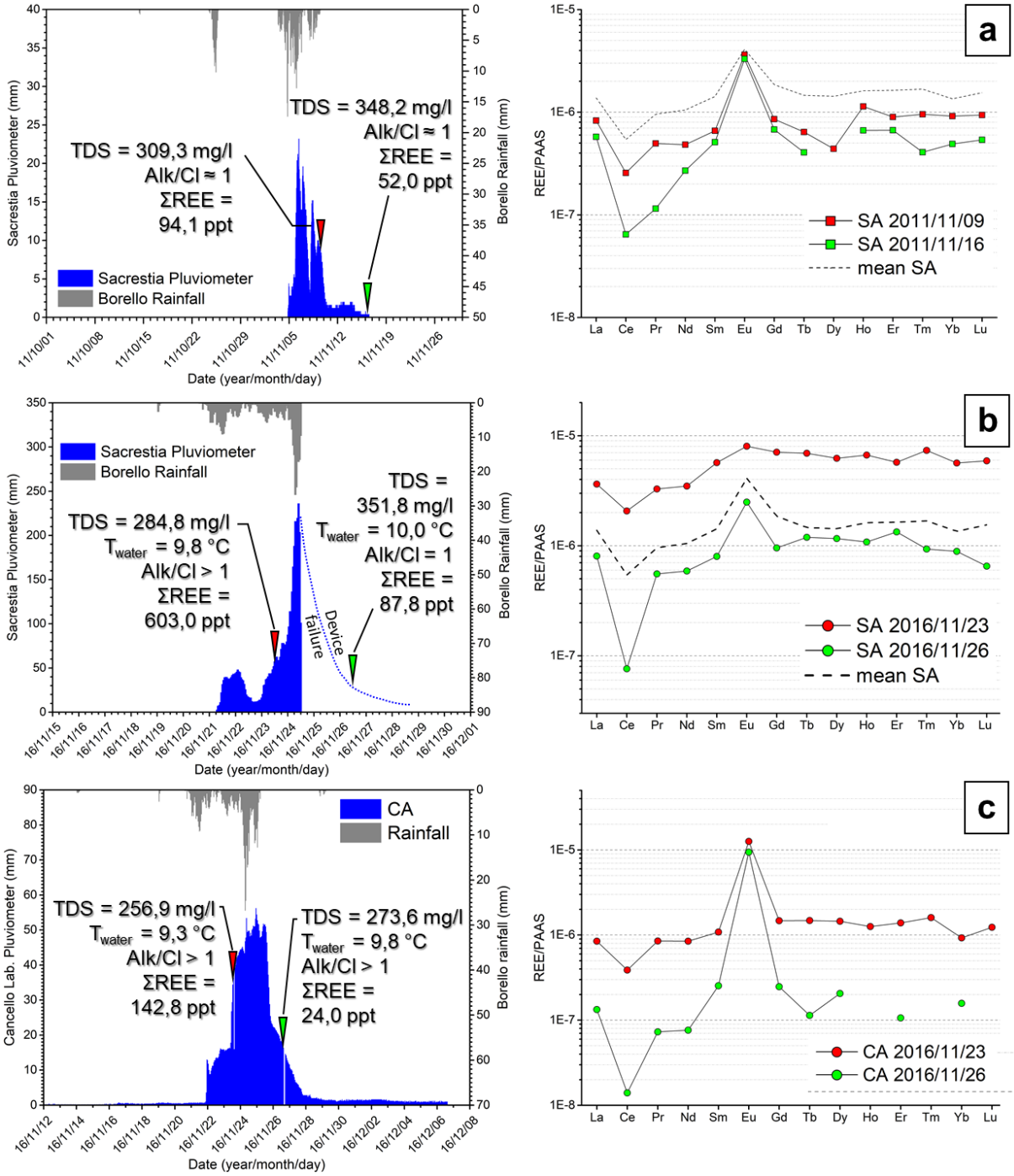

Fig. 6.13. *Sacrestia* hydrological response to the 2011 (a) and 2016 (b) floods. (c) *Cancello* hydrologic monitoring during the November 2016 flood. The hydrochemical details of the samplings carried out during the floods are also reported.

It is not possible to infer the magnitude of the contribution from different host rocks to these unsaturated inflows but both drips drain fracture systems that are characterized by low transmissivity, as verified during some tracer tests for other drip sites (Vigna, personal communication). The water that percolated during these floods must be old water stored in the drip drainage network (i.e. the perched saturated aquifer described in Chapter 3) that was forced out because of the increase in hydraulic pressure due to strong water input into the fracture network. The magnitude of the precipitation combined with the saturation conditions inside the fractures determined the amount of old water discharged.

6.6 Conclusions

The comparison with other significant storms and flood events permitted to recognize the exceptional characteristics of the 2016 flood in terms of meteorological event and hydrodynamic behavior of the system. Overall, *Bossea* had a piston-flow response to the extreme infiltration, similar to the behavior showed during antecedent floods and its reaction is strictly related to its structural and morphological setting. For the first time, it was possible to study in detail the hydrochemical and hydrological evolution. The underground river and some vadose inflows showed a progressive increasing contribution to flow from the impermeable complex during the climax of the flood, highlighting the involvement of broader sectors of the system both at a catchment and at individual vadose drainage system scales. However, the response of each individual portion of the unsaturated zone is strongly influenced by its saturation conditions that are in turn dependent on the fracture network architecture, so the behavior of each drip is regulated, in detail, more by its topology than by the magnitude of the storm. The monitoring of this complex system confirmed the necessity to carry out a detailed investigation of several parameters to be able to unravel the functioning of a “multi-reservoir” karst system. The piston-flow behavior of both the main underground system and the vadose inflows was recognized putting together hydrological, continuous and discrete hydrochemical data, otherwise the interpretation restricted to a limited number of aspects would not have been sufficient. Likewise, the hydrochemical investigation should rely on a multiparametric approach, involving major and minor chemical components because the use of only a certain number of variables can be potentially misleading for inferring the contribution of different reservoirs.

Chapter 7: Conclusions

The aim of this doctoral project was to investigate the unsaturated flow in a karst system strongly influenced by tectonic deformation. The study of the local structural setting sets the basis for the work: the *Bossea* karst system evolution was controlled by structures that formed during different phases of the Alpine orogenesis. The lithologic contrast between the Permian non-carbonate basement rocks and the overlaying Mesozoic carbonate sequence coupled with a transpressional regime determined the development of a disharmonic surface. This surface separates the warped meta-volcanic basement from the tightly folded marble sequence (usually accompanied by folded quartzite and shales). The *Bossea* system developed by taking advantage of this setting: the speleogenesis started in the marble sequence but, once water reached the disharmonic contact, chemical dissolution was replaced by fast mechanical erosion of the meta-volcanics that led to gravitational instability in the marble sequence. This determined the formation of giant halls and roof collapses. The principal circulation pathways developed along the folded bedding surfaces, due to the low to absent matrix porosity of the marbles. Other secondary flow paths are represented by secondary brittle structures that grant interconnectivity between the bedding junctions.

Such a strong control of the structural setting on the speleogenetic process was not recognized before and the model proposed for the evolution of the *Bossea* cave could be applied in other systems developed in orogenic contexts, where tectonic deformation is probably important.

The fracturing of the rock volume coupled with the presence of the disharmonic surface represent two fundamental factors that control the storage capacity of different portions of the system. The detachment surface acts as an aquitard, limiting the vertical flow. However, the strong deformation that occurred in relation to the detachment permitted the development of intermittent flow paths in the bottom damage zone, so that a certain circulation in the low highly deformed permeable meta-volcanics occurs. This and the fracturing of the above carbonate sequence, permitted the formation of small, saturated water reservoirs that feed the so-called *polle*. These underground perennial outflows are influenced by the percolation dynamics in the unsaturated zone, because vertical impulsive transmission of water causes piston flow also in these outlets. The unsaturated part of the karst system should be viewed as a volume in which permeability and saturation conditions are extremely variable, because they are primarily controlled by the architecture of the fracture networks. The sets of fractures characterized by

low permeability and small dimensions can retain important volumes of water, to the point that rock compartments permeated by these fracture networks can be considered as perched saturated aquifers that feed the perennial drip sites. The difference with a "classical" perched aquifer is the absence of an aquiclude/aquitard below these water reservoirs. In the fractured rock volume these aquifers are spatially limited by the dimension and the arrangement of the fractures, so that water percolates until it is not able anymore to overcome the capillary forces in the low permeability fractures. The impulsive infiltration of freshwater (rainfall or snowmelt) can provide enough hydraulic pressure to remobilize larger portions of the water "trapped" in these small fractures, provoking a piston-flow effect in the fracture network and generating discharge pulses at the cave outlet.

This kind of storage is fundamental in a system like *Bossea* where a poor developed epikarst and a scarce soil cover do not grant an additional reservoir in the topmost part of the unsaturated zone, so that the perennial discharge characterizing many of the unsaturated outlet is fed solely by these fractured perched reservoirs. Some of the outlets are fed exclusively by fractured reservoirs made up by small low permeability fractures, so that water can be discharged only during precipitation events capable to transmit sufficient hydraulic pressure. Conversely, other drip sites are fed by more complex fracture systems: the discharge occurs along the main circulation pathways through the marble sequence (i.e. the bedding surfaces) but their reservoirs are made up of several, progressively smaller sets of fracture networks. The activation of each individual fracture set depends upon the saturation conditions in the fracture system and on the balance between precipitation amount and evapotranspiration. The presence of these different architectures was confirmed by the integrated approach of drip recession analysis, cubic law inversion, and fractal analysis.

The combined analysis of water electrical conductivity and water temperature permits to recognize the episodes of piston flow, particularly in a complex system such as *Bossea*. The combined chemographs analysis is the only valid method to recognize each individual piston flow episode in this system, because the analysis of the electrical conductivity alone was demonstrated to be misleading for inferring both *polle*, drip sites and underground river hydrodynamics. The complex architecture of the whole system permits, in fact, water inputs from different lithologies with specific hydrochemical and physico-chemical characteristics. The resulting pulse discharges can be wrongly interpreted as dilution episodes if only one parameter is considered (i.e. electrical conductivity). In this perspective, water hydrochemistry

is a useful tool to better constrain the origin of the discharged water, furthermore it allows to better distinguish individual drainage systems by their specific chemical characteristics. Useful insights can be obtained cross-checking multiple parameters such as ratios between principal and minor compounds and trace elements distributions.

This integrated, multidisciplinary approach coupled with a unique long time series dataset was useful also to better comprehend the behavior of the system during anomalous flooding events, which are commonly difficult to interpret due to their recurrence. The characteristics observed during these events must be contextualized in the normal behavior of each compartment of the system, a necessity that was possible to achieve for the *Bossea* karst thanks to the large amount of data collected in the past 15-20 years.

Appendix 1. Meteorological time series

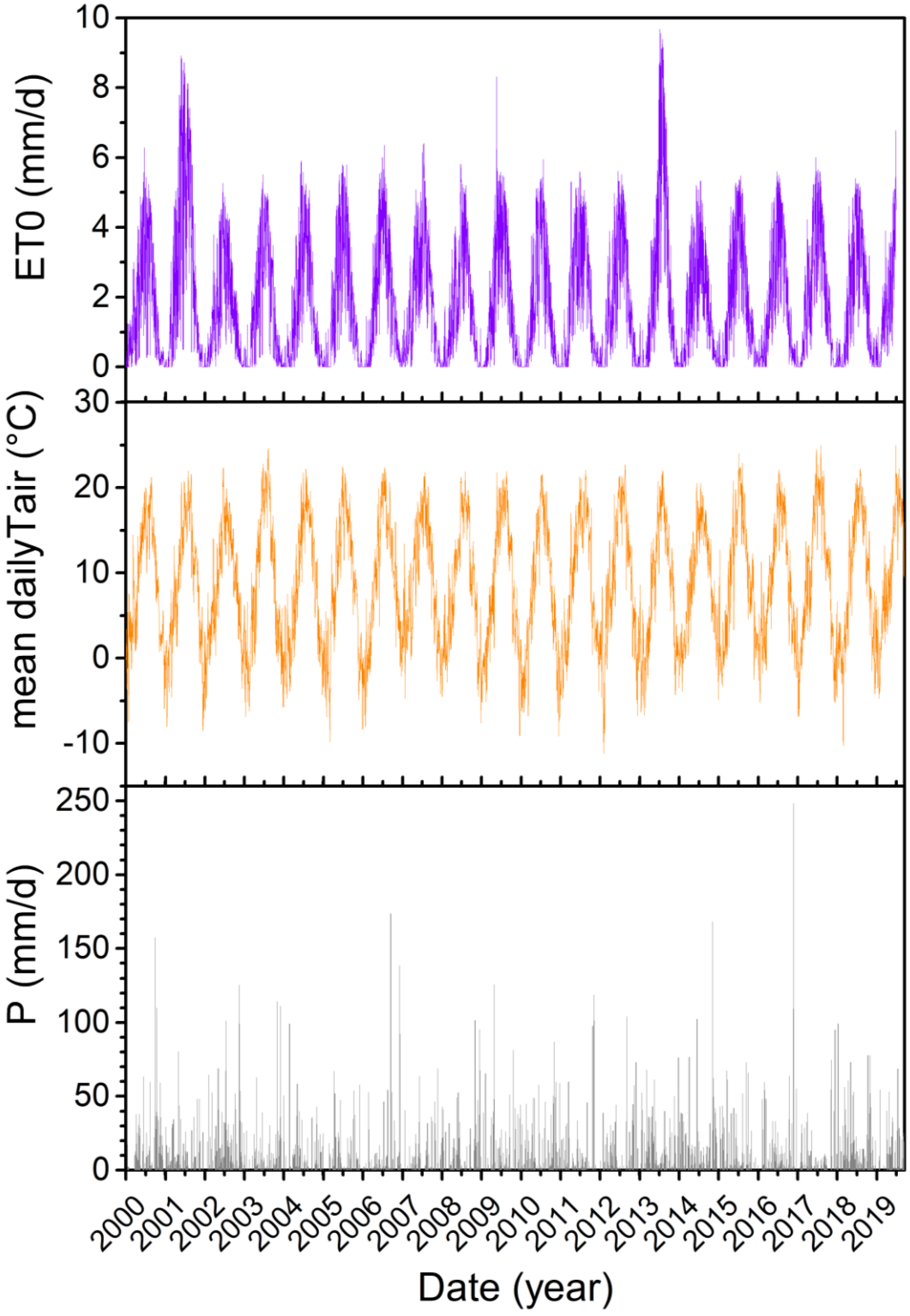

Appendix 1. Daily precipitation (P), mean daily air temperature (Tair) measured by Borello meteorological station and potential evapotranspiration (ET_0) calculated with data measured by Borello and Colle San Bernardo meteorological stations. The methods are reported in Chapter 3.

Appendix 2. Fracture flow hydrographs and chemographs

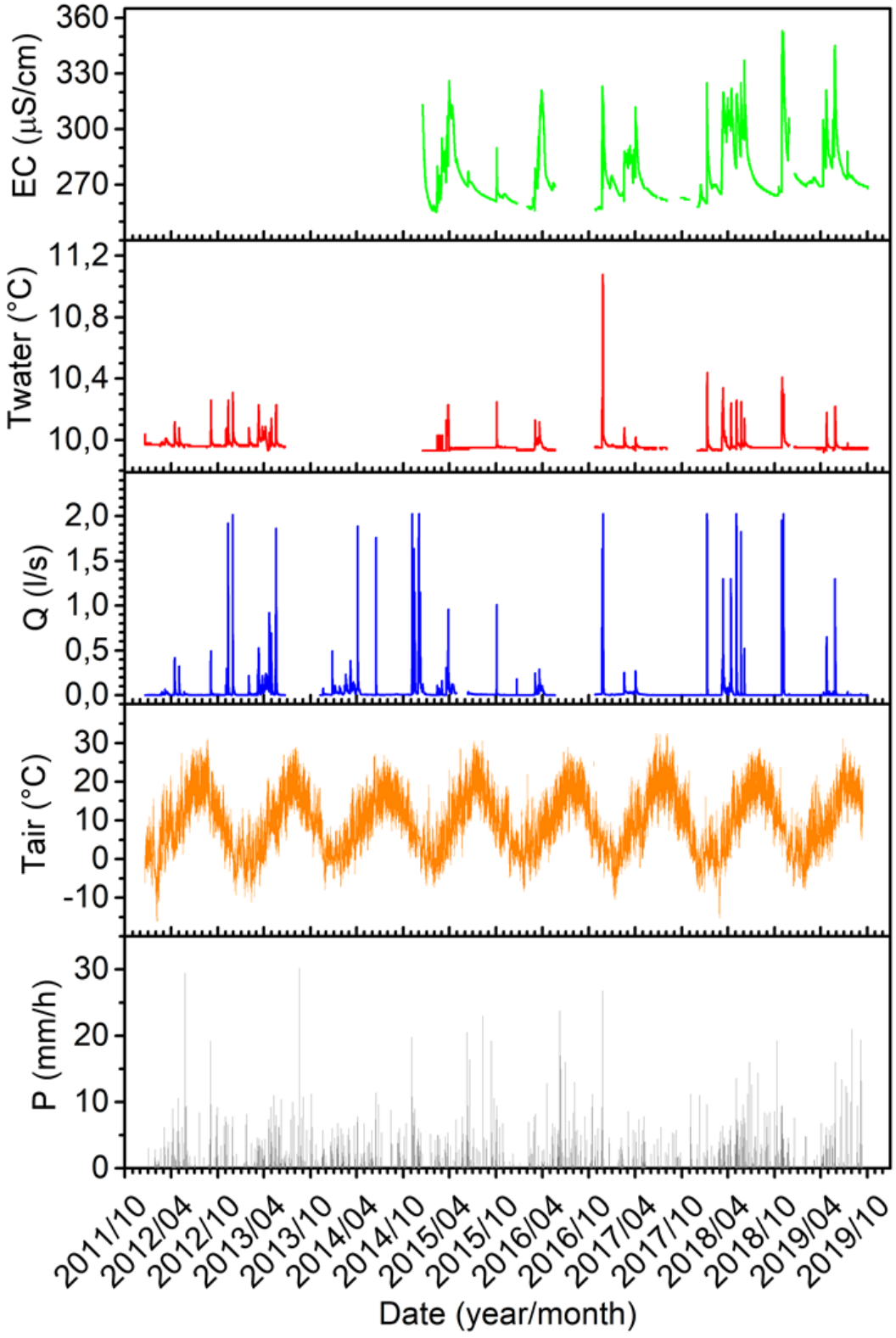

Appendix 2a. *Polla delle Anatre* (PA) hydrograph and chemographs. Hourly precipitation (P) and air temperature measured by Borello station are reported for comparison.

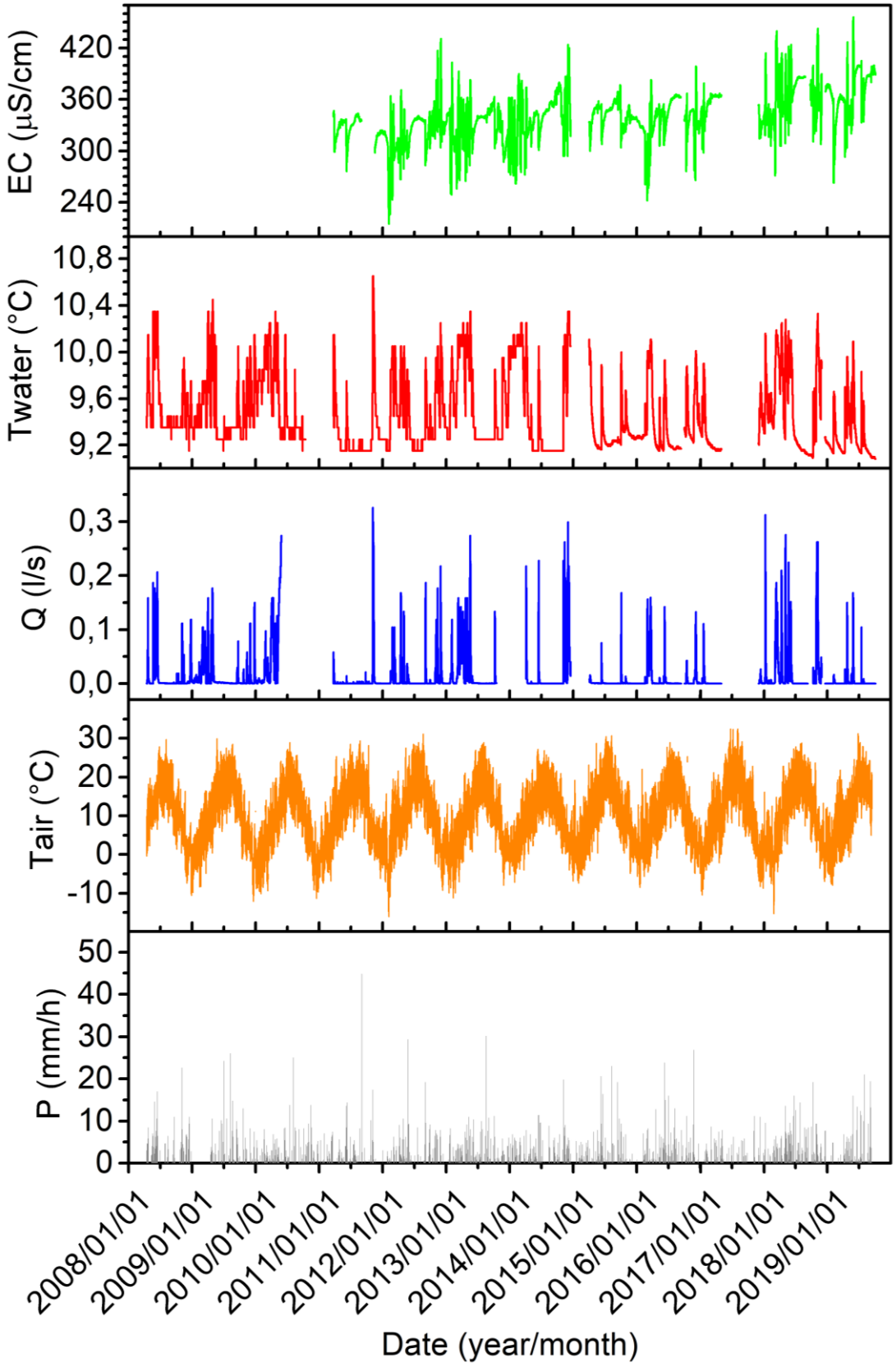

Appendix 2b. *Polletta* (PTTA) hydrograph and chemographs. Hourly precipitation and air temperature measured by Borello station are reported for comparison.

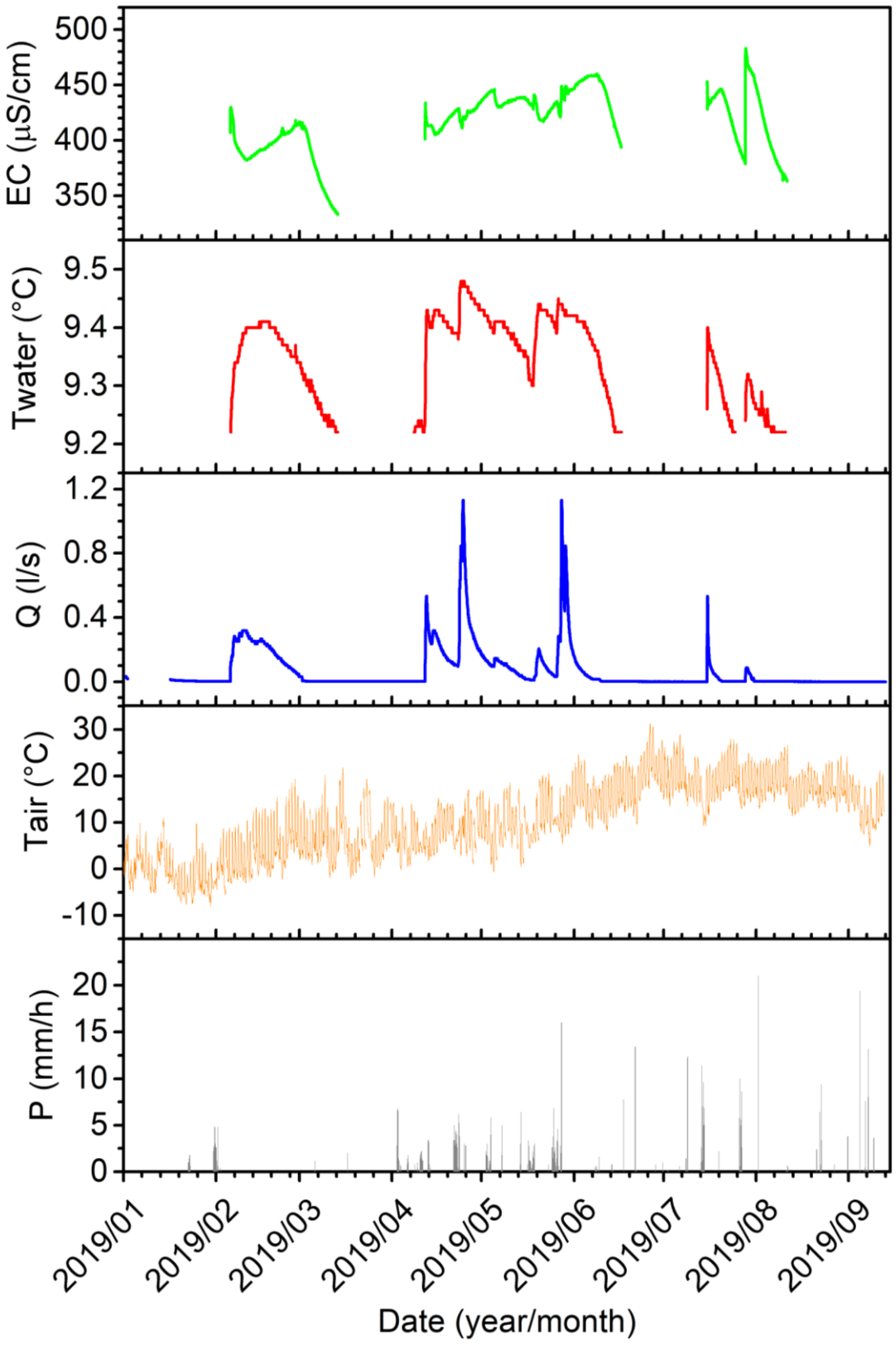

Appendix 2c. *Polla dell'Orso* (PO) hydrograph and chemographs. Hourly precipitation and air temperature measured by Borello station are reported for comparison.

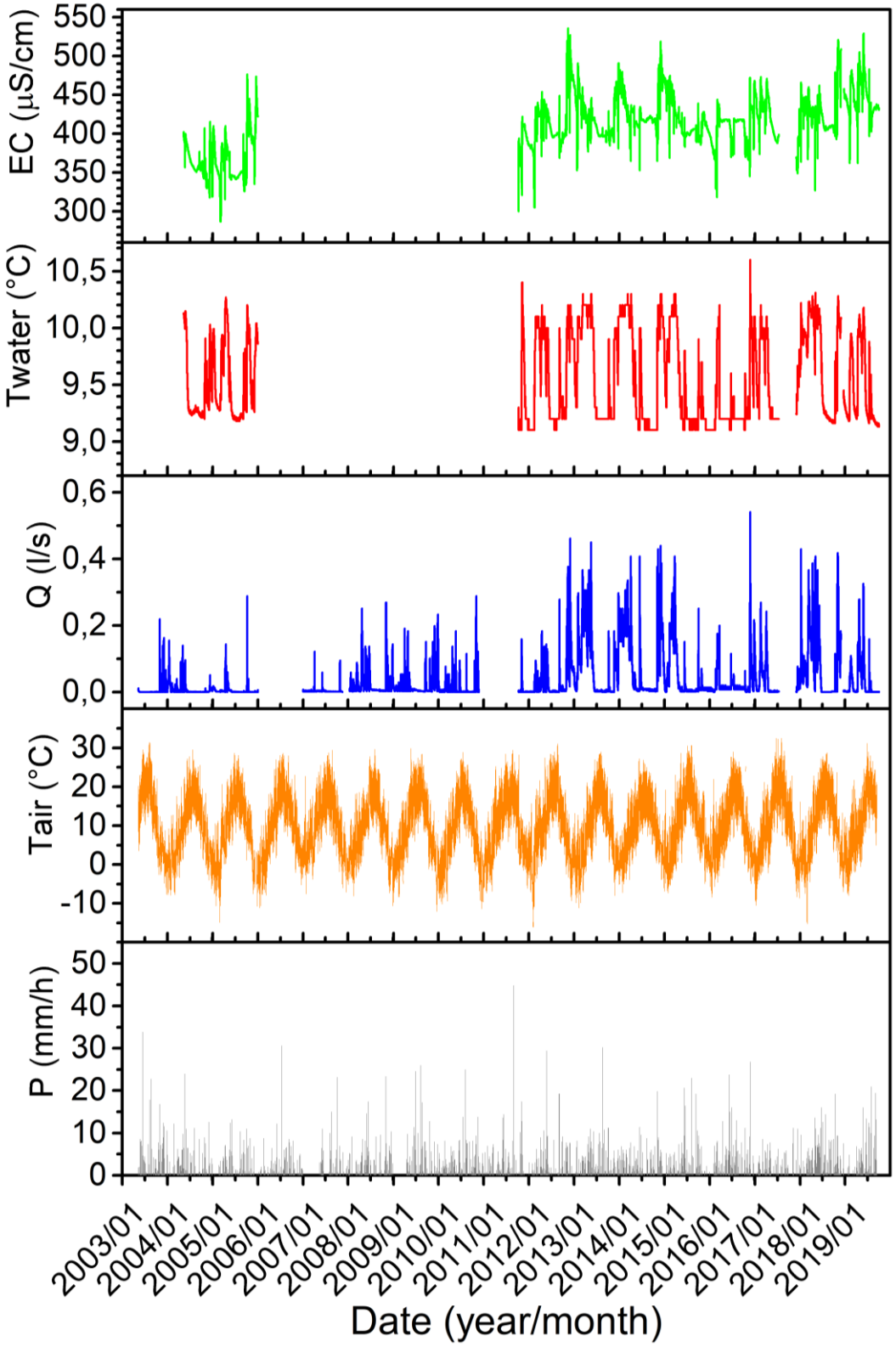

Appendix 2d. *Milano* (M) hydrograph and chemographs. Hourly precipitation and air temperature measured by Borello station are reported for comparison.

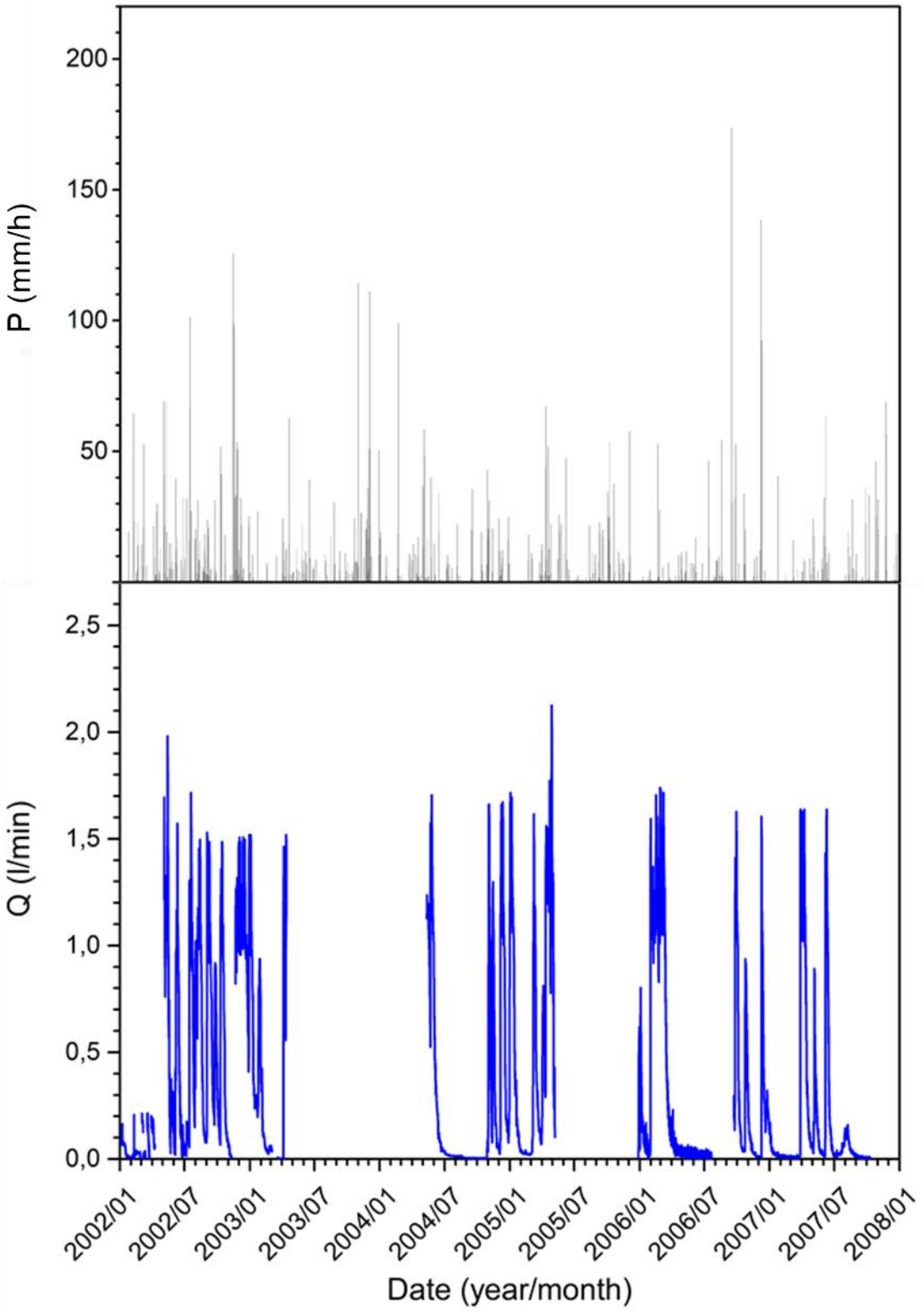

Appendix 2e. *Torre* (TO) hydrograph. Hourly precipitation (P) measured by Borello station is reported for comparison.

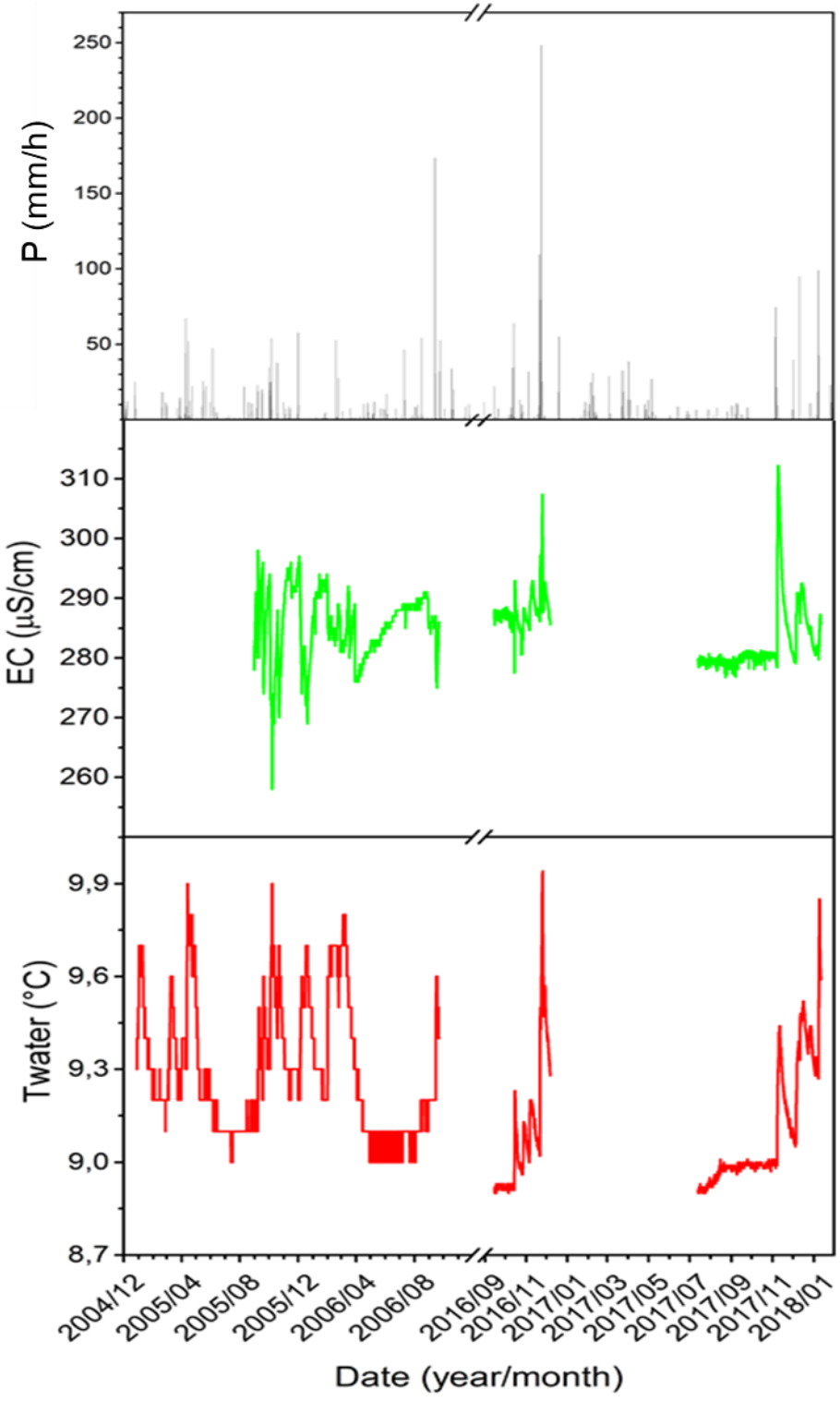

Appendix 2f. *Torre* (TO) chemographs. Hourly precipitation (P) measured by Borello station is reported for comparison.

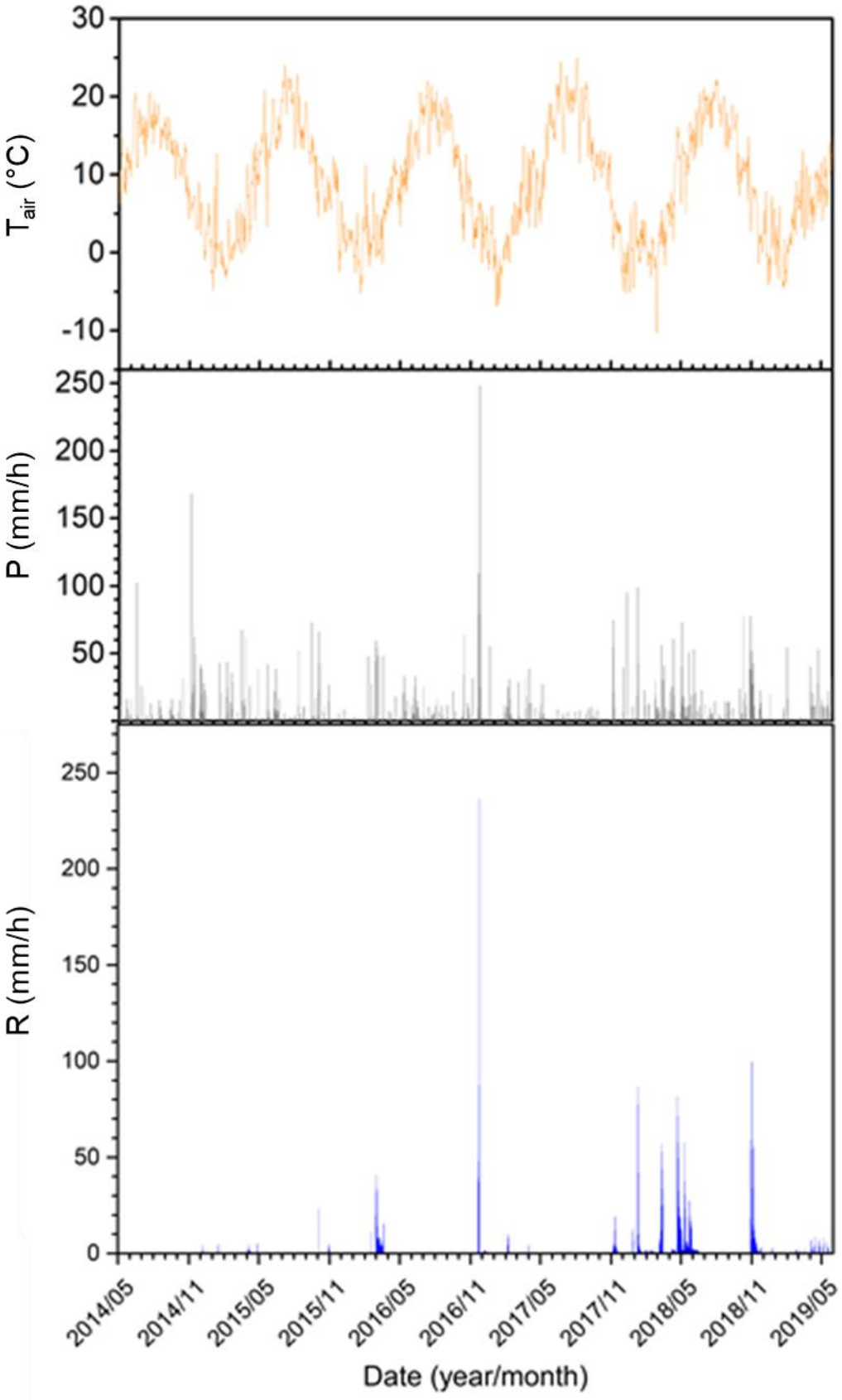

Appendix 2g. *Sacrestia* (SA) *upper* hydrograph (R). Hourly precipitation (P) and air temperature measured by Borello station are reported for comparison.

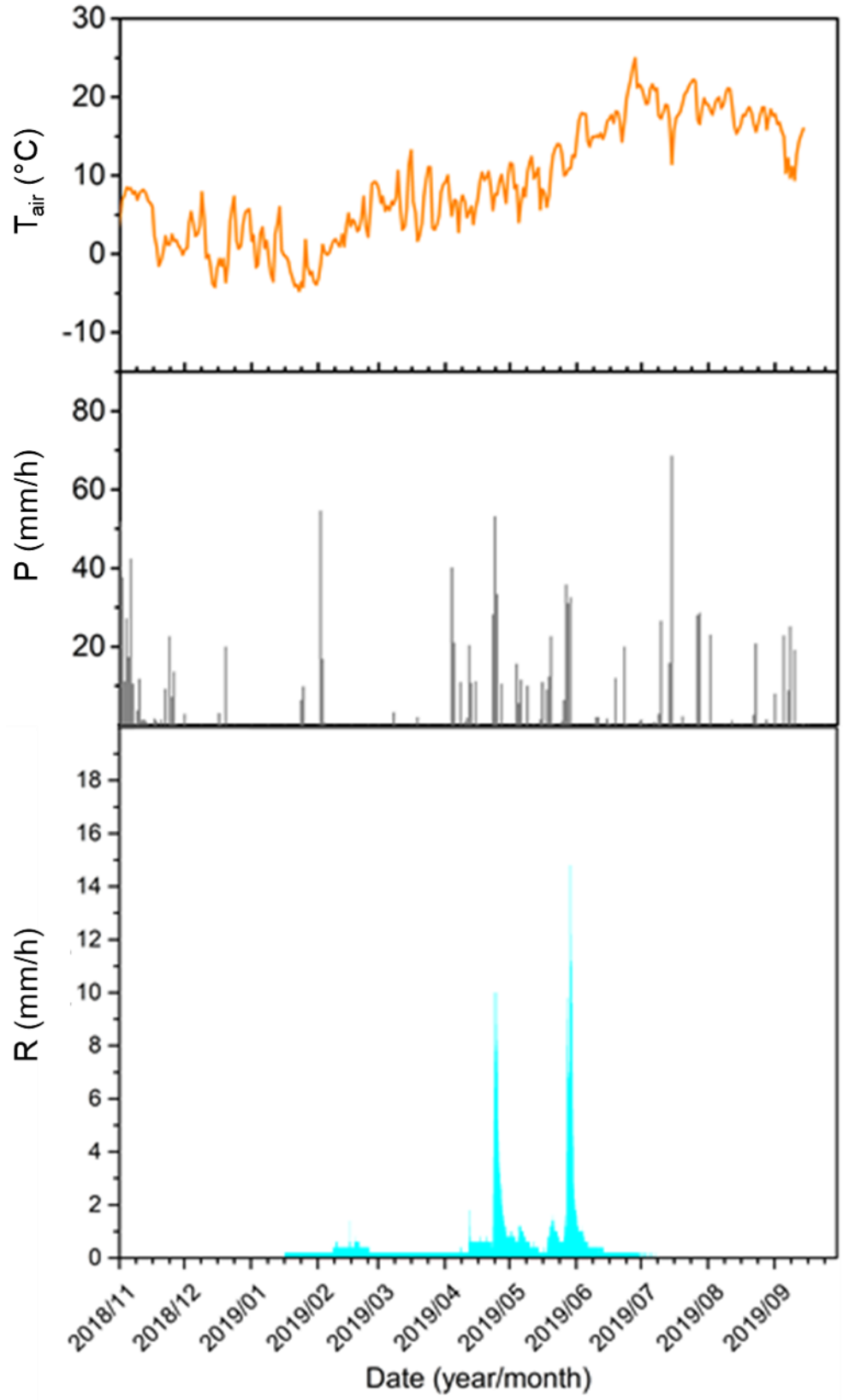

Appendix 2h. *Sacrestia* (SA) *bottom* hydrograph (R). Hourly precipitation (P) and air temperature measured by Borello station are reported for comparison.

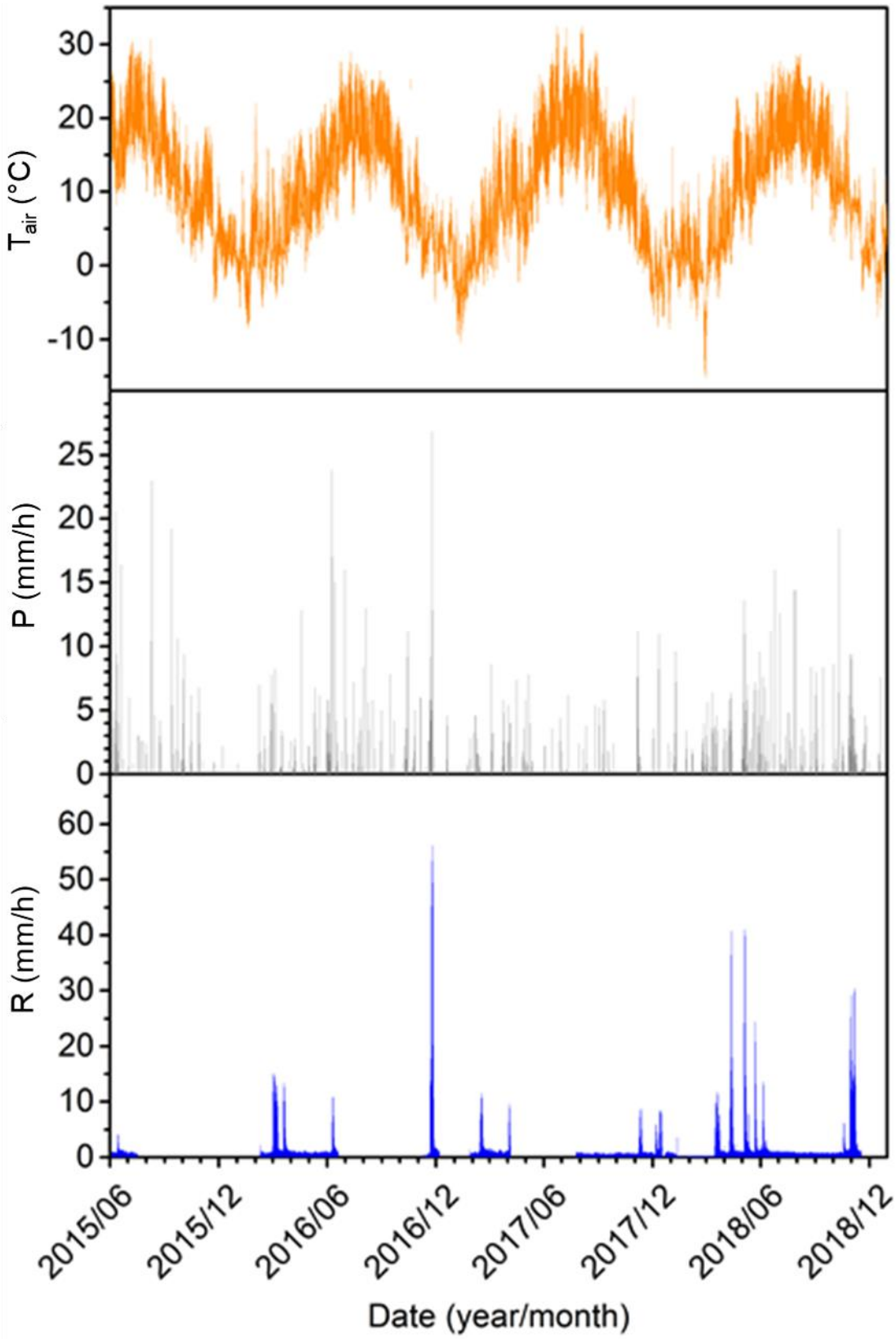

Appendix 2i. *Camcello Lab* (CA) hydrograph (R). Hourly precipitation (P) and air temperature measured by Borello station are reported for comparison.

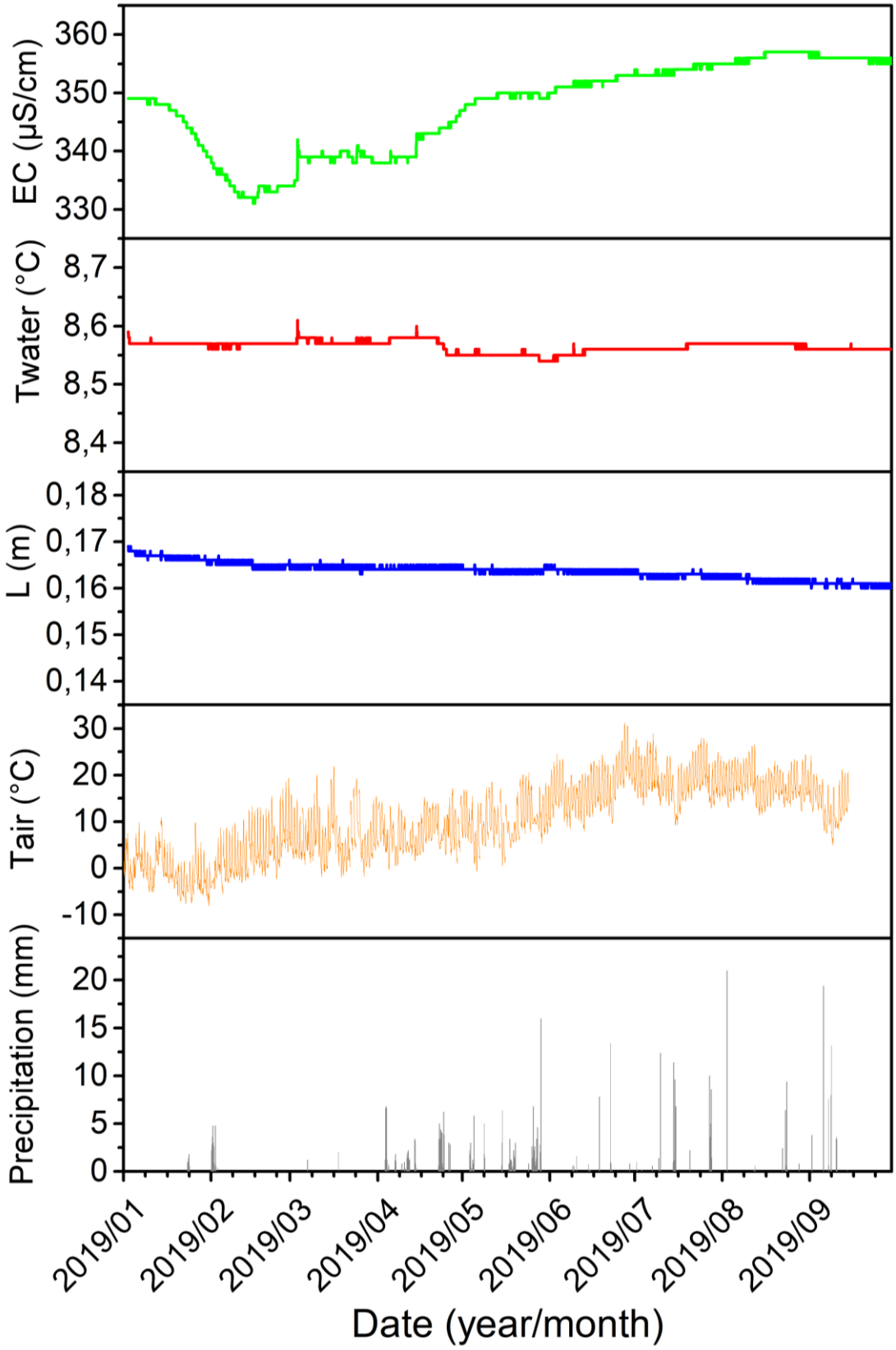

Appendix 2j. *Laghi Pensili* (LP) hydrograph and chemographs. Hourly precipitation and air temperature measured by Borello station are reported for comparison.

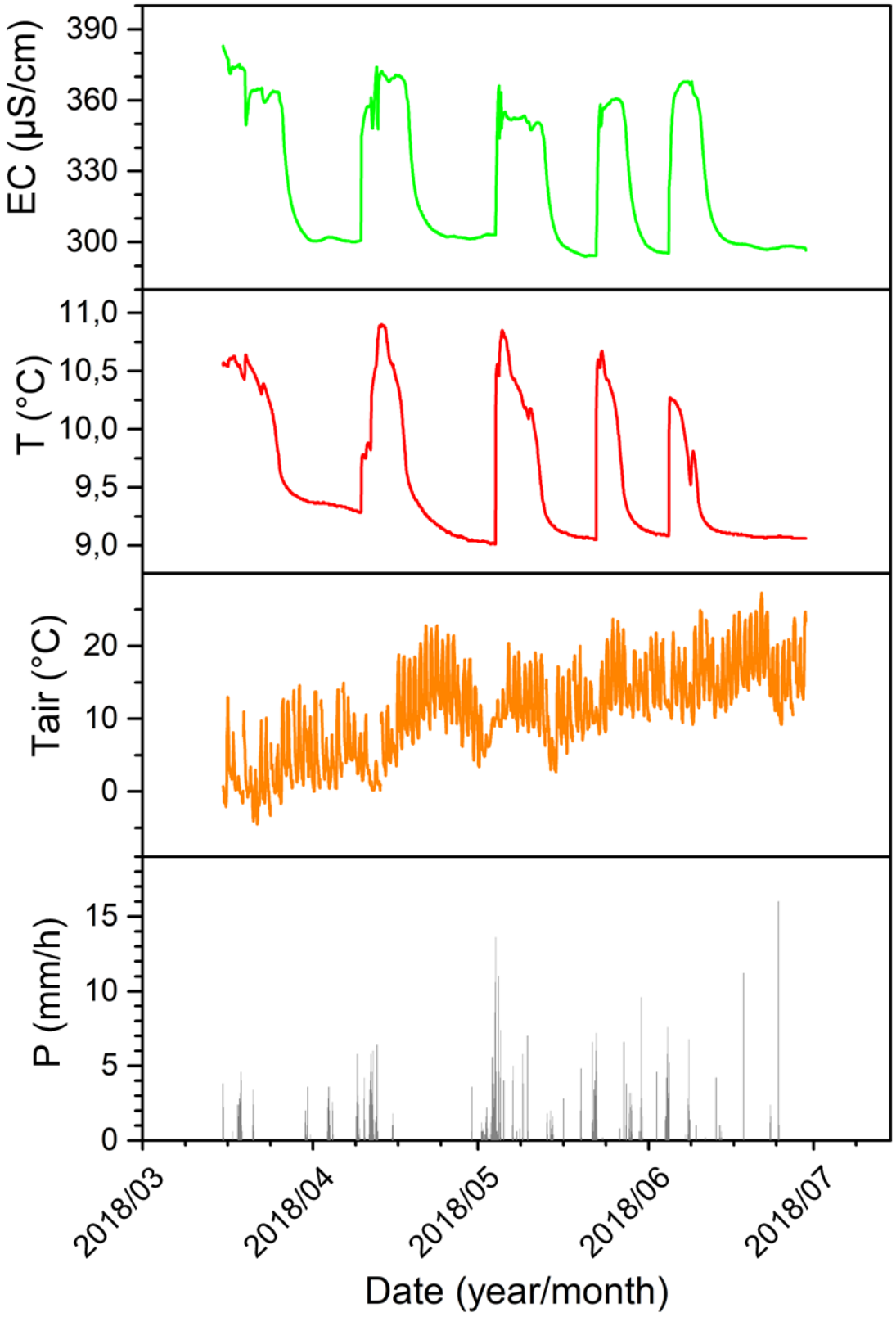

Appendix 2k. *Balena* (BA) chemographs. Hourly precipitation and air temperature measured by Borello station are reported for comparison.

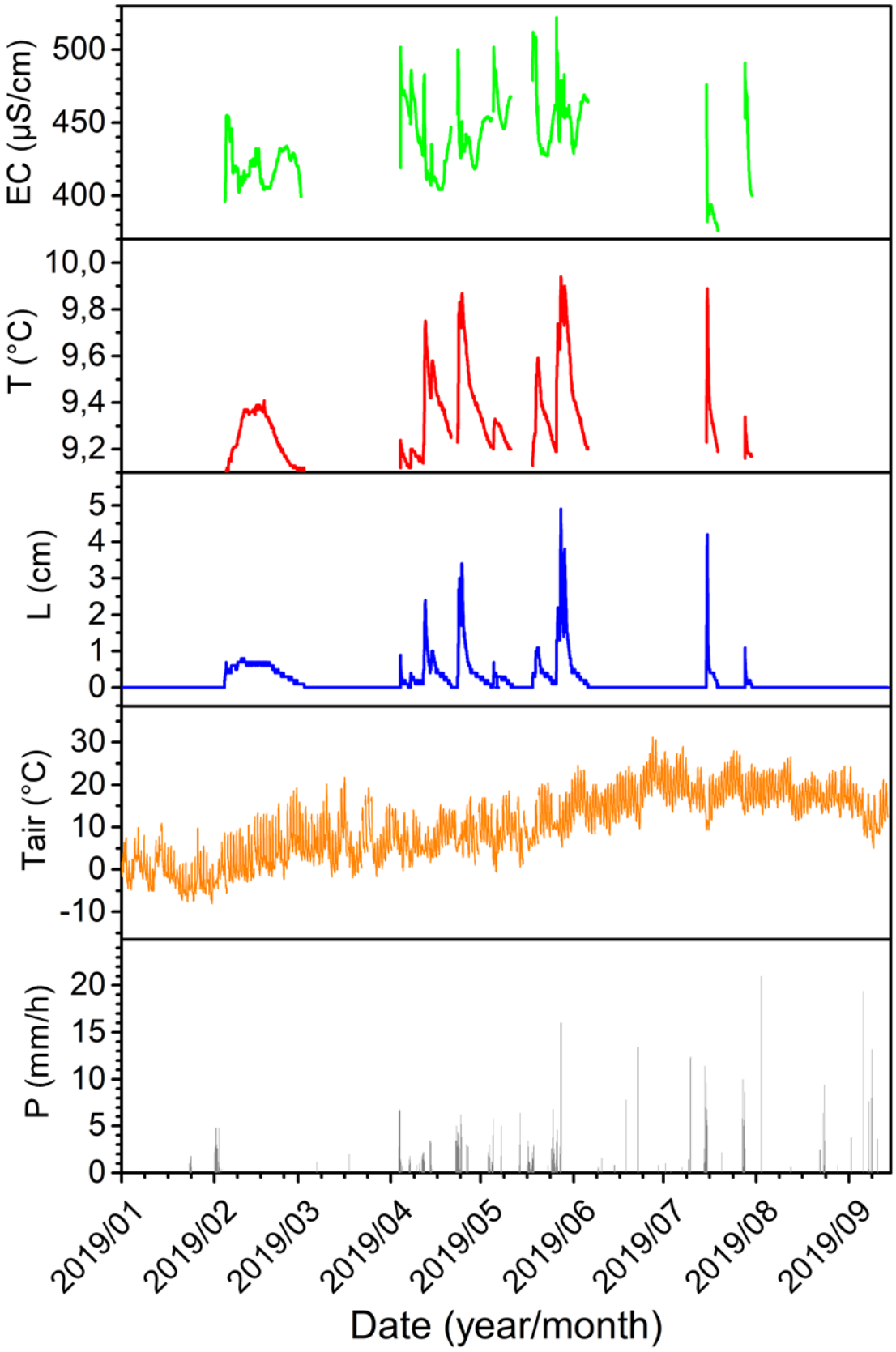

Appendix 2l. *Onda* (ON) hydrograph and chemographs. Hourly precipitation and air temperature measured by Borello station are reported for comparison.

Appendix 3. Mora creek hydrograph and chemographs

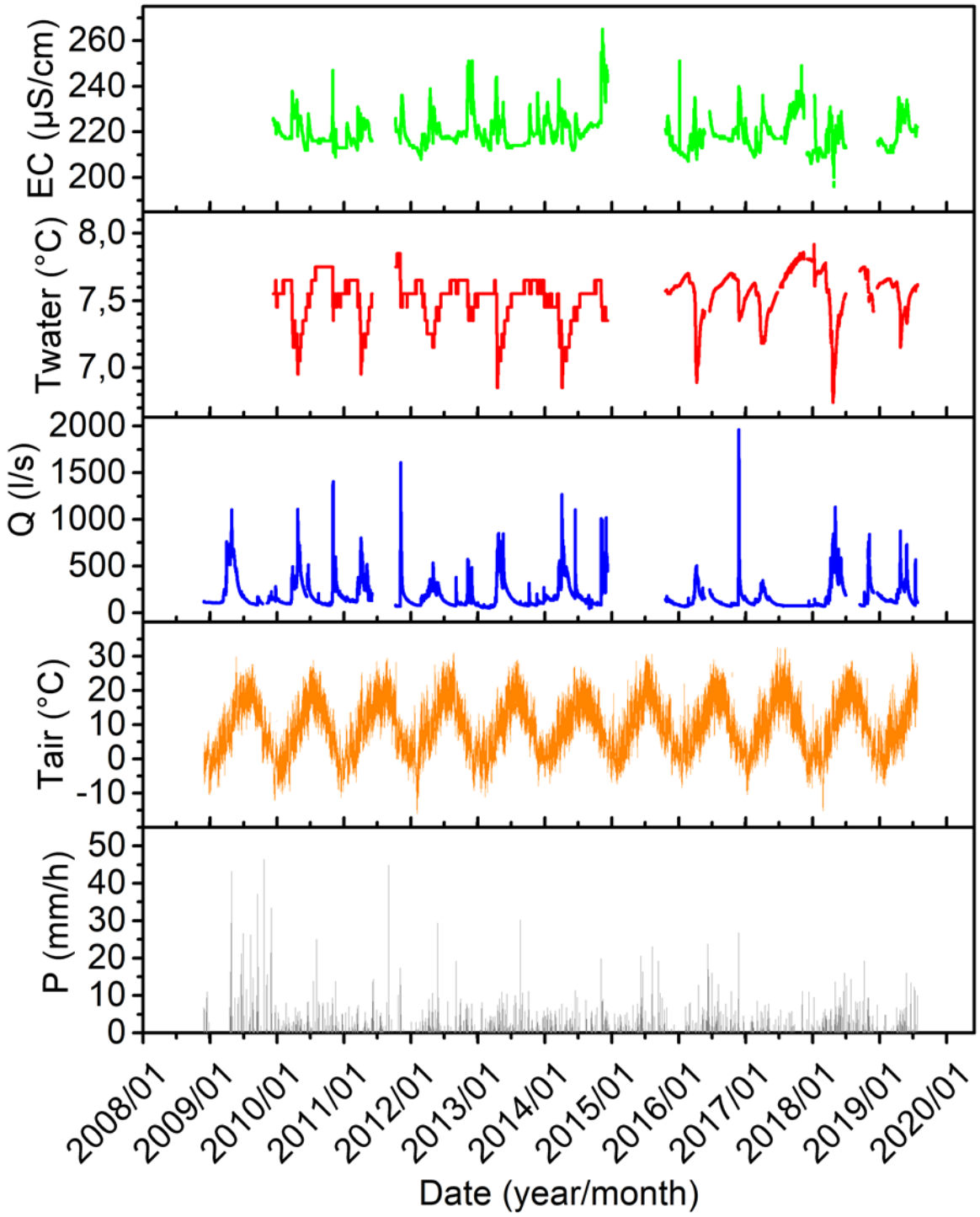

Appendix 3. *Mora creek* (TM) hydrograph and chemographs. Hourly precipitation and air temperature measured by Borello station are reported for comparison.

Appendix 4. Major hydrochemistry

Sampling point	Date day/month/year	Ca meq/l	Mg meq/l	Na+K meq/l	Cl meq/l	SO_4 meq/l	HCO_3 meq/l	NO_3 meq/l	pH [-]	T °C	SIdol [-]	SIcalc [-]
BA	15/03/2018	2.70	1.34	0.03	0.03	0.06	3.87	0.12	8.38	10.87	1.99	1.04
BA	29/10/2018	1.88	1.25	0.03	0.02	0.09	2.96	0.09				
BA	06/11/2018	3.13	1.50	0.03	0.02	0.04	4.50	0.07				
BA	15/02/2019	1.78	1.25	0.02	0.01	0.07	2.63	0.04				
BA	10/04/2019	1.88	1.22	0.02	0.01	0.08	2.76	0.04				
CA	18/06/2015	2.76	0.16	0.04	0.03	0.17	2.76	0.02	8.12	9.90	0.31	0.66
CA	22/03/2016	2.28	0.11	0.02	0.01	0.13	2.22	0.02	8.03	9.80	-0.31	0.41
CA	23/11/2016	3.06	0.15	0.02	0.01	0.10	3.06	0.02		9.27		
CA	26/11/2016	3.18	0.27	0.02	0.01	0.10	3.28	0.01		9.76		
CA	28/09/2017	2.49	0.23	0.03	0.03	0.21	2.44	0.04				
CA	09/01/2018	2.63	0.12	0.05	0.03	0.23	2.45	0.09	7.86	9.60	-0.46	0.33
CA	11/01/2018	3.04	0.09	0.07	0.06	0.17	2.85	0.22	8.10	9.40	0.08	0.69
CA	18/01/2018	2.67	0.29	0.04	0.05	0.14	2.52	0.24	8.01	9.80	0.25	0.50
CA	15/03/2018	2.78	0.24	0.02	0.01	0.18	2.73	0.10	7.76	9.60	-0.25	0.30
LP	31/03/2015	2.56	1.13	0.08	0.06	0.06	3.67	0.01	8.06	9.20	1.21	0.67
LP	11/01/2018	2.19	1.00	0.13	0.15	0.06	3.05	0.05	8.30	9.20	1.43	0.78
LP	18/01/2018	2.21	1.00	0.07	0.07	0.06	3.07	0.05	8.26	9.50	1.36	0.74
LP	15/03/2018	2.38	0.99	0.13	0.15	0.06	3.28	0.05	8.58	9.58	2.08	1.12
LP	15/02/2019	2.44	1.11	0.02	0.01	0.05	3.47	0.03				
LP	10/04/2019	2.52	1.10	0.02	0.01	0.11	3.46	0.03				
M	26/09/2006	3.00	1.47	0.02	0.02	0.06	4.32	0.03	7.97			
M	10/06/2007	3.07	1.94	0.02	0.01	0.06	4.92	0.01	7.42			
M	12/12/2008	3.39	2.27	0.03	0.03	0.07	5.63	0.01				
M	25/11/2010	3.18	2.09	0.04	0.03	0.04	5.15	0.00	7.58	10.10	0.86	0.41
M	09/10/2011	2.66	1.56	0.04	0.02	0.07	4.15	0.02				
M	09/11/2011	2.58	1.73	0.03	0.03	0.05	4.24	0.02	7.67	10.90	0.73	0.34
M	16/11/2011	2.65	1.77	0.03	0.02	0.10	4.30	0.02				
M	11/04/2012	2.80	1.56	0.03	0.01	0.05	4.31	0.01	7.92	9.91		
M	08/11/2012	2.97	2.12	0.04	0.03	0.04	5.03	0.02	8.45	10.10	2.56	1.24
M	15/03/2013	2.86	1.82	0.03	0.01	0.04	4.71	0.01	8.37	10.18	2.27	1.13
M	20/09/2013	2.73	1.54	0.03	0.01	0.05	4.22	0.03	7.77	10.00	0.89	0.46
M	17/02/2014	2.83	1.90	0.03	0.02	0.03	4.71		10.40	7.61	1.15	0.55
M	31/03/2015	2.72	2.00	0.03	0.01	0.04	4.58	0.00	7.77	10.18	1.07	0.49
M	22/03/2016	2.77	1.89	0.02	0.01	0.04	4.55	0.00	7.87	10.70	1.25	0.60
M	23/11/2016	3.01	1.68	0.02	0.02	0.04	4.55	0.01		10.03		
M	26/11/2016	2.78	1.79	0.02	0.02	0.04	4.42	0.00		10.47		
M	09/01/2018	2.90	1.72	0.05	0.03	0.08	4.27	0.23	7.97	10.10	1.37	0.69
M	11/01/2018	2.76	1.99	0.03	0.01	0.07	4.52	0.12	7.84	10.30	1.20	0.56
M	18/01/2018	2.70	1.88	0.06	0.03	0.07	4.35	0.11	8.12	10.30	1.69	0.82
M	15/03/2018	2.92	2.00	0.03	0.01	0.07	4.73	0.09	7.83	10.20	1.24	0.59
M	15/10/2018	2.85	1.40	0.02	0.01	0.07	4.04	0.11				
M	25/10/2018	2.93	1.36	0.03	0.01	0.07	4.11	0.11				
M	29/10/2018	3.03	1.35	0.02	0.02	0.05	4.28	0.10				
M	06/11/2018	3.50	2.18	0.03	0.03	0.05	5.52	0.07				
M	15/02/2019	2.91	1.98	0.03	0.01	0.05	4.78	0.03				
M	10/04/2019	2.82	1.55	0.03	0.01	0.06	4.27	0.04				

Sampling point	Date day/month/year	Ca meq/l	Mg meq/l	Na+K meq/l	Cl meq/l	SO_4 meq/l	HCO_3 meq/l	NO_3 meq/l	pH [-]	T °C	SIdol [-]	SIcalc [-]
ON	09/01/2018	2.56	1.03	0.09	0.09	0.08	3.25	0.19				
ON	15/03/2018	2.84	1.12	0.12	0.12	0.09	3.78	0.09	7.87	10.00	0.89	0.54
ON	15/02/2019	3.28	1.38	0.11	0.06	0.07	4.53	0.02				
ON	10/04/2019	3.37	1.45	0.09	0.06	0.05	4.60	0.03				
PA	10/06/2007	2.52	0.69	0.07	0.02	0.07	3.08	0.06	7.44			
PA	12/12/2008	2.51	0.56	0.07	0.03	0.09	2.91	0.14				
PA	20/11/2009	2.39	0.35	0.04	0.03	0.06	2.74	0.04				
PA	25/11/2010	2.54	0.72	0.07	0.02	0.06	3.10	0.06	7.69	10.00	0.15	0.24
PA	04/04/2011	2.44	0.72	0.06	0.01	0.07	3.08	0.08				
PA	09/10/2011	2.22	0.48	0.04	0.01	0.06	2.65	0.04				
PA	09/11/2011	2.66	0.59	0.06	0.03	0.07	3.19	0.08				
PA	11/04/2012	2.38	0.53	0.06	0.04	0.06	2.76	0.04	7.90	9.94	0.32	0.38
PA	08/11/2012	2.49	0.71	0.04	0.02	0.05	3.15	0.06	8.98	10.00	1.13	0.73
PA	15/03/2013	2.49	0.62	0.07	0.01	0.04	3.07	0.02	8.31	9.10	1.31	0.85
PA	20/09/2013	2.25	0.51	0.04	0.03	0.06	2.59	0.03	7.64	9.40	-0.29	0.07
PA	17/02/2014	2.52	0.51	0.07	0.01	0.06	2.88	0.04	7.76	8.90	0.07	0.27
PA	31/03/2015	2.63	0.87	0.07	0.02	0.04	3.39	0.05	7.84	9.10	0.61	0.43
PA	04/01/2016	2.16	0.51	0.04	0.03	0.06	2.57	0.03				
PA	22/03/2016	2.44	0.76	0.05	0.02	0.06	3.03	0.04	7.83	9.80	0.42	0.35
PA	23/11/2016	2.70	0.56	0.04	0.02	0.05	3.08	0.05		10.28		
PA	26/11/2016	2.72	0.56	0.05	0.02	0.05	3.11	0.04		10.04		
PA	30/08/2017	2.21	0.49	0.04	0.02	0.04	2.64	0.03				
PA	09/01/2018	2.51	0.54	0.02	0.02	0.09	2.62	0.33	7.64	9.42	-0.23	0.11
PA	11/01/2018	2.43	0.57	0.03	0.03	0.08	2.76	0.18	7.90	9.30	0.35	0.38
PA	18/01/2018	2.31	0.49	0.05	0.04	0.08	2.62	0.11	7.80	9.60	0.02	0.24
PA	15/03/2018	2.55	0.57	0.06	0.06	0.09	2.91	0.13	8.02	10.38	0.66	0.55
PA	15/10/2018	2.21	0.47	0.04	0.02	0.08	2.51	0.09				
PA	29/10/2018	2.26	0.43	0.04	0.02	0.07	2.58	0.09				
PA	06/11/2018	2.89	0.61	0.03	0.01	0.06	3.35	0.07				
PA	15/02/2019	2.28	0.55	0.04	0.01	0.07	2.67	0.05				
PA	10/04/2019	1.66	0.55	0.04	0.01	0.07	2.60	0.05				
PO	26/09/2006	3.89	0.42	0.02	0.02	0.09	4.07	0.02	7.61	10.12	0.14	0.44
PO	10/06/2007	3.59	0.38	0.02	0.01	0.10	3.82	0.01	7.15	10.40	-0.91	-0.07
PO	12/12/2008	3.63	0.44	0.03	0.02	0.11	3.98	0.01				
PO	25/11/2010	4.00	0.23	0.05	0.03	0.08	4.21	0.00	6.91	9.36	-1.50	-0.23
PO	04/04/2011	4.07	0.19	0.03	0.03	0.11	4.14					
PO	09/11/2011	3.24	0.41	0.03	0.03	0.07	3.59	0.02	7.56	9.20	-0.14	0.27
PO	16/11/2011	3.62	0.38	0.04	0.04	0.10	3.96	0.02				
PO	11/04/2012	3.64	0.35	0.03	0.02	0.14	3.91	0.00	7.67	9.22	0.12	0.46
PO	08/11/2012	3.60	0.45	0.02	0.02	0.08	3.86	0.04	8.42	9.40	-0.29	0.20
PO	15/03/2013	4.10	0.14	0.03	0.01	0.09	4.15	0.01	8.49	9.40	-0.53	0.35
PO	17/02/2014	3.73	0.26	0.02	0.02	0.07	3.87		7.48	9.70	-0.40	0.27
PO	31/03/2015	3.73	0.43	0.04	0.02	0.07	4.11	0.00	7.54	9.50	0.00	0.36
PO	22/03/2016	3.05	0.41	0.03	0.03	0.07	3.33	0.00	7.55	9.80	-0.25	0.20
PO	23/11/2016	3.55	0.57	0.02	0.03	0.07	4.01	0.01		9.52		
PO	26/11/2016	3.52	0.62	0.02	0.02	0.07	3.98	0.00		9.72		
PO	09/01/2018	3.02	0.40	0.03	0.02	0.11	3.10	0.21	7.46	9.60	-0.59	-0.02
PO	11/01/2018	3.33	0.34	0.04	0.04	0.12	3.28	0.22	7.53	9.60	-0.35	0.21
PO	18/01/2018	3.45	0.34	0.04	0.03	0.13	3.41	0.21	7.68	9.80	0.00	0.39
PO	15/03/2018	3.38	0.60	0.03	0.03	0.13	3.74	0.11	7.65	9.66	0.12	0.25
PO	29/10/2018	4.54	0.42	0.02	0.02	0.11	4.79	0.09				
PO	06/11/2018	3.99	0.34	0.03	0.02	0.08	4.15	0.07				
PO	15/02/2019	3.67	0.36	0.02	0.01	0.13	3.85	0.03				
PO	14/04/2019	1.54	0.61	0.02	0.01	0.13	4.50	0.03				

Sampling point	Date day/month/year	Ca meq/l	Mg meq/l	Na+K meq/l	Cl meq/l	SO_4 meq/l	HCO_3 meq/l	NO_3 meq/l	pH [-]	T °C	SIdol [-]	SIcalc [-]
PTTA	26/09/2006	2.81	0.82	0.02	0.01	0.05	3.53	0.03	7.86	10.35	0.69	0.50
PTTA	10/06/2007	2.91	1.22	0.02	0.02	0.05	3.94	0.01	7.42	10.15	0.07	0.12
PTTA	12/12/2008	2.81	1.22	0.02	0.02	0.06	3.93	0.02				
PTTA	25/11/2010	3.28	0.99	0.02	0.02	0.03	4.32	0.00	7.55	10.05	0.37	0.33
PTTA	04/04/2011	2.44	1.01	0.05	0.04	0.06	3.45	0.00				
PTTA	09/11/2011	2.50	1.32	0.02	0.02	0.04	3.87	0.02	7.64	10.00	0.48	0.27
PTTA	16/11/2011	2.45	0.96	0.02	0.01	0.05	3.41	0.02				
PTTA	11/04/2012	2.48	0.89	0.02	0.01	0.04	3.35	0.01	8.01	9.48	0.93	0.58
PTTA	08/11/2012	2.81	0.85	0.03	0.03	0.04	3.59	0.08	8.62	9.80	0.24	0.27
PTTA	15/03/2013	2.77	1.44	0.03	0.01	0.04	4.21	0.02	8.35	10.08	0.03	0.05
PTTA	20/09/2013	2.87	1.27	0.02	0.01	0.04	4.02	0.04	7.83	9.50	0.92	0.53
PTTA	17/02/2014	2.76	1.33	0.02	0.01	0.03	4.04	0.00	7.63	10.10	0.54	0.32
PTTA	31/03/2015	2.69	1.54	0.04	0.02	0.03	4.25	0.01	7.73	10.16	0.82	0.42
PTTA	22/03/2016	2.66	1.52	0.02	0.01	0.04	4.10	0.01	7.81	10.40	0.94	0.48
PTTA	23/11/2016	2.64	0.96	0.02	0.02	0.04	3.56	0.01		10.04		
PTTA	26/11/2016	2.62	1.34	0.02	0.02	0.04	3.90	0.00		10.67		
PTTA	28/09/2017	2.35	1.28	0.03	0.03	0.05	3.54	0.02				
PTTA	09/01/2018	2.55	0.97	0.02	0.02	0.08	3.08	0.32	8.13	10.00	1.14	0.67
PTTA	11/01/2018	2.79	1.48	0.03	0.03	0.07	3.98	0.20	7.69	10.10	0.68	0.37
PTTA	18/01/2018	2.57	0.86	0.03	0.03	0.07	3.08	0.24	8.18	11.10	1.20	0.73
PTTA	15/03/2018	2.88	1.71	0.03	0.03	0.07	4.41	0.14	7.54	10.30	0.53	0.27
PTTA	15/10/2018	2.91	1.06	0.02	0.02	0.07	3.81	0.11				
PTTA	29/10/2018	2.97	0.77	0.02	0.02	0.05	3.63	0.10				
PTTA	06/11/2018	3.35	1.71	0.03	0.02	0.05	4.86	0.07				
PTTA	15/02/2019	2.72	0.94	0.02	0.01	0.05	3.47	0.04				
PTTA	10/04/2019	2.72	1.28	0.02	0.01	0.05	3.83	0.05				
SA	12/12/2008	3.77	0.06	0.03	0.03	0.12	3.72	0.00				
SA	25/11/2010	4.45	0.07	0.03	0.03	0.08	4.47	0.00	7.40	9.75	-0.93	0.32
SA	04/04/2011	4.30	0.08	0.03	0.02	0.10	4.28					
SA	09/11/2011	3.73	0.08	0.03	0.03	0.07	3.72	0.02				
SA	16/11/2011	4.20	0.10	0.03	0.03	0.07	4.17	0.04				
SA	11/04/2012	4.36	0.18	0.04	0.02	0.08	4.50	0.00	7.68	9.57	0.04	0.60
SA	08/11/2012	3.06	0.39	0.02	0.03	0.05	3.36	0.07	7.98	9.80	0.60	0.64
SA	15/03/2013	4.22	0.13	0.04	0.03	0.07	4.29	0.00	8.45	9.77	1.37	1.34
SA	17/02/2014	4.04	0.22	0.03	0.01	0.07	4.22		7.57	10.10	-0.18	0.43
SA	31/03/2015	4.36	0.11	0.08	0.06	0.07	4.52		7.74	10.33	-0.06	0.66
SA	22/03/2016	3.30	0.08	0.07	0.08	0.08	3.30	0.00	7.93	10.10	-0.18	0.62
SA	23/11/2016	3.27	0.29	0.02	0.02	0.06	3.46	0.01		9.84		
SA	26/11/2016	4.04	0.35	0.03	0.03	0.09	4.27	0.00		9.99		
SA	09/01/2018	2.77	0.46	0.02	0.02	0.09	2.91	0.23	7.70	9.80	-0.05	0.26
SA	11/01/2018	3.13	0.21	0.02	0.02	0.11	3.01	0.17	7.99	9.80	0.27	0.61
SA	18/01/2018	3.06	0.22	0.05	0.05	0.12	2.96	0.12	8.03	10.40	0.35	0.64
SA	15/03/2018	4.11	0.30	0.04	0.04	0.09	4.22	0.06	8.13	9.82	1.08	1.00
SA	29/10/2018	4.23	0.19	0.03	0.03	0.06	4.33	0.08				
SA	06/11/2018	4.42	0.19	0.04	0.04	0.08	4.46	0.07				
SA	15/02/2019	4.02	0.15	0.04	0.01	0.14	3.82	0.01				
SA	10/04/2019	1.59	0.38	0.04	0.01	0.13	3.16	0.02				
TO	26/09/2006	3.10	0.18	0.02	0.01	0.04	3.18	0.01	8.02	9.45	0.32	0.66
TO	10/06/2007	2.78	0.18	0.02	0.02	0.05	2.92	0.03	7.58	9.35	-0.68	0.15
TO	12/12/2008	2.61	0.14	0.02	0.02	0.04	2.71	0.01				
TO	25/11/2010	2.86	0.18	0.02	0.02	0.06	2.98	0.01				
TO	09/11/2011	2.72	0.14	0.02	0.02	0.06	2.79	0.03	7.71	9.50	-0.56	0.25
TO	11/04/2012	2.50	0.09	0.02	0.01	0.03	2.56	0.01	8.05	9.05	-0.18	0.52
TO	08/11/2012	3.00	0.11	0.02	0.02	0.03	3.06	0.04	8.75	9.50	0.32	0.77
TO	15/03/2013	2.52	0.18	0.02	0.01	0.03	2.62	0.02	8.33	9.64	0.71	0.81
TO	20/09/2013	2.63	0.21	0.03	0.01	0.03	2.76	0.02	7.92	9.50	0.01	0.44
TO	17/02/2014	2.56	0.19	0.02	0.01	0.02	2.73	0.00	7.77	10.00	-0.36	0.28
TO	31/03/2015	2.57	0.18	0.02	0.01	0.02	2.74	0.02	8.08	10.10	0.24	0.59
TO	22/03/2016	2.46	0.14	0.03	0.03	0.02	2.60	0.01	8.28	10.00	0.49	0.75
TO	23/11/2016	2.70	0.15	0.01	0.01	0.03	2.81	0.00		9.54		
TO	26/11/2016	2.86	0.21	0.02	0.01	0.03	3.03	0.01		9.89		
TO	09/01/2018	2.71	0.43	0.02	0.02	0.06	2.99	0.09	8.22	9.80		
TO	11/01/2018	2.56	0.18	0.07	0.06	0.06	2.64	0.04	8.02	9.90		
TO	18/01/2018	2.55	0.18	0.03	0.02	0.05	2.58	0.09	8.14	11.40		
TO	15/03/2018	2.45	0.16	0.02	0.02	0.04	2.53	0.03	8.13	10.03		
TO	29/10/2018	3.06	0.21	0.02	0.02	0.04	3.18	0.08				
TO	06/11/2018	3.22	0.22	0.03	0.02	0.04	3.29	0.08				
TO	15/02/2019	2.74	0.17	0.02	0.01	0.04	2.66	0.02				
TO	10/04/2019	1.45	0.45	0.02	0.01	0.04	2.28	0.04				

Sampling point	Date day/month/year	Ca meq/l	Mg meq/l	Na+K meq/l	Cl meq/l	SO_4 meq/l	HCO_3 meq/l	NO_3 meq/l	pH [-]	T °C	SIdol [-]	SIcalc [-]
TM	22/09/2006	1.85	0.33	0.04	0.03	0.05	2.08	0.04	8.01	8.50	0.00	0.27
TM	26/09/2006	1.94	0.31	0.04	0.03	0.05	2.09	0.04	7.89	8.60	-0.24	0.17
TM	10/06/2007	2.06	0.35	0.03	0.03	0.04	2.35	0.01	7.51	7.43	-0.83	-0.14
TM	12/12/2008	1.84	0.28	0.04	0.04	0.06	2.10	0.04				
TM	20/11/2009	1.94	0.20	0.04	0.03	0.05	2.12	0.03				
TM	25/11/2010	2.05	0.23	0.04	0.03	0.04	2.30	0.03	7.67	7.46	-0.70	0.01
TM	04/04/2011	1.79	0.33	0.02	0.02	0.03	2.11	0.04				
TM	09/10/2011	1.91	0.23	0.04	0.04	0.05	2.16	0.05				
TM	09/11/2011	2.03	0.32	0.02	0.02	0.04	2.34	0.03	7.83	7.40	-0.24	0.17
TM	16/11/2011	2.10	0.24	0.03	0.03	0.04	2.24	0.04				
TM	11/04/2012	2.01	0.22	0.03	0.02	0.04	2.16	0.03	7.84	7.28	-0.45	0.15
TM	08/11/2012	2.00	0.53	0.03	0.02	0.04	2.52	0.03	8.96	7.60	0.29	0.32
TM	15/03/2013	1.80	0.35	0.05	0.03	0.05	2.14	0.03	8.55	7.89	0.13	0.31
TM	20/09/2013	1.86	0.22	0.05	0.04	0.05	2.01	0.03	7.72	8.60	-0.77	-0.03
TM	17/02/2014	1.87	0.29	0.05	0.02	0.05	2.15	0.02	7.80	8.40	-0.44	0.08
TM	31/03/2015	2.00	0.43	0.04	0.02	0.04	2.39	0.03	7.99	8.50	0.22	0.34
TM	04/01/2016	1.95	0.25	0.05	0.02	0.07	2.10	0.04				
TM	22/03/2016	1.93	0.23	0.06	0.05	0.05	2.14	0.03	8.10	9.20	0.08	0.39
TM	01/10/2016	2.12	0.15	0.05	0.01	0.04	2.26	0.02				
TM	30/08/2017	1.89	0.29	0.06	0.03	0.04	2.12	0.03				
TM	09/01/2018	1.91	0.37	0.07	0.06	0.07	2.13	0.08	8.07	8.50	0.20	0.35
TM	11/01/2018	1.91	0.51	0.03	0.02	0.07	2.23	0.10	8.30	9.00	0.83	0.59
TM	18/01/2018	1.85	0.35	0.05	0.04	0.07	2.04	0.08	8.21	9.30	0.41	0.46
TM	15/03/2018	1.86	0.40	0.05	0.04	0.06	2.13	0.07	8.03	7.70	0.15	0.30
TM	15/10/2018	1.95	0.29	0.05	0.04	0.07	2.08	0.10				
TM	29/10/2018	1.95	0.27	0.02	0.02	0.07	2.11	0.09				
TM	06/11/2018	2.28	0.15	0.03	0.02	0.05	2.29	0.09				
TM	15/02/2019	1.89	0.20	0.05	0.02	0.06	2.03	0.06				
TM	10/04/2019	1.93	0.32	0.04	0.02	0.06	2.13	0.06				
SdM	11/04/2012	2.04	0.08	0.15	0.02	0.06	2.17	0.01	8.00	9.25	-0.55	0.32
SdM	08/11/2012	1.63	0.19	0.14	0.02	0.06	1.94	0.03	7.70	10.60	-0.95	-0.11
SdM	15/03/2013	1.13	0.20	0.14	0.02	0.08	1.28	0.02	8.75	8.95	0.68	0.61
SdM	31/03/2015	1.13	0.10	0.14	0.01	0.06	1.27	0.02	7.29	9.17	-0.56	0.15
SdM	22/03/2016	1.06	0.06	0.09	0.01	0.07	1.10	0.03	7.53	9.50	-0.41	0.31

BA = Balena

CA = Cancello

LP = Laghi Pensili

M = Milano

ON = Onda

PA = Polla delle Anatre

PO = Polla dell'orso

PTTA = Polletta

SA = Sacrestia

TM = Mora creek

TO = Torre

SdM = Sorgente dei Matti

Appendix 5. Trace elements

site code	Date	Rb (ppb)	Sr (ppb)	Ba (ppb)	La (ppt)	Ce (ppt)	Pr (ppt)	Nd (ppt)	Sm (ppt)	Eu (ppt)	Gd (ppt)	Tb (ppt)	Dy (ppt)	Ho (ppt)	Er (ppt)	Tm (ppt)	Yb (ppt)	Lu (ppt)
CA	23/11/2016	1.150	117.100	66.350	32.300	30.910	7.506	28.710	6.008	13.620	6.862	1.144	6.788	1.249	3.950	0.650	2.615	0.534
CA	26/11/2016	1.229	101.300	71.870	5.084	1.115	0.644	2.590	1.409	10.170	1.152	0.088	0.962	0.021	0.303	0.000	0.445	0.000
CA	28/09/2017	1.203	46.680	27.280	0.828	2.120	1.985	1.463	0.000	4.508	0.000	0.000	1.761	0.000	0.000	0.051	0.219	0.000
LP	31/03/2015	0.000	23.840	2.400	11.040	21.320	2.810	11.760	3.185	0.000	5.818	0.000	4.198	0.000	3.620	0.000	3.279	0.000
LP	11/01/2018				165.400	254.600	6.649	42.630	9.443	1.813	10.920	0.000	4.834	0.210	1.622	0.000	1.747	0.000
LP	18/01/2018				5.420	13.430	0.000	7.680	0.000	0.468	1.532	0.000	0.000	0.000	0.000	0.000	0.000	0.000
M	25/11/2010	0.179	45.820	5.334														
M	09/10/2011	0.264	43.020	4.144	31.990	58.210	8.365	35.270	6.610	2.640	9.964	1.118	4.574	1.445	5.644	1.383	9.882	2.389
M	09/11/2011	0.121	42.200	3.712	23.730	12.230	2.577	12.820	3.208	1.516	2.605	0.444	2.530	0.850	2.466	0.311	2.572	0.280
M	16/11/2011	0.158	39.240	3.985	15.320	11.670	1.442	6.954	2.998	2.134	1.437	0.476	0.318	0.794	2.153	0.314	1.787	0.236
M	11/04/2012	0.130	43.620	4.106	13.240	0.000	2.618	10.270	2.520	1.054	2.746	0.403	2.452	0.545	2.155	0.286	1.708	0.260
M	08/11/2012	0.321	50.330	5.978	32.060	22.510	5.796	14.230	6.394	1.814	5.700	0.886	6.390	1.395	3.691	0.341	2.730	0.446
M	15/03/2013	0.154	40.140	4.296	20.280	47.560	1.764	9.586	0.992	1.339	3.280	0.301	1.270	0.964	2.033	0.116	1.502	0.187
M	20/09/2013	0.241	43.440	5.104	9.722	36.190	2.049	5.863	2.558	0.921	3.733	0.583	2.027	0.747	2.015	0.185	1.669	0.272
M	17/02/2014	0.368	49.370	5.654	60.200	91.840	8.132	24.010	7.149	2.746	5.759	1.068	4.417	0.777	3.829	0.722	2.328	0.576
M	31/03/2015	0.000	27.540	3.201	13.080	8.096	2.976	6.850	0.000	0.000	2.736	0.000	0.074	0.000	0.432	0.000	2.976	0.000
M	22/03/2016																	
M	23/11/2016	0.210	65.820	7.333	111.900	169.400	25.270	104.700	23.730	6.583	30.250	3.849	26.130	5.244	13.680	1.898	10.080	1.780
M	26/11/2016	0.166	53.110	5.066	17.850	4.371	4.027	17.660	3.397	0.745	5.344	0.616	4.255	0.734	2.689	0.190	1.177	0.375
ON	15/02/2019				0.000	1.204	0.000	1.553	0.000	0.362	0.236	0.000	0.249	0.000	0.000	0.029	0.259	0.000
ON	10/04/2019				0.465	3.355	0.389	6.212	0.000	0.651	1.415	0.037	1.119	0.117	0.215	0.232	0.519	0.068
PA	20/11/2009	0.498	94.590	27.380														
PA	25/11/2010	0.599	79.850	20.650														
PA	04/04/2011	0.488	78.160	16.450	13.850	7.540	2.190	12.290	2.610	4.859	4.335	0.439	3.096	0.768	2.063	0.290	1.295	0.266
PA	09/10/2011	0.446	91.360	27.120	288.800	544.800	64.510	232.300	40.350	14.850	52.930	9.046	41.430	14.370	57.080	11.660	84.720	24.740
PA	09/11/2011	0.645	88.160	11.980	40.560	62.540	7.644	45.340	8.610	4.670	8.041	1.626	6.509	2.326	5.461	1.005	4.522	0.948
PA	11/04/2012	0.423	89.580	24.700	6.394	0.000	0.714	3.486	0.792	3.221	1.684	0.289	1.345	0.516	1.466	0.227	0.875	0.199
PA	08/11/2012	0.459	75.820	19.850	16.370	10.860	2.776	13.970	2.616	3.216	2.986	0.949	4.793	1.078	2.796	0.478	2.373	0.318
PA	15/03/2013	0.582	76.080	17.460	15.560	7.589	1.960	1.917	3.472	5.845	2.315	1.137	2.666	1.843	1.848	0.927	2.773	1.651
PA	20/09/2013	0.485	90.130	28.460	2.747	4.497	0.000	0.000	0.714	6.494	1.356	0.117	0.411	0.172	0.503	0.000	0.607	0.194
PA	17/02/2014	0.815	85.850	21.140	28.400	6.437	4.039	15.610	1.657	5.423	2.880	0.446	4.417	1.187	3.537	0.414	1.511	0.294
PA	31/03/2015	0.000	52.080	12.160	35.980	62.390	10.340	27.640	6.448	0.231	11.980	0.000	5.889	0.000	3.082	0.000	8.524	0.000
PA	23/11/2016	0.423	66.010	10.190	166.000	247.200	40.970	168.600	40.710	9.594	39.710	6.648	38.820	8.006	21.690	3.001	17.770	2.436
PA	26/11/2016	0.549	106.600	14.720	128.000	131.700	30.830	123.300	26.880	8.603	32.830	4.792	30.340	6.137	20.740	2.210	15.370	2.297
PA	30/08/2017	1.019	47.350	13.980	34.910	62.600	8.751	24.250	0.000	4.011	2.591	0.000	2.814	0.235	0.837	0.000	0.000	0.000
PA	09/01/2018				434.800	824.400	102.000	449.200	101.100	22.290	117.400	12.130	102.900	17.120	57.550	6.758	42.440	5.416
PA	11/01/2018				61.370	108.500	13.100	73.160	12.000	5.615	17.620	0.000	15.290	1.552	8.112	0.000	4.618	0.000
PA	18/01/2018				24.670	26.070	0.000	6.144	0.000	1.813	2.107	0.000	0.000	0.000	0.000	0.000	0.000	0.000
PO	25/11/2010	0.215	133.400	21.790														
PO	04/04/2011	0.393	148.600	23.650	29.260	11.630	4.961	21.910	4.199	6.031	5.491	0.804	3.886	0.796	3.340	0.366	3.042	0.322
PO	09/11/2011	0.243	132.800	18.670	69.800	104.800	11.590	49.490	9.676	5.468	11.540	1.768	7.844	2.209	7.279	0.907	5.968	0.563
PO	16/11/2011	0.302	142.300	19.410	22.490	8.375	2.038	12.130	3.863	5.138	2.131	0.497	0.666	0.617	2.228	0.310	1.834	0.306
PO	11/04/2012	0.339	149.400	21.070	16.690	0.000	3.316	10.670	3.172	3.987	3.205	1.005	2.908	1.186	2.528	0.873	1.831	0.830
PO	08/11/2012	0.272	135.800	20.150	30.460	9.502	5.602	20.820	4.941	2.391	4.614	0.759	4.066	1.173	2.013	0.444	1.540	0.732
PO	15/03/2013	0.226	128.400	18.170	32.910	28.690	4.018	14.860	0.992	3.957	2.315	0.903	5.460	1.049	1.756	0.319	3.004	0.280
PO	17/02/2014	1.031	143.600	21.140	198.300	201.700	18.830	63.080	7.149	4.607	7.999	1.275	8.249	1.882	4.121	0.491	3.962	0.576
PO	31/03/2015	0.000	80.780	14.260	30.930	19.830	5.396	20.110	1.662	1.737	5.818	0.000	1.449	0.000	2.817	0.000	4.893	0.000
PO	22/03/2016																	
PO	23/11/2016	0.354	153.000	26.460	89.250	66.790	19.820	76.740	16.210	8.154	17.610	2.408	17.810	3.588	10.790	1.344	7.658	1.146
PO	26/11/2016	0.297	153.200	25.480	32.310	16.740	6.153	25.340	4.731	5.250	5.585	0.771	5.872	1.232	3.744	0.357	2.598	0.362
PTTA	26/09/2006																	
PTTA	10/06/2007																	
PTTA	12/12/2008																	
PTTA	25/11/2010	0.100	41.030	3.470														
PTTA	04/04/2011	1.784	40.550	2.872	356.800	282.600	15.060	44.330	2.156	0.938	13.300	0.746	2.371	0.615	2.652	0.244	1.473	0.177
PTTA	09/11/2011	0.116	38.740	2.423	19.950	13.580	1.743	9.231	3.429	1.277	1.334	0.453	1.312	0.959	2.332	0.430	1.004	0.318
PTTA	16/11/2011	0.106	39.020	2.221	27.180	28.980	5.056	23.700	6.456	1.934	5.320	0.989	2.564	1.208	3.537	0.420	2.786	0.383
PTTA	11/04/2012	0.065	39.470	2.119	12.700	0.000	1.865	7.623	1.935	0.647	2.043	0.349	2.488	0.666	1.896	0.205	1.262	0.251
PTTA	08/11/2012	0.106	42.250	2.767	26.270	14.290	5.261	18.710	7.848	1.484	5.971	0.854	6.535	1.332	4.810	0.307	2.521	0.477
PTTA	15/03/2013	0.173	37.350	3.339	18.900	27.100	2.646	8.388	0.744	1.279	0.965	0.234	3.555	0.652	1.478	0.174	1.040	0.187
PTTA	20/09/2013	0.220	44.860	0.000	5.231	16.740	0.887	2.060	1.831	0.732	0.587	0.183	1.703	0.555	1.197	0.000	0.607	0.233
PTTA	17/02/2014	0.144	43.450	3.385	17.840	12.200	2.603	9.402	4.336	1.731	2.240	1.358	1.224	1.309	3.537	0.914	2.001	0.764
PTTA	31/03/2015	0.000	27.080	2.160	22.240	28.400	5.529	10.670	1.444	0.000	7.431	0.000	1.237	0.000	1.227	0.000	2.472	0.000
PTTA	22/03/2016																	
PTTA	23/11/2016	0.103	47.610	2.907	1.361	0.000	0.611	2.374	1.630	0.498	0.000	0.000	0.874	0.033	0.420	0.076	0.313	0.000
PTTA	26/11/2016	0.154	109.500	10.690	38.690	23.660	7.950	31.450	7.580	3.778	9.345	1.133	8.155	1.812	5.623	0.830	5.231	0.504
PTTA	28/09/2017	0.895	24.500	1.615	0.000	0.399	3.056	1.548	0.000	2.949	0.128	0.000	1.469	0.000	0.130	0.116	0.000	0.000

site code	Date	Rb (ppb)	Sr (ppb)	Ba (ppb)	La (ppt)	Ce (ppt)	Pr (ppt)	Nd (ppt)	Sm (ppt)	Eu (ppt)	Gd (ppt)	Tb (ppt)	Dy (ppt)	Ho (ppt)	Er (ppt)	Tm (ppt)	Yb (ppt)	Lu (ppt)
SA	25/11/2010	0.118	133.400	16.620														
SA	04/04/2011	0.085	123.800	14.630	21.910	6.587	2.728	14.330	2.497	4.121	2.987	0.570	2.174	0.643	2.014	0.275	0.987	0.233
SA	09/11/2011	0.083	116.100	12.950	31.700	20.410	4.376	16.390	3.666	3.909	3.991	0.497	2.063	1.130	2.561	0.387	2.583	0.406
SA	16/11/2011	0.085	108.000	12.000	22.000	5.145	1.013	9.148	2.836	3.578	3.167	0.315	0.487	0.660	1.905	0.165	1.383	0.233
SA	11/04/2012	0.096	123.600	14.620	124.800	114.200	22.830	99.260	18.880	6.473	23.310	3.316	19.940	4.516	12.900	1.637	9.464	1.359
SA	08/11/2012	0.305	92.480	13.350	103.300	126.100	19.480	80.640	22.380	9.071	20.090	3.385	16.410	4.757	9.508	2.731	7.118	2.673
SA	15/03/2013	0.089	121.300	13.500	24.030	21.900	2.450	8.148	2.232	2.314	2.122	0.100	1.905	0.567	0.739	0.029	1.155	0.218
SA	17/02/2014	0.172	136.200	15.520	34.230	18.040	4.685	22.910	3.399	4.315	3.200	0.861	3.140	0.573	2.808	0.221	3.145	0.247
SA	31/03/2015	0.000	85.530	12.560	60.080	33.110	10.040	33.640	7.319	1.679	10.370	0.000	7.475	0.000	4.849	0.000	4.691	0.000
SA	22/03/2016																	
SA	23/11/2016	0.196	100.900	13.080	138.800	165.000	28.980	118.000	31.600	8.681	33.010	5.351	29.130	6.615	16.350	2.979	15.960	2.557
SA	26/11/2016	0.111	136.500	15.870	30.800	6.061	4.905	20.010	4.440	2.691	4.455	0.922	5.431	1.072	3.811	0.378	2.507	0.283
SdM	11/04/2012	0.000	115.900	27.150	62.550	42.080	24.290	143.000	51.180	14.860	72.450	11.660	81.360	20.030	66.480	9.289	59.830	8.943
SdM	08/11/2012	0.267	70.390	18.270	57.340	85.100	17.880	104.900	38.900	10.720	57.540	8.351	55.340	15.980	46.420	5.940	40.480	7.607
SdM	15/03/2013	0.160	53.710	14.470	89.860	231.800	45.720	208.500	82.830	15.710	107.100	15.920	101.800	23.480	67.000	10.600	65.970	9.719
SdM	20/09/2013	0.274	116.200	28.130	27.590	8.018	7.554	49.600	13.960	8.383	31.940	5.677	36.080	8.788	32.500	4.487	30.790	4.120
SdM	17/02/2014	0.293	88.870	23.180	90.550	40.830	31.400	205.900	80.280	18.070	89.270	17.950	107.700	28.600	82.610	12.470	83.690	11.860
SdM	31/03/2015	0.000	36.450	12.960	72.370	129.780	39.420	88.940	67.370	13.030	86.370	12.240	81.600	18.500	69.160	7.235	62.800	7.728
TM	20/11/2009	0.720	91.900	45.310														
TM	25/11/2010	0.433	95.880	34.790														
TM	04/04/2011	0.407	74.690	19.680	25.280	13.420	4.179	20.990	4.993	5.227	5.202	0.863	4.677	1.118	3.438	0.610	2.848	0.399
TM	09/10/2011	0.858	105.500	68.600	54.560	65.950	12.540	52.230	13.060	15.840	11.170	1.815	9.727	2.487	7.707	1.403	10.140	2.828
TM	09/11/2011	0.338	90.010	18.340	126.200	172.900	23.670	119.000	24.040	8.247	28.480	4.582	24.430	5.792	16.290	1.972	11.820	1.911
TM	16/11/2011	0.368	93.170	24.480	54.680	45.570	6.652	29.090	7.759	6.588	10.810	1.794	7.286	2.142	5.773	0.720	4.874	0.697
TM	11/04/2012	0.442	90.220	33.390	12.850	0.000	2.086	9.259	2.187	4.794	3.299	0.539	3.371	0.923	3.134	0.339	2.444	0.323
TM	08/11/2012	0.480	76.900	32.170	35.560	14.580	4.920	18.970	4.069	5.030	5.971	0.664	5.083	1.173	4.586	0.546	2.521	0.440
TM	15/03/2013	0.602	83.500	49.930	26.960	7.010	1.617	4.553	2.728	9.315	3.473	0.368	3.682	0.936	2.680	0.116	2.773	0.249
TM	20/09/2013	0.937	101.500	67.400	18.420	10.700	0.581	5.229	3.435	18.020	2.903	0.316	1.703	0.326	2.599	0.000	3.034	0.389
TM	17/02/2014	0.657	88.610	48.730	28.890	4.710	1.526	9.767	0.117	9.945	3.520	0.487	2.714	1.064	3.975	0.683	2.000	0.388
TM	31/03/2015	0.000	53.810	21.720	61.220	66.520	14.980	51.880	10.800	4.228	21.370	1.260	13.920	0.575	7.852	0.000	8.726	0.000
TO	25/11/2010	0.107	37.520	2.808														
TO	09/11/2011	0.109	40.990	2.546	8.857	4.983	0.000	1.005	1.376	0.749	0.000	0.000	0.000	0.358	0.528	0.109	0.440	0.109
TO	11/04/2012	0.024	33.130	1.836	5.906	0.000	0.789	2.922	0.798	0.497	1.294	0.189	1.170	0.322	1.135	0.145	0.863	0.141
TO	08/11/2012	0.229	39.110	3.038	14.470	6.144	2.728	5.007	3.488	0.740	4.343	0.253	1.888	0.888	1.454	0.239	1.370	0.191
TO	15/03/2013	0.085	32.080	2.674	11.400	36.500	0.735	0.959	0.000	0.670	1.736	0.067	1.143	0.425	1.016	0.087	0.231	0.156
TO	20/09/2013	0.214	38.830	2.850	4.849	25.090	1.070	5.229	0.000	1.299	0.843	0.183	0.892	0.687	1.314	0.000	1.214	0.078
TO	17/02/2014	0.232	39.570	2.800	46.240	48.890	6.624	32.410	7.149	1.454	7.359	1.275	6.759	1.800	3.683	0.491	4.778	0.482
TO	31/03/2015	0.000	25.340	1.600	26.110	17.620	5.164	16.580	4.708	0.000	5.231	0.000	3.563	0.000	2.022	0.000	4.691	0.000
TO	22/03/2016																	
TO	23/11/2016	0.085	59.130	4.356	112.100	110.300	23.590	98.340	19.500	5.074	24.950	3.276	18.580	4.268	13.710	1.959	9.981	1.226
TO	26/11/2016	0.158	51.450	3.407	20.560	5.400	3.815	18.720	4.692	0.984	3.976	0.682	4.403	0.801	2.372	0.232	2.406	0.440
BA	29/10/2018				1.248	4.707	0.567	7.563	0.000	0.733	2.623	0.000	1.081	0.000	0.000	0.000	0.000	0.000
BA	06/11/2018				2.611	5.004	2.295	13.610	1.852	1.160	4.237	0.000	3.136	0.000	2.679	0.081	1.881	0.000
BA	15/02/2019				0.134	2.022	0.000	1.997	0.000	0.217	1.179	0.148	1.368	0.264	0.751	0.029	0.649	0.103
BA	10/04/2019				0.217	2.495	0.071	2.662	0.000	0.651	1.651	0.148	0.497	0.293	0.751	0.029	0.000	0.103
BA	10/04/2019				0.000	27.400	0.042	2.543	0.000	0.373	1.909	0.000	1.060	0.229	0.081	0.044	0.000	0.000
BA	10/04/2019				0.000	1.369	0.078	2.141	0.249	0.659	0.779	0.000	0.429	0.109	0.000	0.036	0.158	0.000

Appendix 6. Summary statistics of water hydrochemistry

Polla delle anatre

	Ca	Mg	Na+K	Cl	SO_4	HCO_3	NO_3	pH	T	SIdol	SIcalc	Rb	Sr	Ba
	meq/l	meq/l	meq/l	meq/l	meq/l	meq/l	meq/l	-	°C	-	-	ppb	ppb	ppb
mean	2.42	0.57	0.05	0.02	0.06	2.88	0.07	7.90	9.66	0.37	0.38	0.49	82.64	19.40
median	2.44	0.56	0.04	0.02	0.06	2.88	0.05	7.83	9.70	0.33	0.36	0.49	85.85	19.85
min	1.66	0.35	0.02	0.01	0.04	2.51	0.02	7.44	8.90	-0.29	0.07	0.00	52.08	10.19
max	2.89	0.87	0.07	0.06	0.09	3.39	0.33	8.98	10.38	1.31	0.85	0.82	106.60	28.46
range	1.23	0.52	0.06	0.05	0.06	0.88	0.32	1.54	1.48	1.61	0.78	0.82	54.52	18.27
standard deviation	0.23	0.11	0.02	0.01	0.01	0.26	0.06	0.39	0.47	0.49	0.23	0.18	13.74	6.22
CV	10%	20%	34%	54%	22%	9%	124%	5%	5%	148%	64%	37%	17%	32%

Polla dell'orso

	Ca	Mg	Na+K	Cl	SO_4	HCO_3	NO_3	pH	T	SIdol	SIcalc	Rb	Sr	Ba
	meq/l	meq/l	meq/l	meq/l	meq/l	meq/l	meq/l	-	°C	-	-	ppb	ppb	ppb
mean	3.56	0.39	0.03	0.02	0.10	3.91	0.05	7.62	9.63	-0.33	0.22	0.33	136.48	20.93
median	3.62	0.40	0.03	0.02	0.10	3.96	0.02	7.56	9.60	-0.27	0.26	0.30	142.30	21.07
min	1.54	0.14	0.02	0.01	0.07	3.10	0.00	6.91	9.20	-1.50	-0.23	0.00	80.78	14.26
max	4.54	0.62	0.05	0.04	0.14	4.79	0.22	8.49	10.40	0.14	0.46	1.03	153.20	26.46
range	3.00	0.48	0.03	0.03	0.07	1.69	0.22	1.58	1.20	1.63	0.69	1.03	72.42	12.20
standard deviation	0.56	0.12	0.01	0.01	0.02	0.38	0.07	0.41	0.31	0.45	0.20	0.25	20.35	3.46
CV	15%	31%	27%	35%	23%	10%	302%	5%	3%	-170%	77%	76%	15%	17%

Polletta

	Ca	Mg	Na+K	Cl	SO_4	HCO_3	NO_3	pH	T	SIdol	SIcalc	Rb	Sr	Ba
	meq/l	meq/l	meq/l	meq/l	meq/l	meq/l	meq/l	-	°C	-	-	ppb	ppb	ppb
mean	2.74	1.18	0.02	0.02	0.05	3.81	0.06	7.87	10.13	0.64	0.39	0.31	44.26	3.07
median	2.74	1.22	0.02	0.02	0.05	3.85	0.02	7.81	10.10	0.68	0.37	0.12	40.55	2.77
min	2.35	0.77	0.02	0.01	0.03	3.08	0.00	7.42	9.48	0.03	0.05	0.00	24.50	0.00
max	3.35	1.71	0.05	0.04	0.08	4.86	0.32	8.62	11.10	1.20	0.73	1.78	109.50	10.69
range	1.00	0.94	0.03	0.03	0.05	1.78	0.32	1.20	1.62	1.17	0.68	1.78	85.00	10.69
standard deviation	0.23	0.28	0.01	0.01	0.01	0.41	0.08	0.33	0.38	0.36	0.19	0.50	20.64	2.47
CV	9%	23%	33%	41%	29%	11%	342%	4%	4%	53%	52%	163%	47%	80%

Milano

	Ca	Mg	Na+K	Cl	SO_4	HCO_3	NO_3	pH	T	SIdol	SIcalc	Rb	Sr	Ba
	meq/l	meq/l	meq/l	meq/l	meq/l	meq/l	meq/l	-	°C	-	-	ppb	ppb	ppb
mean	2.90	1.79	0.03	0.02	0.06	4.56	0.05	8.06	10.07	1.36	0.66	0.19	45.30	4.83
median	2.85	1.80	0.03	0.02	0.05	4.47	0.02	7.87	10.18	1.22	0.58	0.17	43.53	4.68
min	2.58	1.35	0.02	0.01	0.03	4.04	0.00	7.42	7.61	0.73	0.34	0.00	27.54	3.20
max	3.50	2.27	0.06	0.03	0.10	5.63	0.23	10.40	10.90	2.56	1.24	0.37	65.82	7.33
range	0.93	0.92	0.04	0.02	0.07	1.59	0.23	2.98	3.29	1.83	0.90	0.37	38.28	4.13
standard deviation	0.21	0.26	0.01	0.01	0.02	0.41	0.06	0.70	0.73	0.56	0.28	0.10	9.17	1.15
CV	8%	14%	28%	47%	30%	9%	258%	9%	7%	46%	48%	51%	20%	24%

Torre

	Ca	Mg	Na+K	Cl	SO_4	HCO_3	NO_3	pH	T	SIdol	SIcalc	Rb	Sr	Ba
	meq/l	meq/l	meq/l	meq/l	meq/l	meq/l	meq/l	-	°C	-	-	ppb	ppb	ppb
mean	2.66	0.19	0.02	0.02	0.04	2.80	0.03	8.07	9.79	0.03	0.52	0.12	39.72	2.79
median	2.66	0.18	0.02	0.02	0.04	2.75	0.02	8.07	9.72	0.12	0.56	0.11	38.97	2.80
min	1.45	0.09	0.01	0.01	0.02	2.28	0.00	7.58	9.05	-0.68	0.15	0.00	25.34	1.60
max	3.22	0.45	0.07	0.06	0.06	3.29	0.09	8.75	11.40	0.71	0.81	0.23	59.13	4.36
range	1.77	0.36	0.05	0.05	0.04	1.02	0.09	1.17	2.35	1.38	0.67	0.23	33.79	2.76
standard deviation	0.35	0.08	0.01	0.01	0.01	0.25	0.03	0.29	0.52	0.46	0.24	0.08	9.61	0.77
CV	13%	47%	53%	69%	33%	9%	119%	4%	5%	381%	43%	66%	24%	27%

Balena

	Ca	Mg	Na+K	Cl	SO_4	HCO_3	NO_3
	meq/l	meq/l	meq/l	meq/l	meq/l	meq/l	meq/l
mean	2.28	1.31	0.03	0.02	0.07	3.34	0.07
median	1.88	1.25	0.03	0.02	0.07	2.96	0.07
min	1.78	1.22	0.02	0.01	0.04	2.63	0.04
max	3.13	1.50	0.03	0.03	0.09	4.50	0.12
range	1.35	0.28	0.01	0.02	0.05	1.87	0.07
standard deviation	0.60	0.11	0.00	0.01	0.02	0.81	0.03
CV	32%	9%	11%	33%	24%	27%	45%

Onda

	Ca	Mg	Na+K	Cl	SO_4	HCO_3	NO_3
	meq/l	meq/l	meq/l	meq/l	meq/l	meq/l	meq/l
mean	3.01	1.24	0.10	0.08	0.07	4.04	0.09
median	3.06	1.25	0.10	0.07	0.08	4.16	0.06
min	2.56	1.03	0.09	0.06	0.05	3.25	0.02
max	3.37	1.45	0.12	0.12	0.09	4.60	0.19
range	0.82	0.42	0.03	0.06	0.04	1.36	0.17
standard deviation	0.38	0.20	0.02	0.03	0.02	0.64	0.08
CV	13%	16%	16%	41%	22%	16%	128%

Laghi Pensili

	Ca	Mg	Na+K	Cl	SO_4	HCO_3	NO_3	pH	T	SIdol	SIcalc
	meq/l	meq/l	meq/l	meq/l	meq/l	meq/l	meq/l	-	°C	-	-
mean	2.38	1.06	0.08	0.08	0.07	3.34	0.04	8.30	9.37	1.52	0.83
median	2.41	1.05	0.08	0.06	0.06	3.37	0.04	8.28	9.35	1.39	0.76
min	2.19	0.99	0.02	0.01	0.05	3.05	0.01	8.06	9.20	1.21	0.67
max	2.56	1.13	0.13	0.15	0.11	3.67	0.05	8.58	9.58	2.08	1.12
range	0.37	0.14	0.11	0.14	0.06	0.62	0.04	0.52	0.38	0.86	0.45
standard deviation	0.16	0.06	0.05	0.06	0.02	0.25	0.02	0.21	0.20	0.38	0.20
CV	6%	6%	66%	99%	39%	7%	40%	3%	2%	27%	26%

Sacrestia

	Ca	Mg	Na+K	Cl	SO_4	HCO_3	NO_3	pH	T	SIdol	SIcalc	Rb	Sr	Ba
	meq/l	meq/l	meq/l	meq/l	meq/l	meq/l	meq/l	-	°C	-	-	ppb	ppb	ppb
mean	3.74	0.20	0.04	0.03	0.09	3.86	0.05	7.87	9.93	0.21	0.65	0.12	116.16	14.06
median	4.04	0.19	0.03	0.03	0.08	4.17	0.02	7.93	9.82	0.04	0.62	0.10	121.30	13.50
min	1.59	0.06	0.02	0.01	0.05	2.91	0.00	7.40	9.57	-0.93	0.26	0.00	85.53	12.00
max	4.45	0.46	0.08	0.08	0.14	4.52	0.23	8.45	10.40	1.37	1.34	0.31	136.50	16.62
range	2.86	0.39	0.06	0.07	0.09	1.61	0.23	1.05	0.83	2.31	1.08	0.31	50.97	4.62
standard deviation	0.72	0.12	0.01	0.02	0.03	0.56	0.07	0.29	0.24	0.64	0.30	0.08	17.47	1.49
CV	18%	63%	52%	63%	31%	14%	333%	4%	2%		49%	65%	15%	11%

Cancello

	Ca	Mg	Na+K	Cl	SO_4	HCO_3	NO_3	pH	T	SIdol	SIcalc
	meq/l	meq/l	meq/l	meq/l	meq/l	meq/l	meq/l	-	°C	-	-
mean	2.77	0.19	0.03	0.03	0.16	2.70	0.08	7.98	9.64	-0.06	0.48
median	2.76	0.16	0.03	0.03	0.17	2.73	0.04	8.02	9.68	-0.08	0.45
min	2.28	0.09	0.02	0.01	0.10	2.22	0.01	7.76	9.27	-0.46	0.30
max	3.18	0.29	0.07	0.06	0.23	3.28	0.24	8.12	9.90	0.31	0.69
range	0.90	0.20	0.05	0.05	0.14	1.07	0.23	0.36	0.63	0.77	0.39
standard deviation	0.29	0.07	0.02	0.02	0.05	0.33	0.09	0.14	0.22	0.32	0.17
CV	10%	45%	61%	72%	28%	12%	230%	2%	2%	-376%	37%

Mora creek

	Ca	Mg	Na+K	Cl	SO_4	HCO_3	NO_3	pH	T	SIdol	SIcalc	Rb	Sr	Ba
	meq/l	meq/l	meq/l	meq/l	meq/l	meq/l	meq/l	-	°C	-	-	ppb	ppb	ppb
mean	1.95	0.30	0.04	0.03	0.05	2.17	0.05	8.03	8.21	-0.09	0.23	0.52	87.14	38.71
median	1.93	0.29	0.04	0.03	0.05	2.13	0.04	8.00	8.45	0.04	0.28	0.46	90.12	34.09
min	1.79	0.15	0.02	0.01	0.03	2.01	0.01	7.51	7.28	-0.83	-0.14	0.00	53.81	18.34
max	2.28	0.53	0.07	0.06	0.07	2.52	0.10	8.96	9.30	0.83	0.59	0.94	105.50	68.60
range	0.49	0.38	0.04	0.04	0.04	0.51	0.09	1.45	2.02	1.66	0.74	0.94	51.69	50.26
standard deviation	0.11	0.09	0.01	0.01	0.01	0.12	0.03	0.35	0.67	0.47	0.19	0.25	13.76	17.43
CV	5%	32%	25%	38%	24%	6%	66%	4%	8%		68%	49%	16%	45%

Sorgente dei Matti spring

	Ca	Mg	Na+K	Cl	SO_4	HCO_3	NO_3	pH	T	SIdol	SIcalc	Rb	Sr	Ba
	meq/l	meq/l	meq/l	meq/l	meq/l	meq/l	meq/l	-	°C	-	-	ppb	ppb	ppb
mean	1.40	0.12	0.13	0.02	0.07	1.55	0.02	7.85	9.49	-0.36	0.26	0.17	80.25	20.69
median	1.91	0.27	0.05	0.02	0.06	2.13	0.03	8.03	8.95	0.13	0.32	0.21	79.63	20.73
min	1.06	0.06	0.02	0.01	0.04	1.10	0.01	7.29	7.60	-0.95	-0.11	0.00	36.45	12.96
max	2.28	0.53	0.15	0.06	0.08	2.52	0.10	8.96	10.60	0.83	0.61	0.29	116.20	28.13
range	1.21	0.47	0.13	0.04	0.05	1.42	0.09	1.67	3.00	1.78	0.72	0.29	79.75	15.17
standard deviation	0.31	0.13	0.04	0.01	0.01	0.35	0.03	0.45	0.77	0.53	0.20	0.14	32.73	6.44
CV	16%	47%	81%	63%	21%	16%	85%	6%	9%	420%	63%	82%	41%	31%

Appendix 7. Water stable isotopes

Sampling point	Sampling date	$\delta^{18}O$ (‰)	s.d.$\delta^{18}O$ (‰)	$\delta^{2}H$ (‰)	s.d.$\delta^{2}H$ (‰)
BA	15/03/2018	-13.06	0.04	-90.38	0.74
BA	29/10/2018	-10.92	0.09	-73.65	0.12
BA	06/11/2018	-9.84	0.04	-63.28	0.15
BA	14/04/2019	-10.93	0.05	-73.02	0.24
BA	18/04/2019	-10.89	0.02	-72.95	0.37
CA	11/01/2018	-12.09	0.04	-84.58	0.28
CA	15/03/2018	-11.96	0.03	-82.57	0.04
LP	11/01/2018	-11.43	0.07	-77.41	0.11
LP	15/03/2018	-11.70	0.02	-78.90	0.14
LP	10/04/2019	-11.06	0.01	-73.63	0.06
LP	18/04/2019	-11.08	0.04	-73.77	0.09
M	23/11/2016	-10.21	0.05	-68.06	0.34
M	26/11/2016	-10.20	0.08	-67.44	0.46
M	11/11/2016	-11.15	0.08	-77.16	0.43
M	13/01/2017	-11.07	0.06	-73.93	0.62
M	09/01/2018	-12.32	0.01	-86.61	0.77
M	11/01/2018	-12.47	0.09	-85.89	0.40
M	15/03/2018	-12.54	0.07	-87.49	0.50
M	8/10/18 22:00	-11.08	0.03	-76.90	0.40
M	9/10/18 4:00	-11.52	0.04	-78.70	0.10
M	9/10/18 10:00	-11.53	0.07	-78.64	0.65
M	9/10/18 16:00	-11.54	0.05	-79.08	0.33
M	9/10/18 22:00	-11.58	0.05	-79.00	0.61
M	10/10/18 4:00	-11.55	0.08	-78.64	0.76
M	10/10/18 10:00	-11.58	0.04	-79.21	0.17
M	10/10/18 16:00	-11.52	0.03	-79.17	0.69
M	10/10/18 22:00	-11.60	0.02	-79.29	0.40
M	11/10/18 4:00	-11.56	0.04	-78.91	0.27
M	11/10/18 10:00	-9.98	0.05	-66.06	0.24
M	11/10/18 16:00	-9.46	0.04	-61.40	0.11
M	11/10/18 22:00	-9.64	0.03	-63.01	0.15
M	12/10/18 4:00	-9.72	0.03	-63.94	0.03
M	12/10/18 10:00	-9.85	0.03	-64.84	0.07
M	12/10/18 16:00	-9.88	0.03	-65.48	0.09
M	12/10/18 22:00	-9.94	0.07	-66.46	0.78
M	13/10/18 4:00	-10.04	0.04	-66.84	0.07
M	13/10/18 10:00	-10.16	0.07	-67.73	0.46
M	13/10/18 16:00	-10.17	0.03	-67.39	0.11
M	13/10/18 22:00	-10.21	0.06	-67.68	0.60
M	14/10/18 4:00	-10.25	0.05	-68.02	0.21
M	14/10/18 10:00	-10.31	0.07	-68.42	0.48
M	14/10/18 16:00	-10.37	0.03	-68.97	0.23
M	15/10/18 11:00	-10.24	0.06	-68.40	0.15
M	15/10/18 17:00	-10.33	0.03	-69.21	0.25
M	15/10/18 23:00	-10.42	0.03	-69.96	0.55
M	16/10/18 5:00	-10.36	0.09	-69.61	0.49
M	16/10/18 11:00	-10.59	0.01	-71.56	0.43
M	16/10/18 17:00	-10.46	0.02	-70.38	0.12
M	16/10/18 23:00	-10.52	0.07	-70.66	0.22
M	17/10/18 5:00	-10.59	0.04	-71.11	0.67
M	17/10/18 11:00	-10.31	0.01	-69.02	0.38
M	17/10/18 17:00	-10.33	0.07	-68.88	0.62
M	17/10/18 23:00	-9.85	0.10	-64.54	0.64
M	18/10/18 5:00	-9.76	0.09	-64.23	0.32
M	18/10/18 11:00	-9.49	0.07	-62.46	0.40
M	18/10/18 17:00	-9.33	0.03	-60.62	0.13
M	18/10/18 23:00	-9.46	0.09	-61.44	0.13
M	19/10/18 5:00	-9.28	0.06	-60.60	0.31
M	19/10/18 11:00	-9.38	0.03	-61.16	0.11
M	19/10/18 17:00	-9.45	0.04	-61.64	0.26
M	19/10/18 23:00	-9.51	0.08	-62.42	0.58
M	20/10/18 5:00	-9.56	0.04	-63.02	0.31
M	20/10/18 11:00	-9.64	0.04	-63.46	0.36
M	20/10/18 17:00	-9.57	0.06	-63.70	0.74
M	20/10/18 23:00	-9.71	0.01	-64.17	0.04
M	21/10/18 5:00	-9.73	0.04	-64.50	0.08
M	21/10/18 11:00	-9.76	0.03	-64.60	0.09
M	25/10/18 16:30	-10.17	0.06	-68.30	0.53
M	26/10/18 8:30	-10.25	0.09	-68.58	0.63
M	26/10/18 16:30	-10.33	0.08	-69.14	0.45
M	27/10/18 0:30	-10.40	0.05	-69.18	0.20
M	27/10/18 8:30	-10.56	0.08	-70.01	0.45
M	27/10/18 16:30	-10.51	0.08	-70.11	0.55
M	28/10/18 0:30	-10.46	0.07	-69.93	0.59
M	28/10/18 8:30	-10.30	0.03	-68.79	0.39
M	28/10/18 16:30	-9.81	0.06	-64.01	0.12
M	29/10/18 0:30	-9.65	0.02	-62.84	0.16
M	29/10/18 8:30	-9.61	0.03	-62.54	0.13
M	29/10/18 16:30	-9.22	0.07	-59.17	0.32
M	30/10/18 0:30	-9.25	0.05	-59.58	0.09
M	30/10/18 8:30	-9.51	0.03	-61.53	0.12
M	30/10/18 16:30	-9.69	0.07	-63.58	0.78
M	31/10/18 0:30	-9.84	0.05	-64.52	0.33
M	31/10/18 8:30	-10.00	0.05	-65.75	0.34
M	31/10/18 16:30	-9.86	0.08	-64.78	0.57
M	1/11/18 0:30	-9.59	0.05	-62.93	0.68
M	1/11/18 8:30	-9.43	0.05	-60.93	0.45
M	1/11/18 16:30	-9.70	0.03	-62.87	0.15
M	2/11/18 0:30	-9.74	0.07	-63.36	0.41
M	2/11/18 8:30	-9.73	0.07	-63.70	0.35
M	2/11/18 16:30	-9.93	0.04	-64.93	0.12
M	29/10/2018	-9.43	0.02	-63.65	0.25
M	06/11/2018	-9.95	0.10	-65.82	0.51
M	10/04/2019	-10.91	0.03	-72.76	0.32
M	18/04/2019	-10.62	0.10	-70.40	0.48
M	10/4/19 22:00	-10.78	0.05	-72.52	0.21
M	11/4/19 4:00	-10.92	0.05	-73.19	0.22
M	11/4/19 10:00	-10.92	0.05	-73.22	0.31
M	11/4/19 16:00	-10.82	0.04	-73.02	0.23
M	12/4/19 4:00	-10.78	0.08	-72.85	0.54
M	12/4/19 10:00	-10.74	0.03	-73.07	0.33
M	12/4/19 16:00	-10.70	0.05	-72.93	0.41
M	12/4/19 22:00	-10.83	0.05	-72.33	0.55
M	13/4/19 4:00	-10.73	0.04	-72.24	0.26
M	13/4/19 10:00	-10.69	0.08	-71.89	0.62
M	13/4/19 16:00	-10.72	0.03	-71.59	0.15
M	13/4/19 22:00	-10.72	0.02	-71.75	0.12
M	14/4/19 4:00	-10.70	0.05	-71.51	0.09
M	14/4/19 10:00	-10.76	0.02	-71.47	0.06
M	14/4/19 16:00	-10.77	0.08	-71.47	0.35
M	14/4/19 22:00	-10.71	0.05	-71.19	0.21
M	15/4/19 4:00	-10.76	0.03	-71.55	0.04
M	15/4/19 10:00	-10.82	0.08	-71.96	0.72
M	15/4/19 16:00	-10.71	0.05	-71.33	0.52
M	15/4/19 22:00	-10.61	0.06	-70.52	0.51
M	16/4/19 4:00	-10.73	0.05	-71.00	0.11
M	16/4/19 10:00	-10.71	0.04	-70.82	0.34
M	16/4/19 16:00	-10.71	0.05	-70.89	0.35
M	18/04/2019	-10.62	0.10	-70.40	0.48
ON	15/03/2018	-13.12	0.03	-91.75	0.19

Sampling point	Sampling date	$\delta^{18}O$ (‰)	s.d.$\delta^{18}O$ (‰)	$\delta^{2}H$ (‰)	s.d.$\delta^{2}H$ (‰)
ON	29/10/2018	-8.61	0.12	-55.45	0.28
ON	06/11/2018	-9.65	0.03	-61.59	0.20
ON	14/04/2019	-10.60	0.03	-71.08	0.45
ON	18/04/2019	-10.55	0.07	-70.54	0.52
PA	23/11/2016	-10.29	0.04	-69.30	0.36
PA	26/11/2016	-10.78	0.04	-72.35	0.31
PA	11/11/2016	-11.59	0.04	-78.92	0.53
PA	13/01/2017	-11.60	0.09	-78.56	0.38
PA	30/08/2017	-11.61	0.02	-79.00	0.12
PA	09/01/2018	-12.68	0.05	-88.42	0.36
PA	11/01/2018	-12.11	0.02	-82.74	0.60
PA	15/03/2018	-12.23	0.05	-83.71	0.10
PA	15/10/2018	-11.90	0.17	-81.13	1.33
PA	29/10/2018	-11.70	0.05	-79.43	0.31
PA	06/11/2018	-10.19	0.08	-67.76	0.38
PA	10/04/2019	-11.71	0.04	-78.94	0.16
PA	14/04/2019	-11.49	0.03	-76.91	0.24
PA	18/04/2019	-11.60	0.05	-78.09	0.15
PO	23/11/2016	-10.04	0.02	-66.81	0.62
PO	26/11/2016	-10.21	0.04	-67.32	0.25
PO	09/01/2018	-12.15	0.03	-84.90	0.16
PO	11/01/2018	-12.47	0.07	-87.03	0.71
PO	15/03/2018	-12.57	0.09	-87.28	0.37
PO	29/10/2018	-9.57	0.04	-63.13	0.05
PO	06/11/2018	-9.95	0.05	-64.45	0.60
PO	14/04/2019	-10.72	0.06	-71.43	0.47
PO	18/04/2019	-10.82	0.04	-72.20	0.50
PTTA	23/11/2016	-9.56	0.07	-63.57	0.37
PTTA	26/11/2016	-10.07	0.02	-65.98	0.18
PTTA	13/01/2017	-11.08	0.02	-74.49	0.04
PTTA	09/01/2018	-12.06	0.03	-84.91	0.21
PTTA	11/01/2018	-12.34	0.09	-85.89	0.11
PTTA	15/03/2018	-12.67	0.07	-88.02	0.65
PTTA	15/10/2018	-10.25	0.10	-68.48	0.80
PTTA	29/10/2018	-8.83	0.01	-57.30	0.08
PTTA	06/11/2018	-9.82	0.09	-63.12	0.67
PTTA	10/04/2019	-10.82	0.07	-71.88	0.38
PTTA	14/04/2019	-10.75	0.02	-72.37	0.21
PTTA	18/04/2019	-10.78	0.06	-72.60	0.49
RAIN	11/04/2019	-17.83	0.05	-132.10	0.50
RAIN	14/04/2019	-15.90	0.03	-115.45	0.57
RAIN	15/03/2018	-13.02	0.05	-91.44	0.38
RAIN	15/10/2018	-10.60	0.09	-68.33	0.24
RAIN	17/10/2018	-5.65	0.04	-27.63	0.15
RAIN	28/10/2018	-10.71	0.03	-76.36	0.14
RAIN	29/10/2018	-11.08	0.04	-73.74	0.22
RAIN	4-6/11/2018	-10.08	0.03	-64.55	0.12
SA	09/01/2018	-12.07	0.05	-84.27	0.38
SA	11/01/2018	-12.13	0.07	-83.79	0.42
SA	15/03/2018	-12.16	0.06	-83.89	0.25
SA	29/10/2018	-9.04	0.03	-58.28	0.12
SA	06/11/2018	-9.63	0.01	-62.71	0.59
SA	10/04/2019	-10.90	0.08	-73.03	0.24
SA	14/04/2019	-10.20	0.06	-67.62	0.60
SA	18/04/2019	-10.28	0.03	-67.86	0.09
TO	09/01/2018	-13.26	0.09	-92.84	0.32
TO	11/01/2018	-12.92	0.08	-90.12	0.17
TO	15/03/2018	-12.95	0.06	-90.46	0.16
TO	29/10/2018	-9.58	0.02	-61.90	0.23
TO	06/11/2018	-9.78	0.03	-62.82	0.16
TO	18/04/2019	-10.94	0.02	-71.56	0.04
TM	30/08/2017	-11.73	0.04	-79.78	0.29
TM	09/01/2018	-11.97	0.05	-80.94	0.63
TM	11/01/2018	-11.97	0.07	-81.77	0.42
TM	15/03/2018	-12.10	0.07	-82.32	0.36
TM	15/10/2018	-11.48	0.05	-77.23	0.13
TM	29/10/2018	-11.73	0.03	-79.01	0.08
TM	06/11/2018	-10.80	0.09	-71.75	0.60
TM	10/04/2019	-11.63	0.07	-77.96	0.43
TM	14/04/2019	-11.57	0.08	-77.43	0.76
TM	18/04/2019	-11.47	0.03	-76.66	0.12

Appendix 8. Summary statistics of water stable isotopes

	Polla delle anatre				*Polla dell'orso*				*Polletta*			
	$\delta^{18}O$	s.d.$\delta^{18}O$	$\delta^{2}H$	s.d.$\delta^{2}H$	$\delta^{18}O$	s.d.$\delta^{18}O$	$\delta^{2}H$	s.d.$\delta^{2}H$	$\delta^{18}O$	s.d.$\delta^{18}O$	$\delta^{2}H$	s.d.$\delta^{2}H$
Mean	-11.53	0.06	-78.24	0.40	-10.94	0.05	-73.84	0.42	-10.75	0.05	-72.39	0.35
Median	-11.61	0.04	-78.94	0.36	-10.72	0.04	-71.43	0.47	-10.77	0.06	-72.13	0.29
Standard deviation	0.72	0.04	5.71	0.32	1.16	0.02	9.88	0.22	1.16	0.03	9.70	0.25
Range	2.49	0.15	20.66	1.24	3.00	0.06	24.14	0.66	3.84	0.09	30.72	0.76
Minimum	-12.68	0.02	-88.42	0.10	-12.57	0.02	-87.28	0.05	-12.67	0.01	-88.02	0.04
Maximum	-10.19	0.17	-67.76	1.33	-9.57	0.09	-63.13	0.71	-8.83	0.10	-57.30	0.80
Count	13	13	13	13	9	9	9	9	12	12	12	12

	Milano				*Torre*				*Onda*			
	$\delta^{18}O$	s.d.$\delta^{18}O$	$\delta^{2}H$	s.d.$\delta^{2}H$	$\delta^{18}O$	s.d.$\delta^{18}O$	$\delta^{2}H$	s.d.$\delta^{2}H$	$\delta^{18}O$	s.d.$\delta^{18}O$	$\delta^{2}H$	s.d.$\delta^{2}H$
Mean	-10.36	0.05	-69.06	0.35	-11.57	0.05	-78.28	0.18	-10.51	0.06	-70.08	0.33
Median	-10.33	0.05	-68.97	0.34	-11.93	0.05	-80.84	0.17	-10.55	0.03	-70.54	0.28
Standard deviation	0.71	0.02	5.90	0.21	1.68	0.03	14.51	0.09	1.67	0.04	13.75	0.15
Range	3.32	0.10	28.32	0.75	3.68	0.08	30.94	0.29	4.51	0.09	36.29	0.33
Minimum	-12.54	0.01	-87.49	0.03	-13.26	0.02	-92.84	0.04	-13.12	0.03	-91.75	0.19
Maximum	-9.22	0.10	-59.17	0.78	-9.58	0.09	-61.90	0.32	-8.61	0.12	-55.45	0.52
Count	107	107	107	107	6	6	6	6	5	5	5	5

	Balena				*Laghi pensili*				*Sacrestia*			
	$\delta^{18}O$	s.d.$\delta^{18}O$	$\delta^{2}H$	s.d.$\delta^{2}H$	$\delta^{18}O$	s.d.$\delta^{18}O$	$\delta^{2}H$	s.d.$\delta^{2}H$	$\delta^{18}O$	s.d.$\delta^{18}O$	$\delta^{2}H$	s.d.$\delta^{2}H$
Mean	-11.13	0.05	-74.66	0.32	-11.32	0.04	-75.93	0.10	-10.80	0.05	-72.68	0.34
Median	-10.92	0.04	-73.02	0.24	-11.25	0.03	-75.59	0.10	-10.59	0.06	-70.44	0.31
Standard deviation	1.18	0.02	9.79	0.25	0.31	0.03	2.64	0.03	1.22	0.02	10.28	0.20
Range	3.22	0.06	27.10	0.62	0.65	0.06	5.27	0.08	3.12	0.07	25.99	0.51
Minimum	-13.06	0.02	-90.38	0.12	-11.70	0.01	-78.90	0.06	-12.16	0.01	-84.27	0.09
Maximum	-9.84	0.09	-63.28	0.74	-11.06	0.07	-73.63	0.14	-9.04	0.08	-58.28	0.60
Count	5	5	5	5	4	4	4	4	8	8	8	8

	Mora Creek				*Rainfall (mean)*			
	$\delta^{18}O$	s.d.$\delta^{18}O$	$\delta^{2}H$	s.d.$\delta^{2}H$	$\delta^{18}O$	s.d.$\delta^{18}O$	$\delta^{2}H$	s.d.$\delta^{2}H$
Mean	-11.64	0.06	-78.49	0.38	-11.86	0.05	-81.20	0.29
Median	-11.68	0.06	-78.49	0.39	-10.90	0.04	-75.05	0.23
Standard deviation	0.37	0.02	3.08	0.23	3.75	0.02	32.21	0.17
Range	1.30	0.06	10.57	0.68	12.19	0.06	104.47	0.45
Minimum	-12.10	0.03	-82.32	0.08	-17.83	0.03	-132.10	0.12
Maximum	-10.80	0.09	-71.75	0.76	-5.65	0.09	-27.63	0.57
Count	10	10	10	10	8	8	8	8

Bibliography

Allmendinger, R.W., Cardozo, N., Fisher, D.M., 2011. Structural geology algorithms: Vectors and tensors. Cambridge University Press.

Amiaz, Y., Sorek, S., Enzel, Y., Dahan, O., 2011. Solute transport in the vadose zone and groundwater during flash floods. Water Resources Research 47, 1–10. https://doi.org/10.1029/2011WR010747

Amit, H., Lyakhovsky, V., Katz, A., Starinsky, A., Burg, A., 2002. Interpretation of Spring Recession Curves. Ground Water 40, 543–551. https://doi.org/10.1111/j.1745-6584.2002.tb02539.x

Andrejchuk, V., 1996. Gypsum karst of the pre-Ural region, Russia. International Journal of Speleology 25, 22.

Antonellini, M., Mollema, P.N., 2019. Outcrop fracture network characterization for unraveling deformation sequence, geomechanical properties distribution, and slope stability in a flysch sequence (Monte Venere Formation, Northern Apennines, Italy). International Journal of Earth Sciences 108, 735–751. https://doi.org/10.1007/s00531-019-01685-y

Antonellini, M., Mollema, P.N., Del Sole, L., 2017. Application of analytical diffusion models to outcrop observations: Implications for mass transport by fluid flow through fractures. Water Resources Research 53, 5545–5566. https://doi.org/10.1002/2016WR019864

Antonellini, M., Nannoni, A., Vigna, B., De Waele, J., 2019. Structural control on karst water circulation and speleogenesis in a lithological contact zone: The Bossea cave system (Western Alps, Italy). Geomorphology 345. https://doi.org/10.1016/j.geomorph.2019.07.019

Arbel, Y., Greenbaum, N., Lange, J., Shtober-Zisu, N., Grodek, T., Wittenberg, L., Inbar, M., 2008. Hydrologic classification of cave drips in a Mediterranean climate, based on hydrograph separation and flow mechanisms. Israel Journal of Earth Sciences 57, 291–310. https://doi.org/10.1560/IJES.57.3-4.291

Arpa Piemonte, 2011. Evento meteoidrologico del 4-8 novembre 2011. Torino.

Arpa Piemonte, Regione Piemonte, 2018. Gli eventi alluvionali in Piemonte - Evento del 21-25 novembre 2016. Arpa Piemonte, Torino.

Atkinson, T., 1985. Present and future directions in karst hydrogeology. Annales de La Société Géologique de Belgique 108, 293–296.

Atkinson, T., 1977. Diffuse flow and conduit flow in limestone terrain in the Mendip Hills, Somerset (Great Britain). Journal of Hydrology 35, 93–110.

Aydin, A., 2000. Fractures, faults, and hydrocarbon entrapment, migration and flow. Marine and Petroleum Geology 17, 797–814.

Bakalowicz, M., 2004. The epikarst, the skin of karst. In: Jones, W.K., Culver, D.C., Herman, J. (Eds.), Epikarst. Special Publication 9. Karst Waters Institute, Charles Town, WV, 16–22.

Bakalowicz, M., 1995. La zone d'infiltration des aquifères karstiques. Méthodes d'étude. Structure et Fonctionnement. Hydrogéologie 4, 3–21.

Bakalowicz, M., 1977. Etude du degré d'organisation des écoulements souterrains dans les aquifères carbonatés par une méthode hydrogéochimique nouvelle. Comptes Rendus de l'Académie Des Sciences 284, 2463–2466.

Bakalowicz, M., Mangin, A., 1980. L'aquifère karstique. Sa définition, ses caractéristiques et

son identification. Mémoires de La Société Géologique de France 11, 71–79.
Baker, A., Barnes, W.L., Smart, P.L., 1997. Variations in the discharge and organic matter content of stalagmite drip waters in Lower Cave, Bristol. Hydrological Processes 11, 1541–1555. https://doi.org/10.1002/(SICI)1099-1085(199709)11:11<1541::AID-HYP484>3.0.CO;2-Z
Baker, A., Brunsdon, C., 2003. Non-linearities in drip water hydrology: an example from Stump Cross Caverns, Yorkshire. Journal of Hydrology 277, 151–163. https://doi.org/10.1016/S0022-1694(03)00063-5
Balbiano D'Aramengo, C., 1993. Le grotte del Piemonte. Guida per l'escursionismo. Via dalla pazza folla, Novara.
Baldini, J.U.L., McDermott, F., Baldini, L.M., Ottley, C.J., Linge, K.L., Clipson, N., Jarvis, K.E., 2012. Identifying short-term and seasonal trends in cave drip water trace element concentrations based on a daily-scale automatically collected drip water dataset. Chemical Geology 330–331, 1–16. https://doi.org/10.1016/j.chemgeo.2012.08.009
Baldini, J.U.L., McDermott, F., Fairchild, I.J., 2006. Spatial variability in cave drip water hydrochemistry: Implications for stalagmite paleoclimate records. Chemical Geology 235, 390–404. https://doi.org/10.1016/j.chemgeo.2006.08.005
Banks, D., Hall, G., Reimann, C., Siewers, U., 1999. Distribution of rare earth elements in crystalline bedrock groundwaters: Oslo and Bergen regions, Norway. Applied Geochemistry 14, 27–39. https://doi.org/10.1016/S0883-2927(98)00037-7
Banzato, C., Dallagiovanna, G., Maino, M., Peano, G., Vigna, B., 2011. Correlation between the geological setting and groundwater flow: the Bossea karst underground laboratory. Geoitalia 2011, Epitome 4, Torino, 19-23 Settembre 2011. 14.
Banzato, C., Marchionatti, F., Vigna, B., 2013. Drainage index calculated with artificial tracers. AQUA Mundi 67–75. https://doi.org/10.4409/Am-059-13-0053
Bar-Matthews, M., Ayalon, A., Matthews, A., Sass, E., Halicz, L., 1996. Carbon and oxygen isotope study of the active water-carbonate system in a karstic Mediterranean cave: Implications for paleoclimate research in semiarid regions. Geochimica et Cosmochimica Acta 60, 337–347.
Barale, L., Bertok, C., Atri, A., Martire, L., Piana, F., Domini, G., D'Atri, A., Martire, L., Piana, F., Domini, G., 2016. Geology of the Entracque–Colle di Tenda area (Maritime Alps, NW Italy). Journal of Maps 12, 359–370.
Barbel-Périneau, A., Barbiero, L., Danquigny, C., Emblanch, C., Mazzilli, N., 2019. Karst flow processes explored through analysis of long-term unsaturated- zone discharge hydrochemistry: a 10-year study in Rustrel, France. Hydrogeology Journal 27, 1711–1723. https://doi.org/10.1007/s10040-019-01965-6
Beck, H.E., Zimmermann, N.E., McVicar, T.R., Vergopolan, N., Berg, A., Wood, E.F., 2018. Present and future Köppen-Geiger climate classification maps at 1-km resolution. Scientific Data 5, 1–12. https://doi.org/10.1038/sdata.2018.214
Becker, A., Davenport, C.A., Eichenberger, U., Gilli, É., Jeannin, P., Lacave, C., 2006. Speleoseismology: A critical perspective. Journal of Seismology 10, 371–388. https://doi.org/10.1007/s10950-006-9017-z
Becker, A., Häuselmann, P., Eikenberg, J., Gilli, É., 2012. Active tectonics and earthquake destructions in caves of northern and central Switzerland. International Journal of Speleology 41, 35–49.
Belkhiri, L., Boudoukha, A., Mouni, L., 2011. A multivariate statistical analysis of groundwater chemistry data. International Journal of Environmental Research 5, 537–544.

Bense, V.F., Gleeson, T., Loveless, S.E., Bour, O., Scibek, J., 2013. Fault zone hydrogeology. Earth-Science Reviews 127, 171–192. https://doi.org/10.1016/j.earscirev.2013.09.008
Berglund, J.L., Toran, L., Herman, E.K., 2019. Deducing flow path mixing by storm-induced bulk chemistry and REE variations in two karst springs: With trends like these who needs anomalies? Journal of Hydrology 571, 349–364. https://doi.org/10.1016/j.jhydrol.2019.01.050
Bertok, C., Martire, L., Perotti, E., d'Atri, A., Piana, F., 2011. Middle-Late Jurassic syndepositional tectonics recorded in the Ligurian Briançonnais succession (Marguareis-Mongioie area, Ligurian Alps, NW Italy). Swiss Journal of Geosciences 104, 237–255. https://doi.org/10.1007/s00015-011-0058-0
Biddau, R., Bensimon, M., Cidu, R., Parriaux, A., 2009. Rare earth elements in groundwater from different Alpine aquifers. Chemie Der Erde 69, 327–339. https://doi.org/10.1016/j.chemer.2009.05.002
Bonacci, O., 1993. Karst springs hydrographs as indicators of karst aquifers. Hydrological Sciences Journal 38, 51–62. https://doi.org/10.1080/02626669309492639
Bonini, L., Dallagiovanna, G., Seno, S., 2010. The role of pre-existing faults in the structural evolution of thrust systems: Insights from the Ligurian Alps (Italy). Tectonophysics 480, 73–87. https://doi.org/10.1016/j.tecto.2009.09.021
Bonnet, E., Bour, O., Odling, N.E., Davy, P., Main, I., Cowie, P., Berkowitz, B., 2001. Scaling of fracture systems in geological media. Reviews of Geophysics 39, 347–383. https://doi.org/http://dx.doi.org/10.1029/1999RG000074
Bortolami, G.C., Ricci, B., Susella, G.F., Zuppi, G.M., 1979. Hydrogeochemistry of the Corsaglia Valley, Maritime Alps, Piedmont, Italy. Journal of Hydrology 44, 57–79. https://doi.org/10.1016/0022-1694(79)90146-X
Bottrell, S.H., Atkinson, T.C., 1992. Tracer study of flow and storage in the unsaturated zone of a karstic limestone aquifer. Tracer Hydrology 207–211.
Boussinesq, J., 1903. Sur un mode simple d'écoulement des nappes d'eau d'infiltration à lit horizontal, avec rebord vertical tout autour lorsqu'une partie de ce rebord est enlevée depuis la surface jusqu'au fond. CR Acad. Sci 137, 11.
Bradley, C., Baker, A., Jex, C.N., Leng, M.J., 2010. Hydrological uncertainties in the modelling of cave drip-water δ18O and the implications for stalagmite palaeoclimate reconstructions. Quaternary Science Reviews 29, 2201–2214. https://doi.org/10.1016/j.quascirev.2010.05.017
Burdon, D.J., Papakis, N., 1963. Handbook of karst hydrology. United Nations Special Fund. Institute for Geology and Subsurface Research, Athens, Greece.
Caetano Bicalho, C., 2010. Hydrochemical characterization of transfers in karst aquifers by natural and anthropogenic tracers. Example of a Mediterranean karst system, the Lez karst aquifer (Southern France). Institute of Science and Industries of Life and Environment.
Caetano Bicalho, C., Batiot-Guilhe, C., Seidel, J.L., Van Exter, S., Jourde, H., 2012. Geochemical evidence of water source characterization and hydrodynamic responses in a karst aquifer. Journal of Hydrology 450–451, 206–218. https://doi.org/10.1016/j.jhydrol.2012.04.059
Caine, J.S., Evans, J.P., Forster, C.B., 1996. Fault zone architecture and permeability structure. Geology 24, 1025–1028.
Čar, J., 2018. Geostructural mapping of karstified limestones. Geologija 61, 133–162. https://doi.org/10.5474/geologija.2018.010
Čar, J., 1974. The covered karst in the near Idrija vicinity. Naše Jame 16, 51–62.

Čar, J., Šebela, S., 1998. Bedding planes, moved bedding planes, connective fissures and horizontal cave passages (examples from Postojnska Jama cave). Acta Carsologica 27, 75–95.
Cazarin, C.L., Bezerra, F.H.R., Borghi, L., Santos, R. V, Favoreto, J., Brod, J.A., Auler, A.S., Srivastava, N.K., 2019. The conduit-seal system of hypogene karst in Neoproterozoic carbonates in northeastern Brazil. Marine and Petroleum Geology 101, 90–107. https://doi.org/10.1016/j.marpetgeo.2018.11.046
Celle-Jeanton, H., Travi, Y., Blavoux, B., 2001. Isotopic typology of the precipitation in the Western Mediterranean region at three different time scales. Geophysical Research Letters 28, 1215–1218.
Celle, H., 2000. Caractérisation des précipitations sur le pourtour de la Méditerranée occidentale: Approche isotopique et chimique. Avignon.
Chelidze, T., Gueguen, Y., 1990. Evidence of Fractal Fracture. International Journal of Rock Mechanics and Mining Sciences & Geomechanics Abstracts 27, 223–225.
Chen, Z., Goldscheider, N., 2014. Modeling spatially and temporally varied hydraulic behavior of a folded karst system with dominant conduit drainage at catchment scale, Hochifen-Gottesacker, Alps. Journal of Hydrology 514, 41–52. https://doi.org/10.1016/j.jhydrol.2014.04.005
Choi, J., Edwards, P., Ko, K., Kim, Y., 2016. Definition and classification of fault damage zones: A review and a new methodological approach. Earth-Science Reviews 152, 70–87. https://doi.org/10.1016/j.earscirev.2015.11.006
Civita, M., Gandolfo, M., Peano, G., Vigna, B., 2005. The recharge-discharge process in Bossea cave underground basin (NW Italy). In: Maraga, F., Arattano, M. (Eds.), Progress in Surface and Subsurface Water Studies at Plot and Small Basin Scale, Turin, Italy, 13-17 October 2004. International Hydrological Programme, Paris, 145–151.
Civita, M., Gregoretti, F., Morisi, A., Olivero, G., Peano, G., Vigna, B., Villavecchia, E., Vittone, F., 1990. Atti della Stazione Scientifica della Grotta di Bossea. L'Artistica di Savigliano, Savigliano.
Civita, M., Vigna, B., 1985. Analysis of Bossea Cave Hydrogeological System (Maritime Alps, Italy). Proceedings of the Ankara-Antalya Symposium. 101–114.
Clark, I., 2015. Groundwater geochemistry and isotopes. CRC press.
Cortesogno, L., Vanossi, M., 1984. Introduzione alla geologia delle Alpi Liguri. Biogeographia – The Journal of Integrative Biogeography 9. https://doi.org/10.21426/B69110161
d'Atri, A., Piana, F., Barale, L., Bertok, C., Martire, L., 2016. Geological setting of the southern termination of Western Alps. International Journal of Earth Sciences 105, 1831–1858. https://doi.org/10.1007/s00531-015-1277-9
Dahan, O., Nativ, R., Adar, E.M., Berkowitz, B., 2001. Water Flow and Solute Transport in Unsaturated Fractured Chalk. Flow and Transport through Unsaturated Fractured Rock. 183–196. https://doi.org/10.1029/GM042p0183
Decarlis, A., Dallagiovanna, G., Lualdi, A., Maino, M., Seno, S., 2013. Stratigraphic evolution in the Ligurian Alps between Variscan heritages and the Alpine Tethys opening: A review. Earth-Science Reviews 125, 43–68. https://doi.org/10.1016/j.earscirev.2013.07.001
Decarlis, A., Lualdi, A., 2008. Late Triassic-early Jurassic paleokarst from the Ligurian Alps and its geological significance (Siderolitico Auct., Ligurian Briançonnais domain). Swiss Journal of Geosciences 101, 579–593. https://doi.org/10.1007/s00015-008-1302-0
Delbart, C., Valdés, D., Barbecot, F., Tognelli, A., Couchoux, L., 2016. Spatial organization

of the impulse response in a karst aquifer. Journal of Hydrology 537, 18–26. https://doi.org/10.1016/j.jhydrol.2016.03.029
Delbart, C., Valdes, D., Barbecot, F., Tognelli, A., Richon, P., Couchoux, L., 2014. Temporal variability of karst aquifer response time established by the sliding-windows cross-correlation method. Journal of Hydrology 511, 580–588. https://doi.org/10.1016/j.jhydrol.2014.02.008
Desmarais, K., Rojstaczer, S., 2002. Inferring source waters from measurements of carbonate spring response to storms. Journal of Hydrology 260, 118–134. https://doi.org/10.1016/S0022-1694(01)00607-2
Dewandel, B., Lachassagne, P., Bakalowicz, M., Weng, P.H., Al-Malki, A., 2003. Evaluation of aquifer thickness by analysing recession hydrographs. Application to the Oman ophiolite hard-rock aquifer. Journal of Hydrology 274, 248–269. https://doi.org/10.1016/S0022-1694(02)00418-3
Dia, A., Gruau, G., Olivié-Lauquet, G., Riou, C., Molénat, J., Curmi, P., 2000. The distribution of rare earth elements in groundwaters: Assessing the role of source-rock composition, redox changes and colloidal particles. Geochimica et Cosmochimica Acta 64, 4131–4148. https://doi.org/10.1016/S0016-7037(00)00494-4
Doctor, D., Alexander, E., Jameson, R., Alexander, S., 2015. Hydrologic and geochemical dynamics of vadose zone recharge in a mantled karst aquifer: results of monitoring drip waters in Mystery Cave, Minnesota. Sinkhole Conference 2015. 19–30.
Doctor, D.H., Alexander, E.C., Petrič, M., Kogovšek, J., Urbanc, J., Lojen, S., Stichler, W., 2006. Quantification of karst aquifer discharge components during storm events through end-member mixing analysis using natural chemistry and stable isotopes as tracers. Hydrogeology Journal 14, 1171–1191. https://doi.org/10.1007/s10040-006-0031-6
Doe, T.W., 2001. What Do Drops Do? Surface Wetting and Network Geometry Effects on Vadose-Zone Fracture Flow. In: National Research Council (Ed.), Conceptual Models of Flow and Transport in the Fractured Vadose Zone. National Academies Press, 243–270.
Duan, W., Ruan, J., Luo, W., Li, T., Tian, L., Zeng, G., Zhang, D., Bai, Y., Li, J., Tao, T., Zhang, P., Baker, A., Tan, M., 2016. The transfer of seasonal isotopic variability between precipitation and drip water at eight caves in the monsoon regions of China. Geochimica et Cosmochimica Acta 183, 250–266. https://doi.org/10.1016/j.gca.2016.03.037
Duvert, C., Cendón, D.I., Raiber, M., Seidel, J.L., Cox, M.E., 2015. Seasonal and spatial variations in rare earth elements to identify inter-aquifer linkages and recharge processes in an Australian catchment. Chemical Geology 396, 83–97. https://doi.org/10.1016/j.chemgeo.2014.12.022
Ekmekçi, M., 2005. Karst in Turkish Thrace: Compatibility between Geological History and Karst Type. Turkish Journal of Earth Sciences 14, 73–90.
Ekmekçi, M., 2003. Review of Turkish karst with special emphasis on tectonic and climatic controls. Acta Carsologica 32, 205–218.
Ennes-Silva, R.A., Bezerra, F.H.R., Nogueira, F.C.C., Balsamo, F., Klimchouk, A., Cazarin, C.L., Auler, A.S., 2016. Tectonophysics Superposed folding and associated fracturing influence hypogene karst development in Neoproterozoic carbonates , São Francisco Craton, Brazil. Tectonophysics 666, 244–259. https://doi.org/10.1016/j.tecto.2015.11.006
Evans, D.D., Nicholson, T.J., Rasmussen, T.C., 2001. Flow and transport through unsaturated fractured rock. Flow and Transport through Unsaturated Fractured Rock Geophysical Monograph Series. American Geophysical Union, Washington DC, 1–18.

Even, H., Carmi, I., Magaritz, M., Gerson, R., 1986. Timing the transport of water through the upper vadose zone in a Karstic system above a cave in Israel. Earth Surface Processes and Landforms 11, 181–191. https://doi.org/10.1002/esp.3290110208
Fairchild, I.J., Baker, A., 2012. Speleothem science: from process to past environments. John Wiley & Sons.
Fairchild, I.J., Smith, C.L., Baker, A., Fuller, L., Spötl, C., Mattey, D., McDermott, F., 2006. Modification and preservation of environmental signals in speleothems. Earth-Science Reviews 75, 105–153. https://doi.org/10.1016/j.earscirev.2005.08.003
Filippini, M., Squarzoni, G., De Waele, J., Fiorucci, A., Vigna, B., Grillo, B., Riva, A., Rossetti, S., Zini, L., Casagrande, G., Stumpp, C., Gargini, A., 2018. Differentiated spring behavior under changing hydrological conditions in an alpine karst aquifer. Journal of Hydrology 556, 572–584. https://doi.org/10.1016/j.jhydrol.2017.11.040
Filipponi, M., Jeannin, P.-Y., Tacher, L., 2009. Evidence of inception horizons in karst conduit networks. Geomorphology 106, 86–99.
Fiorillo, F., 2014. The Recession of Spring Hydrographs, Focused on Karst Aquifers. Water Resources Management 28, 1781–1805. https://doi.org/10.1007/s11269-014-0597-z
Fiorillo, F., 2011. Tank-reservoir drainage as a simulation of the recession limb of karst spring hydrographs. Hydrogeology Journal 19, 1009–1019. https://doi.org/10.1007/s10040-011-0737-y
Fiorucci, A., Moitre, B., Vigna, B., 2015. Hydrogeochemical study of Bossea karst system. In: Kataev, V.N., R, Z.D., Shcherbakov, S. V, Shilova, A. V (Eds.), Proceedings of the International Symposium in Environmental Safety and Construction in Karst Areas. Perm, Russia, 26–29 May 2015. Perm State University, Perm, 290–294.
Flynn, R.M., Schnegg, P.-A., Costa, R., Mallen, G., Zwahlen, F., 2005. Identification of zones of preferential groundwater tracer transport using a mobile downhole fluorometer. Hydrogeology Journal 13, 366–377. https://doi.org/10.1007/s10040-004-0388-3
Ford, D., Williams, P.W., 2007. Karst Hydrogeology and Geomorphology. John Wiley & Sons, Ltd.
Forkasiewicz, J., Paloc, H., 1967. Le régime de tarissement de la Foux de la Vis. Etude préliminaire. Hydrologie Des Roches Fissurées. Actes Du Colloque de Dubrovnik, IASH and UNESCO, Belgium. 2123–2228.
Forti, P., Postpischl, D., 1984. Seismotectonic and paleoseismic analyses using karst sediments. Marine Geology 55, 145–161.
Fossen, H., 2016. Structural geology. Cambridge University Press.
Friedrich, H., Smart, P.L., 1981. Dye trace studies of the unsaturated-zone recharge of the Carboniferous Limestone aquifer of the Mendip Hills, England. Proceedings of the 8th International Congress of Speleology, Vol. 1. 283–286.
Frumkin, A., Fischhendler, I., 2005. Morphometry and distribution of isolated caves as a guide for phreatic and confined paleohydrological conditions. Geomorphology 67, 457–471. https://doi.org/10.1016/j.geomorph.2004.11.009
Genty, D., Deflandre, G., 1998. Drip flow variations under a stalactite of the Pere Noel cave (Belgium). Evidence of seasonal variations and air pressure constraints. Journal of Hydrology 211, 208–232. https://doi.org/10.1016/S0022-1694(98)00235-2
Ghielmi, M., Rogledi, S., Vigna, B., Violanti, D., 2019. La successione messiniana e pliopleistocenica del Bacino di Savigliano (Settore occidentale del Bacino Terziario Piemontese).
Ghielmi, M., Rogledi, S., Vigna, B., Violanti, D., 2002. Evoluzione tettono-sedimentaria della successione plio-pleistocenica nel settore del Piemonte centro-meridionale. Cinematiche

Collisionali: tra esumazione e sedimentazione. 81° Riunione Estiva Della Società Geologica Italiana, Riass.,. Società Geologica Italiana, 181–182.
Gill, L.W., Babechuk, M.G., Kamber, B.S., McCormack, T., Murphy, C., 2018. Use of trace and rare earth elements to quantify autogenic and allogenic inputs within a lowland karst network. Applied Geochemistry 90, 101–114. https://doi.org/10.1016/j.apgeochem.2018.01.001
Gilli, É., 2005. Review on the use of natural cave speleothems as palaeoseismic or neotectonics indicators. 337, 1208–1215. https://doi.org/10.1016/j.crte.2005.05.008
Gilli, É., 2004. Glacial causes of damage and difficulties to use speleothems as palaeoseismic indicators Glacial causes of damage and difficulties to use speleothems as palaeoseismic indicators. Geodinamica Acta 17, 229–240. https://doi.org/10.3166/ga.17.229-240
Gilli, É., 1986. Néotectonique dans les massifs karstiques, un exemple dans les Préalpes de Nice: la grotte des deux Gourdes. Karstologia 8, 50–52.
Goeppert, N., Goldscheider, N., Scholz, H., 2011. Karst geomorphology of carbonatic conglomerates in the Folded Molasse zone of the Northern Alps (Austria/Germany). Geomorphology 130, 289–298. https://doi.org/10.1016/j.geomorph.2011.04.011
Goldscheider, N., 2005. Fold structure and underground drainage pattern in the alpine karst system Hochifen-Gottesacker. Eclogae Geologicae Helvetiae 98, 1–17.
Goldscheider, N., Meiman, J., Pronk, M., Smart, C., 2008. Tracer tests in karst hydrogeology and speleology. International Journal of Speleology 37, 27–40. https://doi.org/10.5038/1827-806X.37.1.3
Güler, C., Thyne, G.D., Mccray, J.E., Turner, A.K., 2002. Evaluation of graphical and multivariate statistical methods for classification of water chemistry data. Hydrogeology Journal 10, 455–474. https://doi.org/10.1007/s10040-002-0196-6
Gunn, J., 1983. Point-recharge of limestone aquifers—a model from New Zealand karst. Journal of Hydrology 61, 19–29.
Gutiérrez, F., Parise, M., De Waele, J., Jourde, H., 2014. A review on natural and human-induced geohazards and impacts in karst. Earth Science Reviews 138, 61–88. https://doi.org/10.1016/j.earscirev.2014.08.002
Hartland, A., Fairchild, I.J., Lead, J.R., Borsato, A., Baker, A., Frisia, S., Baalousha, M., 2012. From soil to cave: Transport of trace metals by natural organic matter in karst dripwaters. Chemical Geology 304–305, 68–82. https://doi.org/10.1016/j.chemgeo.2012.01.032
Hartmann, A., Baker, A., 2017. Modelling karst vadose zone hydrology and its relevance for paleoclimate reconstruction. Earth-Science Reviews 172, 178–192. https://doi.org/10.1016/j.earscirev.2017.08.001
Hartmann, A., Goldscheider, N., Wagener, T., Lange, J., Weiler, M., 2014. Karst water resources in a changing world: Review of hydrological modeling approaches. Reviews of Geophysics 52, 218–242. https://doi.org/10.1002/2013RG000443
Helstrup, T., Jørgensen, N.O., Banoeng-yakubo, B., 2007. Investigation of hydrochemical characteristics of groundwater from the Cretaceous-Eocene limestone aquifer in southern Ghana and southern Togo using hierarchical cluster analysis. Hydrogeology Journal 15, 977–989. https://doi.org/10.1007/s10040-007-0165-1
Henderson, F.M., 1966. Open channel flow.
Henderson, P., 1984. Rare earth element geochemistry. Elsevier.
Herman, E.K., Toran, L., White, W.B., 2009. Quantifying the place of karst aquifers in the groundwater to surface water continuum: A time series analysis study of storm behavior in Pennsylvania water resources. Journal of Hydrology 376, 307–317.

https://doi.org/10.1016/j.jhydrol.2009.07.043
Hess, J.W., White, W.B., 1988. Storm response of the karstic carbonate aquifer of southcentral Kentucky. Journal of Hydrology 99, 235–252. https://doi.org/10.1016/0022-1694(88)90051-0
Hobbs, S.L., Smart, P.L., 1986. Characterisation of carbonate aquifers: a conceptual base. Proceedings of the 9th Interna- Tional Congress of Speleology, Barcelona. 1–14.
Horton, R.E., 1907. Weir experiments, coefficients, and formulas: Water-Supply Paper 200. No. 200, General Hydrographic Investigations, M. Washington D.C.
Hu, K., Chen, H., Nie, Y., Wang, K., 2015. Seasonal recharge and mean residence times of soil and epikarst water in a small karst catchment of southwest China. Scientific Reports 5, 1–12. https://doi.org/10.1038/srep10215
Ingri, J., Winderlund, A., Land, M., Gustafsson, Ö., Andersson, P., Ohlander, B., 2000. Temporal variations in the fractionation of the rare earth elements in a boreal river ; the role of colloidal particles . Chemical Geology 166, 23–45.
Jeannin, P., Sauter, M., 1998. Analysis of karst hydrodynamic behaviour using global approaches: a review. Bulletin d'Hydrogeologie 16, 31–48.
Jex, C.N., Mariethoz, G., Baker, A., Graham, P., Andersen, M.S., Acworth, I.R., Edwards, N., Azcurra, C., 2012. Spatially dense drip hydrological monitoring and infiltration behaviour at the Wellington Caves, South East Australia. International Journal of Speleology 41, 283–296. https://doi.org/10.5038/1827-806X.41.2.14
Johannesson, K.H., Stetzenbach, K.J., Hodge, V.F., 1997a. Rare earth elements as geochemical tracers of regional groundwater mixing. Geochimica et Cosmochimica Acta 61, 3605–3618.
Johannesson, K.H., Stetzenbach, K.J., Hodge, V.F., Kreamer, D.K., Zhou, X., 1997b. Delineation of Ground-Water Flow Systems in the Southern Great Basin Using Aqueous Rare Earth Element Distributions. Groundwater 35, 807–819.
Jukić, D., Denić-Jukić, V., 2015. Investigating relationships between rainfall and karst-spring discharge by higher-order partial correlation functions. Journal of Hydrology 530, 24–36. https://doi.org/10.1016/j.jhydrol.2015.09.045
Kim, Y., Andrews, J.R., Sanderson, D.J., 2000. Damage zones around strike-slip fault systems and strike-slip fault evolution, Crackington Haven, southwest England. Geosciences Journal 4, 53–72.
Klimchouk, A., 2000. The formation of epikarst and its role in vadose speleogenesis. In: Klimchouk, A.B., Ford, D.C., Palmer, A.M., Dreybrodt, W. (Eds.), Speleogenesis. Evolution of Karst Aquifers. National Speleological Society, 91–99.
Klimchouk, A., Auler, A.S., Bezerra, F.H.R., Cazarin, C.L., Balsamo, F., Dublyansky, Y., 2016. Geomorphology Hypogenic origin, geologic controls and functional organization of a giant cave system in Precambrian carbonates, Brazil. Geomorphology 253, 385–405. https://doi.org/10.1016/j.geomorph.2015.11.002
Klimchouk, A., Ford, D.C., 2000. Lithologic and structural controls of dissolutional cave development. Speleogenesis. Evolution of Karst Aquifers. National Speleological Society, Huntsville 54–64.
Klimchouk, A.B., Sauro, U., Lazzarotto, M., 1996. "Hidden" shafts at the base of the epikarstic zone : A case study from the Sette Communi plateau , Venetian Pre-Alps , Italy. Cave and Karst Science 23, 101–107.
Klimczak, C., Schultz, R.A., Parashar, R., Reeves, D.M., 2010. Cubic law with aperture-length correlation: implications for network scale fluid flow. Hydrogeology Journal 18, 851–862. https://doi.org/10.1007/s10040-009-0572-6

Kogovšek, J., 1997. Water tracer tests in the vadose zone. Tracer Hydrology.
Kresic, N., 2007. Hydrogeology and groundwater modeling, Second. ed. CRC Press.
Kresic, N., Stevanovic, Z., 2009. Groundwater hydrology of springs: Engineering, theory, management and sustainability. Butterworth-heinemann.
Kruhl, J.H., 2013. Fractal-geometry techniques in the quantification of complex rock structures: A special view on scaling regimes, inhomogeneity and anisotropy. Journal of Structural Geology 46, 2–21. https://doi.org/10.1016/j.jsg.2012.10.002
La Pointe, P.R., 1988. A Method to Characterize Fracture Density and Connectivity Through Fractal Geometry. International Journal of Rock Mechanics and Mining Sciences & Geomechanics Abstracts 25, 421–429.
Lachniet, M.S., 2009. Climatic and environmental controls on speleothem oxygen-isotope values. Quaternary Science Reviews 28, 412–432. https://doi.org/10.1016/j.quascirev.2008.10.021
Larroque, C., Delouis, B., Godel, B., Nocquet, J.-M., 2009. Tectonophysics Active deformation at the southwestern Alps – Ligurian basin junction (France – Italy boundary): Evidence for recent change from compression to extension in the Argentera massif. Tectonophysics 467, 22–34. https://doi.org/10.1016/j.tecto.2008.12.013
Liu, A.W., Brancelj, A., Brenčič, M., 2014. The hydrochemical response of cave drip waters to different rain patterns (a case study from Velika Pasica Cave, central Slovenia). Carpathian Journal of Earth and Environmental Sciences 9, 189–197.
Liu, A.W., Brancelj, A., Ellis Burnet, J., 2016. Interpretation of epikarstic cave drip water recession curves: a case study from Velika Pasica Cave, central Slovenia. Hydrological Sciences Journal 61, 2754–2762. https://doi.org/10.1080/02626667.2016.1154150
Liu, H.H., Doughty, C., Bodvarsson, G.S., 1998. An active fracture model for unsaturated flow and transport in fractured rocks. Water Resources Research 34, 2633–2646. https://doi.org/10.1029/98WR02040
Liu, Z., Groves, C., Yuan, D., Meiman, J., Jiang, G., He, S., Li, Q., 2004. Hydrochemical variations during flood pulses in the south-west China peak cluster karst: Impacts of CaCO3-H2O-CO2interactions. Hydrological Processes 18, 2423–2437. https://doi.org/10.1002/hyp.1472
Liu, Z., Li, Q., Sun, H., Wang, J., 2007. Seasonal, diurnal and storm-scale hydrochemical variations of typical epikarst springs in subtropical karst areas of SW China: Soil CO2 and dilution effects. Journal of Hydrology 337, 207–223. https://doi.org/10.1016/j.jhydrol.2007.01.034
Locati, M., Camassi, R.D., Rovida, A.N., Ercolani, E., Bernardini, F.M., Castelli, V., Caracciolo, C.H., Tertulliani, A., Rossi, A., Azzaro, R., 2016. DBMI15, the 2015 version of the Italian Macroseismic Database. Roma. https://doi.org//10.6092/INGV.IT-DBMI15
Longinelli, A., Selmo, E., 2003. Isotopic composition of precipitation in Italy: A first overall map. Journal of Hydrology 270, 75–88. https://doi.org/10.1016/S0022-1694(02)00281-0
Lowe, D.J., 2000. Role of stratigraphic elements in speleogenesis: the speleoinception concept. In: Klimchouk, A.B., Ford, D.C., Palmer, A.N., Dreybrodt, W. (Eds.), Speleogenesis: Evolution of Karst Aquifers. National Speleological Society, Huntsville, AL, USA, 65–76.
Luino, F., 1999. The Flood and Landslide Event of November 4-6 1994 in Piedmont Region (Northwestern Italy): Causes and Related Effects in Tanaro Valley. Physics and Chemistry of the Earth, Part A: Solid Earth and Geodesy 24, 123–129.
Maillet, E.T., 1905. Essais d'hydraulique souterraine & fluviale. A. Hermann.
Maino, M., Dallagiovanna, G., Dobson, K.J., Gaggero, L., Persano, C., Seno, S., Stuart, F.M.,

2012. Tectonophysics Testing models of orogen exhumation using zircon (U – Th)/ He thermochronology : Insight from the Ligurian Alps , Northern Italy. Tectonophysics 560–561, 84–93. https://doi.org/10.1016/j.tecto.2012.06.045
Maino, M., Decarlis, A., Felletti, F., Seno, S., 2013. Tectono-sedimentary evolution of the Tertiary Piedmont Basin (NW Italy) within the Oligo – Miocene central Mediterranean geodynamics. 32, 593–619. https://doi.org/10.1002/tect.20047
Mangin, A., 1975. Contribution à l'étude hydrodynamique des aquifères karstiques. Université de Dijon.
Markowska, M., Baker, A., Treble, P.C., Andersen, M.S., Hankin, S., Jex, C.N., Tadros, C. V., Roach, R., 2015. Unsaturated zone hydrology and cave drip discharge water response: Implications for speleothem paleoclimate record variability. Journal of Hydrology 529, 662–675. https://doi.org/10.1016/j.jhydrol.2014.12.044
McLennan, S.M., 1989. Rare earth elements in sedimentary rocks; influence of provenance and sedimentary processes. Reviews in Mineralogy and Geochemistry 21, 169–200.
Messiga, B., 1987. Alpine metamorphic evolution of Ligurian Alps (North-West Italy): chemography and petrological constraints inferred from metamorphic climax assemblages. Contributions to Mineralogy and Petrology 95, 269–277.
Mijatovic, B., 1974. Détermination de la transmissivité et du coefficient d'emmagasinement par la courbe de tarissement dans les aquifères karstiques. Memoires de Congrés de Montpellier, France 225–230.
Miller, T.E., 1996. Geologic and hydrologic controls on karst and cave development in Belize. Journal of Cave and Karst Studies 58, 100–120.
Molin, D., Bernardini, F., Camassi, R., Caracciolo, C.H., Castelli, V., Ercolani, E., Postpischl, L., 2008. Materiali per un catalogo dei terremoti italiani: revisione della sismicità minore del territorio nazionale. Quaderni Di Geofisica 57, 75 p.
Möller, P., Dulski, P., Salameh, E., Geyer, S., 2006. Characterization of the sources of thermal spring- and well water in Jordan by rare earth element and yttrium distribution and stable isotopes of H2O. Acta Hydrochimica et Hydrobiologica 34, 101–116. https://doi.org/10.1002/aheh.200500614
Mosca, P., Polino, R., Rogledi, S., Polino, R., Rogledi, S., Rossi, M., 2010. New data for the kinematic interpretation of the Alps–Apennines junction (Northwestern Italy). International Journal of Earth Sciences 99, 833–849. https://doi.org/10.1007/s00531-009-0428-2
Mudarra, M., Andreo, B., 2011. Relative importance of the saturated and the unsaturated zones in the hydrogeological functioning of karst aquifers: The case of Alta Cadena (Southern Spain). Journal of Hydrology 397, 263–280. https://doi.org/10.1016/j.jhydrol.2010.12.005
National Research Council, 1996. Rock Fractures And Fluid Flow: Contemporary Understanding and Applications. National Academies Press, Washington D.C.
Noack, C.W., Dzombak, D.A., Karamalidis, A.K., 2014. Rare Earth Element Distributions and Trends in Natural Waters with a Focus on Groundwater. Environmental Science and Technology 48, 4317–4326. https://doi.org/10.1021/es4053895
Padilla, A., Pulido-Bosch, A., Mangin, A., 1994. Relative Importance of Baseflow and Quickflow from Hydrographs of Karst Spring. Ground Water 32, 267–277. https://doi.org/10.1111/j.1745-6584.1994.tb00641.x
Peano, G., Vigna, B., Villavecchia, E., 2005. L'evento alluvionale nell'ottobre 1996 nella Grotta di Bossea. In: Gili, R., Peano, G. (Eds.), Atti Del Convegno Nazionale "L'ambiente Carsico e l'uomo." CAI Cuneo, Cuneo, 407–422.

Peano, G., Vigna, B., Villavecchia, E., Agnesod, G., 2011. Radon exchange dynamics in a Karst system investigated by radon continuous measurements in water: First results. Radiation Protection Dosimetry 145, 173–177. https://doi.org/10.1093/rpd/ncr053
Pepe, M., Parise, M., 2014. Structural control on development of karst landscape in the Salento Peninsula (Apulia, SE Italy). Acta Carsologica 43, 101–114.
Perrin, J., Jeannin, P.Y., Zwahlen, F., 2003a. Epikarst storage in a karst aquifer: A conceptual model based on isotopic data, Milandre test site, Switzerland. Journal of Hydrology 279, 106–124. https://doi.org/10.1016/S0022-1694(03)00171-9
Perrin, J., Jeannin, P.Y., Zwahlen, F., 2003b. Implications of the spatial variability of infiltration-water chemistry for the investigation of a karst aquifer: A field study at Milandre test site, Swiss Jura. Hydrogeology Journal 11, 673–686. https://doi.org/10.1007/s10040-003-0281-5
Petras, I., 1986. An approach to the mathematical expression of recession curves. Water SA 12, 145–150.
Phillips, F.M., 2001. Investigating Flow and Transport in the Fractured Vadose Zone Using Environmental Tracers. In: National Research Council (Ed.), Conceptual Models of Flow and Transport in the Fractured Vadose Zone. National Academies Press, 271–294.
Phillips, O., 2009. Geological Fluid Dynamics. Sub-surface Flow and Reactions. Cambridge university press.
Piana, F., Musso, A., Bertok, C., D'Atri, A., Martire, L., Perotti, E., Varrone, D., Martinotti, G., 2009. New data on post-Eocene tectonic evolution of the External Ligurian Briançonnais (Western Ligurian Alps). Italian Journal of Geosciences (Bollettino Della Società Geologica Italiana) 128, 353–366. https://doi.org/10.3301/IJG.2009.128.2.353
Pisani, L., Antonellini, M., De Waele, J., 2019. Structural control on epigenic gypsum caves: evidences from Messinian evaporites (Northern Apennines, Italy). Geomorphology 332, 170–186.
Plan, L., Grasemann, B., Spötl, C., Decker, K., Boch, R., Kramers, J., 2010. Neotectonic extrusion of the Eastern Alps: Constraints from U/Th dating of tectonically damaged speleothems. Geology 38, 483–486. https://doi.org/10.1130/G30854.1
Pollard, D.D., Segall, P., 1987. Theoretical displacements and stresses near fractures in rock: with applications to faults, joints, veins, dikes, and solution surfaces. In: Atkinson, B.K. (Ed.), Fracture Mechanics of Rock. Academic Press, London, 277–349.
Poulain, A., Rochez, G., Bonniver, I., Hallet, V., 2015. Stalactite drip-water monitoring and tracer tests approach to assess hydrogeologic behavior of karst vadose zone: case study of Han-sur-Lesse (Belgium). Environmental Earth Sciences 74, 7685–7697. https://doi.org/10.1007/s12665-015-4696-9
Poulain, A., Watlet, A., Kaufmann, O., Van Camp, M., Jourde, H., Mazzilli, N., Rochez, G., Deleu, R., Quinif, Y., Hallet, V., 2018. Assessment of groundwater recharge processes through karst vadose zone by cave percolation monitoring. Hydrological Processes 32, 2069–2083. https://doi.org/10.1002/hyp.13138
Powell, C.M., 1979. A morphological classification of rock cleavage. Tectonophysics 58, 21–34.
Pronk, M., Goldscheider, N., Zopfi, J., Zwahlen, F., 2008. Percolation and particle transport in the unsaturated zone of a karst aquifer. Ground Water 47, 361–9.
Raiber, M., Webb, J.A., Cendón, D.I., White, P.A., Jacobsen, G.E., 2015. Environmental isotopes meet 3D geological modelling: Conceptualising recharge and structurally-controlled aquifer connectivity in the basalt plains of south-western Victoria, Australia. Journal of Hydrology 527, 262–280. https://doi.org/10.1016/j.jhydrol.2015.04.053

Raiber, M., White, P.A., Daughney, C.J., Tschritter, C., Davidson, P., Bainbridge, S.E., 2012. Three-dimensional geological modelling and multivariate statistical analysis of water chemistry data to analyse and visualise aquifer structure and groundwater composition in the Wairau Plain, Marlborough District, New Zealand. Journal of Hydrology 436–437, 13–34. https://doi.org/10.1016/j.jhydrol.2012.01.045

Ravbar, N., Barberá, J.A., Petrič, M., Kogovšek, J., Andreo, B., 2012. The study of hydrodynamic behaviour of a complex karst system under low-flow conditions using natural and artificial tracers (the catchment of the Unica River, SW Slovenia). Environmental Earth Sciences 65, 2259–2272. https://doi.org/10.1007/s12665-012-1523-4

Rawling, G.C., Goodwin, L.B., Wilson, J.L., 2001. Internal architecture, permeability structure, and hydrologic significance of contrasting fault-zone types. Geology 29, 43–46.

Regione Piemonte, Assessorato Ambiente, 1998. Eventi alluvionali in Piemonte, Direzione Servizi Tecnici e Prevenzione.

Sanchez, G., Rolland, Y., Schreiber, D., Giannerini, G., Corsini, M., Lardeaux, J., 2010. The active fault system of SW Alps. Journal of Geodynamics 49, 296–302. https://doi.org/10.1016/j.jog.2009.11.009

Schnegg, P.-A., Bossy, F., 2001. Sonde for downhole measurement of water turbidity and dye tracer concentration. In: Seiler K P, W.S. (Ed.), New Approaches to Characterising Ground- Water Flow, Vol. 1. Balkema, Lisse, 149–152.

Schoeller, H., 1948. Le regime hydro-geologique des calcaires eocenes du synclinal du Dyr el Kef (Tunisie). Bulletin de La Société Géologique de France 5, 167–180.

Schultz, R.A., Fossen, H., 2008. Terminology for structural discontinuities. AAPG Bulletin 92, 853–867. https://doi.org/10.1306/02200807065

Šebela, S., 2009. Structural geology of the Skocjan caves (Slovenia). Acta Carsologica 38, 165–177.

Šebela, S., Liu, H., 2014. Structural geological characteristics of karst caves and major stone forest, Yunnan, China. Acta Carsologica 43, 115–127.

Seno, S., Dallagiovanna, G., Vanossi, M., 2005a. A kinematic evolutionary model for the Penninic sector of the central Ligurian Alps. International Journal of Earth Sciences 94, 114–129. https://doi.org/10.1007/s00531-004-0444-1

Seno, S., Dallagiovanna, G., Vanossi, M., 2005b. Pre-Piedmont and Piedmont-Ligurian nappes in the central sector of the Ligurian Alps: A possible pathway for their superposition on to the inner Briançonnais units. Bollettino Della Societa Geologica Italiana 124, 455–464.

Shanov, S., Kostov, K., 2015. Dynamic Tectonics and Karst, Cave and Karst Systems of the World. Springer Berlin Heidelberg, Berlin, Heidelberg. https://doi.org/10.1007/978-3-662-43992-0

Shevenell, L., 1996. Analysis of well hydrographs in a karst aquifer: estimates of specific yields and continuum transmissivities. Journal of Hydrology 174, 331–355.

Shiller, A.M., 2010. Dissolved rare earth elements in a seasonally snow-covered, alpine/subalpine watershed, Loch Vale, Colorado. Geochimica et Cosmochimica Acta 74, 2040–2052. https://doi.org/10.1016/j.gca.2010.01.019

Silva, O.L., Bezerra, F.H.R., Maia, R.P., Cazarin, C.L., 2017. Karst landforms revealed at various scales using LiDAR and UAV in semi-arid Brazil: Consideration on karstification processes and methodological constraints. Geomorphology 295, 611–630. https://doi.org/10.1016/j.geomorph.2017.07.025

Smart, L.P., Friedrich, H., 1987. Water movement and storage in the unsaturated zone of a maturely karstified carbonate aquifer. Mendip Hills, England.pdf. Conference on Environmental Problems in Karst Terrains and Their Solution, Bowling Green, Kentucky, 1987. National Water Well Association, 57–87.
Stafford, K., Mylroie, John, Taboroši, D., Jenson, J., Mylroie, Joan, 2005. Karst development on Tinian, Commonwealth of the Northern Mariana Islands: Controls on dissolution in relation to the carbonate island karst model. Journal of Cave and Karst Studies 67, 14–27.
Sue, C., Delacou, B., Champagnac, J.-D., Allanic, C., Tricart, P., Burkhard, M., 2007. Extensional neotectonics around the bend of the Western/Central Alps: an overview. International Journal of Earth Sciences 96, 1101–1129. https://doi.org/10.1007/s00531-007-0181-3
Šušteršič, F., 2006. Relationships between deflector faults, collapse dolines and collector channel formation: some examples from Slovenia. International Journal of Speleology 35, 1–12.
Tîrlă, L., Vijulie, I., 2013. Geomorphology Structural – tectonic controls and geomorphology of the karst corridors in alpine limestone ridges : Southern Carpathians , Romania. Geomorphology 197, 123–136. https://doi.org/10.1016/j.geomorph.2013.05.003
Tooth, A.F., Fairchild, I.J., 2003. Soil and karst aquifer hydrological controls on the geochemical evolution of speleothem-forming drip waters, Crag Cave, southwest Ireland. Journal of Hydrology 273, 51–68. https://doi.org/10.1016/S0022-1694(02)00349-9
Torbarov, K., 1976. Estimation of permeability and effective porosity in karst on the basis of recession curve analysis. Karst Hydrology and Water Resources 1, 121–136.
Tremaine, D.M., Froelich, P.N., 2013. Speleothem trace element signatures: A hydrologic geochemical study of modern cave dripwaters and farmed calcite. Geochimica et Cosmochimica Acta 121, 522–545. https://doi.org/10.1016/j.gca.2013.07.026
Tritz, S., Guinot, V., Jourde, H., 2011. Modelling the behaviour of a karst system catchment using non-linear hysteretic conceptual model. Journal of Hydrology 397, 250–262. https://doi.org/10.1016/j.jhydrol.2010.12.001
Turc, L., 1961. Estimation of irrigation water requirements, potential evapotranspiration: a simple climatic formula evolved up to date. Ann. Agron. 12, 13–49.
Turcotte, D.L., 1997. Fractals and chaos in geology and geophysics. Cambridge university press.
Tweed, S.O., Weaver, T.R., Cartwright, I., Schaefer, B., 2006. Behavior of rare earth elements in groundwater during flow and mixing in fractured rock aquifers: An example from the Dandenong Ranges, southeast Australia. Chemical Geology 234, 291–307. https://doi.org/10.1016/j.chemgeo.2006.05.006
Twiss, R.J., Moores, E.M., 1992. Structural geology. Macmillan.
van Geldern, R., Barth, J.A.C., 2012. Optimization of instrument setup and post-run corrections for oxygen and hydrogen stable isotope measurements of water by isotope ratio infrared spectroscopy (IRIS). Limnology and Oceanography: Methods 10, 1024–1036. https://doi.org/10.4319/lom.2012.10.1024
Vanossi, M., 1991. Guide geologiche regionali-alpi liguri. Società Geologica Italiana, BeMa., Milano.
Vanossi, M., 1984. Geologia delle Alpi liguri. Memorie/Soc. Geol. Italiana 28, 5–75.
Vega, M., Pardo, R., Barrado, E., Debán, L., 1998. Assessment of seasonal and polluting effects on the quality of river water by exploratory data analysis. Water Research 32,

3581–3592.
Vesper, D.J., White, W.B., 2004. Storm pulse chemographs of saturation index and carbon dioxide pressure: Implications for shifting recharge sources during storm events in the karst aquifer at Fort Campbell, Kentucky/Tennessee, USA. Hydrogeology Journal 12, 135–143. https://doi.org/10.1007/s10040-003-0299-8
Vigna, B., Doleatto, D., 2008. La circolazione idrica nella zona non satura di Bossea. In: Gili, R., Peano, G. (Eds.), Ambiente Carsico: I Progressi Degli Studi in Italia Sulla Soglia Del XXI Secolo. Bossea, 21–22 Maggio 2005. Stazione Scientifica di Bossea CAI Cuneo, Cuneo, 51–63.
Vigna, B., Fiorucci, A., Ghielmi, M., 2010. Relations between stratigraphy, groundwater flow and hydrogeochemistry in Poirino Plateau and Roero areas of the Tertiary Piedmont Basin, Italy. Memorie Descrittive Della Carta Geologica d'Italia 90, 267–292.
Vigna, B., Fiorucci, A., Lo Russo, S., 2011. Hydrogeology and groundwater quality in the quaternary alluvial deposits of the Cuneo Plain (NW Italy). GeoHydro2011, Quebec City (Canada), 28-31 August 2011. Quebec City (CA), 1–6.
Vigna, B., Fiorucci, A., Nannoni, A., De Waele, J., 2017a. Vadose Zone Hydrogeology In The Bossea Cave. In: Moore, K., White, S. (Eds.), Proceedings of the 17th International Congress of Speleology, Sydney, NSW, Australia, July 22-28, 2017. Australian Speleological Federation Inc. Sydney, 222–225.
Vigna, B., Peano, G., Villavecchia, E., De Waele, J., 2017b. The Karstological Subterranean Laboratory Of Bossea Cave (N Italy). In: Moore, K., White, S. (Eds.), Proceedings of the 17th International Congress of Speleology, July 22–28, Sydney, NSW Australia. Australian Speleological Federation Inc., Sydney, 447–451.
Weinberger, E., Rosenthal, G., 1998. Reconstruction of natural groundwater flow paths in the multiple aquifer system of the northern Negev (Israel), based on lithological and structural evidence. Hydrogeology Journal 6, 421–440.
White, W.B., 2002. Karst hydrology: Recent developments and open questions. Engineering Geology 65, 85–105. https://doi.org/10.1016/S0013-7952(01)00116-8
White, W.B., 1969. Conceptual models for carbonate aquifers. Groundwater 7, 15–21.
Whitherspoon, P.A., Wang, J.S., Iwai, K., Gale, J.E., 1980. Validity of the cubic law for fluid flow in a deformable rock fracture. Water Resources Research 16, 1016–1024.
Williams, P.W., 2008. The role of the epikarst in karst and cave hydrogeology: A review. International Journal of Speleology 37, 1–10. https://doi.org/10.2307/2423146
Williams, P.W., 1983. The role of the subcutaneous zone in karst hydrology. Journal of Hydrology 61, 45–67.
Willis, S.S., Johannesson, K.H., 2011. Controls on the geochemistry of rare earth elements in sediments and groundwaters of the Aquia aquifer , Maryland , USA. Chemical Geology 285, 32–49. https://doi.org/10.1016/j.chemgeo.2011.02.020
Wray, R.A.L., Sauro, F., 2017. An updated global review of solutional weathering processes and forms in quartz sandstones and quartzites Earth-Science Reviews An updated global review of solutional weathering processes and forms in quartz sandstones and quartzites. Earth-Science Reviews 171, 520–557. https://doi.org/10.1016/j.earscirev.2017.06.008
Wu, J., Li, P., Qian, H., Duan, Z., 2014. Using correlation and multivariate statistical analysis to identify hydrogeochemical processes affecting the major ion chemistry of waters: a case study in Laoheba phosphorite mine in Sichuan, China. Arabian Journal of Geosciences 7, 3973–3982. https://doi.org/10.1007/s12517-013-1057-4
Wu, X., Pan, M., Zhu, X., Cao, J., Zhang, M., 2018. Effect of extreme precipitation events on the hydrochemistry index and stable isotope compositions of drip water in a subtropical

cave, Guangxi, SW China. Carbonates and Evaporites 33, 123–131. https://doi.org/10.1007/s13146-017-0338-5
Zhao, L., Xia, J., Xu, C., Wang, Z., Sobkowiak, L., 2013. Evapotranspiration estimation methods in hydrological models. Journal of Geographical Sciences 23, 359–369. https://doi.org/10.1007/s11442-013-1015-9